

Soil-structure interaction of guardrail posts under static and dynamic loads

Mohamed Aly Mohamed Soliman

Vollständiger Abdruck der von der TUM School of Engineering and Design der Technischen Universität München zur Erlangung eines

Doktors der Ingenieurwissenschaften (Dr.-Ing.)

genehmigten Dissertation.

Vorsitz: Prof. Dr.-Ing. Martin Mensinger

Prüfende der Dissertation:

1. Prof. Dr.-Ing. Roberto Cudmani
2. Prof. Dipl.-Ing. Dr. techn. Dietmar Adam
3. Prof. Dr.-Ing. Frank Rackwitz

Die Dissertation wurde am 19.12.2023 bei der Technischen Universität München eingereicht und durch die TUM School of Engineering and Design am 27.06.2024 angenommen.

Preface

Vehicle Restraint Systems must contain the colliding vehicles and absorb the impact energy to reduce the acceleration acting on the vehicles' occupants in different crash scenarios. Both requirements are concurrent: fulfilment of the first condition requires a deflection limitation, whereas absorbing the impact energy requires the VRS to undergo large deformations and enter the plastic regime. Besides the performance, other requirements, such as minimising material consumption and costs, facilitating installation and maintenance, and minimising the impact on other road users (e.g. pedestrians and cyclists), must be considered in the design of VRS.

Owing to this complexity, certification of Vehicle Restraint Systems (VRS) requires an assessment of the system's dynamic response as a whole. According to European regulations, this process entails full-scale crash tests, component tests and finite element analyses (FEA). Particularly in the FEA, it is often assumed that the behaviour of the structural elements primarily governs the response of a VRS, while the soil and soil-post interaction, extremely simplified in the simulations, plays a negligible role. For this reason, systematic experimental investigations of the soil-post interaction are rare, and experimentally validated numerical models to describe the nonlinear load-deflection behaviour and predict the horizontal bearing capacity of the post in crash test simulations of VRS are missing in the literature. In principle, guardrail posts are similar to single piles under lateral loading, but other than piles they must undergo deformations of multiple times the diameter, and even fail during a vehicle collision to ensure sufficient impact energy dissipation. These particularities limit the transferability of the knowledge of laterally loaded piles to guardrail posts.

In this context, Mohamed Soliman's research focuses on the experimental testing of the single post under lateral monotonic and dynamic loading and the development of numerical models to realistically simulate this interaction. The series of static and dynamic loading tests conducted under controlled conditions, including various soil types and densities, post types, and loading axes, combined with the soil characterisation, is so far unique. Owing to the high quality of the experimental data, the conclusions regarding the influence of the considered variables on the post behaviour are highly reliable.

The modelling of the soil-post interaction with the finite element method, including geometric and material nonlinearity, is the second highlight of the thesis. The parametric investigations with the validated models revealed the significance of the different influencing quantities on the performance of the posts under static and dynamic loading, and complemented the knowledge gained from the experiments. Assessing the single post response considering the absorbed energy and the maximum deceleration is an innovative idea, which can be used to select a post type and embedment depth that fulfils specific performance requirements for given soil conditions. The developed Lumped-Parameter Model (LPM), which is much more efficient than FEA, can be calibrated based on laboratory experiments and used for the simulation of the soil-post interaction in crash event simulations.

With his research, Mohamed Soliman has improved the state of the art in testing and modelling the soil-post interaction and notably contributed to understanding its role in the complex mechanical behaviour of VRS.

Acknowledgement

The success of this research project is a resultant of the author's effort and the support of many persons, to whom I would like to express my gratitude. I would like to deeply thank *Prof. Dr.-Ing. Roberto Cudmani* for giving me the opportunity to join the Chair of soil mechanics and foundation engineering at the Technical university of Munich. I worked on this thesis under his supervision during my employment time as a research associate.

The experimental and numerical work in this thesis was conducted in the framework of the research project "Auswirkung des Bodens auf das Verhalten von Fahrzeug-Rückhaltesystemen" in cooperation with TÜV-Süd and was financed by the German federal highways' authority BAST. I gratefully acknowledge the support of the BAST as project controller and TÜV-Süd as project partner. Many thanks to *Dr.-Ing. Daniel Rebstock* for his technical support and guidance throughout the research project.

I would like to show my gratitude to all my colleagues for the friendly technical discussions and helpful tips. Special thanks go to the laboratory and field services team for their support during the exhausting experimental work phases.

No adequate words can describe my gratitude to my wife, *Maha Elansary* and my daughters *Jana & Hana*. They gave me the motivation to continue this journey and endured hard times with me.

I would like to dedicate this doctoral thesis to my parents, *Dr. Aly & Samia*, to whom I owe all success in my life. Without their continuous support and encouragement, it would have been impossible to finish this thesis. I extend my thanks to my siblings and especially to my brother, *Dr. Mahmoud Osman*, for his technical and spiritual support.

Last but not least, I would like to thank and praise the almighty God, who gave me the knowledge and power to accomplish this work.

Abstract

The response of steel vehicle restraint systems (VRS) is governed by many factors, where the interaction between the soil and the vertical post plays a significant role in preventing fatal accidents. A VRS is responsible for containing and redirecting errant vehicles in a crash event and protecting the occupants from serious injuries. So far, there is no unified method to model the soil-structure interaction of guardrail posts embedded in soil in crash test simulations. The influence of the soil properties and post characteristics on the crash test simulations' results is not clearly defined.

In this study, we investigated this aspect experimentally and numerically to contribute to the standardisation of the crash test simulations as a part of the VRS certification process. First, a series of full-scale field tests were conducted on single posts in selected standard road shoulder materials under quasi-static and impact loading to evaluate the soil-post interaction. The novel approach applied in the field testing allows for comparing separate influence factors, e.g. soil type, post characteristics and impact intensity, while keeping all other conditions unchanged. The road shoulder materials were tested extensively in the laboratory to determine the soil mineralogy, grain characteristics and mechanical properties. The field testing results show that the soil's relative density and the post embedment length are the most significant factors influencing the post response and failure mechanism.

In the next step, the soil-post interaction is investigated using the finite element method (FEM) under quasi-static and dynamic impact loading. The soil is modelled using an advanced hypoplastic constitutive relationship. For comparison with the common practice, the soil is also modelled using a conventional elastoplastic model. The material models are calibrated using the results of the laboratory tests conducted on soil and post material specimens. The FE models were then validated using the conducted full-scale field tests. A parametric study was carried out to investigate the influence of selected factors on the soil-post response. Based on the investigation results, performance assessment criteria were developed for the single post.

The experience acquired from the experimental and numerical investigations was then compiled to develop a computationally efficient Lumped-Parameter Model (LPM). In this model, the system's mechanical properties are simulated by rheological elements. The simulation results were compared to the conventional approaches available in the literature and applied standards for the analysis of laterally loaded piles. With the help of the LPM, the single post response could be simulated consistently under quasi-static and impact loading. The performance of the developed numerical models was evaluated with respect to the experimental data using statistical methods. The results show that the developed numerical modelling techniques are able to simulate the post response with sufficient accuracy.

The research findings based on the conducted comprehensive investigations provide a deeper understanding of the soil-post interaction under different loading conditions. The proposed numerical modelling techniques contribute to more realistic crash test simulations based on experimental data. The study conclusions and recommendations can be considered in the testing and development of VRS, allowing for safer and more economical design based on a realistic soil-post interaction.

Keywords: Soil-structure interaction, guardrail posts, impact loading, numerical modelling, crashworthiness

Kurzfassung

Das Tragverhalten von Fahrzeug-Rückhaltesystemen (FRS) aus Stahl wird von vielen Faktoren bestimmt, wobei die Wechselwirkung zwischen dem Boden und dem vertikalen Pfosten eine wichtige Rolle bei der Verhinderung tödlicher Unfälle spielt. Ein Fahrzeug-Rückhaltesystem hat die Funktion, von der Fahrbahn abkommende Fahrzeuge umzulenken und die Insassen vor schweren Verletzungen zu schützen. Bislang gibt es kein geotechnisch validiertes Verfahren zur Modellierung der Boden-Bauwerk-Interaktion von in Boden eingebetteten Leitplankenpfosten in Crashtest-Simulationen. Der Einfluss der Boden- und der Pfosteneigenschaften auf das Verhalten in Crashtest-Simulationen ist bisher nicht eindeutig quantifiziert.

In dieser Studie wurden experimentelle und numerische Untersuchungen durchgeführt, um zur Standardisierung von Crashtest-Simulationen als Teil des Zertifizierungsprozesses von FRS beizutragen. Zunächst wurde eine Reihe von Probelastungen an einzelnen Pfosten in ausgewählten Bankettmaterialien unter lateraler quasi-statischer und dynamischer Belastung durchgeführt, um die Boden-Pfosten-Interaktion experimentell zu untersuchen. Das neuartige Versuchskonzept, das bei den Feldversuchen angewandt wurde, ermöglicht den Vergleich einzelner Einflussgrößen, z. B. des Bodenzustands, der Pfosteneigenschaften und der Aufprallenergie. Andere Einflussgrößen blieben dabei unverändert. Die Bankettmaterialien wurden im Labor umfangreich getestet, um die Mineralogie, die Kornbeschaffenheit und die mechanischen Bodenkennwerte zu bestimmen. Die Ergebnisse der Feldversuche zeigen, dass die Lagerungsdichte des Bodens und die Einbindelänge des Pfostens die Hauptfaktoren sind, die die Systemreaktion und den Versagensmechanismus bestimmen.

Im folgenden Schritt wurde die Boden-Pfosten-Interaktion mit Hilfe der Finite-Elemente-Methode (FEM) unter Verwendung von Kontinuumselementen bei verschiedenen Belastungsbedingungen untersucht. Dabei wurde der Boden mit dem hochwertigen hypoplastischen Stoffgesetz modelliert. Um die Ergebnisse mit der gängigen Praxis zu vergleichen, wurde das Bodenverhalten in weiteren Simulationen mit einem elasto-plastischen Stoffgesetz modelliert. Die Stoffmodelle wurden anhand der Ergebnisse von Laborversuchen an Boden- und Stahlproben kalibriert. Die FE-Modelle wurden dann mit Hilfe der Feldversuchsergebnissen validiert. Die validierten FE-Modelle wurden für eine Parameterstudie verwendet, um den Einfluss ausgewählter Parameter auf die Boden-Pfosten-Interaktion zu untersuchen. Auf der Grundlage der Untersuchungsergebnisse wurden Kriterien zur Leistungsbeurteilung für den einzelnen Pfosten entwickelt.

Die aus den experimentellen und numerischen Untersuchungen gewonnenen Erfahrungen wurden dann zur Entwicklung eines rechnerisch effizienten Lumped-Parameter-Modells (LPM) zusammengeführt. In diesem vereinfachten Modell werden die maßgebenden mechanischen Eigenschaften des Systems, z. B. nichtlineare Elastizität, irreversible Verformungen, Massenträgheit und Energiedissipation, durch idealisierte rheologische Elemente simuliert. Die Ergebnisse wurden mit den in der Literatur und Normen verfügbaren Ansätzen für die Berechnung von horizontalbelasteten Pfählen verglichen. Mit Hilfe des entwickelten LPM konnte die Reaktion der einzelnen Pfosten konsistent simuliert werden. Schließlich wurden die numerischen Modelle mit den Versuchsdaten verglichen und die Leistung der Modelle statistisch ausgewertet.

Die Ergebnisse zeigen, dass die entwickelten numerischen Modellierungsverfahren in der Lage sind, die Boden-Pfosten-Interaktion realitätsnah nachzubilden.

Die Forschungsergebnisse, die auf den durchgeführten umfassenden Untersuchungen beruhen, ermöglichen einen vertieften Einblick in die Boden-Pfosten-Interaktion unter verschiedenen Belastungsbedingungen. Die vorgeschlagenen numerischen Modellierungsverfahren tragen zu realistischeren Crashtestsimulationen auf der Grundlage experimenteller Daten bei. Die Schlussfolgerungen und Empfehlungen dieser Forschungsarbeit können in den Prüf- und Entwicklungsprozessen von FRS für einen sicheren und wirtschaftlichen Entwurf auf Grundlage eines realistischen Tragverhaltens miteinbezogen werden.

Schlüsselwörter: Boden-Bauwerk-Interaktion, Leitplankenpfosten, Anprallbelastung, Numerische Modellierung, Crashverhalten

Content

ACKNOWLEDGEMENT	I
ABSTRACT.....	II
KURZFASSUNG	III
CONTENT.....	V
1 INTRODUCTION.....	1
<i>Research questions and methodology.....</i>	<i>3</i>
<i>Thesis organization.....</i>	<i>5</i>
2 LITERATURE REVIEW	6
<i>Experimental investigation of guardrail posts under lateral loading</i>	<i>6</i>
<i>Numerical simulation of guardrail posts behaviour.....</i>	<i>8</i>
<i>Analysis of post response under lateral static loading.....</i>	<i>9</i>
<i>Analysis of post response under lateral dynamic loading</i>	<i>13</i>
3 FULL-SCALE TESTING OF SINGLE POSTS.....	19
3.1 EXPERIMENTAL TESTING PROGRAM	20
<i>Selection of soil materials</i>	<i>22</i>
<i>Soil mineralogy and grain strength</i>	<i>27</i>
<i>Grain shape characteristics.....</i>	<i>29</i>
<i>Soil placement and in-situ testing</i>	<i>32</i>
<i>Vehicle restraint system.....</i>	<i>35</i>
<i>Post properties and installation</i>	<i>38</i>
3.2 STATIC LOADING TESTS	40
<i>Instrumentation and test procedure</i>	<i>42</i>
<i>Reference test results</i>	<i>48</i>
<i>Variation of loading axis.....</i>	<i>51</i>
<i>Variation of soil material</i>	<i>53</i>
<i>Variation of embedment length.....</i>	<i>55</i>
<i>Variation of post-section.....</i>	<i>56</i>
3.3 DYNAMIC LOADING TESTS	57
<i>Instrumentation and test procedure</i>	<i>58</i>
<i>Reference test results</i>	<i>64</i>
<i>Variation of post-section.....</i>	<i>70</i>
<i>Variation of loading axis.....</i>	<i>72</i>
<i>Variation of soil material</i>	<i>74</i>
<i>Variation of soil relative density.....</i>	<i>76</i>
<i>Variation of embedment length.....</i>	<i>78</i>
3.4 DISCUSSION AND CONCLUSIONS	79
4 LABORATORY TESTING OF SOIL MATERIALS	82
<i>Classification and identification tests.....</i>	<i>82</i>
<i>California bearing ratio tests</i>	<i>85</i>
<i>Large-Oedometer tests</i>	<i>86</i>
<i>Triaxial compression tests.....</i>	<i>88</i>
<i>Angle of repose tests</i>	<i>91</i>

5	NUMERICAL ANALYSIS	92
5.1	FINITE ELEMENT MODEL	93
5.2	MATERIAL MODELS AND PARAMETERS CALIBRATION.....	99
	<i>Hypoplastic soil model</i>	99
	<i>Steel and rubber material models</i>	104
5.3	VALIDATION OF THE FE MODEL	107
	<i>Simulation of the quasi-static loading tests</i>	108
	<i>Influence of the mesh discretisation</i>	114
	<i>Influence of the transition body geometry</i>	115
	<i>Simulation of the impact loading tests</i>	117
	<i>Influence of model boundary extent</i>	123
5.4	SIMULATIONS USING AN ELASTOPLASTIC SOIL MODEL.....	126
5.5	PARAMETRIC STUDY	132
	<i>Variation of soil relative density</i>	133
	<i>Effect of Layering: Loose layer</i>	138
	<i>Effect of Layering: very dense layer</i>	140
	<i>Variation of embedment length</i>	142
	<i>Variation of loading height</i>	148
	<i>Variation of section modulus</i>	153
	<i>Variation of post-section</i>	157
5.6	DISCUSSION AND CONCLUSIONS	161
6	ANALYSIS OF SOIL-POST INTERACTION BY MEANS OF LPM.....	167
6.1	EXPERIMENTAL P-Y CURVES	167
6.2	LUMPED-PARAMETER MODEL FOR GUARDRAIL POSTS	173
	<i>Components of the soil resistance model</i>	175
	<i>LPM performance under quasi-static loading</i>	185
	<i>LPM performance under impact loading</i>	191
6.3	DISCUSSION AND CONCLUSIONS	195
7	SUMMARY AND CONCLUSIONS	201
8	RECOMMENDATIONS AND PERSPECTIVES.....	204
	REFERENCES	206
	APPENDIX [A]: IN-SITU SOIL TESTING	212
	APPENDIX [B]: LABORATORY TEST PROTOCOLS	215
	APPENDIX [C]: QUASI-STATIC TESTS	219

1 Introduction

Road safety is a vital factor influencing the well-being of communities and is a catalyst for initiating a large sector of projects. Safe roads are essential for a prosperous economy and a healthy society. Due to its interdisciplinary nature, road safety has always been a challenge for engineers in modern times. Several engineering fields are involved in realising road safety, amongst others, Transportation and Traffic engineering, Automobile engineering, Structural and Geotechnical engineering.

The main target of road safety engineering is to reduce the risk and severity of crash events and reduce casualties. Longitudinal road barriers are one of the most important road infrastructure elements that function to achieve this target. These are also known as Guardrails or Vehicle Restraint Systems (VRS). As per DIN EN 1317-1 [22] and the technical specifications ZTV FRS [97], the function of a VRS is to contain and redirect an errant vehicle and prevent it from crashing into the existing road structures. In addition to these functions, the Quality Association for steel VRS in Germany (Gütegemeinschaft Stahlschutzplanken e.V.) requests from the manufacturers to develop economic VRS, i.e. have reasonable cost and effort for installation, maintenance and disposal of the sacrificial elements. Before installation of a VRS on the road, it has to fulfil specific crashworthiness criteria. Among them, the energy absorbed by the system is crucial for the safety of the vehicle occupants in a crash event.

The VRS is often installed on highways in the road shoulder. As per definition, the road shoulder is the part of the road cross-section adjacent to the carriageway, often delimited laterally by an embankment [97]. It does not serve vehicular traffic, but can be used in case of emergency, installations or maintenance. The road shoulder has a structural load-bearing function as well as a drainage function. During a crash event, the response of a VRS depends on the interaction between the VRS and the soil medium, i.e. the road shoulder material in which it is installed. Therefore, the role of Geotechnical engineering in the conception and design of efficient VRS cannot be ignored.

The kinetic energy of a vehicle colliding with the VRS is partially dissipated in deforming the VRS steel members, the errant vehicle, and the surrounding soil, as well as in mechanical waves propagating in the soil medium. The failure mode of the system is governed by the properties and conditions of the soil material as well as by the interaction of the VRS with the soil. Therefore, the understanding of this interaction under different loading conditions in different soil materials is essential to ensure the system's serviceability.

In this contribution, the institute of Soil Mechanics and Foundation Engineering at the Technical University of Munich (Zentrum Geotechnik) was assigned by the German federal highways' authority (BAST) to design and execute a research project in cooperation with TÜV- SÜD for the investigation of steel VRS behaviour embedded in soil. Our scope was the investigation of the soil-structure interaction of the single post, while TÜV-SÜD was responsible for the crash test simulations of the complete system.

In the framework of this research project, the influence of the soil material properties and state on the behaviour of VRS was examined and evaluated. In the preparatory phase, a literature review was carried out to identify the common soils and backfill materials encountered in the road shoulder, where the guardrail posts are installed. The particular focus is given to the soil classification, layering and properties from the earthworks' point of view.

Following that, the behaviour of the single post was investigated experimentally under lateral quasi-static and impact loads in various soil materials. Further parameters such as the post profile, section asymmetry, and loading direction were also considered. The soil's mechanical properties were identified experimentally through extensive laboratory tests. The stress level under which the parameters were determined is an essential aspect, since the post response is governed by the shallow layer properties, which is not usually the focus of conventional geotechnical problems.

In the next phase, numerical simulations implementing advanced constitutive material models were carried out and validated using the conducted field and laboratory tests. Different modelling techniques were investigated, and a comprehensive parametric study of the influence factors on the post response was performed. A numerically efficient lumped-parameter model for the soil-post interaction is developed in light of the experimental and numerical results.

Parallel to the investigations on single posts, two full-scale crash tests were conducted on a complete VRS utilizing standard test vehicles, according to the specifications of DIN EN 1317. The results of the experimental and numerical investigations on single posts were used by TÜV-SÜD in the development, validation and simulation of the crash tests and for further parametric studies.

Finally, the individual investigations and analysis outcomes were included in a research report in the form of conclusions and practice recommendations for the design of guardrail posts considering the soil and post characteristics.

Research questions and methodology

The soil properties and conditions, as well as the post-section characteristics, are decisive for the performance of a VRS. In a crash event, if the soil-post response is soft, i.e. the soil deforms excessively, the system will be inadequate to contain and redirect the vehicle. However, an excessively stiff soil-post response could jeopardise the safety of the vehicle occupants.

Based on a comprehensive literature review within the scope of the research project with TÜV-SÜD, the influence factors affecting the VRS response can be categorised into four groups, as shown in Fig. 1-1. In this research work, we will focus on the categories road shoulder and guardrail posts.

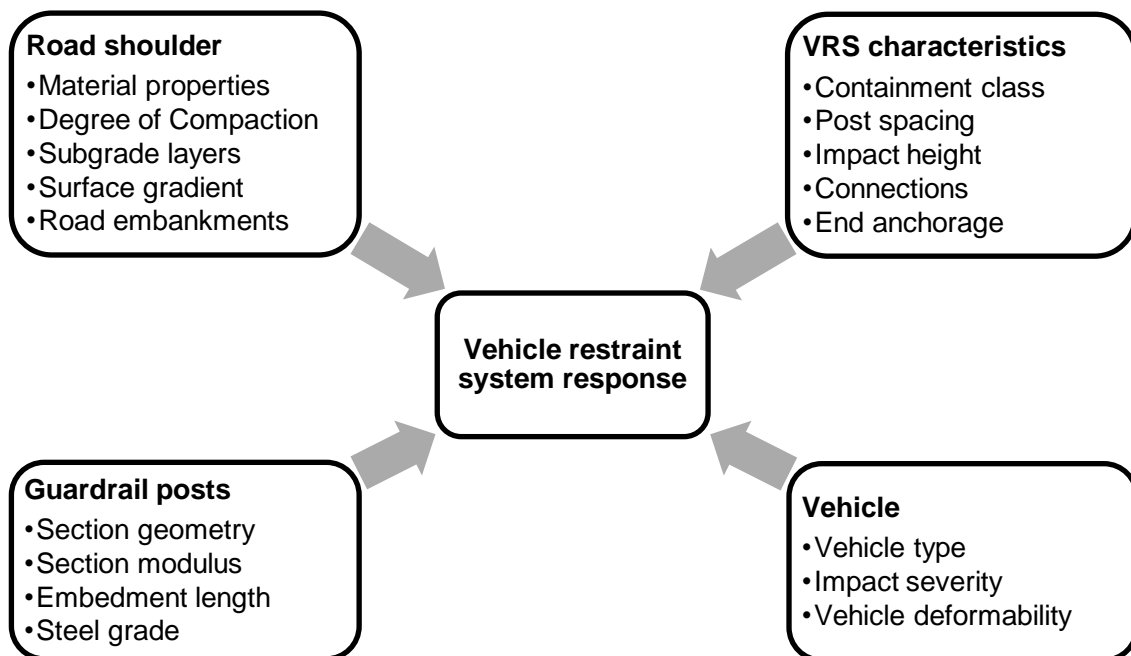


Fig. 1-1: The most relevant factors influencing the vehicle restraint system response

For the certification of a VRS, the system must be tested in a real crash test. From the geotechnical point of view, the current characterization and documentation of the soil of the testing field, as described in DIN EN 1317-5 [24] is insufficient. The soil is categorised based on a push- or pull-test conducted on a standard HEB120 post with an embedment of 1 m. The test specifies a standard loading rate (≤ 10 mm/s) up to 40 cm deflection. Based on the measured load-deflection curve, the soil is categorised as rigid, hard, medium or soft. This categorization does not give any information about the soil material, relative density or mechanical properties, which generally govern the soil-structure interaction. It is observed through experimental tests that the same results can be obtained in soils exhibiting different materials and different compaction levels, mainly if the soil contains coarse gravel or cobbles. Moreover, this indirect test assesses the soil-post response under quasi-static loading conditions, which differs from the crash test's dynamic loading conditions. Due to inertial effects and the higher loading rate, the soil resistance during impact loading is expected to differ considerably from the static resistance. A further important aspect is the representability of the testing field soil for the road shoulder material installed on the highways.

With the continuous development and availability of powerful computer processors, numerical simulations offer a more economical and time-saving alternative for real crash tests. The standard DIN EN 16303 [26] specifies the requirements and the methodology for the validation and verification of the numerical models of VRS and vehicles in crash test simulations. However, the modelling technique of the embedment soil, as well as the interaction properties with the post, is not specified. This deficiency opens the door for unrealistic modelling methods of the soil-post interaction, which can lead to unreliable simulation results.

The inadequate characterization of the testing soil in the certification crash test can result in an inaccurate assessment of the VRS performance. Moreover, the lack of requirements for modelling the soil-structure interaction is a deficit of the standards that needs to be clarified in a research framework. In general, the misprediction of a VRS containment level can jeopardise the safety of road users and even lead to fatal accidents.

The overarching goal of this doctoral thesis is to close this knowledge gap between road safety engineering and geotechnical engineering. The main questions that were investigated in this research can be formulated as follows:

- What is the influence of the soil properties, including grain shape, grain hardness, grain size distribution and relative density, on the soil-post interaction?
- What is the influence of the post characteristics, including embedment length, cross-section and symmetry, on the total resistance and the failure mechanism?
- Is a quasi-static loading test in-situ enough to evaluate the post performance under impact loading?
- How can the soil-post interaction be modelled realistically in crash test simulations?

To investigate and analyse the above-mentioned aspects, experimental and numerical methods were applied. A program of full-scale field tests is carried out to understand the behaviour of guardrail posts embedded in different soil materials under different loading conditions. The selected road shoulder materials are tested in the laboratory and in-situ to determine the soil material properties and in-situ condition. Since the systematic testing of all influence factors in-situ is expensive and highly time-consuming, some influence factors, e.g. relative density and post embedment length, are tested numerically. The acquired results build a basis for the development and validation of finite element models (FE models). First, the results of the field tests and the interpreted soil parameters are used to validate a FE model for the simulation of the quasi-static test. Then, utilizing the validated FE model, and with minor modifications, the dynamic impact test is modelled. The dynamic simulations comprise posts exhibiting the same properties and soil conditions impacted by four different energy levels. Two different constitutive soil models have been applied for comparison: an advanced hypoplastic soil model and a common elastoplastic model with Mohr-Coulomb failure criteria. Based on the experimental and numerical investigation results, a Lumped-Parameter Model (LPM) is developed to simulate the soil-post response under different loading conditions. The advantage of the LPM is that it is computationally less expensive compared to the FE continuum model. For a dynamic single post simulation, the application of the LPM can save up to 95% of the time required using the same processor.

The conclusions and recommendations of the research shall be transferred to the practice, and implemented in field testing and numerical simulations of crash tests.

Thesis organization

This thesis comprises five main sections, investigating the soil-post interaction and the influence factors governing the post response, according to the proposed methodology.

In the first section, the theoretical background of the guardrail posts problem is discussed, and the relevant literature and standards are reviewed. The different approaches considered for the analysis of the post response under static and dynamic loading are discussed and compared to the conventional methods for design of laterally loaded piles.

In the second section, the experimental full-scale tests conducted on single posts under quasi-static and dynamic impact loading are presented and discussed. The results of the laboratory testing of the soil materials, in which the posts were tested, are presented in this section.

In the third section, the conducted field tests are simulated numerically using the finite element method. The parameters required for the constitutive models of the soil materials are determined from the laboratory test results. Using the validated numerical models, a parametric study is conducted to examine the influence of the mechanical soil properties and the post characteristics on the post response.

In the fourth section, the soil-structure interaction of the posts is analysed. A multi-degree of freedom lumped-parameter model is developed to simulate the single post's behaviour under lateral quasi-static and impact loading. The input quantities required for the model components are determined from the executed experimental field and laboratory tests and the numerical simulations. A calibration routine is proposed for the determination of the model parameters. The performance of the LPM and the FE models, in which the soil is modelled as continuum elements, is compared to the field tests.

Finally, the most important results and conclusions of the investigations conducted using the experimental and numerical methods are summarised. Based on the study findings, the most significant factors influencing the post response are illustrated. Recommendations are drawn for the testing and simulation of the soil-post interaction, to be considered in crash test simulations and VRS design.

2 Literature review

Despite their relatively small cross-section, guardrail posts can be considered as single piles under lateral loading. A structural pile fails to fulfil its function, when one of the following failure modes is reached [10]:

- The horizontal soil bearing capacity is exceeded, resulting in large translatory or rotational deformations of the pile, i.e. geotechnical failure.
- The loading may generate excessive bending or shear stresses in the pile material, leading to failure of the pile material, i.e. structural failure.
- The loading may induce large pile deflections that impair the serviceability of the structure.

However, in a crash event, guardrail posts are susceptible to large deflections and may experience either geotechnical or structural failure. Further, the guardrail post embedment is relatively short, i.e. the shallow soil layer neglected in most conventional geotechnical applications is very relevant for the post behaviour. These factors limit the transferability of the pile design methods to the guardrail posts. Moreover, the design criteria for guardrail posts differ from those of foundation piles in terms of serviceability. For a guardrail post, large deformations exceeding the conventional failure criteria in geotechnical engineering practice (e.g. 10% of the pile diameter as per EA-Pfähle [36]) are allowed, as long as the function of containing and redirecting a vehicle in a crash event is fulfilled. Due to the nature of the impact loading in a crash event, the dynamic loading is not harmonic and is unknown in advance. Therefore, the dynamic frequency-dependent analysis approaches for machine foundations or piles under alternating loading cannot be transferred directly for guardrail post analysis. Moreover, the VRS posts mobilised in a crash event are loaded with different intensities depending on their distance from the collision point, which increases the complexity of the problem.

Due to the reasons mentioned above, the conventional design approaches for piles cannot be applied directly to guardrail posts.

Experimental investigation of guardrail posts under lateral loading

Many researchers have investigated the behaviour of guardrail posts embedded in soil under static and dynamic loading. A brief survey of selected studies focusing on the soil-post interaction is presented here.

MICHIE [53] conducted in 1970 a series of static and dynamic pendulum tests on timber posts in two soil types. The first was uniformly graded sand placed by flooding without compaction, and the second was well-graded gravel placed and compacted in layers. The study concluded that the post resistance is directly related to the soil shear strength under both loading conditions. The ratio between the dynamic-to-static resistance force at a given deflection was found to range between 2 and 4, depending on the soil type. This ratio was interpreted for an impact energy range between 2 and 46 kJ. However, no relation could be established between the dynamic and static response as a function of the post or soil properties.

DEWEY et al. [15] performed similar tests in 1983 with the aim of comparing the dynamic and static post response. A cable-driven massive cart resembling a vehicle was used for the

dynamic loading. It was observed that the maximum dynamic post resistance at an impact velocity of 8 m/s is approximately 6-fold the static resistance in well-graded crushed limestone. The impact energy cannot be determined as the cart mass is not mentioned.

The dynamic impact tests conducted by COON et al. [11] in 1999 using a bogie vehicle in coarse subbase material showed primarily soil failure and rotation of the posts. The post resistance increased significantly by increasing the impact energy up to 38 kJ (at 9 m/s). For higher impact velocities, no measurable increase in the reaction force or the absorbed energy was observed [11].

WU & THOMSON [95] performed in 2007 dynamic impact tests and quasi-static tests on sigma-posts embedded in gravel. The posts were hit in the impact test using a bogie vehicle with a velocity of 5 m/s, generating an impact energy of 12.9 kJ. The results show that the ratio between the maximum dynamic force and the maximum quasi-static force was about 2. Worth mentioning is that the loading rate of 200 mm/s applied in the quasi-static tests is relatively high compared to the maximum loading rate of 10 mm/s as prescribed in the DIN EN 1317-5 for post loading tests in soil [24]. An increase of the loading rate may lead to overestimation of the static reaction force due to triggering inertial effects of the soil and post, or even due to undrained behaviour in cohesive soils.

In 2015, BIELENBERG et al. [4] executed a series of dynamic tests on C- and I-section posts embedded in coarse crushed limestone. The loading was applied once in the strong axis and once in the weak axis. A comparison of the maximum resistance in the weak axis to the strong axis shows a reduction of about 35 to 50% for both section types. The failure mode observed was bending and twisting of the posts under an impact energy of approximately 35 kJ [4]. Whether the failure in both post-sections was mainly due to twisting or bending is not further discussed. This information is important, since the C-section is asymmetric in the strong axis and the centre of shear is shifted from the centre of area.

In all the studies mentioned above, no laboratory tests were conducted to evaluate the mechanical behaviour of the embedment soil. The soil was characterised solely based on the material classification and the in-situ test results.

ATAHAN et al. [3] recently conducted in 2019 dynamic pendulum tests on C120 posts to determine the optimum embedment depth in three different soil conditions. The pendulum was set to apply an impact energy of 14.7 kJ in all tests. The soil consisted of poorly graded sand (as per USCS classification) with relative densities of 25%, 57% and 84%. The results were evaluated based on the energy absorbed by the post and the observed post and soil deformations. It was found that posts with embedment of 0.8 m in loose soil, 0.75 m in medium dense soil, and 0.70 m in dense soil can absorb equal energies without either buckling or pulling out of the ground. The systematic testing of the posts provides convenient results for the post optimization process with respect to the soil's relative density. No static tests have been conducted as a reference. The study included the determination of the shear strength parameters through laboratory tests. However, these were not correlated to the lateral post resistance.

The conclusions from the experimental studies discussed above show the necessity of further systematic investigations of the soil-post interaction and the influence on the post resistance with the variation of the soil condition and mechanical properties. Moreover, the variation of

the impact intensity has to be considered in the dynamic tests. This is due to the fact that the posts involved in a crash event are subjected to different impact energy levels depending on their distance from the crash location. Based on the impact intensity, the post deflection ranges from complete yielding of the post section or reaching the lateral bearing capacity to imperceptible quasi-elastic vibration.

Numerical simulation of guardrail posts behaviour

The soil-post interaction can be modelled in the crash test simulations using different techniques. Regarding the finite element method, the soil can be modelled using continuum elements or rheological models consisting of masses, springs and dashpots. Based on the model purpose, the post can be modelled either using beam or shell elements resembling the section geometry.

In its simplest form, the post can be modelled as a two-dimensional beam with a translation and rotation fixation at a predefined depth. This approach was adopted by RAY & PATZNER [71] for the simulation of VRS posts under collision. In this case, only the post deflection is captured, and the soil deformation due to eventual post translation and rotation is neglected. This assumption leads to an overestimation of the soil-post stiffness in medium and soft soils, as the failure mode is a combination of post rotation and lateral translation, as observed in our full-scale field tests (see 3 *Full-scale testing of single posts*).

To simulate the system response more realistically, the soil-post interaction can be modelled as a beam supported by elastic subgrade in the lateral direction, i.e. Winkler model. This approach was utilised by PLAXICO et al. [66] in a finite element model to simulate single wooden posts embedded in soil under impact loading. The horizontal subgrade modulus, i.e. spring coefficients, was estimated as a function of the effective overburden pressure and the lateral deflection as per HABIBAGAH & LANGER [38]. However, this approach requires extensive calibration, as it incorporates a lateral bearing capacity factor N_q , which is determined empirically from experimental conventional pile test data. The non-linear subgrade method was extrapolated by PLAXICO et al. [66] beyond the test data to account for large deformations. Moreover, the horizontal subgrade modulus was assumed to be independent of the loading type, whether static or dynamic, which is unrealistic.

The approach was further developed by SASSI & GHRIB [79] to consider the inertial effects and damping of the soil under impact loading by incorporating dashpots and point masses to form a lumped parameter model (LPM). A FE continuum model and an experimental field test were used to calibrate and validate the LPM. The lumped mass was determined from the FE model in each depth increment based on an assumed threshold displacement of 2 mm. The soil damping is considered as a dashpot in the model, and its coefficient was determined through back-analysis and calibration to a dynamic post test conducted by COON et al. [11]. They concluded that the lumped mass mobilised in the impact is depth-dependent, and a gap between the post and the springs has to be introduced to account for the installation effects of the post [79]. In a further study using the same model, they found that the maximum reaction force and deflection increase linearly with the impactor velocity. The peak force was found to be directly proportional to the soil density [80]. Although the LPM is computationally efficient compared to the FE approach, the calibration of the LPM requires a FE model as well as experimental data. Moreover, the LPM parameters were calibrated to a single test with a

certain impact energy. However, the LPM parameters may vary, if the model is calibrated to a field test with a different impact intensity.

Many researchers utilised the Lagrangian FEM to model the soil-post interaction. The most common constitutive soil models used for this purpose are the models available in the FE-code LS-DYNA [49], e.g. DRUCKER-PRAGER model, applied by BLIGH et al. [5], Soil & Concrete model, applied by WU & THOMSON [95], and FHWA soil model, applied by WOO et al. [93]. These models are mainly elastoplastic constitutive relations with additional selected material features. For example, the FHWA soil model incorporates strain hardening, strain softening or strain-rate dependency.

Further modelling techniques that can be applied to model the soil-post interaction include the Arbitrary Lagrangian-Eulerian FEM (ALE), Discrete Element Modelling (DEM) and Smoothed particle Hydrodynamics (SPH). WOO et al. [93] utilised a hybrid approach combining three-dimensional FEM and meshless SPH to model posts near embankment slopes. The purpose of the SPH method was to overcome the numerical problems due to large mesh distortions in soil elements generated by the post deflections. The SPH particles are defined only in the post vicinity. The FEM elements and SPH nodes are modelled using the FHWA soil model with standard parameters with minor modifications. The results were compared only to quasi-static test results, since no impact tests were conducted. In comparison to a Lagrangian FE model, the hybrid approach showed lower post resistance. This may be attributed to the large distortion effect of the soil meshes in the Lagrangian FE mesh, as mentioned by WOO et al. [93]. Further, the soil parameters were assumed without experimental test data. However, the approach seems to be appropriate for modelling posts close to embankments, where FEM suffer numerical instabilities.

Analysis of post response under lateral static loading

In general, laterally loaded piles are subjected either to active or passive lateral loading [73]. Active loading refers to loads imposed by the structure on the pile top, for example, pile foundation under wind loads, breasting dolphins in a harbour or guardrail posts in a crash event. Passive lateral loading refers to loads induced by soil movement relative to the pile, e.g. piles used for slope stabilisation. This categorisation is not to be confused with the active and passive earth pressure. Active pile loading can be categorised based on the nature of the applied load [36]. Loads exhibiting a constant magnitude and direction over time are defined as static loads. A quasi-static load is a load applied at a very slow rate, so that the inertial and damping effects can be neglected. At each time increment, the pile is considered in equilibrium with the applied load and can be analysed as an analogue to piles under static loads.

The German Recommendations for Pile foundations "EA-Pfähle" [36] categorises the transient time-dependent actions on piles into cyclic, dynamic and impact loads. However, this categorisation of transient loads shows overlapping in some applications, where the loads can fall into more than one category. Cyclic loads refer to repeated low-frequency actions, such as water waves and wind, where the inertial effects on soil and pile can be neglected. Dynamic loads refer to actions triggering considerable inertial effects, like in the case of earthquakes and machine foundations. Dynamic loads can be periodic or non-periodic. Impact or pulse-like loads refer to non-periodic actions that act once on the structure in a relatively short time duration. This duration can be in the range of milliseconds, like an explosion or a collision. An impact load is characterised by the rise time, the maximum value and the pulse duration.

The approaches applied to analyse laterally loaded piles under static loads can be classified into the following categories [73]:

- **Limit state methods** (e.g. BLUM [6], HANSEN [39], BROMS [9]):

This method considers the pile as a rigid element, and the behaviour of the surrounding soil is assumed to be rigid-plastic with a yield condition according to Mohr-Coulomb (drained conditions) or Tresca (undrained conditions). Based on this assumption, the equilibrium at the limit state can be established to determine the ultimate lateral soil resistance. Thus, this method provides an upper limit value of the straining actions on the pile. The method is not appropriate for verification of the serviceability, i.e. pile deflections and rotations.

One of the most common ultimate capacity methods is the approach proposed by BROMS [9] in the 60's. He classified the laterally loaded pile behaviour based on the embedment length into short and long piles. For short piles in cohesionless soil with free-head condition, the soil resistance distribution is assumed, as shown in Fig. 2-1. The pile is unrestrained against rotation, and soil failure is reached. The ultimate lateral resistance is equal to three times the Rankine passive pressure (see Equ. 2-1). For a long pile with free-head condition in cohesionless soil, BROMS assume the failure to occur in the pile material and a plastic hinge is formed at an assumed depth below ground level. No criteria were given to differentiate short from long piles. Due to the several assumptions and simplifications, the approach is only useful for preliminary pile design.

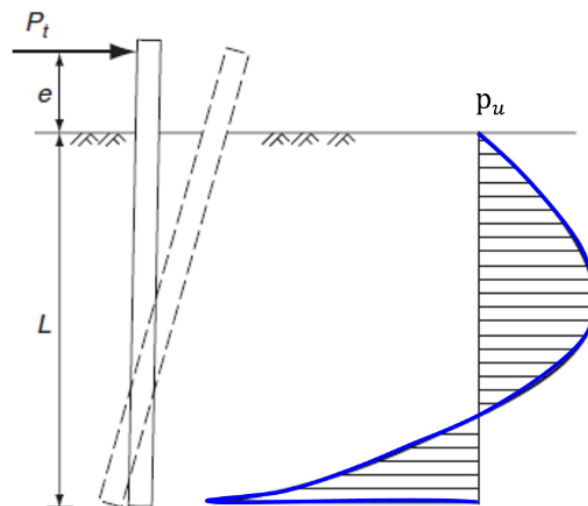


Fig. 2-1: BROMS method for short piles in cohesionless soil [73]

$$P_t = \frac{\gamma \cdot D \cdot L^3 \cdot K_p}{2(e + L)} \quad \text{Equ. 2-1}$$

P_t	[kN]	maximum lateral load
γ	[kN/m ³]	soil unit weight
D	[m]	pile width
L	[m]	embedment length
e	[m]	lever arm above ground level
K_p	[-]	coef. of passive earth pressure
p_u	[kN/m]	ultimate soil resistance per unit length

- **Elastic continuum method** (e.g. POULOS & DAVIS [67]):

In this method, the subsoil is modelled as a homogeneous, isotropic elastic half-space. The pile is also regarded as an elastic material. The deformations are calculated as a function of the force at any point in the interior of the half-space. This method is not commonly used due to its limitation to consider large soil deformations, i.e. the non-linear behaviour of soil and pile.

- **Subgrade reaction method** (e.g. TERZAGHI [89]):

In this method, the pile is modelled as a one-dimensional beam supported by linear-elastic perfectly-plastic springs (also known as the Winkler model). The soil spring coefficient is the subgrade reaction modulus and is defined as the quotient of the lateral soil resistance per unit length by the corresponding pile deflection. The yield pressure is the maximum soil pressure mobilised at a given depth.

- **p-y method** (e.g. REESE et al. [72], API RP 2GEO [2]):

The p-y method is based on the subgrade reaction method by TERZAGHI with an adaption to consider the non-linearity of the soil response. Assuming small deflections, the lateral displacement of the elastic post under lateral loads can be described by the differential equation of EULER-BERNOULLI's beam for a homogenous cross-section as follows:

$$EI \frac{d^4 y}{dz^4} - p(z, y) = 0 \quad \text{Equ. 2-2}$$

$$p(z, y) = \begin{cases} k_B(z, y) \cdot y, & k_B(z, y) \cdot y < p_{max}(z) \\ p_{max}(z), & k_B(z, y) \cdot y > p_{max}(z) \end{cases}$$

where; EI is the pile flexural rigidity, y is the lateral deflection as a function of the depth increment z and $p(z, y)$ is the lateral distributed load per unit length acting on the post embedment length. This equation assumes no axial loads acting on the post and neglects shear deformations of the cross-section.

The p-y curves provide the soil resistance $p(z, y)$ as a function of the pile deflection $y(z)$ and can be estimated using curve fitting to pile load test measurements or estimated from field test results. This method is suitable for large deformation problems and can be adjusted to reflect the strongly variable stress-strain behaviour of different soils under static, cyclic and dynamic loading.

REESE et al. [72] was one of the first researchers to develop p-y curves for pile design. In 1974, he conducted full-scale lateral loading tests on 641 mm diameter piles in different soils. The piles were fully instrumented to allow for the measurement of bending moments and consequently determine the lateral soil resistance. For the unit load-deflection curves obtained in sand, REESE et al. developed a piecewise function (see Fig. 2-2 & Equ. 2-3). The curve segments resemble the linear elastic phase, hardening phase and the ultimate soil resistance. The approach differentiates between shallow and deep pile embedment.

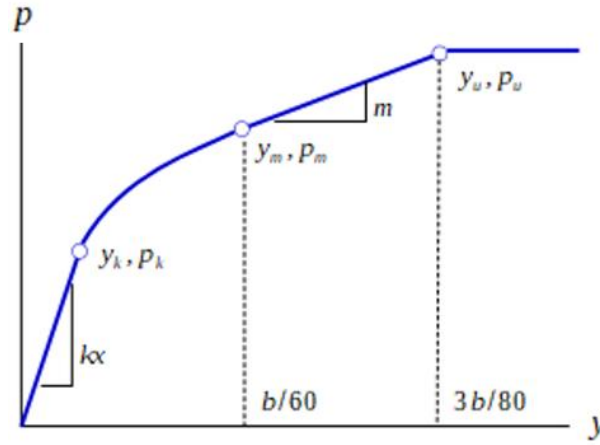


Fig. 2-2: p-y curves for sand after REESE et al. 1974 [73]

$$p = \begin{cases} 0 < y < y_k, & p = (k_{py} \cdot z)y \\ y_k < y < y_m, & p = \bar{C} \cdot y^{\frac{1}{n}} \\ y_m < y < y_u, & p = m \cdot y \\ y_u < y & , & p_u = \bar{A}_s \cdot p_s \end{cases} \quad \text{Equ. 2-3}$$

$$y_m = \frac{D}{60}, \quad y_u = \frac{3D}{80}$$

$$p_m = B_s \cdot p_s, \quad m = \frac{p_u - p_m}{p_u - p_m}$$

$$p_s = \min\{p_{us}, p_{ud}\}$$

$$p_{us} = \frac{K_0 z \tan \phi' \sin \beta}{\cos \alpha \tan(\beta - \phi')} + \frac{\tan \beta}{\tan(\beta - \phi')} (z \tan \beta \tan \alpha + D) + K_0 z \tan \beta (\tan \phi' \sin \beta - \tan \alpha) - K_a D$$

$$p_{ud} = \gamma' z D K_a [(\tan \beta)^8 - 1] + \gamma' z D K_0 \tan \phi' (\tan \beta)^4$$

z	[m]	calculation depth
y	[m]	lateral deflection
p	[kN/m]	soil resistance per unit length
p_{us}	[kN/m]	ultimate soil resistance at shallow depths
p_{ud}	[kN/m]	ultimate soil resistance at deep depths
k	[kN/m ³]	subgrade reaction modulus
\bar{A}_s	[-]	empirical adjustment factor
B_s	[-]	non-dimensional coef. of soil resistance
\bar{C}	[-]	hyperbolic function fitting coef.

The American Petroleum Institute recommends the design of laterally loaded oil platform foundations using the p-y curves as per API RP 2GEO [2]. This approach is also adopted by DIN EN ISO 19901-4 2017 for the design of offshore structures. The p-y curves for sand are described by a hyperbolic function, as shown in Fig. 2-3 and Equ. 2-4. The approach is extended to account for cyclic loading by means of adjustment factors. Compared to REESE's piecewise function, the API approach proposes a continuous function, which is more practical for numerical implementation. Both approaches are described here in detail to be used later in this thesis for comparison with the developed LPM (see 6 Analysis of soil-post interaction by means of LPM).

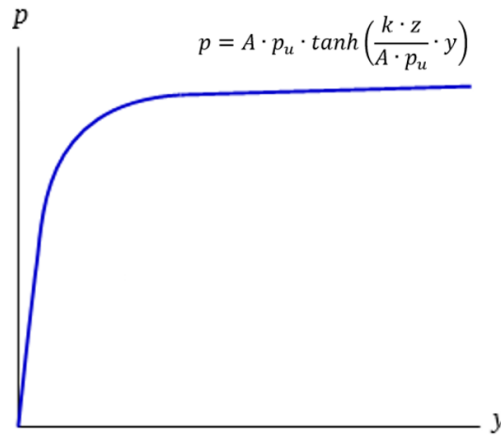


Fig. 2-3. P-y curves for sand as per API RP 2GEO 2014 [2]

$$p = A \cdot p_u \cdot \tanh\left(\frac{k \cdot z}{A \cdot p_u} \cdot y\right) \quad \text{Equ. 2-4}$$

$$p_u = \min \begin{cases} p_{us} = (C_1 \cdot z + C_2 \cdot D) \cdot \gamma' \cdot z \\ p_{ud} = C_3 \cdot D \cdot \gamma' \cdot z \end{cases}$$

$$A = \left(3.0 - 0.8 \frac{z}{D}\right) \geq 0.9 \quad (\text{loading type factor for static loading})$$

$$C_1 = \frac{(\tan \beta)^2 \tan \alpha}{\tan(\beta - \phi')} + K_0 \frac{\tan \phi' \sin \beta}{\cos \alpha \tan(\beta - \phi')} + \tan \beta (\tan \phi' \sin \beta - \tan \alpha)$$

$$C_2 = \frac{\tan \beta}{\tan(\beta - \phi')} K_a, \quad C_3 = K_a [(\tan \beta)^8 - 1] + K_0 \tan \phi' (\tan \beta)^4$$

$$\alpha = \frac{\phi'}{2}, \quad \beta = 45 + \frac{\phi'}{2}$$

C_i [-] coefficients of soil resistance

- **Finite element method:**

Finite element analyses (FEA) can provide numerical solutions of the pile-soil interaction under lateral loading, considering the material's non-linearity. Nevertheless, selecting a suitable constitutive model of the soil, defining contact properties and determining the model parameters are challenging tasks. Moreover, the formation of a gap around the pile and soil heaving have to be considered in the model. Due to the complexity of the FEM compared to the aforementioned methods, it is deemed laborious and time-consuming in the engineering practice. However, the three-dimensional FEM is nowadays more widely-used due to the continuous improvement of computer processors' efficiency and the comprehensive nature of the FEM. The numerical modelling using FEM is further discussed in chapter 5 *Numerical analysis*.

Analysis of post response under lateral dynamic loading

The problem of the guardrail post under lateral impact can be treated in its simplest form as a collision between two bodies. To understand the physical behaviour of colliding objects, some basic concepts are discussed in this section. When two solid objects collide, the impact

response of these objects, e.g. energy transfer and rebound, is governed by the material properties, the generated impact force and the contact time [37]. In classical mechanics, the linear momentum P of an object is the product of its mass and velocity vector. The conservation of momentum states that the total amount of momentum within a closed domain remains constant. In other words, the total momentum of colliding objects remains unchanged, as long as no external forces are active on these objects.

As per Newton's laws of motion, the net force acting on a body is equal to the rate of change of its momentum. This leads to the definition of impulse J , which is equal to the integral of the acting force F over its time duration $(t_2 - t_1)$ or the rate of change of momentum ΔP :

$$\Delta P = J = \int_{t_1}^{t_2} F(t) dt \quad \text{Equ. 2-5}$$

Considering an example of a rigid sphere colliding with a cantilever beam, three types of impact can be defined [37]:

- Perfectly elastic impact: The rebound velocity of the sphere is equal to the approach velocity, whereby the cantilever shows an elastic behaviour and returns to its original position at the end of the process. During impact, the kinetic energy is temporarily stored as elastic energy in the cantilever, which returns to the sphere at the end of the impact. No loss of energy takes place.
- Perfectly plastic impact: The kinetic energy of the colliding sphere is completely dissipated by the plastic deformation of the beam, and the rebound velocity vanishes. The resulting deflection of the cantilever is completely irreversible.
- Elastoplastic impact: Only a part of the kinetic energy is dissipated by the cantilever, and the rebound velocity does not vanish. The deflection of the cantilever is partially reversible. The rebound velocity depends on the amount of elastic energy stored in the cantilever during the impact.

These types of impact responses were described by COSTA 1964 [12] for the collision of a ship with breasting dolphins. The part of kinetic energy transferred from the vessel to the dolphin can be determined as the integral of the product of the dolphin reaction force and the ship velocity over the contact time before rebound. The kinetic energy absorbed by the dolphin is equal to the work done by the impact force F to deform the breasting dolphin:

$$E_{abs} = \int_{t_0}^{t_r} (F \cdot v) dt = W = \int_{u_0}^{u_r} F \cdot du \quad \text{Equ. 2-6}$$

Where, E_{abs} is the strain energy history equal to the work done by the colliding body, u is the dolphin deflection and v is the velocity of the vessel. The same approach is described by RAY [70] for the evaluation of the strain energy history in a crash event of a vehicle with a rigid structure.

The case of breasting dolphins is similar to the guardrail posts under collision. In both cases, the structure is subjected to a lateral impact load, which is transferred to the soil through a single pile with large deflections. However, breasting dolphins exhibit a relatively larger

diameter and embedment length. According to the German recommendations for "Waterfront Structures, Harbours and Waterways" EAU 2021 [34], the internal forces on breasting dolphins can be determined either using the BLUM 1932 method or the p-y curves approach. The BLUM method is an ultimate capacity approach, in which the limit soil pressure on the pile is estimated. The method thus provides an upper limit value for the bending and shear forces acting on the dolphin. As a modification of the BLUM method, the EAU 2021 recommends calculating the soil resistance using the three-dimensional passive earth pressure as per DIN 4085 [21]. For the verification of the serviceability limit state, the BLUM method is only suitable to a limited extent, as it underestimates the dolphin deflection. On the other hand, the p-y curves approach allows for more realistic modelling of the soil-dolphin interaction, since the soil non-linearity and the soil deformations required to mobilise the passive earth resistance can be considered.

RUDOLPH et al. [78] provided comparative calculations for the design of dolphins utilizing both methods, and concluded that both are appropriate for the ultimate limit state analysis. Nevertheless, for the serviceability limit state, the p-y curve method is preferred. The guardrail posts are sacrificial elements, which undergo large deflections to fulfil their function. The evolution of the lateral resistance with the lateral deflection is relevant to the VRS response. Therefore, the analysis of the soil-post interaction using ultimate capacity methods is insufficient.

The pile response under dynamic loading can be analysed using two different approaches: time-domain analysis and frequency-domain analysis. For problems involving periodic loading, in which the frequency of the applied load is known, frequency-domain analysis is applied. The response of the pile is defined by an analytical transfer function, which relates the input force to the output displacement amplitude of the system for a range of frequencies. The relationship between the soil reaction force and the pile displacement defines the complex impedance function [63]. The dynamic reaction of the soil P_d can be represented by a spring and a dashpot. The soil complex dynamic stiffness K consists of the real part K_1 , which represents the dynamic spring stiffness, and the imaginary part K_2 , which describes the damping:

$$P_d = K \cdot y = (K_1 + iK_2)y \quad \text{Equ. 2-7}$$

The frequency-dependent coefficients K_1 and K_2 can be derived from closed solutions for a pile embedded in an elastic half space.

MYLONAKIS & CRISPIN [58] analysed the problem of a pile subjected to a steady harmonic oscillation. The soil-pile interaction is analysed using a modified Winkler model, i.e. beam supported laterally on a series of springs and dashpots. The governing differential equation for the response is given by [58]:

$$E_p^* I_p \frac{d^4 y^*(z)}{dz^4} + k(z) \cdot y^*(z) + i\omega \cdot c(z) \cdot y^*(z) - \rho_p A_p \omega^2 \cdot y^*(z) = 0$$

$$\text{Equ. 2-8}$$

where; $E_p^* = E_p(1 + 2i\beta_p)$ is the complex pile stiffness including β_p the hysteretic material damping of the pile material, I_p is the second moment of inertia of the pile section. ρ_p and A_p are the pile material density and cross-section, respectively. The pile response $y^*(z) =$

$y^*(z, t) e^{-i\omega t}$ is the time-dependent lateral deflection profile over pile length. ω is the angular frequency of the applied load. $k(z)$ is the spring coefficient accounting for the soil stiffness and $c(z)$ the coefficient of soil damping accounting for both material and radiation damping.

This approach is useful for loading inducing small shear strain amplitude in the soil, for which the behaviour can be assumed to be linear elastic, e.g. vibrations due to machine foundations and weak earthquakes. For non-periodic loads, Fourier series can be used to break down the load into a series of harmonic sinusoids of different frequencies, amplitudes and phase shifts. The differential equation is solved for each term of the Fourier series and the response of the structure is computed by superposing the solutions obtained for each harmonic sinusoid [45].

Piles under lateral impact loading shall be analysed in the time domain rather than the frequency domain, when a non-linear behaviour of the soil is expected to affect the response of the system significantly. Moreover, in the time-domain analysis, the damping variation with the deflection rate can be considered [33]. Therefore, time-domain analysis is better suited to capture the transient behaviour of the pile under impact loading.

The soil-structure interaction of guardrail posts under lateral impact loading is rarely addressed in the literature. In the case of impact loading, the inertial effects of the soil and post mass, the damping of the material and geometrical as well as the dynamic soil stiffness have to be considered. Therefore, the soil-post system can be modelled substantially as a beam exhibiting lumped mass points supported by springs and dashpots in each depth increment. Based on the BERNOULLI beam theory and considering the above-mentioned effects, the non-linear partial differential equation describing the beam deflection under a lateral loading $F(t)$ can be written as:

$$EI \frac{\partial^4 y(z, t)}{\partial z^4} + (m_p + M_s) \frac{\partial^2 y(z, t)}{\partial t^2} + c(y) \frac{\partial y(z, t)}{\partial t} + k(y) \cdot y(z, t) = 0 \quad \text{Equ. 2-9}$$

where; EI is the pile flexural rigidity, m_p is the mass of the mobilised pile segment, M_s the inertial contribution of the soil, $k(y)$ and $c(y)$ are the subgrade and damping coefficients. The latter depend on the unknown lateral deflection y which is a function of the depth increment z and time t . If the model parameters m , k and c are independent of the deflection, Equ. 2-9 can be solved in both the time- and frequency domain, otherwise the analyses can be only carried out in the time-domain. Different expressions for M_s , k and c have been derived in the literature assuming linear elastic behaviour of the soil and the pile. However, these solutions are not applicable to dynamic loading of piles and guardrail posts in the elastoplastic regime, for which time-domain analyses are mandatory.

The above-mentioned approach was applied successfully by ELNAGGAR & BENTLEY [33] in 2000 for the analysis of structural piles under horizontal dynamic loading, the so-called static lateral loading tests. They proposed a model utilizing static p-y curves and the plane strain soil reaction assumptions developed by NOVAK [63] in the framework of viscoelasticity. The analysis is conducted in the time domain. The approach is characterised by the definition of a near-field and a far-field (see Fig. 2-4). In the near field, the material damping is defined by non-linear dashpots, and the soil stiffness is defined by non-linear springs.

In the far field, radiation damping is considered through a linear dashpot coefficient and a parallel linear spring, where the soil is assumed to exhibit elastic behaviour. Using this model,

ELNAGGAR & BENTLEY derived closed-form solutions by means of regression for producing dynamic p-y curves for a loading frequency range in clay or sand. For a given frequency ω of the external force, the dynamic soil reaction P_d is given by:

$$P_d = P_s \cdot [\alpha + \beta a_o^2 + \kappa a_o (\frac{\omega y}{d})^n] \quad \text{Equ. 2-10}$$

where; P_s is the static soil reaction, d is the pile diameter, α, β, κ and n are material-dependent parameters determined by curve fitting of the dynamic response of the pile. The parameter $a_o = r_o \cdot \omega / V_s$ is the dimensionless frequency. The equation is valid for P_d less than or equal to the ultimate soil resistance calculated as per API p-y curve approach [2]. This approach is well-established in the literature and was applied by other researchers for different applications, e.g. BIN ZHU et al. 2012 for the analysis of ship collisions on elevated lateral piles.

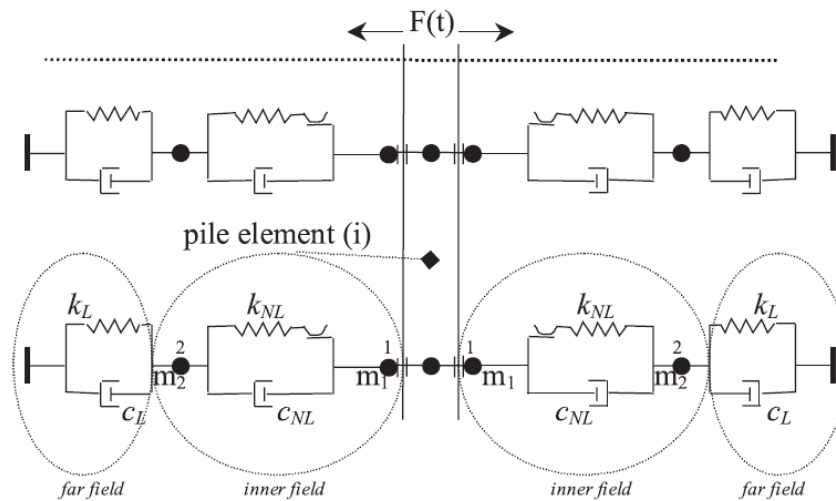


Fig. 2-4: Soil-pile interaction model proposed by ELNAGGAR & BENTLEY [33] for piles under lateral dynamic loads

ASSADOLLAHI & BRIAUD [56] proposed a soil-structure interaction model for the analysis of in-line post barriers under vehicle impact. The system consists of a group of posts (5 to 8 posts) installed in-line for the purpose of perimeter protection against vehicle collision. The single posts are modelled by a single degree of freedom model (SDOF) connected together by a horizontal beam (see Fig. 2-5). The model's main purpose is to estimate the dynamic penetration, i.e. the maximum deflection of the barrier under collision. The SDOF model incorporates a spring, a dashpot and a slider to simulate the soil stiffness, damping and the bearing capacity of the post, respectively. The mass of the pile and the activated soil wedge in the impact event are modelled together in a lumped mass. The plastic yielding and strain rate dependency of the post and beam material are not included in the model.

Combining the EULER-BERNOULLI beam theory and the equations of motion, the governing partial differential equation of the system is given by:

$$E_B I_B \frac{\partial^4 y}{\partial z^4} + M \frac{\partial^2 y}{\partial t^2} + C \cdot \frac{\partial y}{\partial t} + K \cdot y = 0 \quad \text{Equ. 2-11}$$

where; $E_B I_B$ is the flexural rigidity of the beam, M is the mass of the post and mobilised soil wedge plus a beam segment, K and C are the stiffness and damping coefficients of the beam-pile-soil system, and y is the dynamic penetration, i.e. deflection of the beam.

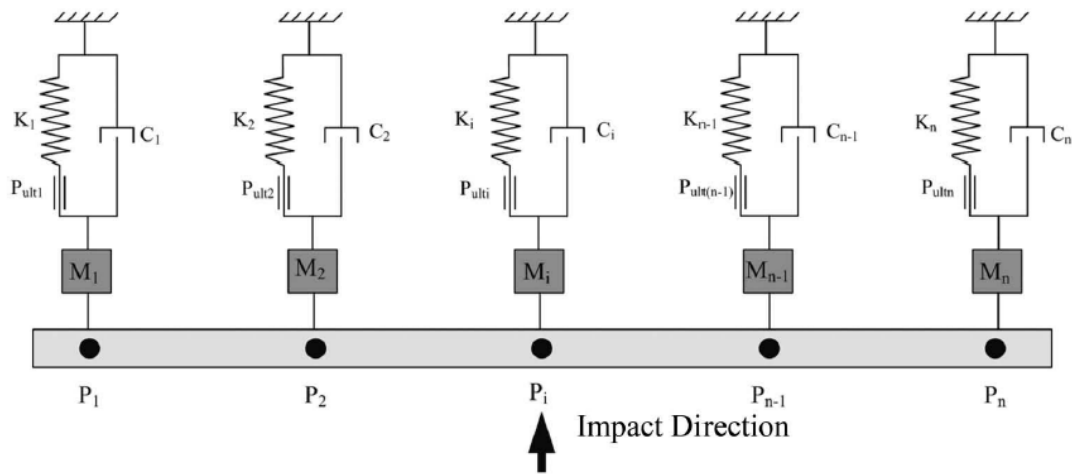


Fig. 2-5: A SDOF model proposed by ASSADOLLAHI & BRIAUD [56] for the analysis of soil-post interaction of in-line post groups (plan view)

The Equ. 2-11 is solved using the finite difference method for y . Knowing the impact velocity of the colliding vehicle, the deflection of the node under impact is applied as an initial condition. Considering the system as hinged at the first and last pile, the bending and shear forces can be set to zero at these nodes at the boundaries of the beam. The model parameters rely mainly on in-situ pressuremeter (PMT) test results. Based on the analytical approach developed by BRIAUD [8], the laterally loaded pile response is analysed analogue to the cylindrical expansion of the PMT. Based on this assumption, the system stiffness K is evaluated as a function of the post embedment length, impact height and PMT first loading modulus. The damping coefficient C is determined as a function of the soil shear wave velocity, pile width B and system stiffness K . The mobilised soil wedge is defined by a prism with dimensions $B * 2B$ at ground level and depth to the zero-shear point. The model is found to deliver acceptable results compared to the full-scale tests and can be used for the prediction of the barrier maximum deflection reasonably.

The review of the different methods applied for the analysis of piles and posts under lateral loading shows that the nature of loading, soil type and element dimensions cannot be neglected when selecting the analysis method. It can be concluded that there is no fully validated method for the analysis of guardrail posts under lateral collision. The lumped parameter models in which the soil resistance is described by p-y-curves and dashpots as well as the FEM are the most promising techniques to model the strongly non-linear dynamic behaviour of single guardrail post under lateral impact loading.

Comprehensive experimental data are required to calibrate and validate the numerical models developed with both modelling techniques for different soils and post types. Since the single post is a main component of the VRS, the realistic simulation of its dynamic response is crucial to assess the performance of VRS through numerical simulations of crash tests. A particular focus has to be applied on determining the proposed model parameters and correlating them to the soil mechanical properties. In light of this literature review, it is clear that the soil non-linearity, energy dissipation mechanisms and the inertial effects of the soil and post mass must be considered for a realistic simulation of the soil-post interaction.

3 Full-scale testing of single posts

In a crash event, the kinetic energy generated by the impact of a vehicle with the VRS is dissipated in deforming the posts and surrounding soil as well as in stretching the guardrail beam under tension loads. The posts involved are loaded with different magnitudes depending on the severity and angle of collision. Depending on the post position from the impact location, the post either rotates in the soil or the post section undergoes yielding [88]. Analysing the structural behaviour of the VRS under such loading conditions is complex. This is attributed to the non-linearity of the embedment soil, large deformations of the system and eventual material failure of the post. Moreover, the load distribution or rather the contribution of each element to the energy dissipation is not known in advance. In the praxis, this problem is analysed in the framework of the certification of the VRS using full-scale crash tests and component tests as well as finite element simulations. In these simulations, less focus is often applied to the soil behaviour, and therefore it is modelled using rudimentary methods.

In this chapter, we investigated this aspect experimentally to gain a deeper understanding of the influence of the different factors on the single post response. A series of guardrail posts were tested in selected standard road shoulder materials under quasi-static and dynamic impact loads to evaluate the soil-post interaction. The novel approach applied in this testing program allows for a better comparison and understanding of the results. First, the post is tested under quasi-static load up to 0.4m deflection. Then, under the same soil conditions and post characteristics, further posts were tested under impact loads with different intensities at the same height of the quasi-static test. The road shoulder materials specimens were tested extensively to determine the mechanical soil properties and grain characteristics. A special focus is applied to the terms; maximum reaction force, post deflection, rotation, and energy dissipation.

The author published the substantial findings of the experimental field tests in the peer-reviewed publication SOLIMAN et al. [84]. Parts of the experimental investigations presented in this chapter have been included in the final report of the research project "Auswirkung des Bodens auf das Verhalten von Fahrzeug-Rückhaltesystemen". The results, text and figures presented in this thesis were created and compiled by the author.

In the following chapters, the author conducted numerical simulations of the executed field tests using the experimentally determined soil properties. The experimental results are used for the validation of a numerical model for the single post embedded in soil material. These would allow for a deeper understanding of features that could not be measured experimentally, e.g. mobilised soil wedge under impact loading and the energy dissipation distribution. Based on the experimental results and the numerical analysis, a simplified Lumped-Parameter Model capturing the soil-post interaction was developed. This model shall be implemented in crash test simulations to enable a realistic simulation of the VRS behaviour with high computational efficiency.

3.1 Experimental testing program

The test program was designed to consider selected factors influencing the soil-structure interaction of single posts under different loading conditions (see Fig. 3-1). To allow for a systematic comparison of the influence factors, a reference test condition is defined. The post behaviour under variation of the different factors is then compared to the reference conditions behaviour.

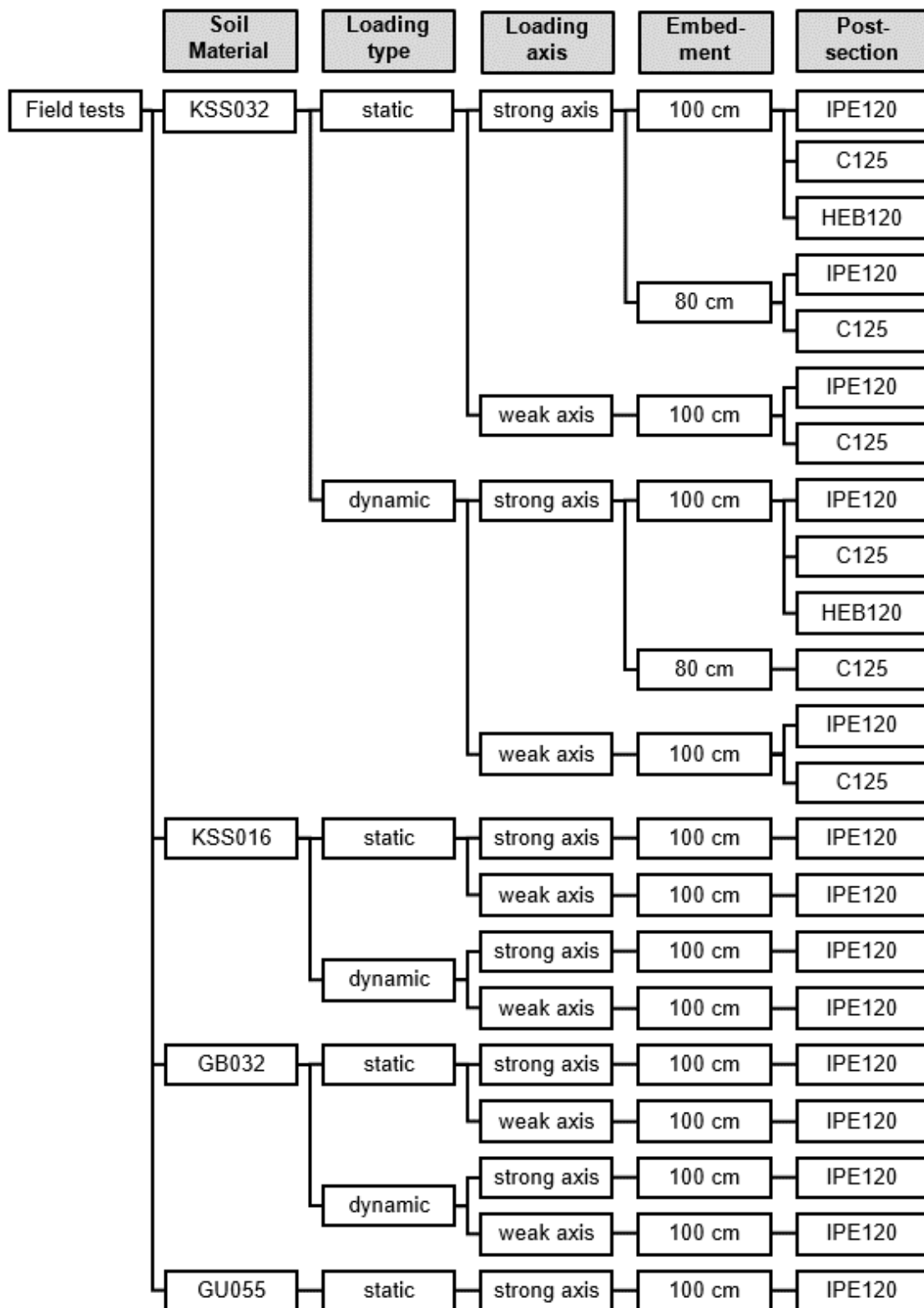


Fig. 3-1: Full-scale field test program conducted on single guardrail posts

Focusing on steel guardrail posts embedded in soil, the following factors were investigated in the experimental tests:

- The variation of soil material in terms of grain size distribution, mineralogy and relative density.
- The nature of loading, whether quasi-static loading or dynamic impact loading triggering the effects of inertia and damping.
- The variation of post cross-section properties in terms of bending stiffness, symmetry and loading axis.
- The post embedment length.

The reference condition for the soil material is dense crushed limestone with a grading of 0 to 32 mm (KSS032). The reference post is the IPE120 with an embedment of 100 cm length, loaded in the strong axis. These reference conditions apply under the quasi-static and dynamic impact loading.

The variation of the soil material grading comprises testing posts in crushed limestone with a grading of 0 to 16 mm (KSS016). To test the effect of relative density in the same material, the crushed limestone KSS032 was installed in one test area with less density, i.e. medium dense. To test the influence of grain strength and mineralogy, a soil variation with crushed granite with a grading of 0 to 32 mm (GB032) was considered. A further soil material comprising very dense natural silty gravel (GU055) was considered as a variation of the material density and grain shape.

The variation of the post-section comprises C125 and HEB120 posts. The C125 is comparable to the IPE120 regarding the section area and modulus. However, the C125 is asymmetric and exhibits a uniform flange and web thickness. The HEB120 is a much stiffer post-section with ca. triple the section modulus $W_{el,y}$ of the IPE120 (see section properties Table 3-4). Therefore, the HEB120 is used in soil testing before crash tests, since it excludes the yielding of the post material under lateral loading. The variation of the post embedment was considered in selected tests, where the embedment length was reduced to 80 cm or 85 cm.

The selected posts were tested under the above-mentioned conditions, once in the strong axis and once in the weak axis. The differentiation between the post behaviour in both directions is decisive for the overall response, as in a crash event, the vehicle collides with the post with an angle less than 90°.

Particularly, the variation of the loading type is what makes this test campaign unique. The posts are tested first under a quasi-static lateral pull test. Under the same conditions, new posts are tested under lateral impact loading. The impact is applied with different intensities on at least three separate posts. The applied impact intensity levels were set equal for each variation to allow for cross-comparisons of the test results.

The field test program, as described above, enables the investigation of the influence of different factors separately. Based on the results, the influence of the investigated parameters on the post resistance could be quantified, which is one of the purposes of this research. Closer details about the selected materials and testing procedure are given in the following sections.

Selection of soil materials

To investigate the effects attributed to the embedment soil material on the post behaviour, different materials fulfilling the requirements of the ZTV E-StB 17 [96] for road shoulder materials have been selected for the field tests. This standard regulates the technical specifications and the contractual aspects of earthworks in road construction in Germany.

According to the ZTV E-StB 17, a road shoulder material has to fulfil two contrasting requirements. On one hand, it should exhibit a high load-bearing capacity and should be resistive to weathering effects, i.e. insensitive to freeze-thaw cycles. On the other hand, the material must have a high pollutant retention capacity, i.e. stable filter criterion, to prevent the pollution of groundwater. To fulfil these requirements, the soil matrix must consist mainly of a durable coarse grain skeleton to achieve the required bearing capacity. The voids between the grains must be filled with fines to decrease the permeability of the material. However, increasing the percentage of fine materials in the matrix can lead to a decrease in the bearing capacity. Therefore, the grading of the material and the fines content are decisive for the bearing behaviour, stability and durability of the road shoulder. Comprehensive research has been conducted at Zentrum Geotechnik by KOUKOULIDOU et al. [44] and CUDMANI et al. [14] to investigate the optimum road shoulder material composition and compaction properties. The research findings are in line with the technical specifications of the ZTV E-StB 17. These can be summarised as follows [96]:

- The road shoulder material should consist of an unbound granular mixture of the soil group silty/clayey gravel (GU-GT) as per DIN EN ISO 14688-1 [27]. The material must comprise a fine content of 8 to 12%.
- The material shall consist either of a natural aggregate or a crushed stone.
- The mixture should be well-graded with a maximum grain size of 32 mm.
- As per the Unified Soil Classification System USCS, a road shoulder material fulfilling these requirements can be classified depending on the uniformity and curvature coefficients as well-graded gravel with silt/clay and sand (GW-GM or GW-GC) or poorly graded gravel with silt/clay and sand (GP-GM or GP-GC).
- Regarding soil placement and compaction, the installed layers shall not exceed a thickness of 30 cm, and a degree of compaction of $D_{Pr}=100\%$ must be reached on a minimum 90% quantile in each layer.
- Further requirements refer to the deformation moduli on the final surface. A minimum value of the deformation modulus E_{v2} of 80 MPa when conducting a static plate load test (as per DIN 18134 [20]) and a dynamic deformation modulus E_{vd} of 40 MPa when conducting a dynamic plate load test (as per TP BF-StB) is required. These values have to be fulfilled on a minimum 90% quantile of the measurements.

Based on the research work conducted at Zentrum Geotechnik [44] [14], ZTV E-StB 17 and the Technical terms of delivery of unbound materials TLSoB-StB [90], the upper and lower bounds for the grain size distribution of the road shoulder materials can be defined as shown in Fig. 3-2.

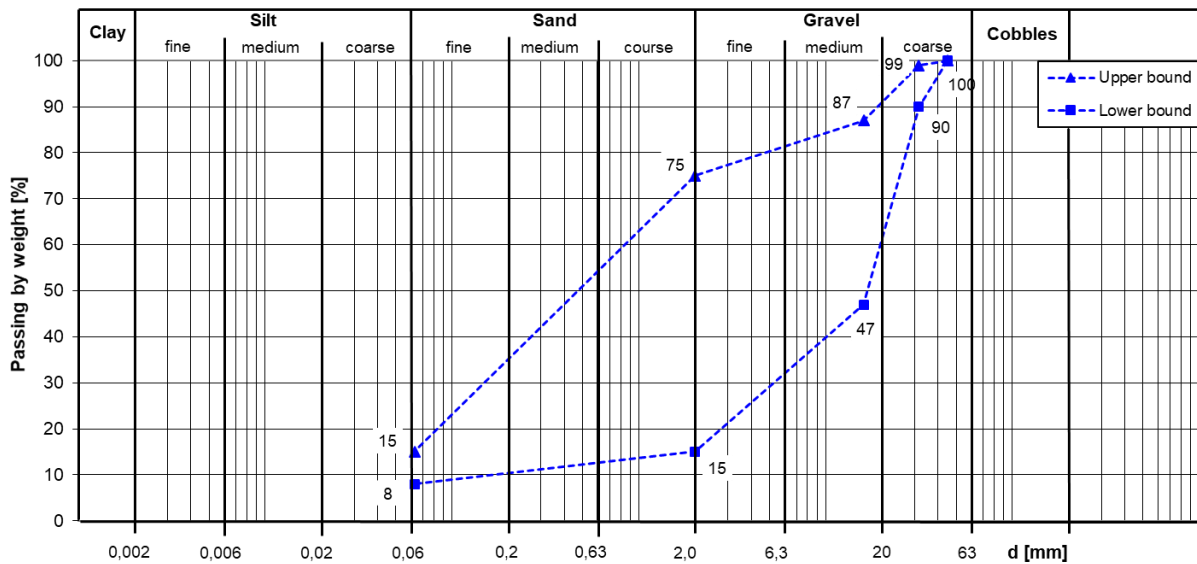


Fig. 3-2: Upper and lower bounds of road shoulder materials grain size distribution after CUDMANI & HENZINGER et al. [14] and acc. to TL SoB-StB 2007 [90]

The selected materials for field testing (see Fig. 3-3) included crushed limestone and crushed granite, fulfilling the aforementioned grading and fine content criteria. An additional material with higher gravel content (GU055) and a maximum grain size of 55 mm was further selected. This soil material was installed on the crash test site, where the VRS certification tests were conducted.

Crushed limestone 0-32 mm (KSS032)



Crushed limestone 0-16 mm (KSS016)



Crushed granite 0-32 mm (GB032)



Silty gravel 0-55 mm (GU055)



Fig. 3-3: Photos of the road shoulder materials selected for the experimental field tests

The reference tests were performed on posts embedded in crushed limestone with a grain size of 0 to 32 mm (KSS032) and a fine content of 7.6 to 11.8%. This material was selected to meet the ZTV E-StB 17 [96] requirements for road-shoulder materials (silty/clayey gravel with a fine content of 8 to 12%). The material was installed on two test areas with different degrees of compaction. The in-situ material characteristics are shown in Table 3-1. Further material properties and mechanical soil parameters are presented and discussed under *4 Laboratory testing of soil materials*.

Table 3-1: Characterization of the tested soil materials

Soil material		crushed limestone	crushed limestone	crushed limestone	crushed granite	round gravel, silty
Notation		KSS032	KSS032	KSS016	GB032	GU055
Grading		0-32 mm	0-32 mm	0-16 mm	0-32 mm	0-55 mm
Gravel	[%]	47.1 – 67.4	47.1 – 67.4	44.9 – 57.4	57.8 – 58.7	74.1 – 75.9
Sand	[%]	24.9 – 41.1	24.9 – 41.1	33.4 – 46.6	33.6 – 34.1	17.7 – 15.1
Fines	[%]	7.6 – 11.8	7.6 – 11.8	8.6 – 10.3	7.7 – 8.1	8.2 – 9.0
Field dry density	ρ_d [t/m ³]	2.073	1.938	2.062	2.024	2.249
Relative density	I_D [-]	dense	med. dense	dense	dense	very dense
Degree of compaction	D_{Pr} [%]	94.3	88.2	93.0	94.6	97.6

To assess the effect of grain size distribution and sand content, the second material tested was crushed limestone with a grain size of 0 to 16 mm (KSS016). The third testing material was crushed granite with a grain size of 0 to 32 mm (GB016). This material differs from the first materials in the mineralogy of the grains and exhibits a higher particle strength. The last material was a silty/clayey natural round gravel with a grain size of 0 to 55 mm (GU055). This material deviates from the standard road shoulder materials with regard to the maximum grain size.

The structural design of road pavement and layer configuration in Germany is standardised in the Guidelines for standardisation of pavement of transportation roads RStO12 [77] and ZTV SoB-StB [98]. The technical specifications and terms stated in these guidelines are obligatory for tendering and contracting in road construction. Fig. 3-4 shows a typical cross-section of a highway pavement structure and the configuration of the road shoulder layer. Based on the standard pavement layers from the RStO 12 and the pavement shoulder design from the ZTV SoB-StB, and considering the installation heights and set-backs according to VRS installation manual, the position of the posts relative to the pavement and the layers encountered in the embedment can be defined.

The width of the road shoulder is specified in the Guidelines for the construction of highways RAA [69]. For newly constructed roads, the standard road shoulder width is 1.5 m. However, on existing highways, the width can reach up to 2.0 m, while on narrow highways, the width can be reduced to 1.0 m.

The drainage requirements of the road shoulder is stated in the Guidelines for Road Drainage Systems REwS [76]. The road shoulder surface gradient is chosen depending on the pavement cross-direction gradient and whether a drainage ditch or channel is installed on the road side. The road shoulder surface gradient in the cross-direction ranges between 6% on the higher pavement side and 12% on the lower side.

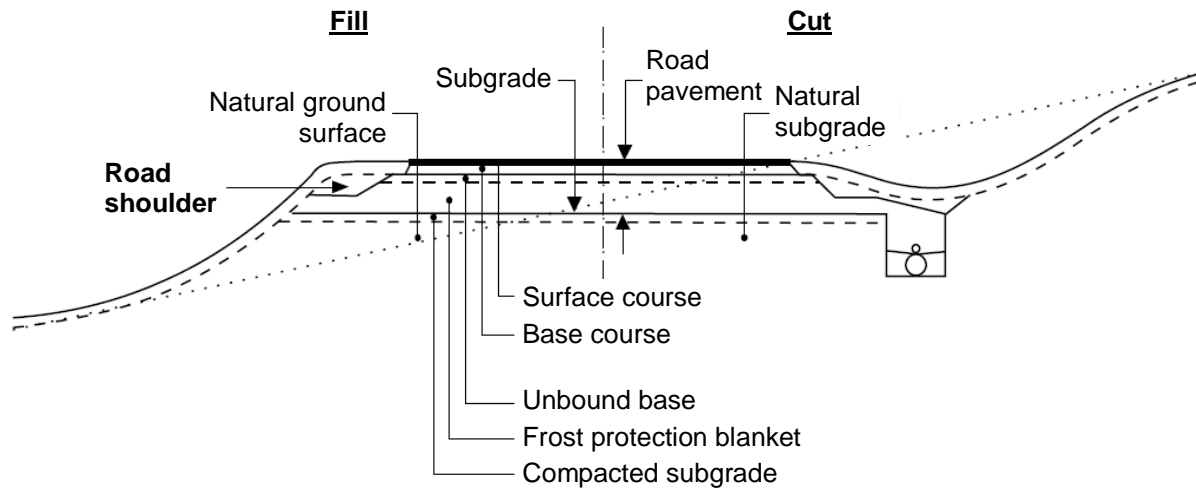


Fig. 3-4: A typical cross-section of a highway pavement structure acc. to ZTV SoB-StB [98]

For the reference VRS Super-Rail Eco, chosen for this study, a comprehensive analysis has been conducted for the different combinations of pavement types, loading classes and subgrade frost sensitivity. The results show that the posts can be embedded in 2 to 3 different layers depending on the road construction variation. The embedment length of the posts in the road shoulder material is 1/3 to 2/3 of the total embedment length. The rest is embedded in the frost protection blanket and the subsoil. According to the bearing requirements of each layer, the embedment layers exhibit a stiffness contrast defined through the static plate load test deformation modulus E_{v2} . The RStO 12 requires, as an acceptance criterion, a deformation modulus of $E_{v2} \geq 45$ MPa on the compacted subgrade layer and $E_{v2} \geq 120$ to 150 MPa on the frost protection blanket. The ZTV E-StB 17 [96] requires a deformation modulus of $E_{v2} \geq 80$ MPa for the road shoulder material.

From the variation analyses, the extreme cases regarding the stiffness contrast over a 1 m post embedment in standard road shoulder are shown in Fig. 3-5. The post has a total length of 1.9 m and a height of 0.9 m measured from the pavement surface. Assuming a surface gradient for drainage of 6% of the road shoulder and measuring the depths related to the pavement elevation, the upper 5 cm of the 1 m embedment are laterally unsupported. In the first case (Fig. 3-5a), describing direct construction on the compacted subgrade, the result is an embedment of 53 cm in the road shoulder material ($E_{v2} \geq 80$ MPa) and 42 cm in the subgrade ($E_{v2} \geq 45$ MPa). The second case (Fig. 3-5b), which is construction on frost-sensitive soils, shows embedment of 64, 24 and 7 cm in the road shoulder material, frost protection blanket and compacted subgrade, respectively.

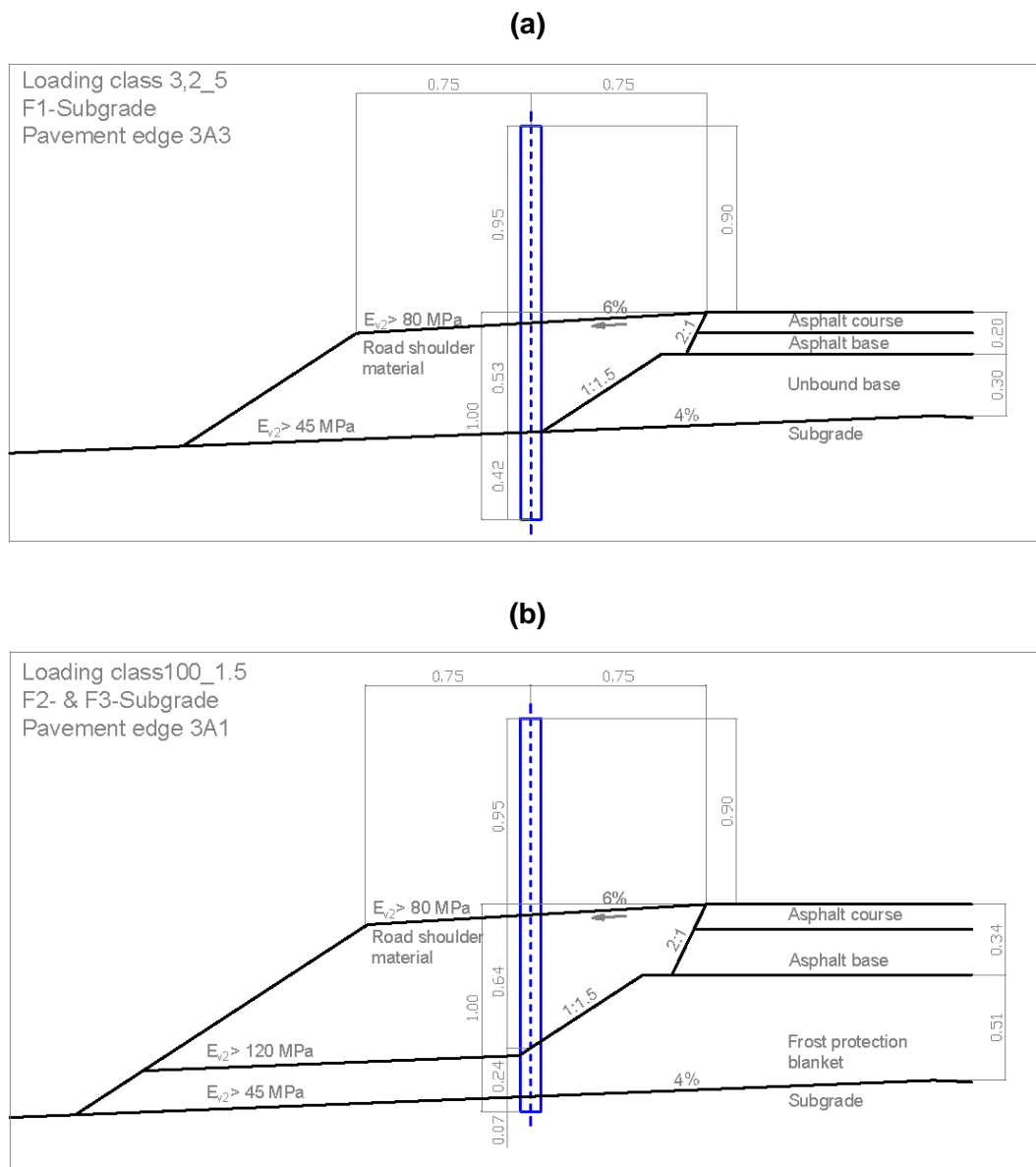


Fig. 3-5: Variation of the road construction layers in the road shoulder with respect to the post embedment

As a matter of fact, these stiffness contrasts cannot be realised in-situ, especially if the thickness of the layers are relatively small. In practice, it is more common to construct the fill layers over the entire surface and then level and reprofile the road shoulder. In addition, the intensive compaction of the upper fill layers leads to further compaction of the underlying layers. Therefore, the soil stiffness varies over the post embedment length and shows a gradual variation rather than sharp step jumps in the values.

For the purpose of comparison, no subgrade layering was considered in the experimental field tests, i.e. the posts were fully embedded in a homogenous soil layer. The tested soil materials were placed and compacted in separate testing fields, where the compaction requirements and homogeneity were tested by various methods. The effects of soil layering and stiffness contrasts are investigated later using the finite element method (see 5 Numerical analysis).

Soil mineralogy and grain strength

As the road shoulder aggregate mineral is not specified by the guidelines, several grain mixtures can be applied, e.g. natural gravel, crushed stone or even recycled construction materials. In the field tests, we tried to figure out the influence of material grain strength and characteristics on the post response. The selected limestone is a sedimentary rock often used as a subbase material in road construction in many regions. In contrast, granite was selected as an igneous rock with higher strength and lower abrasiveness.

The X-ray diffraction (XRD) technique was applied to determine the mineralogical components of the road shoulder materials. XRD is based on the principle of ray diffraction, where X-rays interact with the atoms in a sample and cause them to scatter in different directions. The resulting diffraction pattern is unique for each mineral and can be used to identify the minerals present in the sample [40].

To perform XRD analysis on a soil material, a sample is first prepared by grinding it to a fine powder. A representative specimen, including all grain sizes, was extracted from each road shoulder material. The specimen was then ground to a fine powder with a grain size of < 0.5 mm. The powder is then placed in a sample holder and placed in an X-ray diffractometer. X-rays are directed at the sample, and the diffraction pattern is captured by a detector. The diffraction pattern is then analysed using specialized software to identify the minerals existing in the sample. The software compares the diffraction pattern to a database of known diffraction patterns to identify the minerals and quantify each mineral's proportion.

The mineralogical components of each material are shown in Table 3-2. The crushed limestone consists of 97.7% calcite and dolomite. The rest is quartz sand. The crushed granite specimen consists mainly of feldspars (61.5%) and quartz (23.4%). The material also comprises 5.7% mica and 5.8% of the clay mineral smectite. The silty gravel specimen is composed mainly of 63.9% calcite and dolomite, and 28.8% quartz. The remaining 7.3% comprises feldspar, mica and kaolinite.

Table 3-2: Quantitative mineral content of the soil specimens according to results of the X-ray diffractometer analyses

Soil Material	crushed Limestone	crushed Granite	silty Gravel
Mineral [Mass %]	KSS032/016	GB032	GU055
Quartz	2.1	23.4	28.8
Alkaline Feldspar	-	31.3	1.4
Plagioclase Feldspar	-	30.5	1.7
Calcite	54.6	1.3	30.8
Dolomite	42.8	-	33.1
Biotite (mica)	-	5.7	-
Muscovite (mica)	<1	-	1.7
Kaolinite	<1	-	1.6
Chlorite	-	1.9	0.9
Smectite	-	5.8	-
Apatite	-	<1	-

In terms of uniaxial compressive strength q_u , intact granite q_u value ranges between 50 and 250 MPa, while intact limestone q_u ranges between 25 and 100 MPa (after PRINZ & STRAUß [68]). The resistance of a rock to abrasiveness, i.e. hardness, can be compared using the Mohs' scale of mineral hardness [68]. The scale is commonly used in the engineering geology and tunnel construction. The scale ranges from 1 for soft rock like talc to 10 for the hardest known rock, which is diamond. On the Mohs' scale, the granite scores 6 to 7, while the limestone scores 3.

The single grain crushing strength (σ_F) is decisive for the behaviour of the granular material in applications where the individual grains experience high effective stresses. The stress concentrations at the contact points can cause fracture of the grains, which consequently affects the bearing behaviour and stability of the material. The single grain crushing strength can be determined experimentally as the maximum axial load, which the grain can bear before being split in 2 or 3 equal fractions [81]. Indirectly, σ_F can be determined from the grain breakage factor B , defined as the amount of grain breakage developed in a specimen under an oedometric compression test.

The single grain crushing strength is influenced by several factors. In a comprehensive experimental study conducted by SEFI & LAV [81] the single grain crushing strength and the breakage factor of calcareous and basalt origin grains were investigated. The most important factors influencing σ_F were found to be the loading stress level, grain shape and mineralogical heterogeneity. The loading rate was found to have a negligible effect. The mean grain size d_{50} is observed to decrease under increasing axial stresses as a result of grain crushing as follows:

$$d_{50} = (d_{50})_0 \cdot e^{-(C \cdot \sigma_v')} \quad \text{Equ. 3-1}$$

where; C is a material-dependent constant equal to 0.019 and 0.013 for calcareous and basalt grains, respectively. The soil pressure developed in the quasi-static and dynamic tests was analysed numerically in our research (see chapter 5 *Numerical analysis*). The maximum mean pressure was found to reach up to 0.5 MPa around the post. For a stress range up to 1.0 MPa, the change in d_{50} estimated according to Equ. 3-1 does not exceed 1% and 2% for the calcareous and basalt grains, respectively. Based on these results, the influence of grain crushing on the load-bearing behaviour of the guardrail posts can be neglected.

In road construction, the California Bearing Ratio test (CBR) is conducted to evaluate the strength of the base and subbase layers. As per DIN EN 13286-47 [25], the test gives an indication of the stiffness and bearing strength of a grain mixture. However, the test results are not intended to be used for evaluation of the soil stiffness or shear strength parameters. The CBR ratio measures the penetration resistance force to a specific depth in the compacted material compared to that in a standard crushed rock. In this research project, the CBR ratio was determined for the selected road shoulder materials. All specimens were prepared with the optimum water content and then compacted to the standard proctor density. The results are shown in Fig. 3-6. More details about the conducted CBR tests are presented in chapter 4 *Laboratory testing of soil materials* and in *Appendix [B]: Laboratory test protocols*.

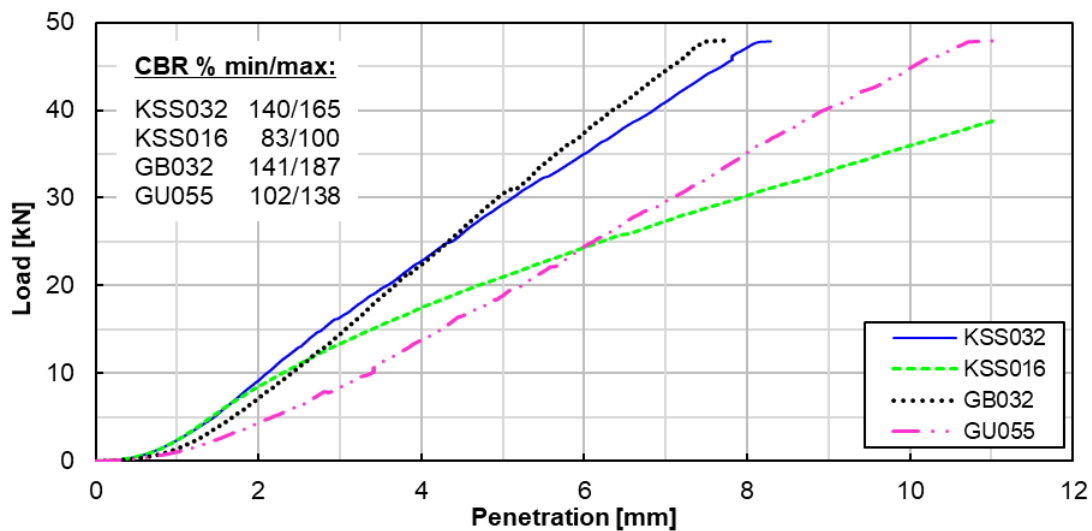


Fig. 3-6: CBR load-penetration curves and the evaluated CBR ratios for the tested road shoulder materials

The characteristic of the load-penetration curves of the crushed limestone and granite was found to be nearly identical. The CBR ratio evaluated for the granite is slightly higher than the limestone, indicating a higher material strength. The silty gravel exhibits a lower CBR ratio. The crushed limestone with the highest sand content KSS016 shows the lowest CBR ratio (ca. 40% less compared to KSS032). This drop demonstrates the influence of the gravel fraction in the soil matrix on the bearing strength of the material.

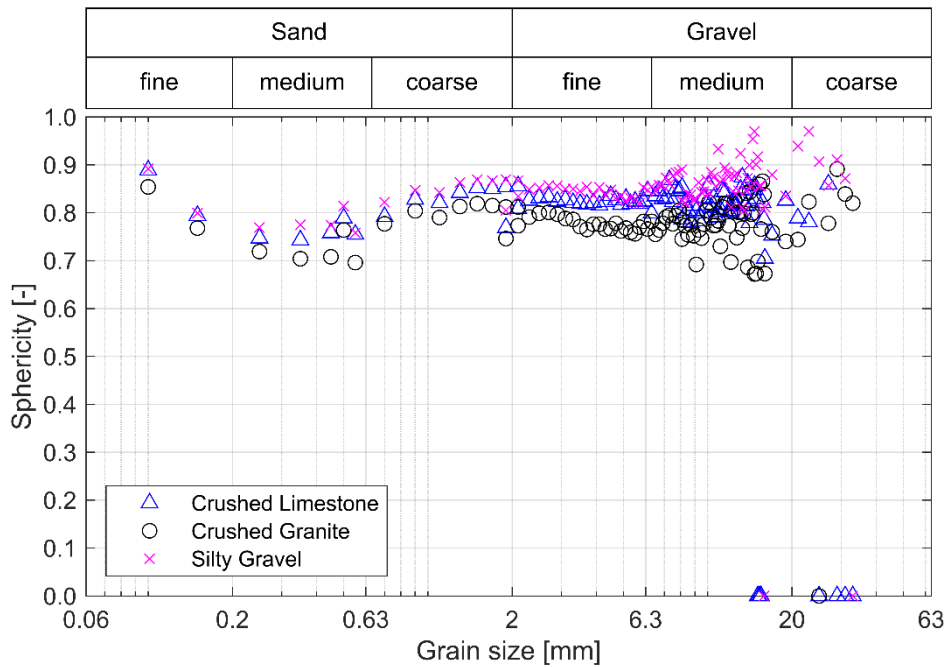
Grain shape characteristics

The road shoulder material can be prepared out of the selected limestone or granite in the quarry with the specified grain size distribution and delivered to the construction site. The crushing process during production defines the shape and texture of the aggregate grains. The natural fluvial gravel exhibits less angular grains compared to both materials. The geometric properties of the individual soil grains play an essential role in determining the mechanical behaviour of non-cohesive soils. The grain shape and surface texture influence the interlocking between grains in the soil skeleton, which is decisive for the compressive and shear strength of the material. On a macroscopic observation level, the shape of a single grain as well as the surface features, can be described quantitatively using the grain shape factors. For the description of the global shape of a grain, the aspect ratio, convexity and sphericity are considered. In contrast, roundness and angularity are used to describe the grain surface features. In this study, the sphericity and roundness of the grains were analysed.

Sphericity (S) is the parameter quantifying the resemblance of a particle to a circle considering two dimensions or a sphere considering three dimensions. In general, the sphericity parameter ranges between 0 and 1, where 1 corresponds to a perfect sphere. KRUMBEIN & SLOSS [46] defined sphericity in 1963 as the aspect ratio of the particle width to length to simplify the evaluation of the particle shape using visual charts. The recent advancements in image processing technologies have allowed for more complicated and realistic definitions. As per the US Corps of Engineers, the sphericity can be defined as the ratio of the surface area of a sphere exhibiting the same volume as the examined particle to the surface area of the particle.

Roundness (R) is the parameter quantifying the relative sharpness of the particle edges. It is calculated as the average curvature radii of all edges and corners divided by the radius of the maximum circle inscribed in the examined particle [46]. As per the definition, the roundness is also an indication of the grain angularity. The roundness parameter values range between 0 and 1. As the grain corners' sharpness increases, the radii sum decreases, and the roundness approaches 0. For round particles, the roundness approaches a value of 1.

(a) Grain sphericity



(b) Grain roundness

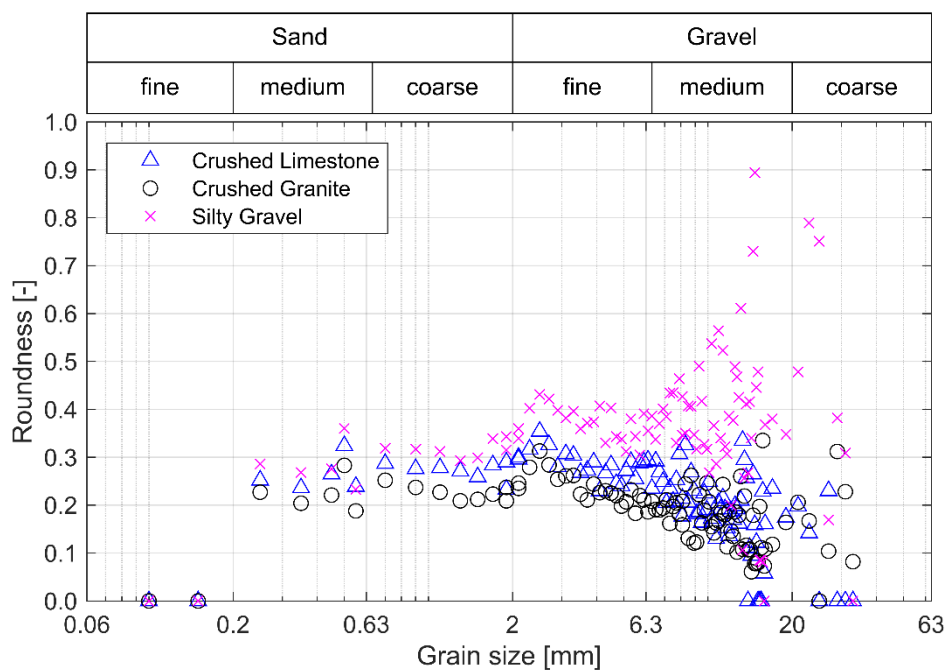


Fig. 3-7: Grain shape factors over grain size distribution determined for the tested road shoulder materials (a) sphericity (b) roundness

The grain shape characteristics of the road shoulder materials selected for the field tests were analysed using Dynamic Image Analysis (CAMSIZER provided by Microtrac Retsch GMBH). The grain dimensions as well as the shape features, were determined for a grain size range of 0.2 to 32 mm. The grains were divided into subclasses of 0.2 mm. The determined values of sphericity and roundness are shown in Fig. 3-7. The values are calculated using the particle's inner width, i.e. the particle diameter determined from the smallest of all maximum chords of the particle projection. This approach is suitable for comparison with calculations based on grain size from sieve analysis.

The sphericity mean values of the crushed granite, crushed limestone and silty gravel were determined to $S=0.78$, 0.81 and 0.86 , respectively. These results are in line with the material's grain nature. Limestone exhibits lower hardness compared to granite. Therefore, the crushed particles tend to be more spherical. On the other hand, the silty gravel shows the highest sphericity due to its natural formation by weathering conditions. The roundness of the crushed limestone and granite lies in the same range, with a mean value of $R=0.20$ - 0.22 . The silty gravel shows a higher roundness of $R=0.37$, which gives an indication of less grain sharpness compared to the crushed materials.

Using the sphericity and roundness values, the grain shape can be qualitatively estimated from the KRUMBEIN & SLOSS chart, as presented in Fig. 3-8. The silty gravel shows the most rounded grains, while the crushed limestone and granite can be described as angular to sub-rounded. Based on the grain shape analysis results, the tested materials do not comprise flaky or elongated grains.

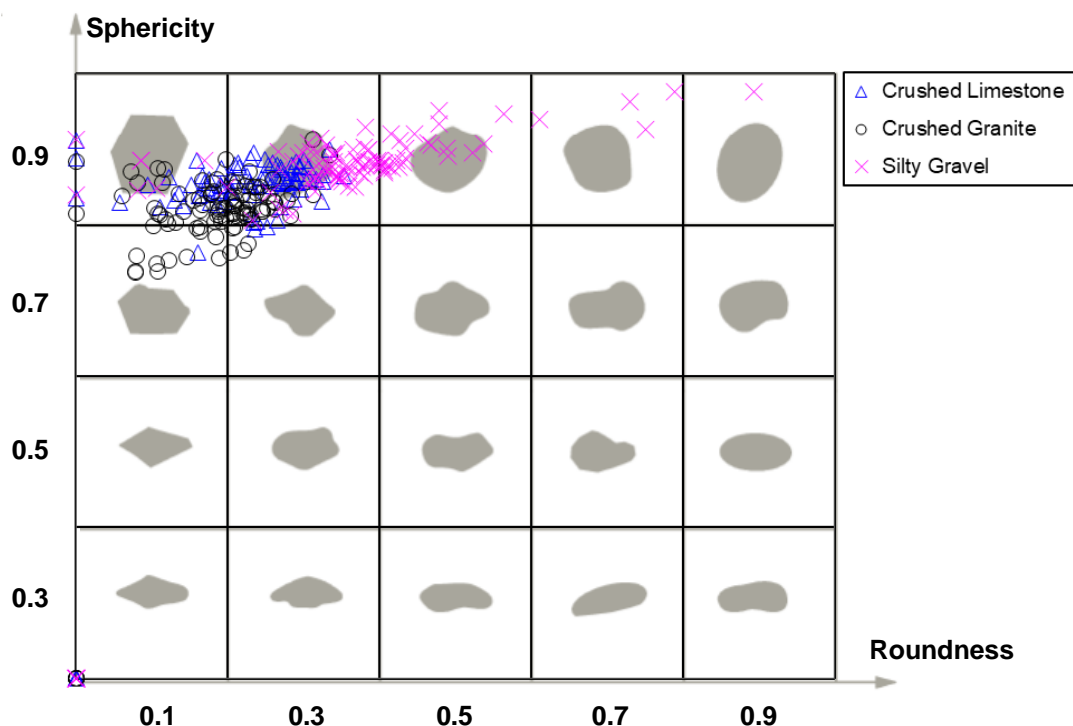


Fig. 3-8: Evaluation of grain shape based on sphericity and roundness parameters using the reference chart after KRUMBEIN & SLOSS [46]

Soil placement and in-situ testing

According to the installation manual for the reference VRS (Super-Rail Eco), the post embedment ranges between 0.90 and 1.01 m [32]. Therefore, only the first meter in the test field was excavated and replaced by the selected road-shoulder materials. Fig. 3-9 and Fig. 3-10 show the test field at Zentrum Geotechnik during excavation and replacement works. The soil was placed, levelled, and compacted in three layers, each of about 35 cm thickness. The soil materials KSS032, KSS016 and GU032 were installed and tested at Zentrum Geotechnik test field. The soil material GU055 was installed on the crash test field (see Fig. 3-17).



Fig. 3-9: Excavation and replacement of the soil on the testing field at Zentrum Geotechnik



Fig. 3-10: Compaction works after placement of each soil layer using 0.4 and 1.6 t tandem rollers

In each installed soil layer, the homogeneity of compaction was tested directly after placement using the dynamic plate load test (Fig. 3-12c). This test is considered an indirect compaction control method. A summary of the values achieved in each material and layer is presented in *Appendix [A]: In-situ soil testing*. The mean value of the deformation modulus E_{vd} ranged between 39 and 48 MPa. According to ZTV E-StB 17 [96], a minimum value for the dynamic deformation modulus of $E_{vd} = 40$ MPa is required. The 10% quantile of the measured E_{vd} values i.e. proportion of the cumulative probability distribution under 0.1 is ca. 42 MPa for the materials KSS032 and GU055 (see Fig. 3-11). For the materials KSS016 and GB032 the 10% quantile dropped to 38 and 35 MPa, respectively. However, the mean E_{vd} values for the materials KSS016 and GB032 equal 50.1 and 40.9 MPa, respectively, and are higher than 40 MPa.

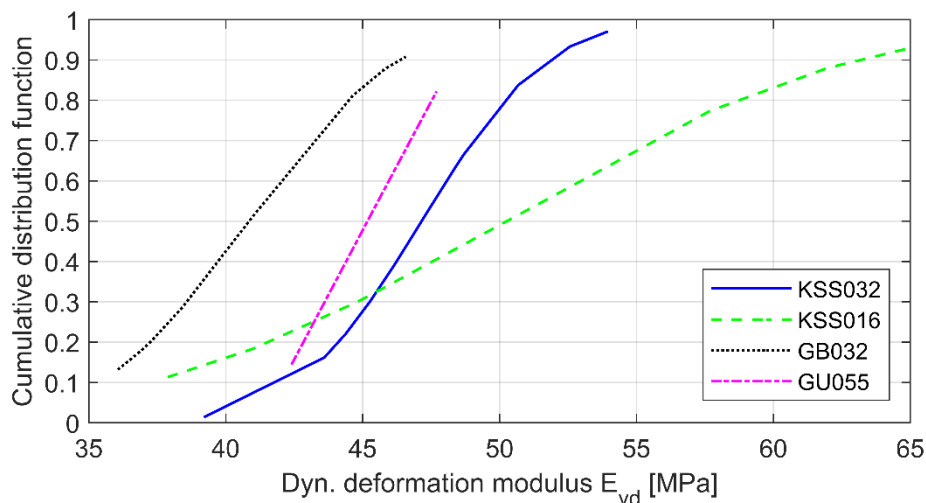


Fig. 3-11: Probability distribution of the dynamic plate load test deformation modulus E_{vd}

The density of the soil was determined in-situ using the rubber-balloon method acc. to DIN 18125-2 [17] (see Fig. 3-12a). A cavity is excavated into the soil with a depth of ca. 25 cm, and the excavated material is dried in the oven and weighed. The volume of the cavity is measured using a rubber balloon attached to a manual piston filled with a known water volume. The balloon is positioned on the cavity surface, and using the piston pressure the water presses the balloon against the cavity walls. The water volume filling the balloon can be read directly on the piston. The dry density is the quotient of the dry mass and the measured volume.

In parallel, the dry field density and moisture content were measured using the nuclear densometer, also known as the nuclear density gauge (Fig. 3-12b). The nuclear density gauge measures the density of the soil by means of gamma radiation. The device is equipped with an emitter mounted on a probe that sends photons through the soil material, and a detector that counts the photons travelled through the soil over a predefined distance. The higher the density of the soil material, the lower the radiation amount received by the detector. Comparing the amount of radiation released to the received amount, and knowing the density of a calibration material, the soil density can be determined [74].

The rubber-balloon method and the nuclear density gauge are considered direct compaction control methods. A summary of the field dry density determined using both methods in each material is presented in *Appendix [A]: In-situ soil testing*. Comparing the field dry density determined by both methods, the rubber-balloon method gives higher values. Due to the relatively large grain size and sharp edges of the tested materials, the balloon cannot lean entirely on the irregular cavity walls during the test. This results in an underestimation of the

excavated volume, and consequently to an overestimation of the calculated density. To verify this interpretation, the test was conducted in the same location using balloons with different thicknesses. The finer balloon with a thickness of 0.25 mm measured a larger volume for the same excavation hole than the balloon with a thickness of 0.50 mm. However, the finer balloon burst perpetually due to the sharp grain edges. Therefore, the field dry density measured using the calibrated nuclear densometer was considered for the degree of compaction D_{Pr} achieved in each material (see Table 3-1).

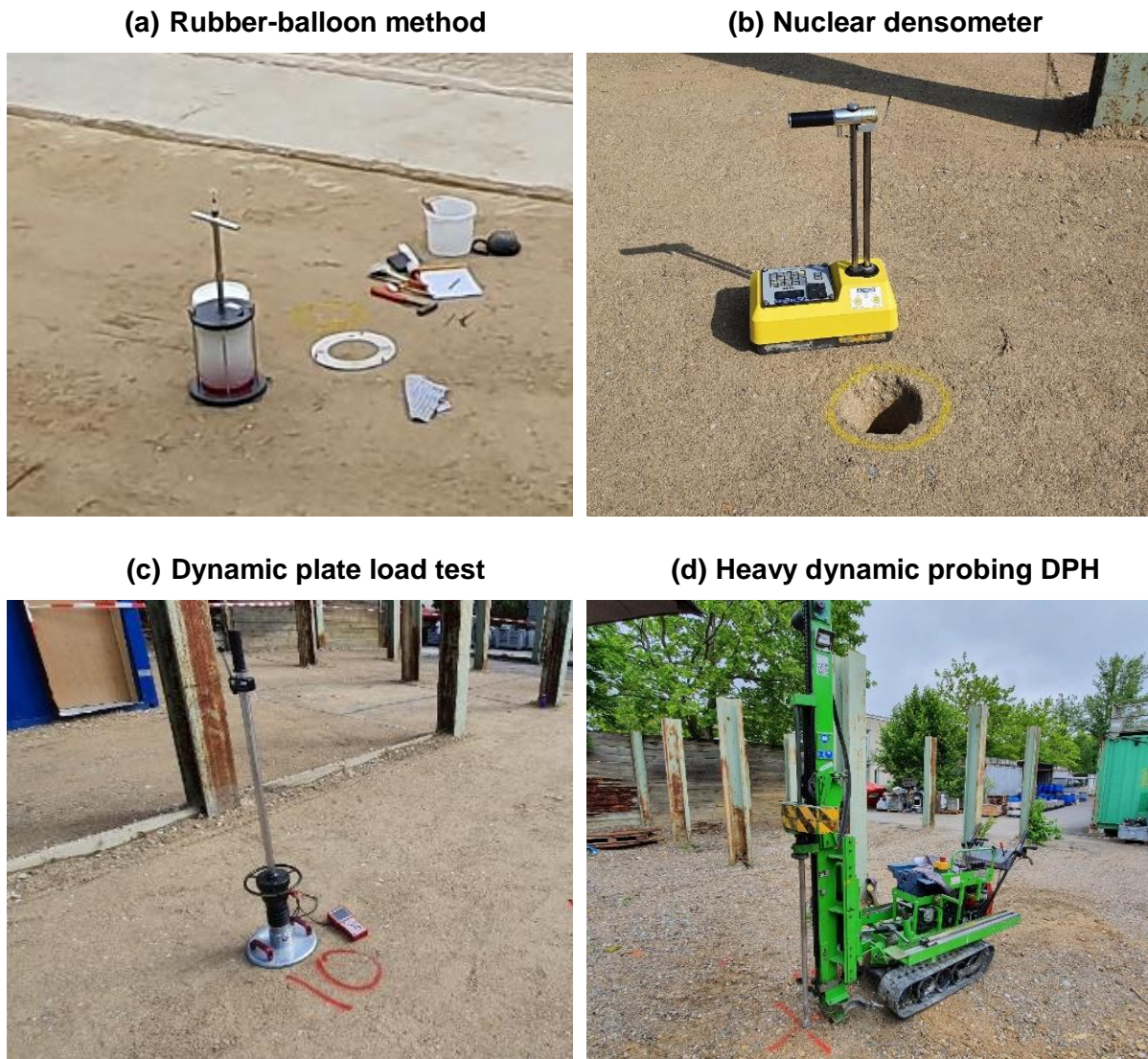


Fig. 3-12: Determination of the soil homogeneity and field dry density using different methods

The degree of compaction is calculated as the ratio between the field dry density and the maximum dry density determined using the standard proctor test. The test compares the soil compaction achieved in the field to a soil compacted under a standardised compaction energy in the laboratory. A compaction degree of 93.0 to 94.6% was reached in the crushed limestone and granite. The silty gravel installed on the crash test field reached a compaction degree of 97.6%. The purpose of constructing the testing soils with a degree of compaction less than 100% is to allow for a soil failure rather than a steel failure during the post testing. The effect of the soil compaction degree on the post failure mode is discussed in chapter 3 *Full-scale testing of single posts*.

The final ground surface was levelled, i.e. no surface gradient was constructed. After finishing the soil replacement works, a series of heavy dynamic probing (DPH) acc. to DIN EN ISO 22476-2 [31] were performed to test the compaction performance over depth (Fig. 3-12d). The probing was conducted with a standard hammer weight of 50 kg and a hammer drop of 0.5 m. The cone used exhibits a cross-section area of 15 cm². The number of blows is counted over 10 cm penetration. The DPH-logs for each material are presented in *Appendix [A] In-situ soil testing*. The blow counts ranged between 6 and 12 in the KSS032 and GB032. The blow counts ranged between 3 and 11 in the KSS016. The GU055 shows higher blow counts ranging between 12 and 50. This is attributed to the higher degree of compaction and the larger grain size of the material.

Vehicle restraint system

In this research, the Super-Rail Eco, a commonly installed VRS on the European highways, was chosen as a reference system (see Fig. 3-13). Super-Rail Eco system consists of C125 posts of steel grade S355JR installed with a spacing of 2.0 m. The posts are 1.9 m long and are driven in soil to a nominal embedment length of 1.01 m. A single guardrail beam (also W-beam) is connected to the posts through steel brackets at a height of 0.7 m (upper guardrail beam edge). Longitudinal box beam segments of 4 m in length are placed on top of the posts and are fastened using steel angles [32].

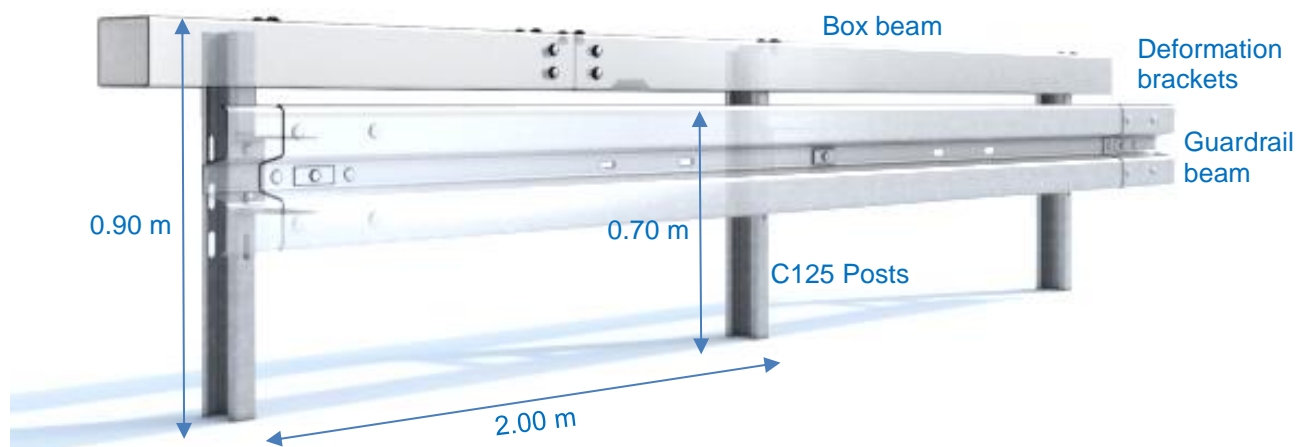


Fig. 3-13: Super-Rail Eco vehicle restraint system¹


As per DIN EN 1317, the Super-Rail Eco system is categorised in the containment class H2, which is a high containment level. In the certification and approval process, the full VRS is tested in two separate crash tests using the typical testing vehicles TB11 and TB51, which exhibit different impact severity (see Table 3-3).

¹ Retrieved from: <https://www.volkman-rossbach.de/> (01.11.2022)


Table 3-3: Test vehicles applied in the crash tests for certification of the Super-Rail Eco

Test vehicle	Vehicle type	Mass [tons]	Impact velocity [km/h]	Impact angle [°]	Severity Index [kJ]
TB11	Passenger vehicle	0.9	100	20	41
TB51	Transportation Bus	13.0	70	20	287

TB11



TB51



For the longitudinal barriers in general, the impact severity IS is calculated as the kinetic energy component acting perpendicular to the barrier [51]:

$$IS = \frac{1}{2} \cdot M \cdot (V \sin\theta)^2 \quad \text{Equ. 3-2}$$

where, M is the mass of the vehicle, V is the impact speed and θ is the impact angle.

For the certification crash test, the VRS is installed with a total of 52 posts. The guardrail beam and the box beam are anchored at the two ends of the VRS in the soil. The vehicle impact point is set nearly at the middle of the system length.

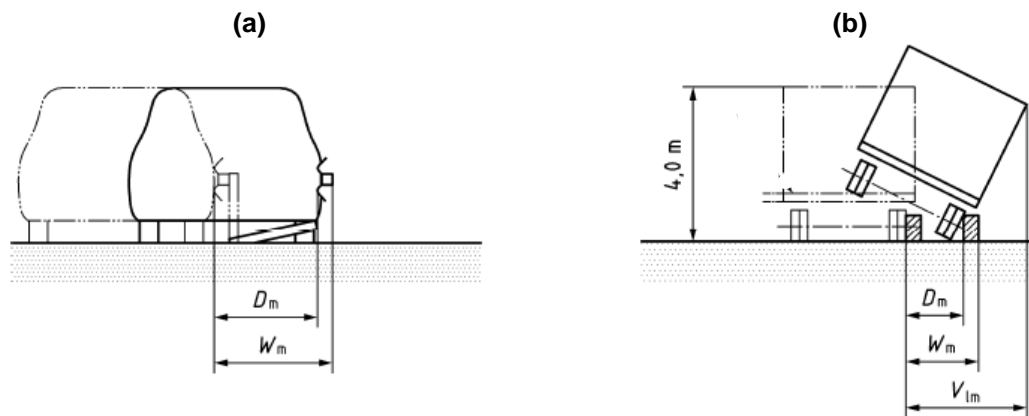


Fig. 3-14: Definition of the dynamic deflection D_m , working width W_m and vehicle intrusion V_{Im} as per DIN EN 1317-2 (a) passenger vehicle (b) heavy goods vehicle

The standard DIN EN 1317-2 [23] specifies the acceptable safe behaviour of a VRS. The colliding vehicle should be contained and redirected without complete breakage of the systems' longitudinal elements. The individual VRS elements are not allowed to become detached from the system, since these can jeopardise the safety of the traffic and road users. Further, the VRS elements are not allowed to penetrate the colliding vehicle, especially the occupants' compartment, to avoid serious injuries.

During the crash test, several parameters are measured and documented, e.g. the acceleration severity index *ASI*, theoretical head impact velocity *THIV*, dynamic deflection D_m , working width W_m and vehicle intrusion VI_m . The vehicle deformation is documented for the evaluation of the vehicle cockpit deformation index. The tested VRS has to fulfil the containment class performance criteria to ensure the safety of the vehicle occupants and the road users. The requirements and thresholds of these parameters are specified in the European standard DIN EN 1317-2 [23].

The parameters *ASI* and *THIV* are used for the evaluation of the occupant's risk of injury, while the deformation parameters D_m and W_m (see Fig. 3-14) evaluate the capability of the VRS to contain and redirect the vehicle.

ASI is calculated for acc. to DIN 1317-2 from the orthogonal vehicle accelerations measured at the centre of mass during impact as follows:

$$ASI = \max [ASI(t)] \quad ASI(t) = \left[\left(\frac{\bar{a}_x}{\hat{a}_x} \right)^2 + \left(\frac{\bar{a}_y}{\hat{a}_y} \right)^2 + \left(\frac{\bar{a}_z}{\hat{a}_z} \right)^2 \right]^{0,5} \quad \text{Equ. 3-3}$$

where, $\bar{a}_{x,y,z}$ are the average vehicle accelerations in the longitudinal, lateral and vertical directions, and $\hat{a}_{x,y,z}$ are the corresponding threshold values ($\hat{a}_x = 12g$, $\hat{a}_y = 9g$, $\hat{a}_z = 10g$, $g = 9,81 \text{ m/s}^2$). The Impact severity level of a VRS is classified as follows:

Class A	Low severity	$ASI \leq 1,0$
Class B	Medium severity	$ASI \leq 1,4$
Class C	High severity	$ASI \leq 1,9$

As per the certification of the Super-Rail Eco VRS the performance parameters are as follows²:

Containment classes:	H2, N2, L2
Acceleration severity index <i>ASI</i> :	≤ 1.0 (Class A: low severity)
Theo. head impact velocity <i>THIV</i> :	$\leq 27 \text{ km/h}$ (Class A: low severity)
Working width class <i>W4</i> :	$\leq 1.3 \text{ m}$ (normalised working width W_N)
Dynamic deflection D_m :	$\leq 0.7 \text{ m}$ (normalised dynamic deflection D_N)
Vehicle intrusion class <i>VI4</i> :	$\leq 1.3 \text{ m}$ (normalised Vehicle intrusion VI_N , only relevant for Heavy goods vehicle)

A VRS is designed to fulfil the performance criteria of a target class. If this is not achieved in the certification crash test, the VRS is either downgraded to a lower containment class or the design is further enhanced.

² Retrieved from: <https://www.ivs-siegen.de/stahlschutzplanken> (01.11.2022)

Post properties and installation

The reference tests on single posts were conducted on the IPE120 post-section, which exhibits approximately the same flexural rigidity and weight as the Super-rail Eco post standard C125 (see Fig. 3-15). Due to the symmetry of the IPE-section, it can be instrumented with strain gauges easily in the strong axis to determine the bending strains without interference with the torsional effects. This allows for a better assessment of the instrumentation measurements and a better understanding of the soil-post interaction. Additional tests were conducted on the C125 for comparison. Further tests were conducted on a heavier section HEB120 for comparison, as recommended in the standard DIN EN 1317-5 [24] for static push/pull tests. The tested posts are of steel grade S355. The cross-section properties of the tested posts are listed in Table 3-4

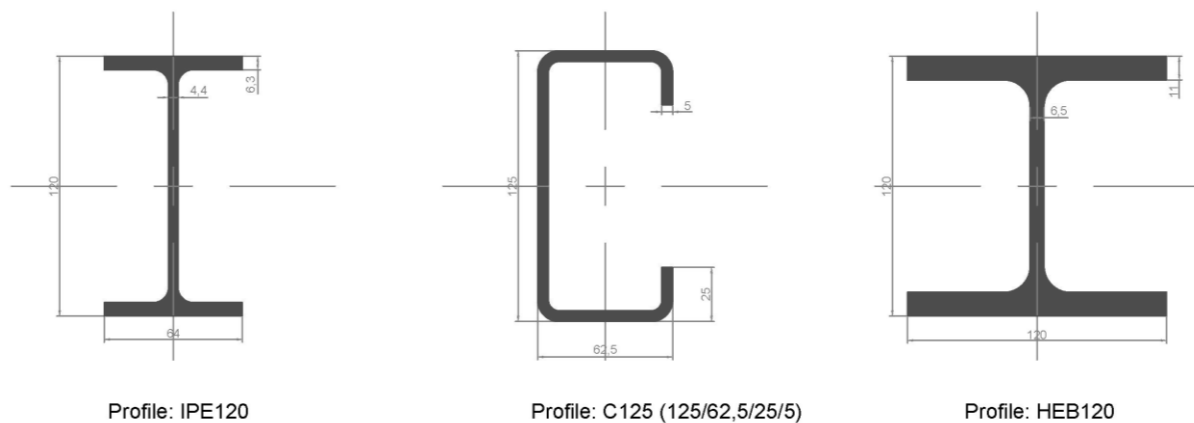


Fig. 3-15: Selected post-sections for the full-scale tests

The posts were instrumented in the laboratory with strain gauges and then driven in the test field as per the installation manual for VRS [32]. Further instrumentation was installed in-situ after installation. The posts were then tested under quasi-static and dynamic impact loading in the longitudinal and transversal direction of the post cross-section at the same height. The posts were subdivided into two groups for the static and the dynamic tests. These were installed in the test field 6 to 7 days before conducting the loading tests to ensure comparable conditions.

Table 3-4: Section properties of the tested post profiles

Post section	Dimensions h/w [mm]	Sec. Area A [cm ²]	Weight per meter M [kg/m]	Steel grade [-]	Second moment of area		Section modulus*	
					strong axis I_y [cm ⁴]	weak axis I_x [cm ⁴]	elastic $W_{el,y}$ [cm ³]	plastic $W_{pl,y}$ [cm ³]
IPE120	120/64	13.2	10.70	S355	318.0	27.7	53.0	60.7
C125	125/62.5	13.4	10.74	S355	309.9	78.7	49.6	57.5
HEB120	120/120	34.0	27.40	S355	864.0	318.0	144.0	165.0

Note: *Section modulus in the strong axis.

The posts were driven using a standard hydraulic hammer for post installation on highways (see Fig. 3-16). The inclination, as well as the installation height, were controlled to meet the quality requirements of the system (maximum inclination 10% of the post height, tolerance post height ± 1.5 cm) [32]. The posts were embedded 100 cm ± 1.0 cm into the ground. A minimum spacing of 1.5 m was held between the installed posts to avoid interference of the influence zones.



Fig. 3-16: Installation of instrumented posts using a hydraulic guardrail post driver

The posts tested in the GU055 on the crash test field were installed using a pneumatic hammer. This equipment is also common for the installation of roadside safety hardware. However, in highly compacted soils or in soils containing larger grain sizes, the installation using this equipment consumes more energy and requires a longer time. This was obvious when comparing the installation time of the posts in the GU055 to the other soil materials. A single post required 75 seconds in average for 1 m embedment in the GU055. While in all other soil materials, a single post required 15 seconds on average for 1 m embedment. The documentation of the installation time of a single post is requested by the Technical specifications of vehicle restraint systems ZTV-FRS [97], to give an indication of the soil compaction. However, from the geotechnical point of view, the recorded installation time does not give any indication about the soil's relative density or strength properties. Compared to a standard probing test like the DPH, the hammer energy applied per unit penetration depth is not unified. During post installation, the hammer frequency is adjusted to meet the productivity criteria. Moreover, the hydraulic and pneumatic hammers apply different impact forces per blow, which should also be considered.

3.2 Static loading tests

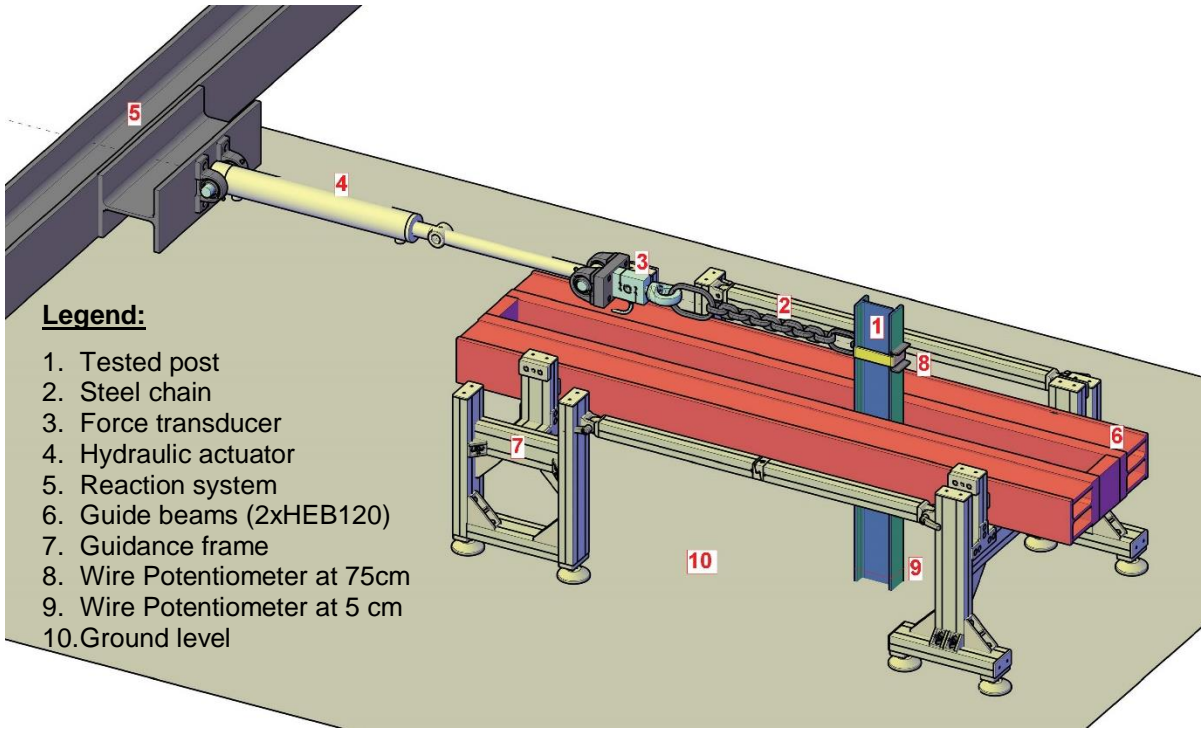
The first group of posts was tested under a quasi-static lateral load up to a total deflection of at least 40 cm. The load was applied using a hydraulic actuator with an average displacement rate of 2 to 4 mm/s at a height of 75 cm above ground level. This loading rate complies with the requirement of the standard DIN EN 1317-5 [24]. The actuator was connected to the post with a steel chain attached to a lifting sling wrapped around the post. The sling was embedded in a U-channel bolted to the back of the post to prevent it from slipping during the test. The actuator was fastened to a steel reaction system constructed to resist horizontal loading up to 50 kN (see Fig. 3-17).



Fig. 3-17: Static loading test setup in-situ (IPE120 in GU055 crash test field)

The posts had to be constrained against deflection out of the loading plane in order to minimise the effects of torsion on the measurements. This constraint is observed to occur in the real VRS due to the longitudinal box beam and the guardrail beam attached to the posts. Therefore, all static tests were conducted with a parallel guidance frame placed about 20 cm below the loading point (see Fig. 3-18). To prevent lateral displacement of the whole system, the guidance frame was braced in the transversal direction using ground anchors. The spacing between the guide beams was set equal to the width of the post plus 2 mm. The inner sides of the beams were lubricated to minimise friction with the tested posts.

(Isometric view)



(Side view)

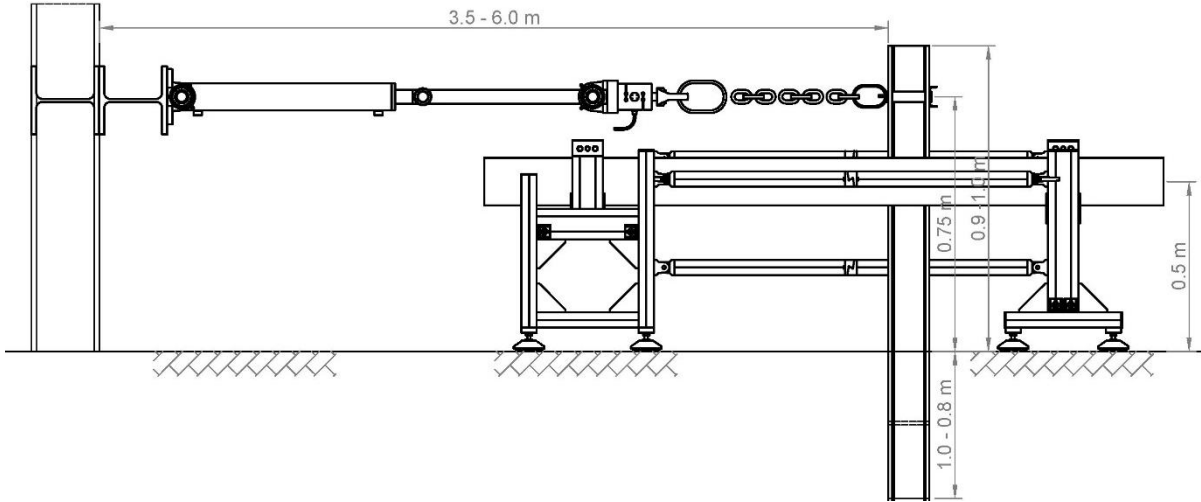


Fig. 3-18: Isometric and side view of the quasi-static test setup

Instrumentation and test procedure

The mechanical quantities to be measured in the static test are mainly the applied force, post lateral deflection and the bending strains in the post. The instrumentation used to measure these quantities in the quasi-static test is shown in Fig. 3-19a to Fig. 3-19c. The accelerometers in Fig. 3-19d were applied only in the dynamic impact test.

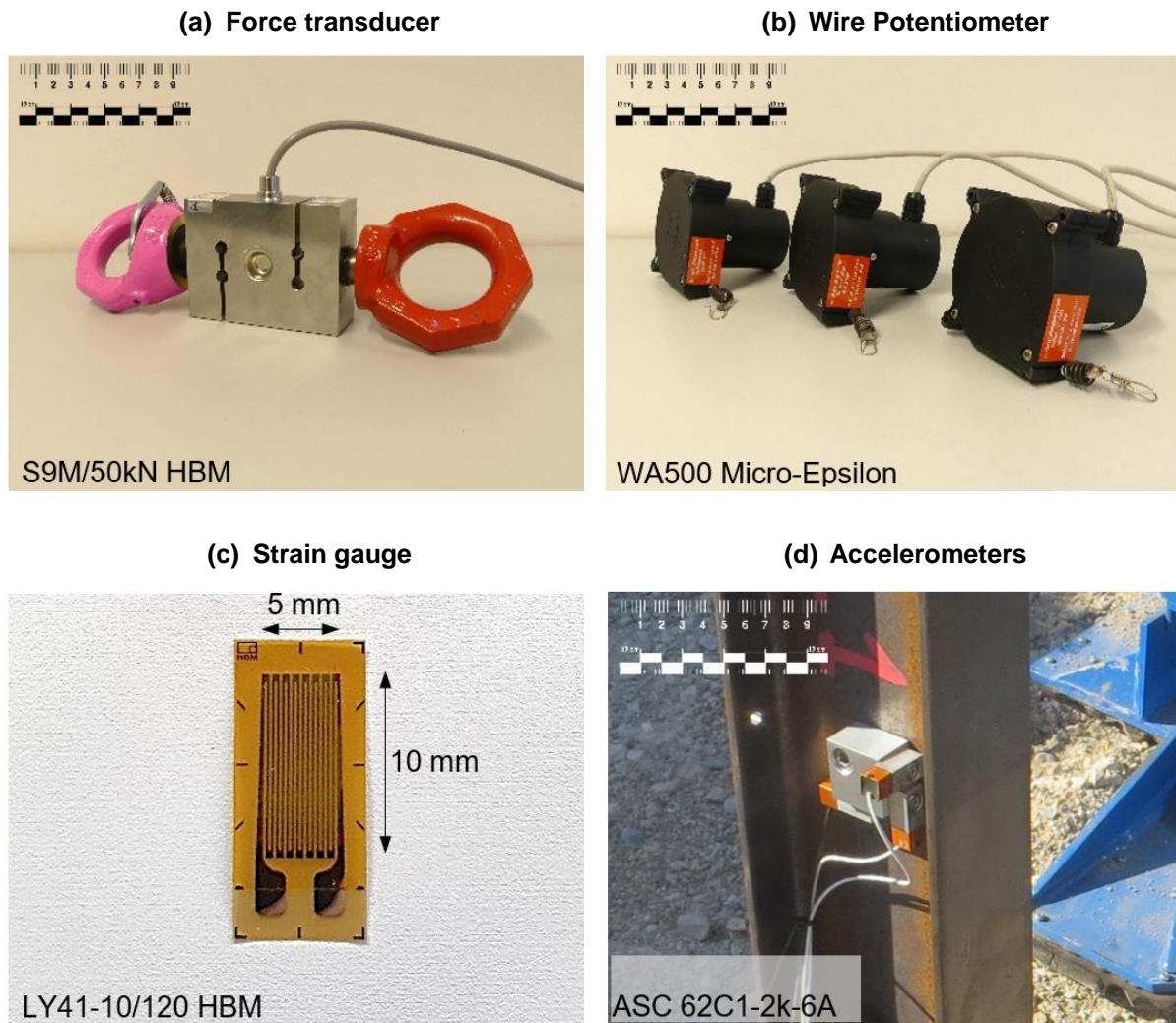


Fig. 3-19: Instrumentation installed in the quasi-static and impact loading field tests

The applied force was measured at the level of the load application point using a load transducer attached between the actuator and the post. The load transducer was connected to the steel chain using two eyebolts that were free to rotate around the tension axis to avoid constraining the transducer. This load transducer measures forces up to 50 kN with a resolution of 0.02 kN. The deflection was measured using two wire potentiometers positioned at the load application point of 75 cm and the transition to embedment at 5 cm above ground level. The measuring range of the potentiometers used is 5000 mm with a precision of 0.1 mm.

Fig. 3-20 shows a schematic illustration of the fully instrumented IPE120 post prepared for the quasi-static test.

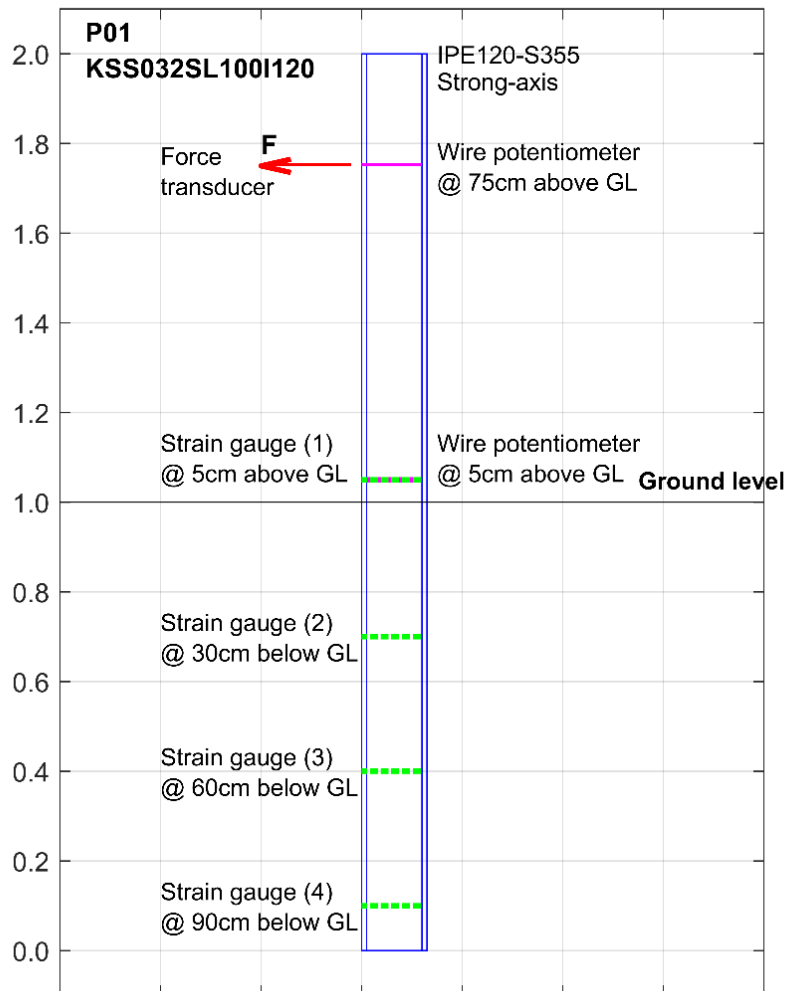


Fig. 3-20: Illustration of the post instrumentation for the quasi-static test

The posts were instrumented with strain gauges in the laboratory before the post driving in-situ. In its simplest form, a single linear strain gauge consists of an insulated metallic foil pattern, which is attached to the specimen’s surface using an adhesive material. The strain gauge is then connected to an electric circuit. When the specimen deforms, the length of the foil pattern changes and consequently its electrical resistance.

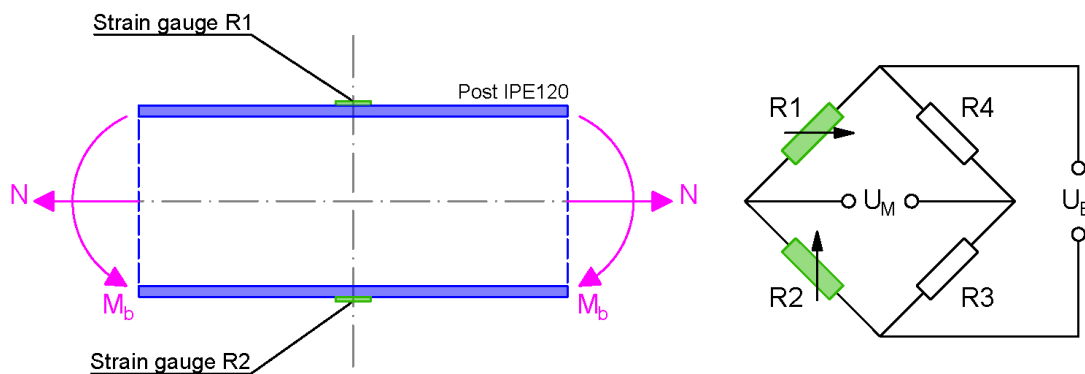


Fig. 3-21: Configuration of the applied Wheatstone half-bridge circuit

As the ratio of the change in resistance to the undeformed resistance $\Delta R/R_0$ is directly proportional to the strain $\varepsilon = \Delta L/L_0$ up to a certain range of deformation, using the proportionality factor of the foil pattern material, the strain can be measured [42]. The strain gauges were mounted longitudinally along the post axis in pairs on the outer sides of the flanges opposite to each other to form a Wheatstone half-bridge circuit. A schematic illustration of the connection configuration is shown in Fig. 3-21.

The gauges R1 and R2 are the physically installed strain gauges. The gauges R3 and R4 are completed by the data acquisition device by means of internal resistors to complete the circuit.

The half-bridge Wheatstone connection is the most suitable for measuring the bending stresses M_b in the steel post, as recommended by KEIL S. [42] in his book. The strain values measured on the top flange (ε_1 in active strain gauge R1) and bottom flange (ε_2 in active strain gauge R2) are added to the circuit. As the bending stress induced in the post cross-section by the lateral loading is much higher than the tension stress component in the post axis, the strains due to normal stresses ε_N are compensated by the circuit as follows:

strain measurement in the upper strain gauge R1

$$\varepsilon_1 = \varepsilon_{Mb} + \varepsilon_N \quad \text{Equ. 3-4}$$

strain measurement in the lower strain gauge R2

$$\varepsilon_2 = \varepsilon_{Mb} - \varepsilon_N \quad \text{Equ. 3-5}$$

absolute strain measured by the circuit

$$|\varepsilon_1 + \varepsilon_2| = 2 \varepsilon_{Mb} \quad \text{Equ. 3-6}$$

The output signal of the half-bridge circuit thus becomes:

$$\frac{U_M}{U_B} = \frac{k}{4} (2 \cdot \varepsilon_{Mb}) \quad \text{Equ. 3-7}$$

where, U_M/U_B is the ratio of the output and the input voltage, k is the proportionality factor of the foil pattern material and ε_{Mb} is the bending strain.

No additional temperature compensation is required for the Wheatstone half-bridge connection. This is due to the fact that equal changes in resistance in the same direction in neighbouring bridge branches (here R1 and R2) cancel each other, while equal changes in resistance in the opposite branches (e.g. R1 and R4) are added together [42]. Using the above-described configuration, the circuit is not susceptible to torsional moments acting around the beam axis. The applied strain gauges are linear in the range of strains $\pm 50\,000 \mu\text{m/m}$ (equivalent to $\pm 5\%$).

The strain gauges were installed in a section at 5 cm above ground level and in three sections with a spacing of 30 cm along the embedment length. The strain gauges and the connecting cables were sealed with epoxy resin to protect them from humidity and from mechanical abrasion during the post driving. In a series of trial tests, different methods were applied and compared for the protection of the strain gauges.

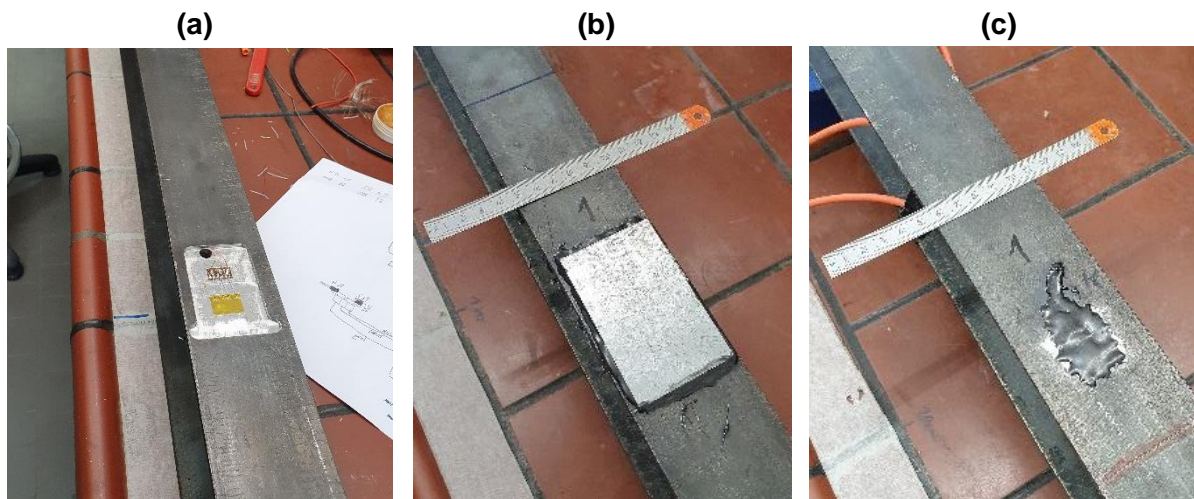


Fig. 3-22: Protection of the strain gauges using different methods

The first method was milling windows of 2 mm thickness on the outer flanges of the post, attaching the strain gauges and sealing it with an epoxy resin (Fig. 3-22a). The results were dissatisfying, as the post section yielded prematurely under lateral loading due to the reduced cross-section area. In the second method, the strain gauges were applied directly on the flange surface without milling and sealed with an additional thin steel plate and epoxy resin (Fig. 3-22b). This constellation worked well against mechanical abrasion. However, it was very tedious to adjust the volume of epoxy resin to be equal in all gauge locations. The resulting strains needed to be adjusted with a separate factor for each side. Moreover, the steel plate, together with the epoxy resin, added to the strength of the post section, which obviously reinforced the cross-section. These two methods were excluded, as they alter the section properties in the measuring sections and lead to inhomogeneity of the beam properties.

The third method was applying the strain gauges directly on the flange surface and sealing it only with a thin layer of epoxy resin (Fig. 3-22c). This method worked well against mechanical abrasion and did not alter the measurements or the section properties, as proven through the calibration and trial test. Therefore, this method was adopted for the protection of all the posts instrumented with strain gauges.



Fig. 3-23: Calibration of the installed strain gauges

After sealing the strain gauges, the instrumented post was calibrated, as shown in Fig. 3-23 and Fig. 3-24. The post was set as a simple beam configuration supported on a roller and a hinge. A concentrated load was then applied by hanging weights in the middle of the beam. The beam was loaded stepwise from 20 to 140 kg and then unloaded. In each step, the load was held constant for 20 seconds. The corresponding strains were measured in each step. This calibration routine was applied to all posts instrumented with strain gauges for the static as well as the dynamic tests.

The measured values were compared to the values calculated according to the elastic beam theory (see Fig. 3-24). The elastic strain was calculated at a given section as follows:

bending Moment

$$M = (\xi \cdot F \cdot L)/2 = E \cdot I \cdot \theta \quad \text{Equ. 3-8}$$

section curvature

$$\theta = 2 \cdot \varepsilon / h \quad \text{Equ. 3-9}$$

elastic strain

$$\varepsilon = (\xi \cdot F \cdot L \cdot h)/(4 \cdot E \cdot I) \quad \text{Equ. 3-10}$$

where, F is the applied concentrated load, L is the beam span, h is the height of the cross-section, EI is the flexural rigidity, and ξ is the ratio of strain gauge distance from the support to the beam span.

The measured strains show a maximum deviation of 2.4 to 5.1 % from the calculated values. The exact deviation was determined for each strain gauge section and was applied as an adjustment factor for the strain measurements. The measured strains show stable values under constant loads.

The strain measurements are used later for the determination of the soil reaction and the deflections along the embedment length developed during the loading tests. The approach followed for the analysis of the soil-structure interaction and development of unit load-transfer curves is discussed under *6.1 Experimental p-y curves*.

The test progress was documented using a high-resolution camera using the time-lapse feature (1 frame per second). The camera was set at a distance of 1.5 to 2.0 m perpendicular to the loading path, far enough to ensure that the soil heave during the test does not affect the camera position. The generated image series were used to amend the wire potentiometer measurements at further points along the post and to verify the measured deflection values. Using the deflection measurements and the automatic object tracking analysis of the images (Particle Image Velocimetry), it was possible to determine the rotation of the post above the ground level during the test. For the tests where no plastic deformations occurred in the post, the position of the rotation point underground could be determined by means of extrapolation. The measurements were acquired using the universal data acquisition module QuantumX-MX840A, capable of sampling rates up to 40 kHz. The data of the static test (force, displacements and strains) were acquired and recorded synchronously with a sampling rate of 10 Hz and were smoothed using a Bessel low pass filter. The static loading tests were conducted 7 days after installation of the posts. At that time, the soil exhibited on the surface a moisture content of 2 to 3%.

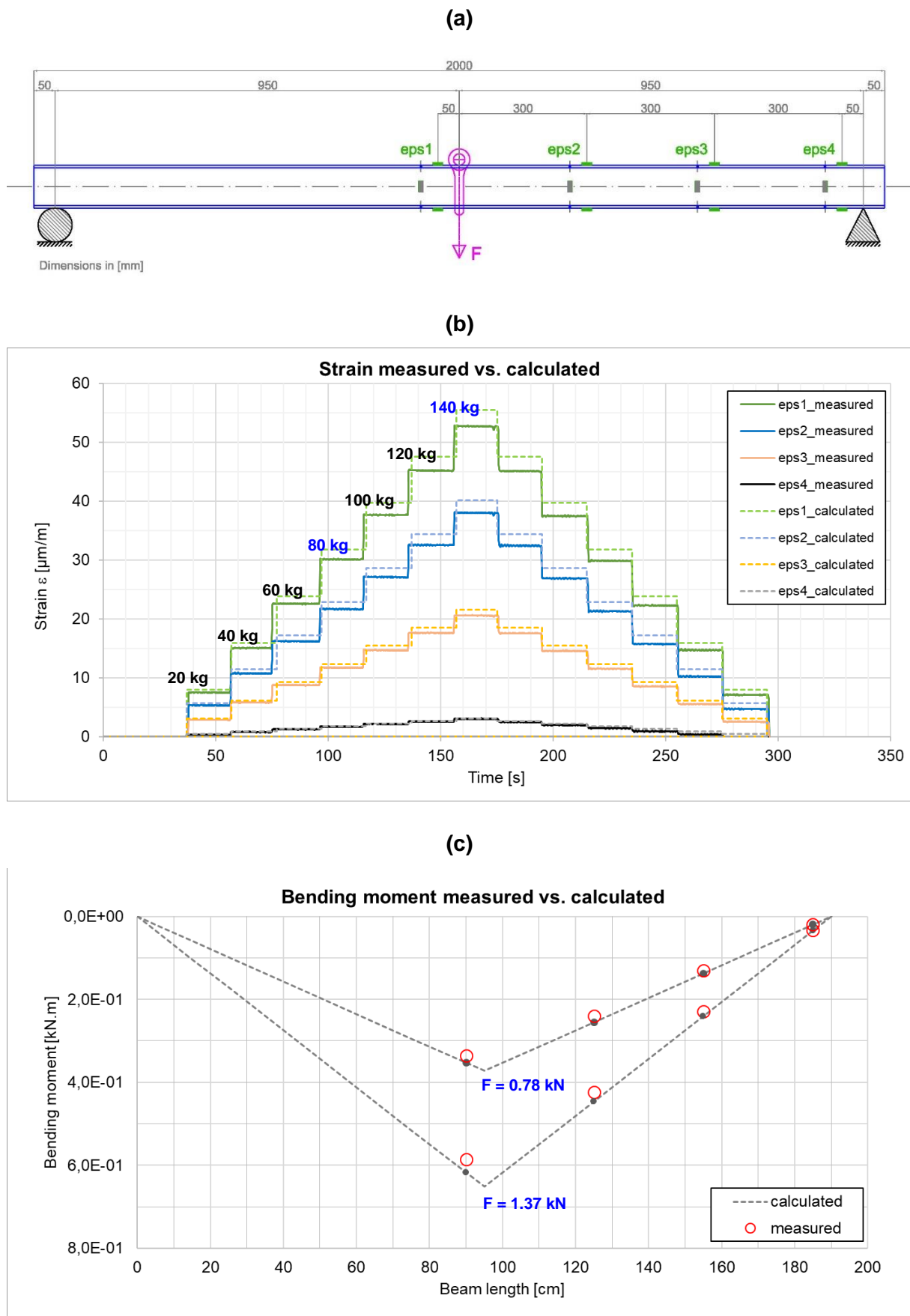


Fig. 3-24: (a) Configuration of an instrumented IPE120 post during calibration (b) Strain gauge measurements (c) Bending moments for the steps 80 kg and 140 kg

Reference test results

In this section, the results of the quasi-static tests are presented. First, the results of the tests conducted under reference conditions (soil KSS032 dense, post IPE120, embedment length 100 cm) are discussed. Then followed by the results of the variation of the loading axis, soil materials, embedment length and post section. Three posts were loaded in the strong axis under reference conditions up to 0.4 m. For illustration, the results of the first test P01 are presented in Fig. 3-25. The applied load measured by the force transducer and the deflection measured by the wire potentiometer at the loading point are used to construct the load-deflection curve (Fig. 3-25a). The post rotation (Fig. 3-25b) is calculated at each time increment as the difference between the measured deflection at the loading point at 75 cm above GL and at 5 cm above GL divided by the post segment length 70 cm. The loading rate (Fig. 3-25c) shows a nearly constant low rate of ca. 3.2 mm/s, which is necessary to exclude any inertial effects or undrained behaviour. Using the load-deflection data, the horizontal system stiffness evaluated as a secant modulus was calculated at selected steps, as shown in Fig. 3-25d. The results show a significant degradation of the system stiffness after reaching 20% of the maximum load (corresponding to a deflection of 11 mm).

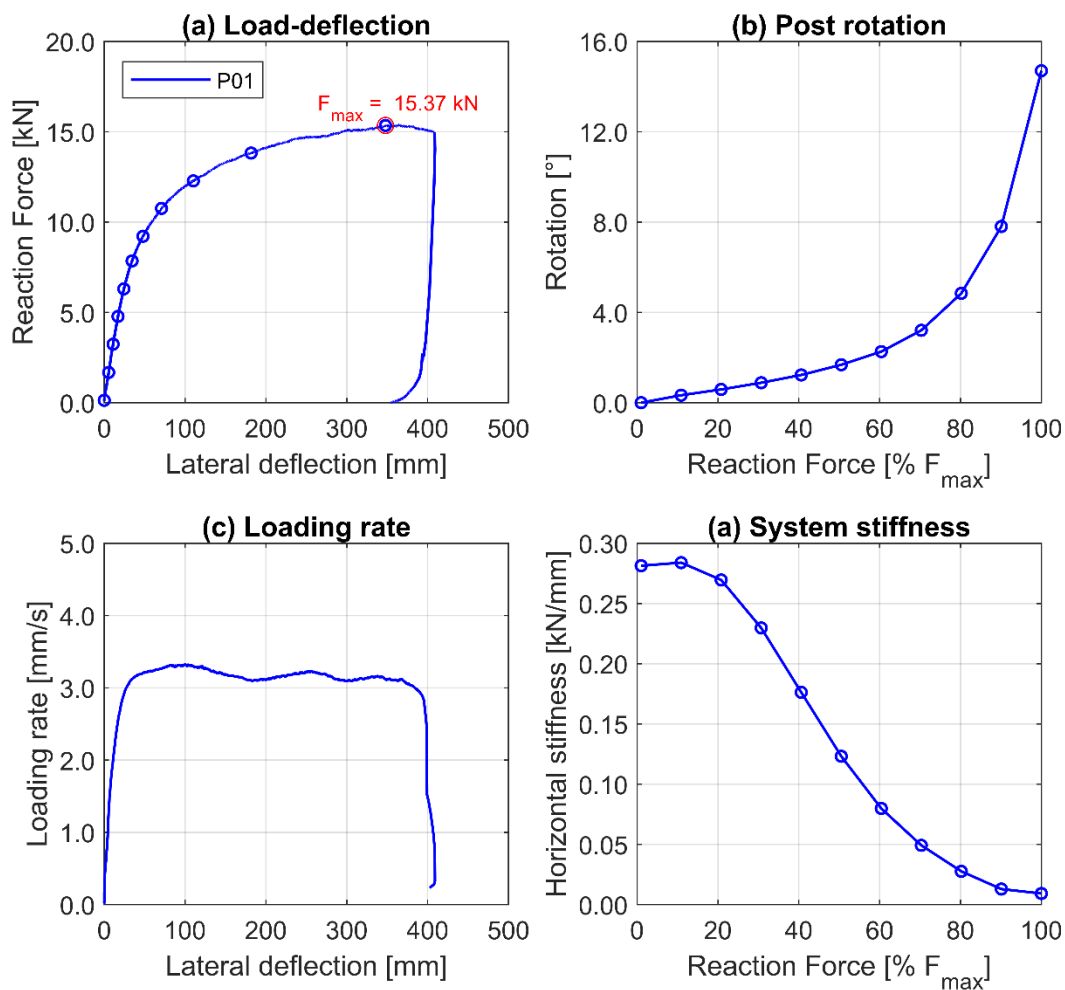
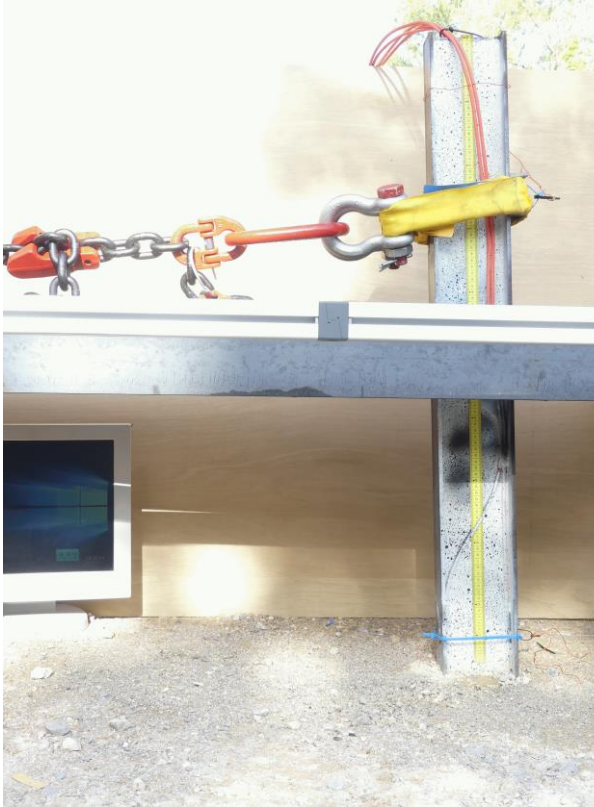


Fig. 3-25: Results of the quasi-static loading test P01; Load-deflection curve, loading rate, post rotation and evaluated linear stiffness

$t = 0 \text{ s}$, $u = 0 \text{ mm}$,
 $F = 0.0 \text{ kN}$, $F = 0\% F_{\text{max}}$



$t = 24 \text{ s}$, $u = 5 \text{ mm}$,
 $F = 1.54 \text{ kN}$, $F = 10\% F_{\text{max}}$



$t = 36 \text{ s}$, $u = 33 \text{ mm}$,
 $F = 7.69 \text{ kN}$, $F = 50\% F_{\text{max}}$



$t = 133 \text{ s}$, $u = 340 \text{ mm}$,
 $F = 15.37 \text{ kN}$, $F = 100\% F_{\text{max}}$



Fig. 3-26: Static test P01 sequential photos at 0%, 10%, 50% and 100% of the maximum force



Fig. 3-27: Soil heave in the loading direction and formation of a gap behind the post

Sequential photographs of the reference test P01 are shown in Fig. 3-26. The soil is observed to heave in front of the post in the loading direction to the extent of ca. 60 cm. A gap is formed behind the post, which extends to a depth of ca. 40 cm at the end of the test. During the test, the soil behind the post pours down the gap and closes it partially.

The reference test was conducted three times under the same conditions in the longitudinal direction (strong axis) and two times in the transversal direction (weak axis). The load-deflection curves of the reference static tests in the strong axis (soil KSS032 dense, post IPE120, embedment length 100 cm) are shown in Fig. 3-28. In both cases, the results show good repeatability.

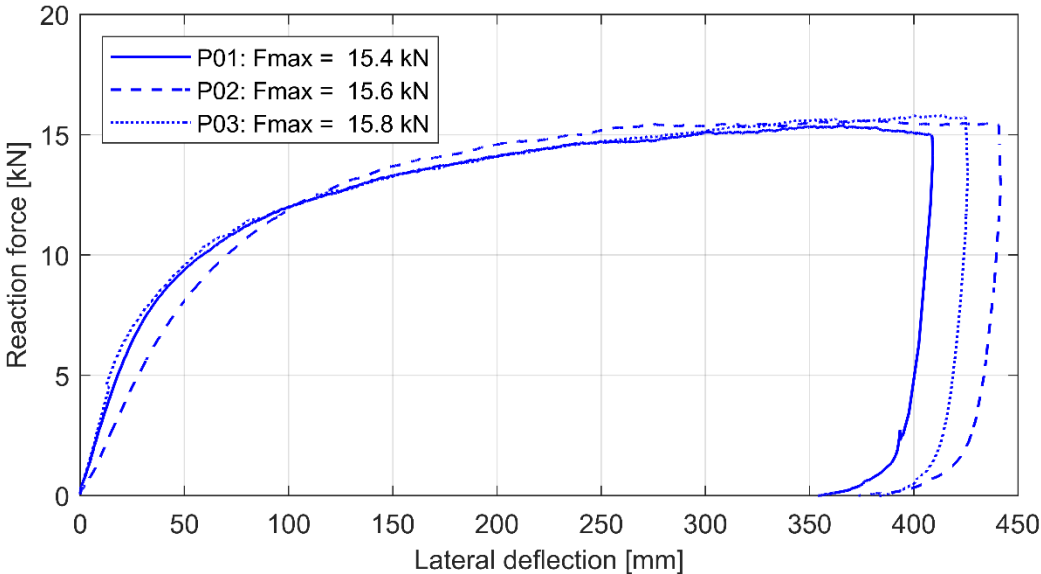


Fig. 3-28: Load-deflection curves of the quasi-static reference tests conducted in the strong axis

The results and sequential photographs of the tests P02 and P03 are presented in *Appendix [C]: Quasi-static tests*. The maximum value of the reaction force reached in the strong axis was between 15.4 kN and 15.8 kN (Fig. 3-28). The force shows an approximately linear increase with displacement in the first section up to 30% of maximum force. Afterwards, a strong non-linearity of the force development is observed before reaching the maximum force. The complete unloading of the posts resulted in an elastic relaxation of the deflection of 10 to 12 % of the maximum deflection.

The posts were excavated after the test, and no plastic deformations were observed. The posts behaved as a rigid body and rotated about a point below ground level. The soil yields at the ground level with a horizontal deflection of 15 cm at the maximum reaction force. Using extrapolation of the measured deflections above GL, the rotation point was estimated at a depth between 40 and 60 cm below GL.

Variation of loading axis

The load-deflection curves of the tests conducted in the weak axis show nearly identical behaviour (see Fig. 3-29). The maximum value of the reaction force reached at 400 mm ranged between 7.6 kN and 8.0 kN. The force increased linearly up to 50% of the maximum reaction force. The excavated posts show evident plastic deformations due to bending. Torsion of the post was excluded due to the application of the guidance frame. A plastic hinge was formed at a depth between 15 and 20 cm below ground level. The horizontal deflection at ground level reached 10.5 cm at the maximum reaction force. The ratio of the maximum reaction force in the strong axis to the weak axis is ca. 50% (evaluated at 400 mm). The posts tested in the weak axis in KSS016 and GB032 showed similar loading-displacement behaviour and maximum resistance, with a slight variation in the initial stiffness. This indicates that the section's material properties govern the weak axis's behaviour.

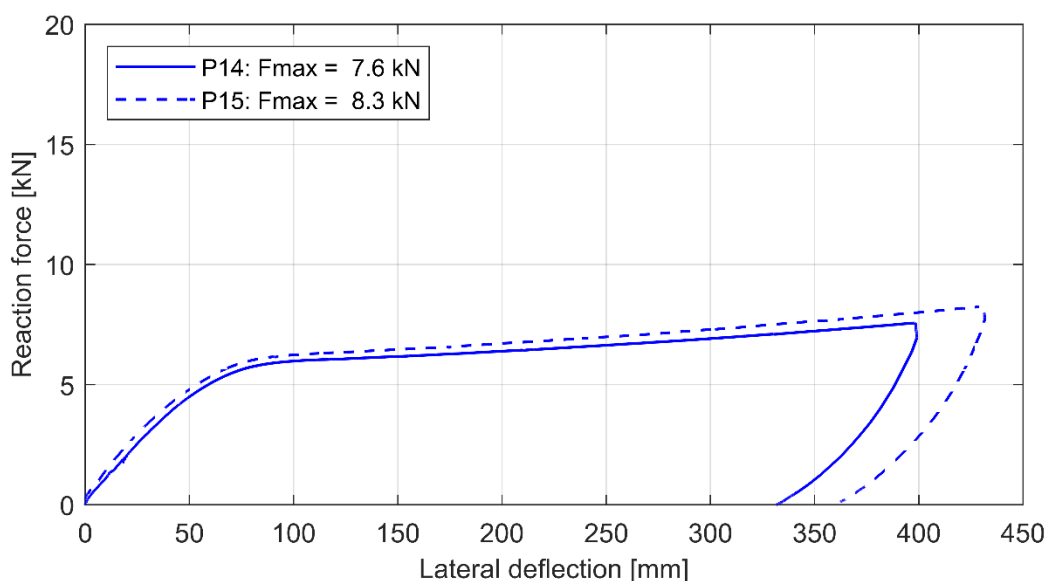


Fig. 3-29: Load-deflection curves of the quasi-static reference tests conducted in the weak axis

Sequential photographs of the reference test P14 conducted in the weak axis are shown in Fig. 3-30. The excavated posts tested in the weak axis are shown in Fig. 3-31. The posts show a rotation angle of 22° to 23°.

$t = 0 \text{ s}$, $u = 0 \text{ mm}$,
 $F = 0.0 \text{ kN}$, $F = 0\% F_{\text{max}}$



$t = 23 \text{ s}$, $u = 5 \text{ mm}$,
 $F = 0.76 \text{ kN}$, $F = 10\% F_{\text{max}}$



$t = 40 \text{ s}$, $u = 39 \text{ mm}$,
 $F = 3.79 \text{ kN}$, $F = 50\% F_{\text{max}}$



$t = 134 \text{ s}$, $u = 385 \text{ mm}$,
 $F = 7.57 \text{ kN}$, $F = 100\% F_{\text{max}}$



Fig. 3-30: Static test P14 sequential photos at 0%, 10%, 50% and 100% of the maximum force



Fig. 3-31: The excavated posts tested in the weak axis P14 and P15 showing yielding of the steel post

Variation of soil material

Fig. 3-32 shows the load-deflection curves of the IPE120 post with 100 cm embedment length, loaded in the strong axis under variation of the soil material. The materials were compacted to reach approximately the same relative density ($I_D = 76 - 82\%$ dense). Curve no. 1 represents the reference test conducted in dense crushed limestone 0-32 mm (KSS032). The variation of the grain size distribution in the same material (curves 1 and 2) shows a reduction of the reaction force by 3.0 kN for the KSS016. However, the curves nearly coincide in the first section up to 50% of the maximum force.

Curves no. 1 and 3 in Fig. 3-32 show the effect of the variation of the mineralogy and grain strength of the soil material on the post response. The crushed granite GB032 (curve 3) exhibits a stiffer response compared to the crushed limestone (curve 1), although both have the same relative density. The maximum force increased by 16% compared to the KSS032 and by 42% compared to the KSS016.

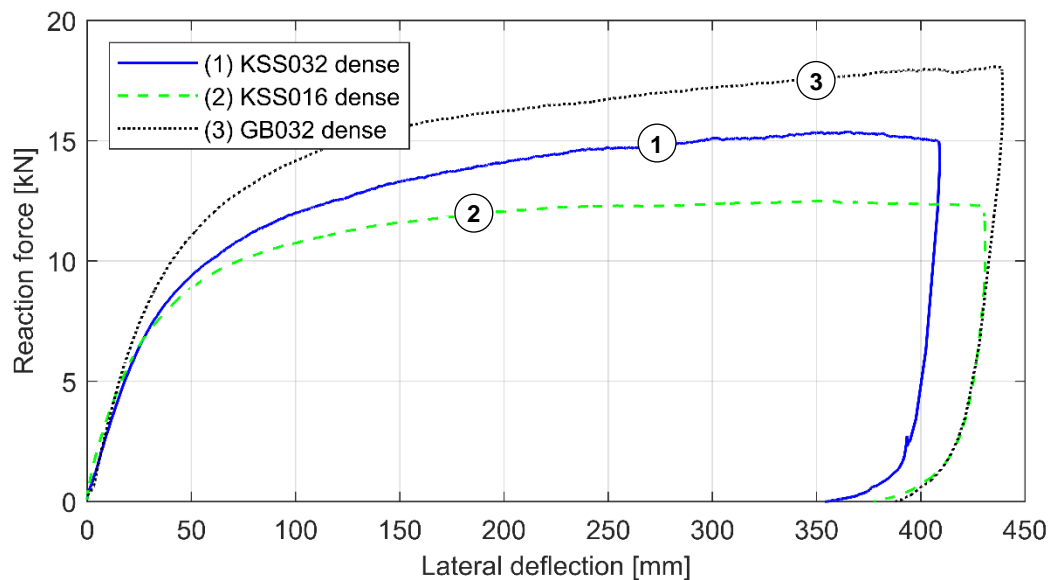


Fig. 3-32: Load-deflection curves under variation of the soil material with the same relative density

The results of the variation of the relative density on the post response are shown in Fig. 3-33. The soil material KSS032 was compacted on one test area with less energy to a relative density of $I_D=55\%$ (medium dense). A comparison of curves 1 and 2 shows that a reduction of the relative density by 31% has led to a reduction of the maximum force by 19% and reaching the non-linear phase earlier.

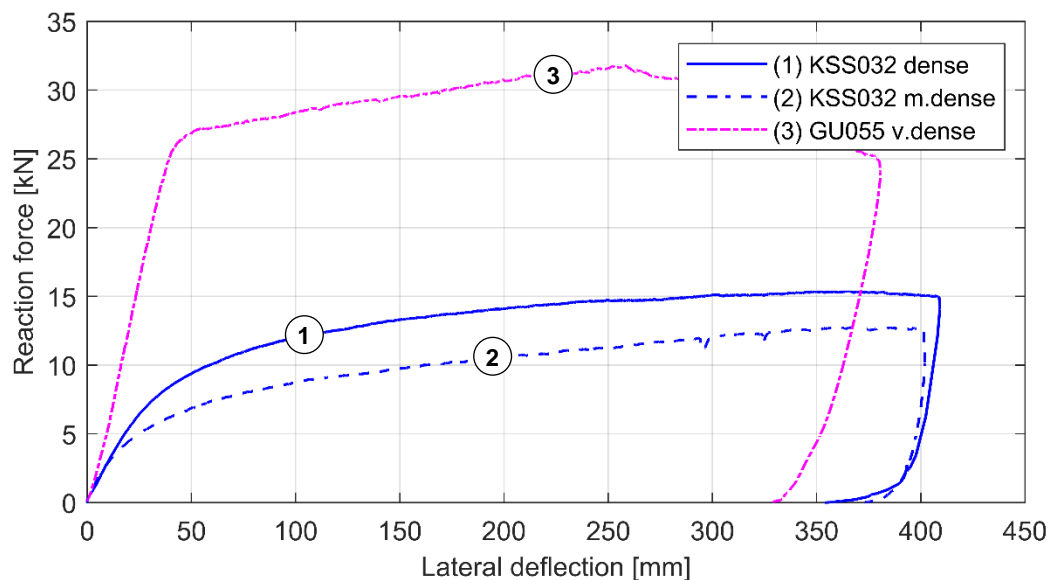


Fig. 3-33: Load-deflection curves under variation of the soil material and relative density

The silty gravel GU055 exhibits a much stiffer response due to its high relative density ($I_D=94\%$). Worth mentioning here is that this soil contains larger grains compared to the KSS032, which may have added to the soil's stiffness and, consequently, to the post resistance. The reaction force increases linearly up to 40 mm deflection, and then the steel post starts to yield at 25.5 kN. The force then increases linearly to reach the maximum force of 31.8 kN at a deflection of 260 mm. Afterwards, torsion of the post section was observed, which explains the declining trend of the force with further loading.

As shown from the test results, the increase in the relative density of the embedment soil leads not only to the increase of the reaction force, but also changes the post failure mechanism. The very dense soil developed a fixation and the post acts as a cantilever under lateral load. The properties of steel material govern the response in this case. In contrast, the dense and medium dense soil allowed the post to rotate without plastic deformations of the steel section. The failure mechanism is investigated numerically in section 5.5 *Parametric study*.

Variation of embedment length

To investigate the influence of the variation of the post embedment length, two tests were conducted on IPE120 posts with a reduced embedment of 80 cm and 85 cm in the dense KSS032. The load-deflection curves are presented in Fig. 3-34. With a reduction of the embedment length by 20 cm, the maximum reaction force was reduced by 51%. The maximum force is reached earlier at a deflection of 23 cm compared to 41 cm in the reference test. With an embedment length of 85 cm, the maximum reaction force was reduced by 40% and was reached at a deflection of 22 cm.

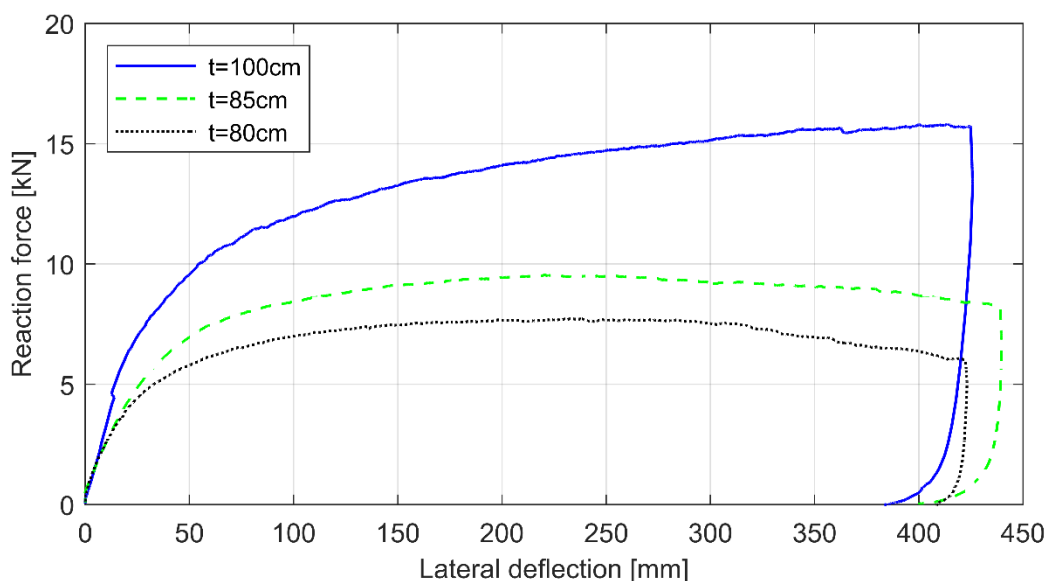


Fig. 3-34: Load-deflection curves of the variation of the post embedment length under reference conditions

This variation is very important for the design of a VRS. The mobilised post reaction force is very sensitive to the reduction of the post embedment length. Field tests with an embedment length larger than 100 cm have not been conducted to evaluate the influence on the post response. However, this variation was considered in the numerical parametric study (see 5.5 Variation of embedment length).

Variation of post-section

The load-deflection curves of three different post cross-sections, tested in dense crushed limestone KSS032 in the strong axis are presented in Fig. 3-35. Compared to the IPE120, the C125 post showed a lower initial stiffness and a lower reaction force of 13.3 kN at 350 mm deflection. However, the C125 post reaction force increased linearly after reaching the non-linearity and did not reach a plateau (maximum 14.0 kN). The HEB120 post exhibited a slightly higher initial stiffness compared to the IPE120 and reached the maximum force earlier (15.6 kN at 235 mm deflection). The reaction force tends to decline with further loading. The maximum force reached by both post sections is approximately equal. No plastic deformations were observed on the excavated C125 and HEB120 posts.

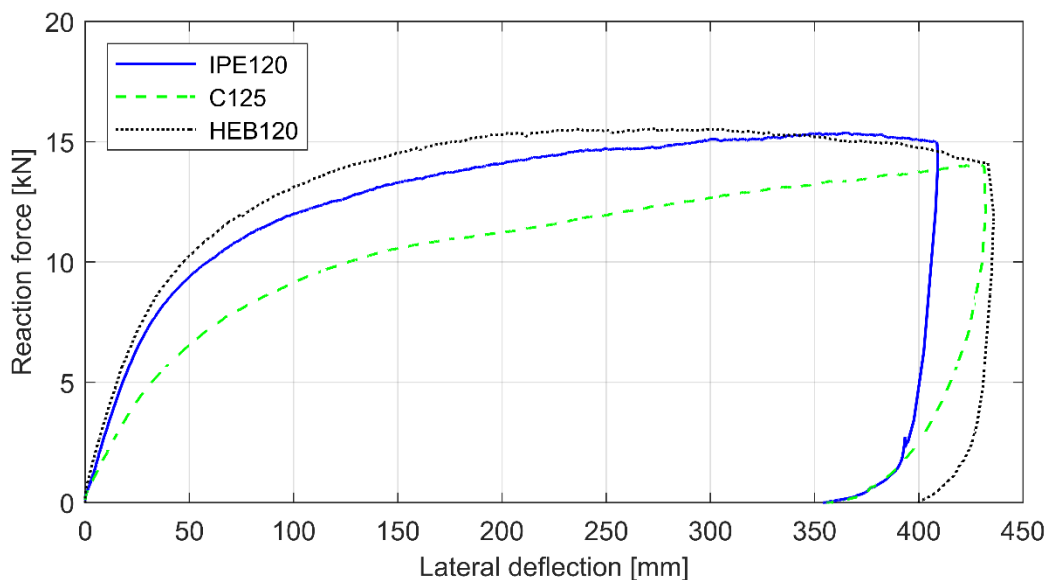


Fig. 3-35: Load-deflection curves of the variation of the post section under reference conditions

The results of the post section variation show that the post width in the loading direction, i.e. flange width, does not have a significant influence on the reaction force. At least in the range of the tested post sections and as long as the failure of the system is governed by the failure of the soil. The HEB120 exhibits a flange width of 1.9 folds that of the IPE120, however, the reaction force did not increase with the same factor. For both sections, the elastic section modulus did not play a role in the post resistance, since the failure mode was a rigid post rotation and soil yielding.

The section geometry has a rather more significant influence on the resistance. The C125 section is asymmetric when loaded in the strong axis. The centre of area and the shear centre do not coincide in the strong axis, which leads to twisting of the post section around its own axis. Twisting, i.e. torsion, is constrained in the height of the guidance frame and at the loading point. Nevertheless, the post section can warp below the guidance frame and under the ground level. Due to torsion, the post resists the applied lateral load with a rotated section, which exhibits in this case, a flexural rigidity lower than the strong axis. The results of the quasi-static test conducted in C125 in the weak axis are shown in *Appendix [C]: Quasi-static tests*. The maximum reaction force measured was 10.9 kN at a lateral deflection of 395 mm. The influence of the section geometry on the post response is further discussed in section 5.5 Parametric study.

3.3 Dynamic loading tests

The second group of posts was tested under impact loads with different intensities. The dynamic impact was applied to the post using the THOR-3 impact-loading device manufactured by AISICO srl. The loading device is equipped with two pneumatic cylinders used to accelerate an impactor with a mass of 192 kg. By varying the pressure in the pneumatic cylinders, different impact forces can be realised. The impulse was applied at a height of 75 cm above ground level, analogue to the static test. With a cylinder pressure of up to 40 bar, an impact energy of a maximum 10.5 kJ could be achieved. Compared with the vehicle impact energy in the crash test as per DIN EN 1317, this corresponds to 25.7% of the impact energy of TB11 (0.9 Tons vehicle, speed 100 km/h and impact angle 20°) and 3.7% of the impact energy of TB51 (13 Tons vehicle, speed 70 km/h and impact angle 20°) [23].



Technical Data:

Identification

Model	T.H.O.R. III
Manufacturer	AISICO SRL
Powering	Electrical
Serial number	20-001

Dimensions

Length	192 cm
Width	175 cm
Height	173 cm
Mass	3020 kg

Compressor

Power	2.6 kW
Operating pressure	5-60 bar
Hammer weight	192 kg

Fig. 3-36: Dynamic testing equipment THOR3 developed by AISICO srl.

The advantage of conducting the impact tests using this equipment, compared to the boogie vehicle, is that it requires no acceleration track and can be applied on a smaller test field. This allows the test posts to be installed in a closer vicinity, which can reduce the soil homogeneity problems compared to a larger field. The boogie vehicle has another problem, which is the ride-over of the post. The post is not free to recoil after the impact, and the final position is falsified by the boogie vehicle chassis. Moreover, the boogie ride-over may lead to destroying the instrumentation and losing the test measurements. This issue is excluded here, as the maximum impactor stroke is limited. Compared to pendulum testing equipment, less setup is required to reach a relatively high impact energy. Using a pendulum system and swinging the same mass of 192 kg to achieve a comparable impact velocity like the maximum achieved in our testing program (10.4 m/s), a lever arm of 5.5 m would be required. Although the mechanical assessment of the results would be easier, such a huge pendulum setup would require laborious safety measurements and is difficult to handle.

Instrumentation and test procedure

Due to the highly dynamic nature of the impact loading, the force and deflection instrumentation had to be adapted compared to the quasi-static test. The force at the impact point was measured by two load transducers installed behind the impactor head. The displacement of the impactor was recorded by a built-in incremental encoder (see Fig. 3-37). The impactor force and displacements were recorded internally in the loading device with a sampling rate of 5 kHz. An additional accelerometer was mounted on the impactor head to measure the accelerations in the impact direction.

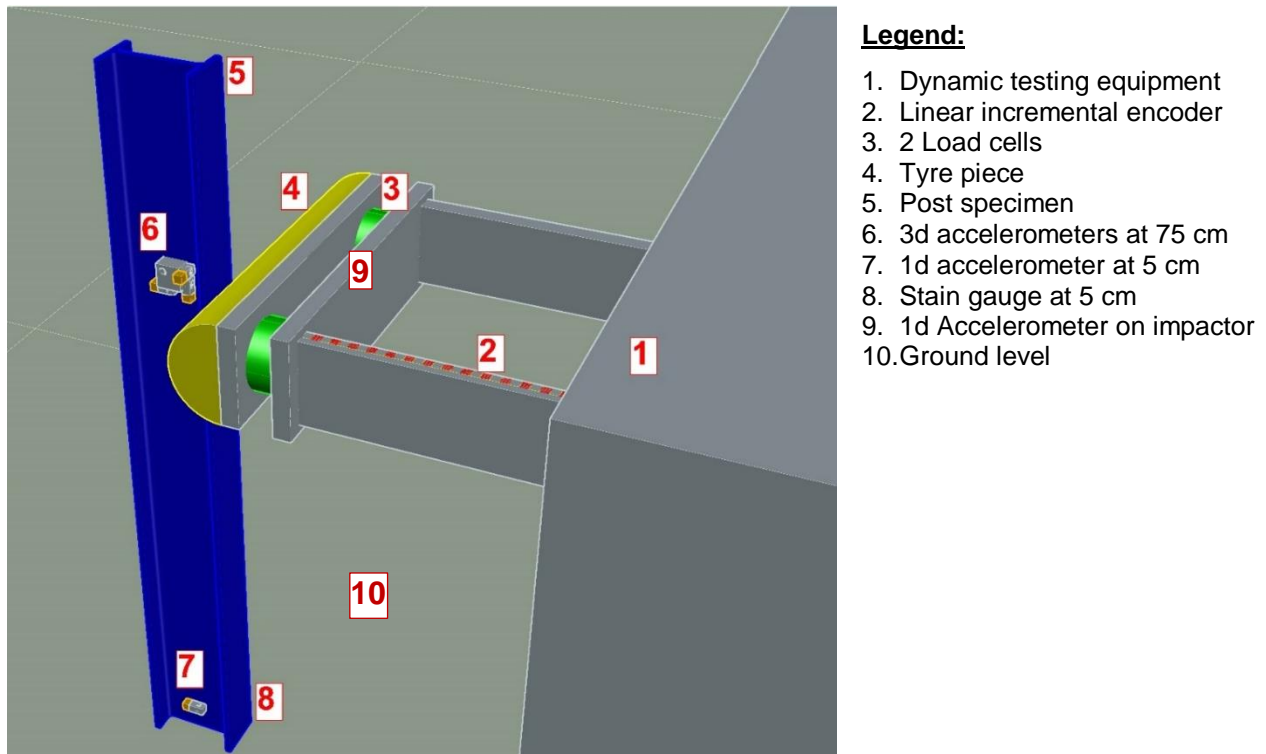


Fig. 3-37: Isometric view of the test setup and instrumentation of the dynamic loading test

A direct measurement of the post deflection using the wire potentiometer is not possible, as the inertia of the mechanical parts inside the sensor leads to the breaking of the wire during loading. Moreover, the mechanical roller inside the sensor jams under fast recoil. Therefore, the post deflections were measured indirectly using accelerometers. The tested posts were instrumented with 4 MEMS (Microelectromechanical systems) piezoresistive uniaxial accelerometers (see Fig. 3-19d). Three sensors were fastened together on a solid block to form a triaxial accelerometer and were installed at the height of the impactor of 75 cm. A single accelerometer was installed at 5 cm above ground level, with the measuring axis set in the loading direction. The installed accelerometers have a shock resistivity of up to ± 5000 g and are common in the field of automotive crash testing.

Two high-speed cameras were used to record the impactor displacement and the post deflection with a frame rate of 500 frames per second. One high-speed camera was positioned to capture the impact in the loading plane, and the other camera was positioned in front of the post.

The posts were further instrumented with strain gauges analogue to the posts in the static tests. The strain gauges were calibrated through the same routine described in section 3.2.

Instrumentation and test procedure. The strain gauge measurements were acquired and recorded synchronously with a sampling rate of 1 kHz and were smoothed using a Bessel low-pass filter. The accelerometer measurements were sampled with a frequency of 100 kHz and were not filtered. The measurements were sampled using the data acquisition module QuantumX-MX410B, optimised for highly dynamic measurements up to 200 kHz. The dynamic loading tests were conducted six days after the installation of the posts. At that time, the soil exhibited a moisture content of 2 to 3% on the surface.

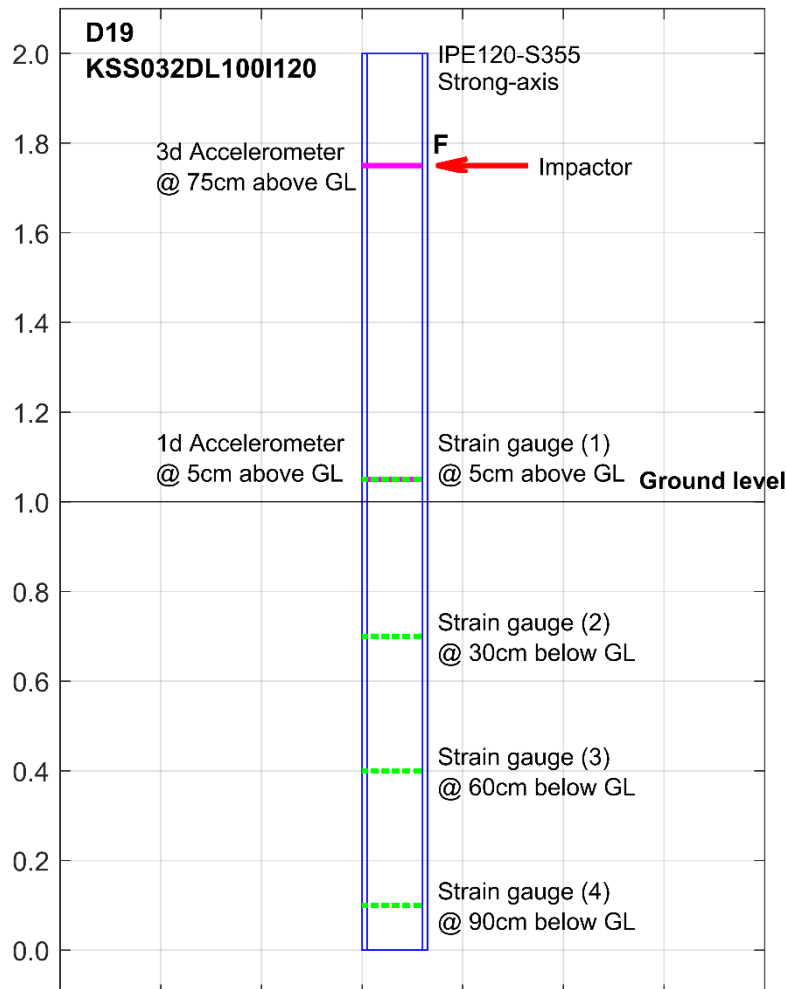


Fig. 3-38: Illustration of the post instrumentation in the dynamic test

The dynamic tests were conducted on unguided free posts since the loading equipment had to be located at a distance of a maximum of 50 cm away from the tested post. Moreover, applying the guidance frame may falsify the reaction force, as the post may slightly twist and lock in between the guide beams, and consequently mobilize additional inertial forces due to the mass of the guidance frame. The high-speed camera recordings showed no significant post twisting or deflection out-of-plane during the impact. The built-in guidance of the impactor frame was sufficient for the stabilization of the impactor and post.

In order to simulate different impact situations, the impact force was applied with varying intensities to posts under the same soil conditions. That impact intensity was controlled in the testing equipment by setting the pneumatic cylinder pressure. A direct setting of the impact

energy or impactor velocity was not possible. Therefore, the cylinder pressure was increased step-wise in additional tests on a training field, and a correlation between the cylinder pressure and the impactor kinetic energy was concluded (Fig. 3-39). For the tests conducted in the strong axis of the post, the pressure was set to 10 bar in the first test and increased by a step of 10 bar in the higher intensities. For the tests conducted in the weak axis, the pressure was set to half of these values. Using these settings, the impact energy ranged between 2.1 and 10.5 kJ.

In the framework of the research project, a crash test simulation was conducted by TÜV-SÜD for the impact energy distribution between the Super-Rail Eco elements under TB51 collision. The results show that the maximum impact energy dissipated by the posts was concentrated in the two posts at the collision location with a magnitude of 8.9 to 9.4 kJ. The posts standing further from the impact location experienced lower impact energy levels. The percentage of the energy dissipated deforming the posts and soil together is approximately 46% of the total strain energy.

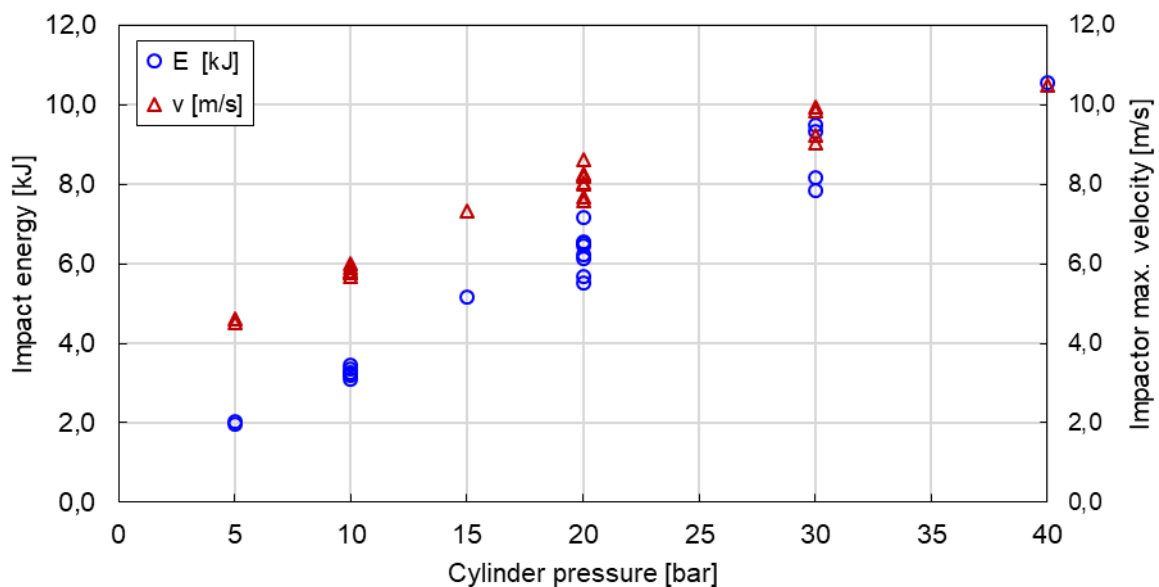


Fig. 3-39: Correlation between the loading equipment cylinder pressure, maximum impactor velocity and the resulting kinetic energy at impact

The first step in analysing the measured data was synchronizing the timeline of the applied independent measurement systems. These are the impactor internal data acquisition system, the accelerometers and strain gauges on an external data acquisition system and the high-speed camera videos analysed using the Tracker-software.

The synchronization is illustrated here as an example on the reference Test No. D19 executed on an IPE120 post in the strong axis, embedded to 100 cm in dense KSS032. As shown in Fig. 3-40, all the measurements were shifted to Time = 0 ms, which indicates the impact time point. The impact time point was determined from the data of the accelerometer mounted on the impactor, as the point at which the impactor starts to decelerate ($dv/dt = 0$). The recoil time point, i.e. change of velocity vector direction, is determined at approximately 85 to 90 ms.

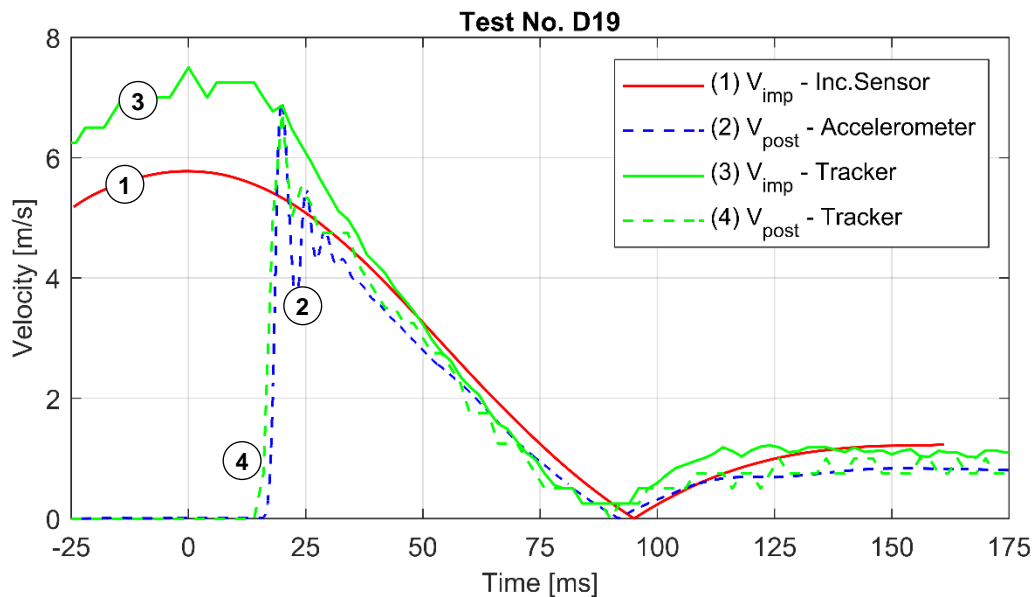


Fig. 3-40: Synchronisation of the measurements in the velocity time-history for the impact test D19 conducted under 3.2 kJ

The impactor velocity derived from the video analysis (Tracker) shows a deviation from that derived from the incremental encoder. This can be attributed to a parallax error in the video analysis of the impactor path. The camera was set perpendicular to the impactor path in front of the post. The images are distorted at the points far from the camera's focal point, i.e., close to the frame edges. Therefore, the total projected length of the impactor path is shorter than the actual length. Since the farthest point from the focal point is the impactor location at rest, the error is at its maximum in the segment before hitting the post. Although the frame rate is constant for both paths, the impact velocity is overestimated in the first segment. The post peak velocity at impact derived from the accelerometer measurements was observed to be approximately equal to the post velocity derived from the video analysis (± 0.2 m/s), which confirms this interpretation. Based on the above observations, the impact velocity was determined as the maximum velocity derived from the impactor displacement measurements.

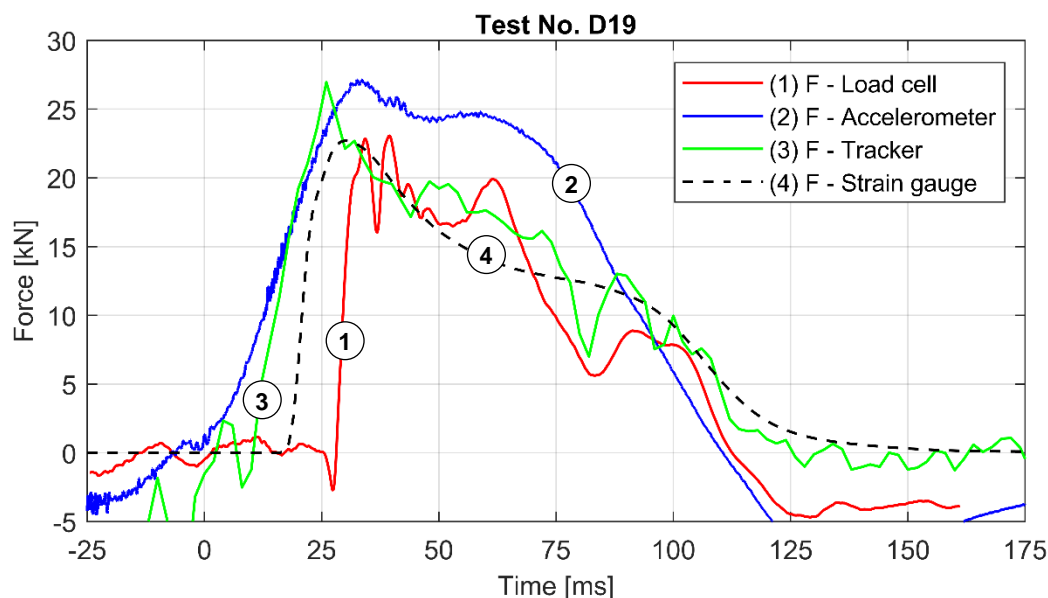


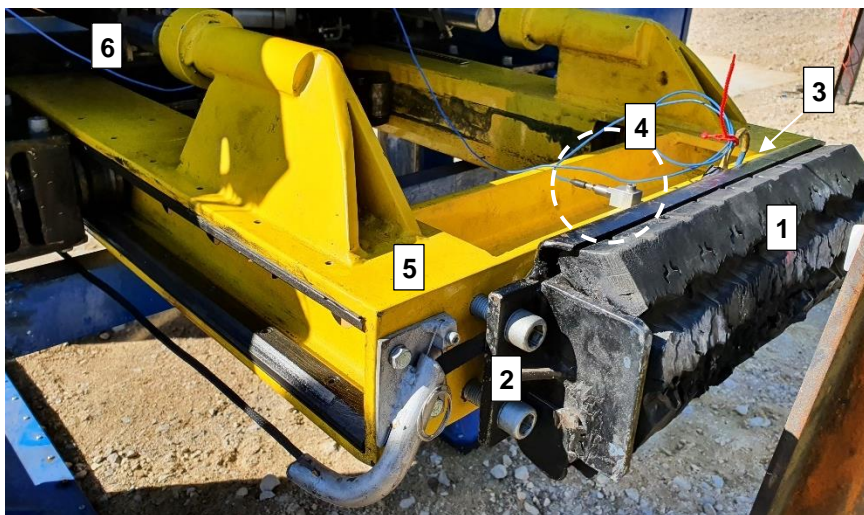
Fig. 3-41: Determination of the reaction force using different approaches for the impact test D19 conducted under 3.2 kJ

Different approaches were considered to evaluate the reaction force of the system. The force time-history curves evaluated for Test D19 are presented in Fig. 3-41.

The first method is measuring the impact force directly using the load cells mounted behind the impactor head (Fig. 3-41 curve 1). The total force is the sum of the two measured force components. Fig. 3-42 shows the configuration of the impactor head and the instrumentation installed. The forces measured by this method show strong fluctuations during the impact due to the configuration of the impactor head. The load cells are located between the impactor head, consisting of a steel plate covered by a tyre piece, and the steel frame connected to the pneumatic cylinders. To keep the load cells unloaded at rest conditions, a couple of springs are built parallel to the load cells, pushing the steel plate outwards. The elasticity of the tyre material together with the springs leads to oscillations of the measured force, and in some cases, to losing contact between the impactor and the post.

At the first contact of the impactor with the post during the test, the tyre piece is compressed before the springs and the load cells start measuring forces. At this moment, the whole impactor starts to decelerate. Due to the deformation, i.e. time lag required before triggering the load cells, the first contact time cannot be determined directly from the load cell measurements. Therefore, the time point of the first contact was determined from the measurements of the accelerometer mounted on the impactor. The deceleration time point was further verified by the high-speed camera video analysis.

The initial dip at the beginning of the impact observed in all force time-histories measured by the load cells is attributed to the inertial effects of the impactor head. Here for example, at 25 ms on curve 1 in Fig. 3-41. This phenomenon was also observed by REID et al. [75] during impact testing of posts using a bogie vehicle.



Legend:

1. Impactor head tyre piece
2. Impactor head steel plate
3. Load cells mounted behind the impactor head
4. Accelerometer mounted on impactor frame
5. Impactor steel frame
6. Pneumatic cylinders

Fig. 3-42: Configuration of the impactor head and installed instrumentation

The second method is calculating the impact force as per Newton's second law of motion. The force is equal to the mass of the moving body, i.e. impactor mass, multiplied by the rate of change of velocity, i.e. the acceleration. Using the readings of the accelerometer mounted on the impactor frame and the impactor mass of 192 kg, the reaction force was calculated (Fig. 3-41 curve 2). The range in which the impactor is decelerated indicates the total contact time.

The third method is the same as the second method, but the acceleration history is determined from the analysis of the high-speed camera videos (Fig. 3-41 curve 3). A mark placed on the impactor is tracked through the video frames, and knowing the frame rate, the velocity was calculated. Then, the acceleration was calculated by differentiating the velocity over time.

The fourth method is evaluating the lateral force from the bending strain acting on the post at ground level (Fig. 3-41 curve 4). In this case, the post is considered as a cantilever. Using the strain gauge measurements in the section located at 5 cm above ground level, the curvature of the section can be calculated. The curvature is then multiplied by the post flexural rigidity to determine the section bending moment. At this elevation, the soil resistance does not have an effect on the shear force distribution. However, the inertia of the post segment above ground has to be considered. The presented curve does not include the fluctuations due to the mass inertia. The inertial force is assumed to be acting in the middle of the post segment above the strain gauge level opposite to the impact direction. The lateral force from bending strain was calculated as follows:

$$F = \frac{M}{h} + m \cdot a \cdot \frac{L^2}{2 \cdot h} \quad \text{Equ. 3-11}$$

Where, M is the bending moment, h is the lever arm of 70cm, m is the mass of the post per unit length, a is the mean acceleration from the levels 75 and 5 cm, L is the post segment length above the strain gauge level.

The course of the force time-history is comparable for all methods. The force jumps to its maximum value directly after the impact moment, then decreases at a slow rate till reaching the recoil point. Afterwards, the force diminishes rapidly till the point of losing contact between the impactor and the post. The maximum force evaluated using the last three methods compared to the force measured directly using the load cells shows a deviation of 5 to 15%. The time point of losing contact nearly coincides for all methods.

The response time point of the impactor and post show a minor lag, although the recoil time point coincides for all elements. This is clear in the late respond (about 15 ms) of the post compared to the impactor from the Tracker video analysis (see Fig. 3-40 curves 3 and 4). The same lag is observed for the strain gauge measurements (see Fig. 3-41 curve 4). The Load cell measurements show the same lag, but with additional lag due to the inertial effects in the load cell (see Fig. 3-41 curve 1).

From the above discussion, the force evaluation method using strain gauge measurements was chosen here for the results presentation and further calculations of the post "reaction force". This approach was also adopted by MIRDAMADI [54] for the measurement of posts lateral reaction forces. He examined the behaviour of single posts with relatively larger dimensions under lateral truck impact. The measurements are less susceptible to the dynamic effects in the impactor head and are therefore more reliable in the elastic range of the material. Moreover, the strain gauges were calibrated in the laboratory before installation, and the measurements were verified. Since not all posts were instrumented with strain gauges or were partially damaged during post driving, in those tests, the impactor load cell measurements are presented instead and denoted as "impact force".

Reference test results

In this section, the results of the dynamic impact tests are presented. First, the results of the tests conducted under reference conditions (soil KSS032 dense, post IPE120, embedment length 100 cm) are discussed. Then followed by the results of the variation of the post characteristics and axis and soil materials. Three posts were loaded in the strong axis under the same conditions with impact energies of 3.2, 5.7 and 8.2 kJ corresponding to impactor velocities of 5.7, 7.7 and 9.2 m/s. Sequential photographs of the first test executed under an impact energy of 3.2 kJ are shown in Fig. 3-44.

For the purpose of comparison, the measurements of the three tests were offset to the same time point, which indicates the impact time point. Fig. 3-43a shows the impact force-time history of the conducted tests. The average impact force measured at the impact intensity 8.2 kJ is approximately double that measured at 3.2 kJ. The average force is calculated from the force-displacement curves shown in Fig. 3-43b, as the area under the curve divided by the maximum displacement. The area is approximated to a rectangle. Approximating the area to a parallelogram results in an average force of about 5 to 10% higher. The maximum impactor displacement measured was 171, 282 and 440 mm for the conducted tests 3.2, 5.7 and 8.2 kJ, respectively.

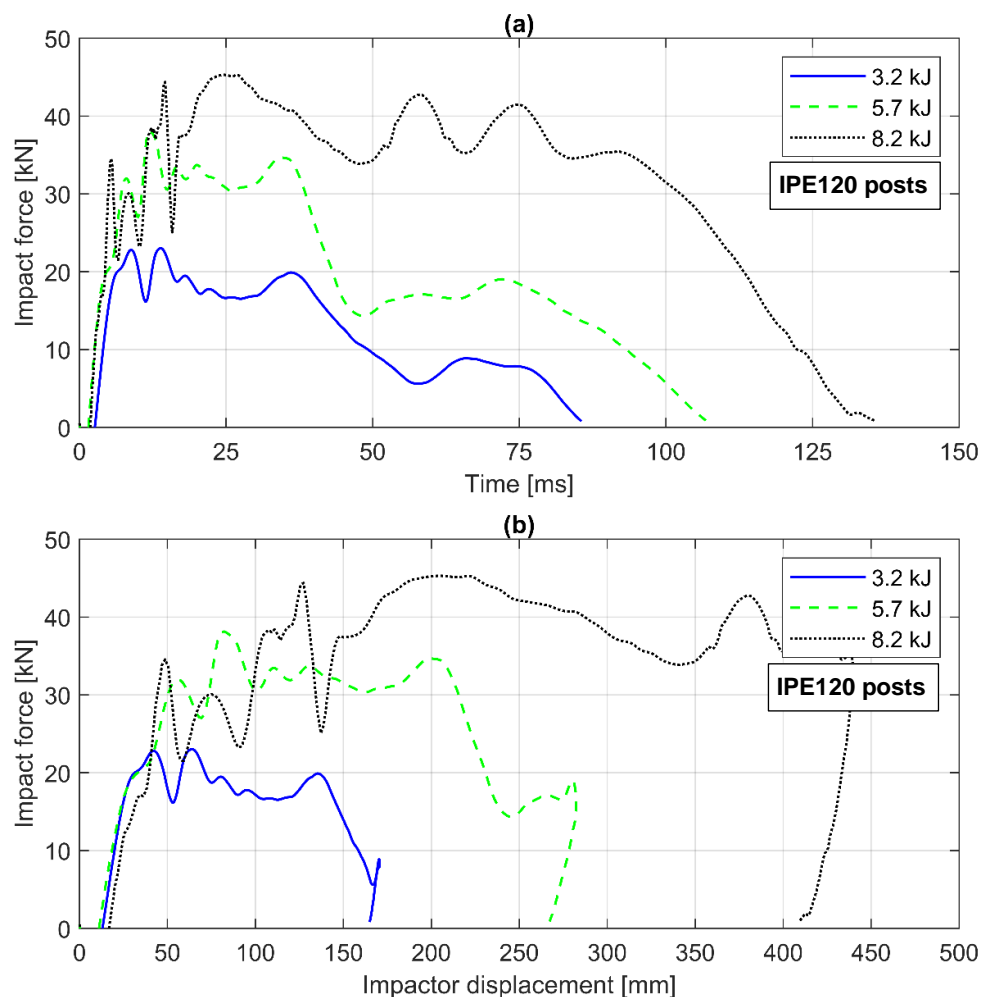


Fig. 3-43: Dynamic test conducted on three IPE120 posts in KSS032 loaded in the strong axis (a) Impact force-time history (b) Impactor force-displacement curves

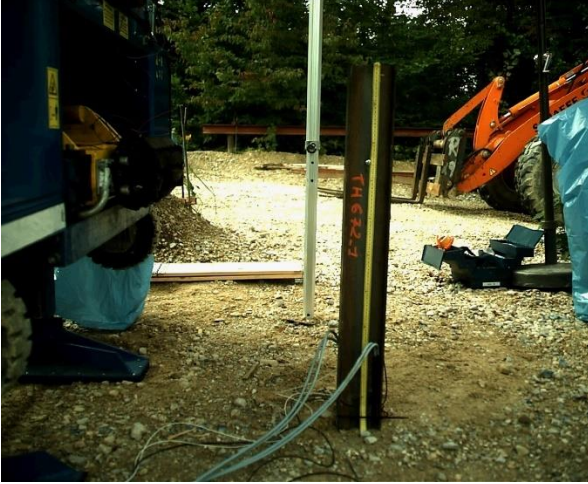


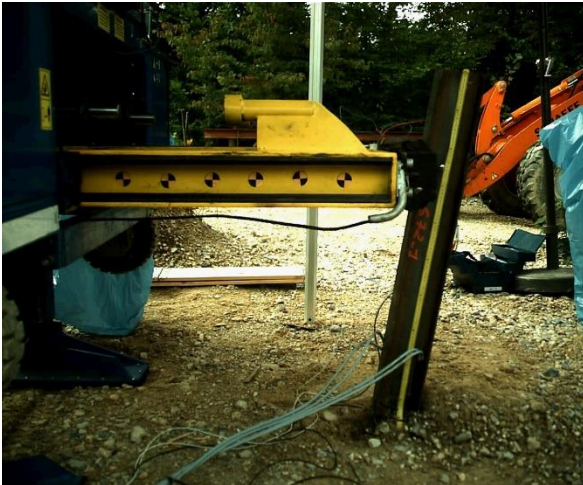


Test No. D19	IPE120, KSS032, strong-axis, t=100 cm
<p>Initial position $t < 0$ ms, $u_{\text{post}} = 0$ mm, $F = 0.0$ kN</p>	<p>Time of contact $t = 0$ ms, $u_{\text{post}} = 0$ mm, $F = 0.0$ kN</p>
	
<p>Maximum impact force $t = 14$ ms, $u_{\text{post}} = 58$ mm, $F = 23.02$ kN</p>	<p>Maximum post deflection (recoil) $t = 72$ ms, $u_{\text{post}} = 176$ mm, $F = 7.88$ kN</p>
	
<p>Time of separation $t = 89$ ms, $u_{\text{post}} = 171$ mm, $F = 0.0$ kN</p>	<p>Final position $t = 150$ ms, $u_{\text{post}} = 121$ mm, $F = 0.0$ kN</p>
	

Fig. 3-44: Dynamic test D19 sequential photos (impact energy 3.2 kJ)

The sequential photographs presented in Fig. 3-44 for the test conducted with 3.2 kJ show the different impact test phases. The impactor head is released with a given velocity from a distance of 45 to 50 cm to collide with the post at $t=0$ ms. The post then deflects to nearly 34% of the total deflection and reaches the maximum force at $t=15$ ms. In the next phase, the post is decelerated significantly till zero velocity at $t=72$ ms. At this time point, the maximum deflection is reached, and the force drops to ca. 30% of the maximum measured value. A part of the kinetic energy absorbed by the post is stored as potential energy. This potential energy is transformed into kinetic energy again, and the post acts as a spring and pushes the impactor back. The impactor recoils along its impact path, however, the embedment soil experiences irreversible deformations, which prevents the post from recoiling to its original position. Moreover, the gap formed behind the post is filled partially with soil and blocks the post. At the time point of separation between the impactor and post ($t=89$ ms), the contact force drops to zero. The final position is reached at $t=150$ ms, with an irreversible deflection of 121 mm due to soil deformation. The post was excavated and showed no yielding of the steel section.

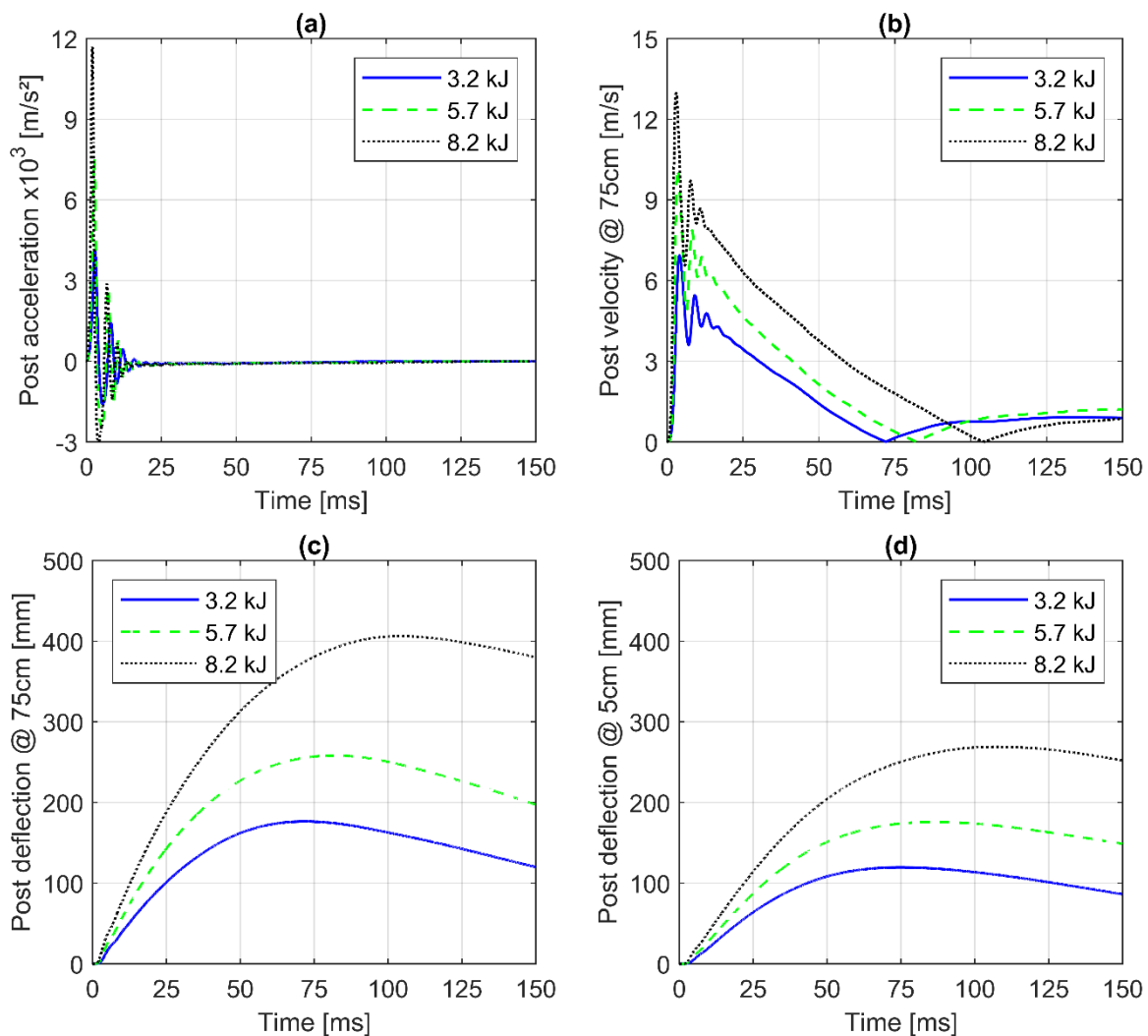


Fig. 3-45: Dynamic test conducted on three IPE120 posts in KSS032 (a) Post acceleration-time history (b) Post velocity-time history (c) Post deflection at the impact height (d) Post deflection at 5 cm above ground level

Fig. 3-45 presents the post acceleration measurements and the integrated velocities and deflections for the three tests. The deceleration of the impactor, i.e. the rate of decrease of the post velocity after the first 20 ms, is in the same range for all tests (ca. 80–90 m/s²). The accelerations measured in the transversal direction are negligible compared to the acceleration in the impact direction. The velocities derived from the acceleration measurements are shown in Fig. 3-46.

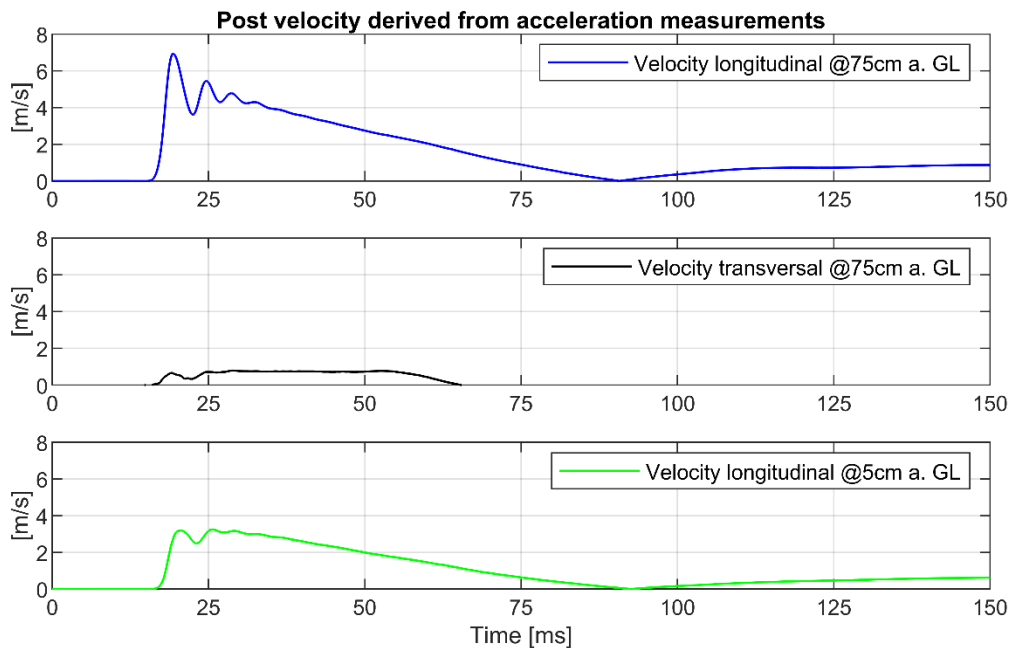


Fig. 3-46: Post velocity derived from acceleration measurements in the longitudinal, transversal directions at different elevations (reference dynamic test 3.2 kJ)

The velocity-time history shows a recoil after a total contact time of 72 to 105 ms. The ratio of the post maximum velocity to the impactor maximum velocity is 20%, 30% and 40% higher for the three tests, respectively. By increasing the impact energy from 3.2 to 8.2 kJ, the maximum post deflection, measured at the impact height, increased from 176 to 406 mm. At 5 cm above ground level, the maximum post deflection increased from 120 to 269 mm. No plastic deformation of the posts occurred in the first two impact levels. A slight curvature was observed at the impact energy 8.2 kJ. Since the excavated posts were found undeformed after impact, the post rotation was evaluated from the deflections at both elevations. The maximum post rotation reached 8.2°, 14.5° and 21.0° respectively.

Selected frames from the high-speed videos of the three tests at maximum deflection are shown in Fig. 3-47. The recordings show that the surface soil particles in front of the post were obviously accelerated by the impact. In the third test, the particles were catapulted up to 2 m away from the post. Soil heave in the vicinity of about 0.5 m to 1.5 m around the post was observed. A gap is formed behind the post and stays open after the test.

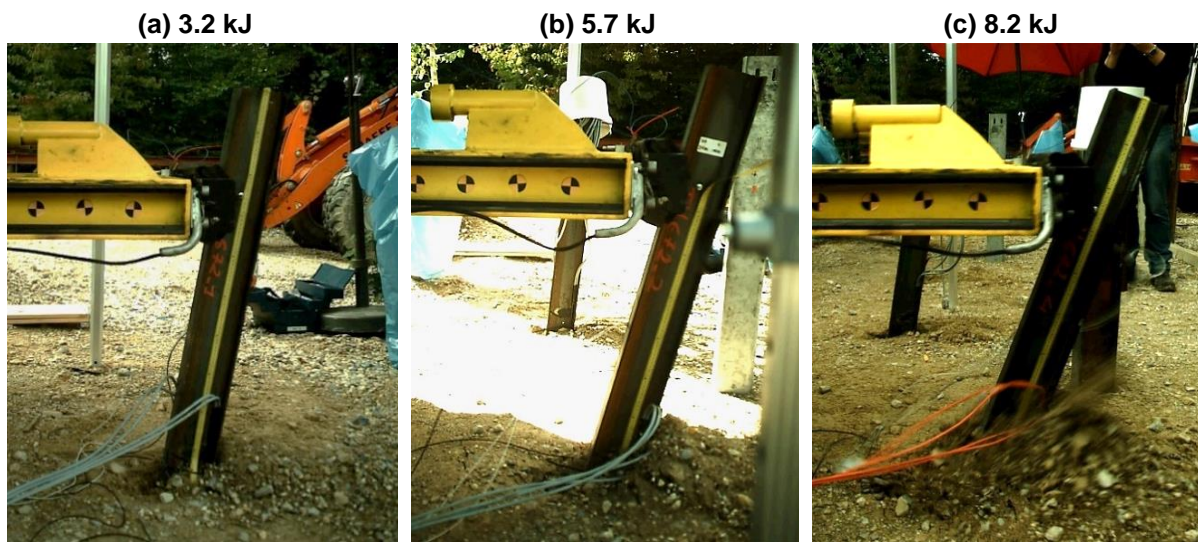


Fig. 3-47: Maximum deflection of IPE120 post in reference conditions under dynamic impact of (a) 3.2 kJ (b) 5.7 kJ (c) 8.2 kJ

An additional test with a higher impact energy of 10.5 kJ was conducted under the same conditions. Due to a technical error, only the upper accelerometer at 75 cm and the strain gauge measurements could be rescued. The results of the four tests 3.2, 5.7, 8.2 and 10.5 kJ are shown in Fig. 3-48. The reaction force (Fig. 3-48a) was evaluated from the strain gauge measurements at the height of 5 cm above ground level, as described earlier under *Instrumentation and test procedure*. The force-deflection curves are shown in Fig. 3-48b. A first peak of the reaction force due to inertia is observed between 3 and 5 ms. The reaction force increases then to its maximum at ca. 15 ms after impact. The force then diminishes and runs nearly asymptotic till the point of losing contact with the impactor. The abrupt drop of the force in the fourth test can be attributed to catapulting a relatively large soil wedge in front of the post, which was also observed and documented during the test.

The maximum reaction force is comparable to the maximum impact force (Fig. 3-43a) for the first and second impact energy levels. The energy absorbed by the post, i.e. work done by the acting force, is calculated as the integration of the reaction force over the post deflection (Fig. 3-48c). This approach is recommended by RAY [70] for the assessment of the strain energy history in a crash event. The work done on the post must equal the strain energy dissipated, since the colliding body can be considered rigid [70]. For the tests 3.2 and 5.7 kJ, the evaluated absorbed energy is observed to be equal to or slightly lower than the impact kinetic energy. For the tests 8.2 and 10.5 kJ, the evaluated absorbed energy is higher than the impact kinetic energy, which is not possible from the physical point of view. This can be attributed to the overestimation of the reaction force after reaching the maximum force due to the plastic deformation of the post in both tests, since the approach for the determination of the reaction forces from the strain gauges is valid only in the elastic range of the steel section.

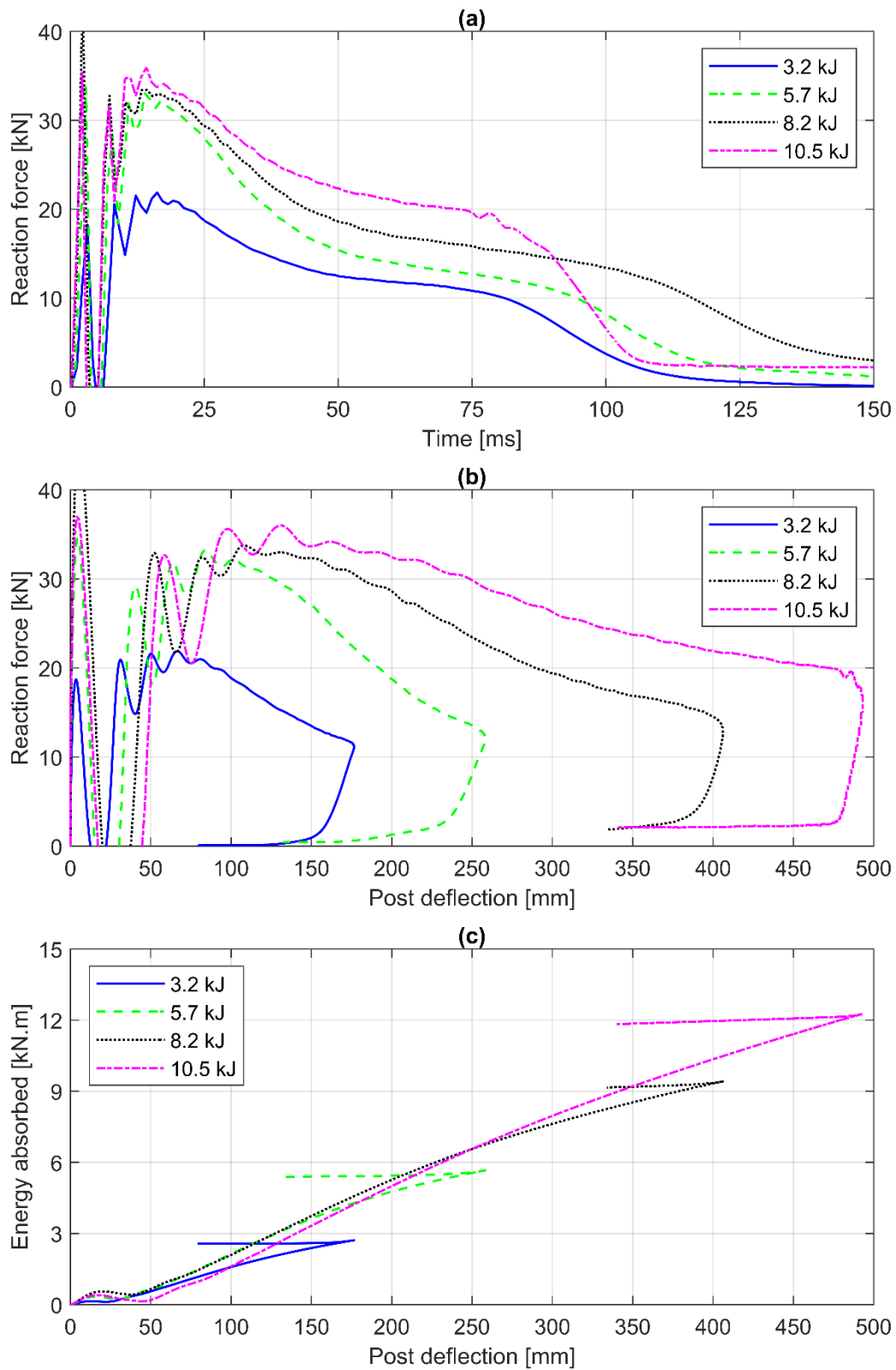


Fig. 3-48: Dynamic test conducted on three IPE120 posts in KSS032 (a) Reaction force time-history (b) Force-deflection curves (c) Energy absorbed by the post over deflection

Variation of post-section

To investigate the influence of the section geometry and flexural rigidity on the post response, three C125 posts and three HEB120 posts were tested under impact energy levels comparable to the range of the reference test. The posts were tested under the same soil conditions as the reference test. The posts were not instrumented with strain gauges.

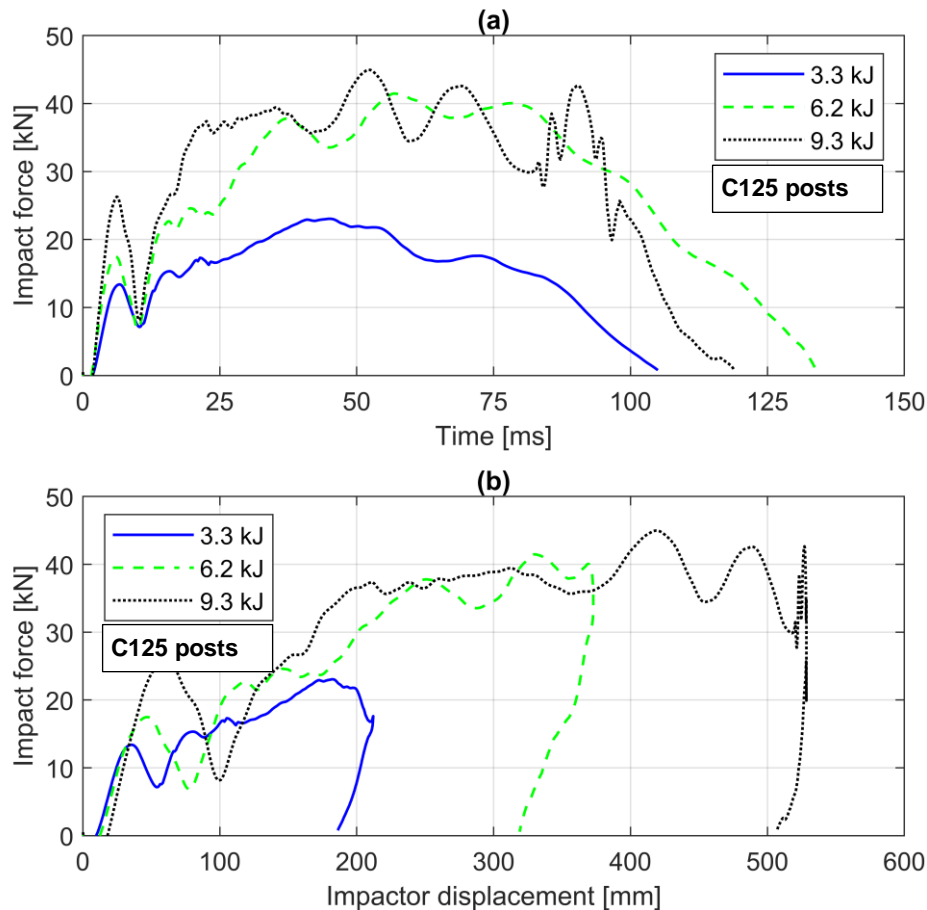


Fig. 3-49: Dynamic test conducted on three C125 posts in KSS032 loaded in the strong axis (a) Impact force-time history (b) Impactor force-displacement curves

The impactor load-displacement curves of the C125 posts tested in the strong axis are shown in Fig. 3-49. The impact force increases approximately linear with the impactor displacement up to 10 kN. In contrast to the IPE-section, in the first and second tests, the impact force increases with the displacement and does not reach a plateau before recoiling. This load-displacement curve characteristic was also observed for the C125 post under static tests. The second and third tests reach a plateau together, starting from a displacement of ca. 220 mm. This gives an indication that the soil has reached its ultimate resistance at ca. 35 to 40 kN with an impact energy higher than 6 kJ. In the reference dynamic test, the third test was observed to reach a plateau at the same impact force range with 8.2 kJ (see Fig. 3-43b).

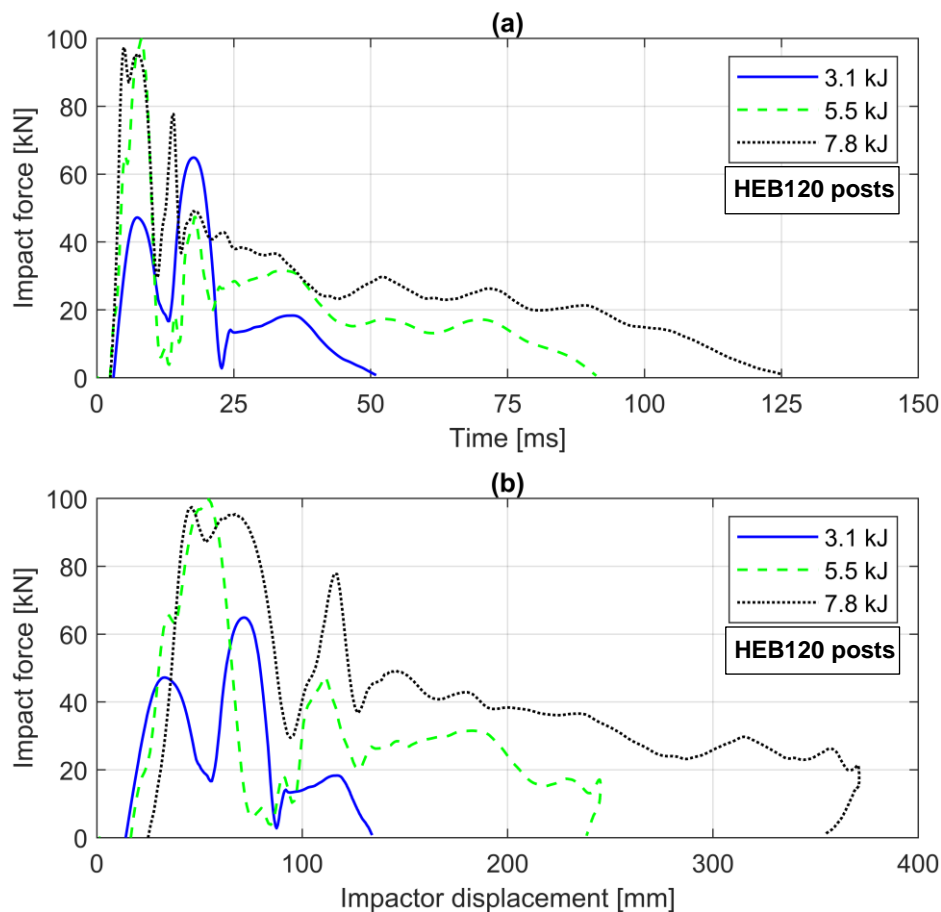


Fig. 3-50: Dynamic test conducted on three HEB120 posts in KSS032 loaded in the strong axis (a) Impact force-time history (b) Impactor force-displacement curves

The HEB120 posts tested in the strong axis show stiffer behaviour compared to the IPE120 and C125 posts. The maximum force is reached in a peak in the first 20 ms with a displacement between 20 and 75 mm (see Fig. 3-50). This force peak lies for the tests 5.5 and 7.8 kJ at ca. 98 kN. This curve characteristic is different from the IPE120 and C125 post sections. The force then decreases with the displacement. The load-displacement curve in the third test conducted under 7.8 kJ runs along a plateau of around 30 to 40 kN before recoiling. The posts were excavated and were found to be straight with no signs of yielding.

To understand the influence of the post-section properties on the response, the load-displacement curves of the posts tested in the same impact energy range are compared in the same diagram (see Fig. 3-51). The HEB120 post exhibits the highest maximum impact force compared to the IPE120 and C125. The peak force can be attributed to the inertial effect of the post mass, since the HEB120 is 2.6 folds heavier than the other tested sections.

The C125 post exhibits the lowest maximum force and the largest deflection values. This can be attributed to the torsional effects due to the section asymmetry. The load-displacement curves of all three post-sections were observed to run along a plateau before recoiling. This plateau is at ca. 20 kN for an impact energy of 3.1 to 3.3 kJ and at ca. 30 kN for an impact energy of 5.5 to 6.2 kJ. This indicates that the soil properties govern the post behaviour in this phase.

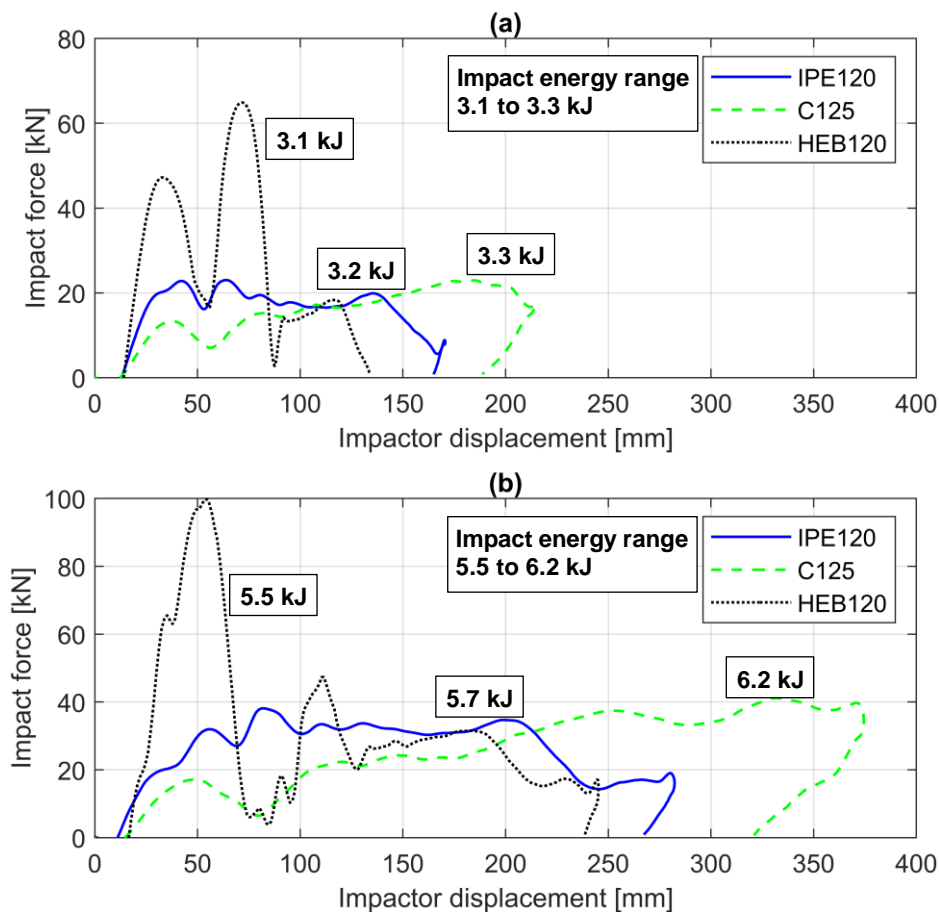


Fig. 3-51: Impactor force-displacement curves for different post-sections tested in dense KSS032 loaded in the strong axis under the same impact energy range (a) ca. 3.2 kJ (b) ca. 5.8 kJ

Variation of loading axis

Three IPE120 posts were tested in soil reference conditions under three impact energy levels in the weak axis. The load-displacement curves and impact force-time histories are shown in Fig. 3-52. No strain gauges were installed in the weak axis. A photograph of the excavated posts is shown in Fig. 3-53. The excavated posts show a plastic hinge formed at 10 to 20 cm under the ground level. The average impact force in the weak axis, evaluated as the area under the curve divided by the maximum displacement, is 20% lower than that measured in the strong axis under the same impact energy. This is due to the significant swinging of the post in front of the impactor, which leads to losing contact momentarily and measuring zero forces.

Nevertheless, the maximum peak force is approximately 50 to 60% of the maximum force measured in the strong axis. The maximum impactor displacement measured in the weak axis is 2 to 2.5 folds compared to the strong axis.

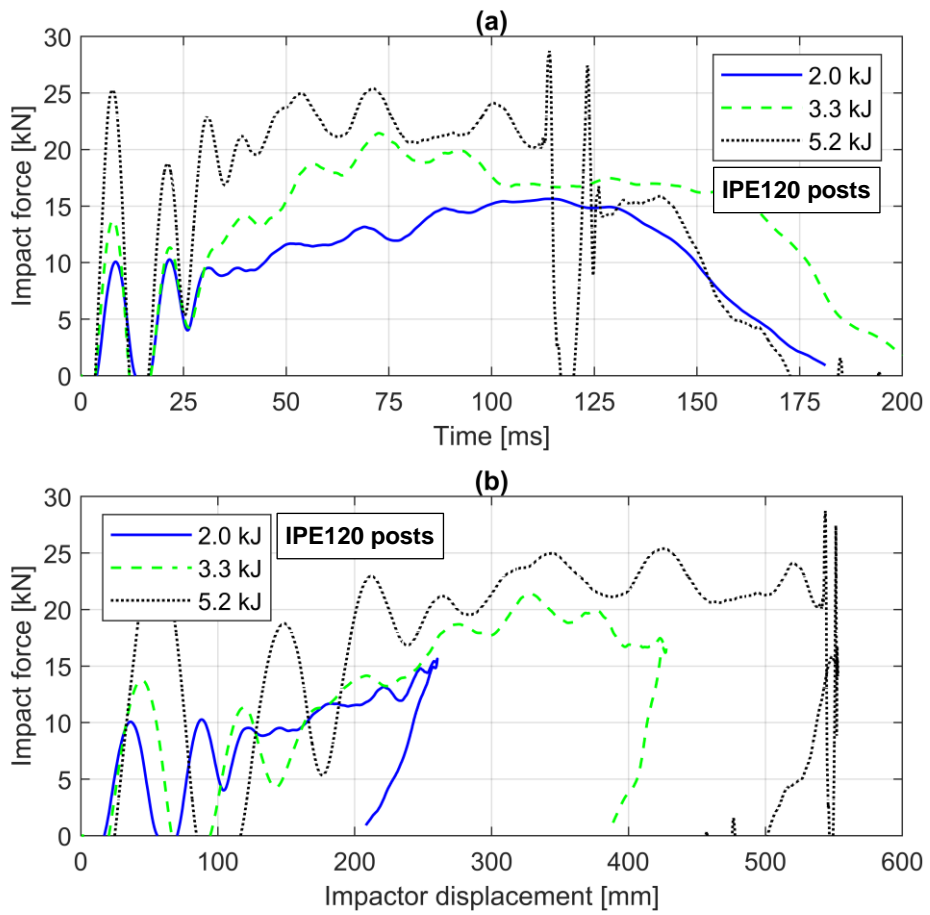


Fig. 3-52: Dynamic test conducted on three IPE120 posts in KSS032 loaded in the weak axis (a) Impact force-time history (b) Impactor force-displacement curves



Fig. 3-53: The excavated IPE120 posts tested in the weak axis under different impact energy levels showing yielding of the steel post

Further, three C125 posts were tested in the weak axis under reference conditions. The load-displacement curves are shown in Fig. 3-54. The posts were set with the closed section side facing the impactor to be comparable to the posts on the highway installed with the closed side facing the traffic direction. The impact energy levels were chosen in the same range as the IPE120 test in the weak axis. The excavated posts show yielding of the post-section at an elevation of 10 to 20 cm under the ground level. The first peak force measured between 5 and 15 ms is comparable to that of the IPE120. The average reaction force ratio in the weak axis to the strong axis is observed to be 16% higher at 3.3 kJ and 31% higher at 6.5 kJ.

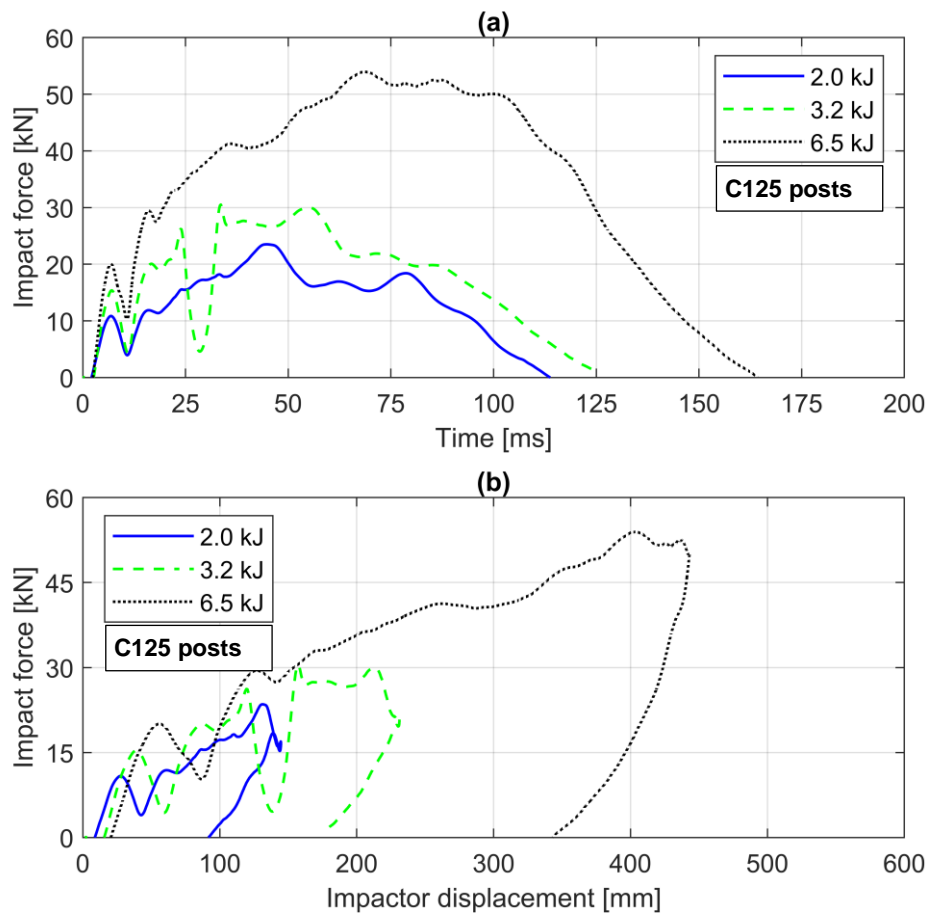


Fig. 3-54: Dynamic test conducted on three C125 posts in KSS032 loaded in the weak axis (a) Impact force-time history (b) Impactor force-displacement curves

Variation of soil material

The results of the variation of the soil material under the same impact energy range are presented in Fig. 3-55 for 3.2 to 3.5 kJ and Fig. 3-56 for 5.7 to 6.6 kJ. The tests were conducted in the crushed limestone 0-32 mm and 0-16 mm and crushed granite 0-32 mm. The post response seems to be identical in the tested soil materials for a given impact energy. The initial stiffness is coinciding for the three tests up to 20 kN. The average maximum force lies in the same range $\pm 10\%$ for the same impact energy. The KSS032 exhibits a lower maximum displacement compared to the other soils, which can be attributed to the slightly lower impact energy. The load-deflection curves' characteristics are nearly identical for the conducted tests.

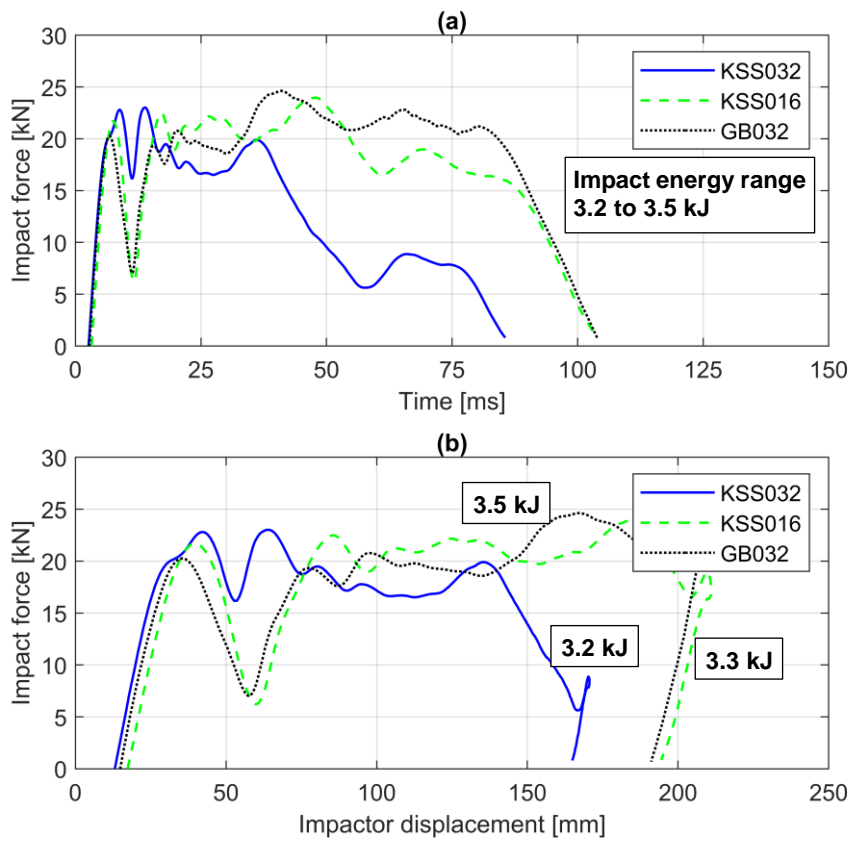


Fig. 3-55: Dynamic test conducted on three IPE120 posts in different soil materials loaded in the strong axis under an average impact energy of 3.3 kJ (a) force-time history (b) force-displacement curves

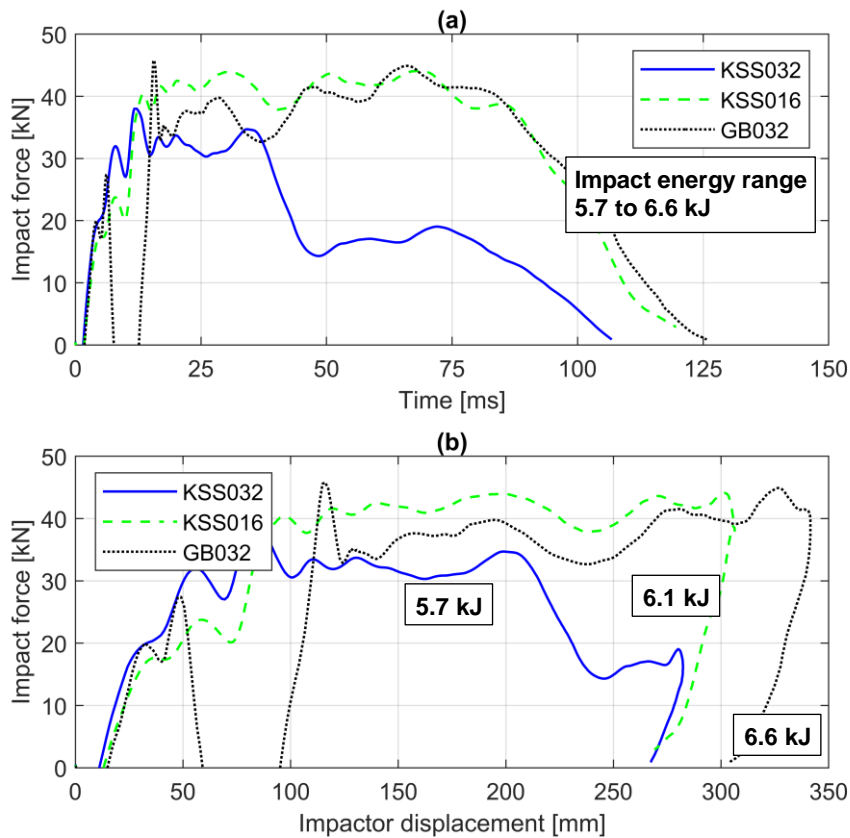


Fig. 3-56: Dynamic test conducted on three IPE120 posts in different soil materials loaded in the strong axis under an average impact energy of 6.1 kJ (a) force-time history (b) force-displacement curves

Variation of soil relative density

The influence of the soil relative density was tested exemplarily on one IPE120 post. The post was installed in medium dense KSS032 ($I_D=55\%$) and impacted by 6.4 kJ. The test results are compared to the test conducted in dense KSS032 at 5.7 kJ (see Fig. 3-57 and Fig. 3-58).

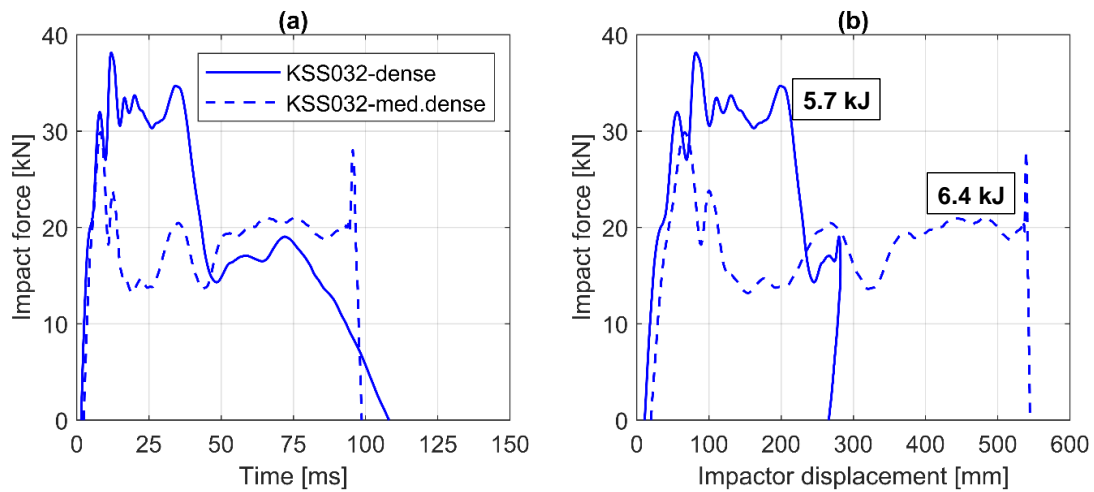


Fig. 3-57: Dynamic test conducted on two IPE120 posts in KSS032 with different relative densities loaded in the strong axis (a) Force-time history (b) Force-displacement curves

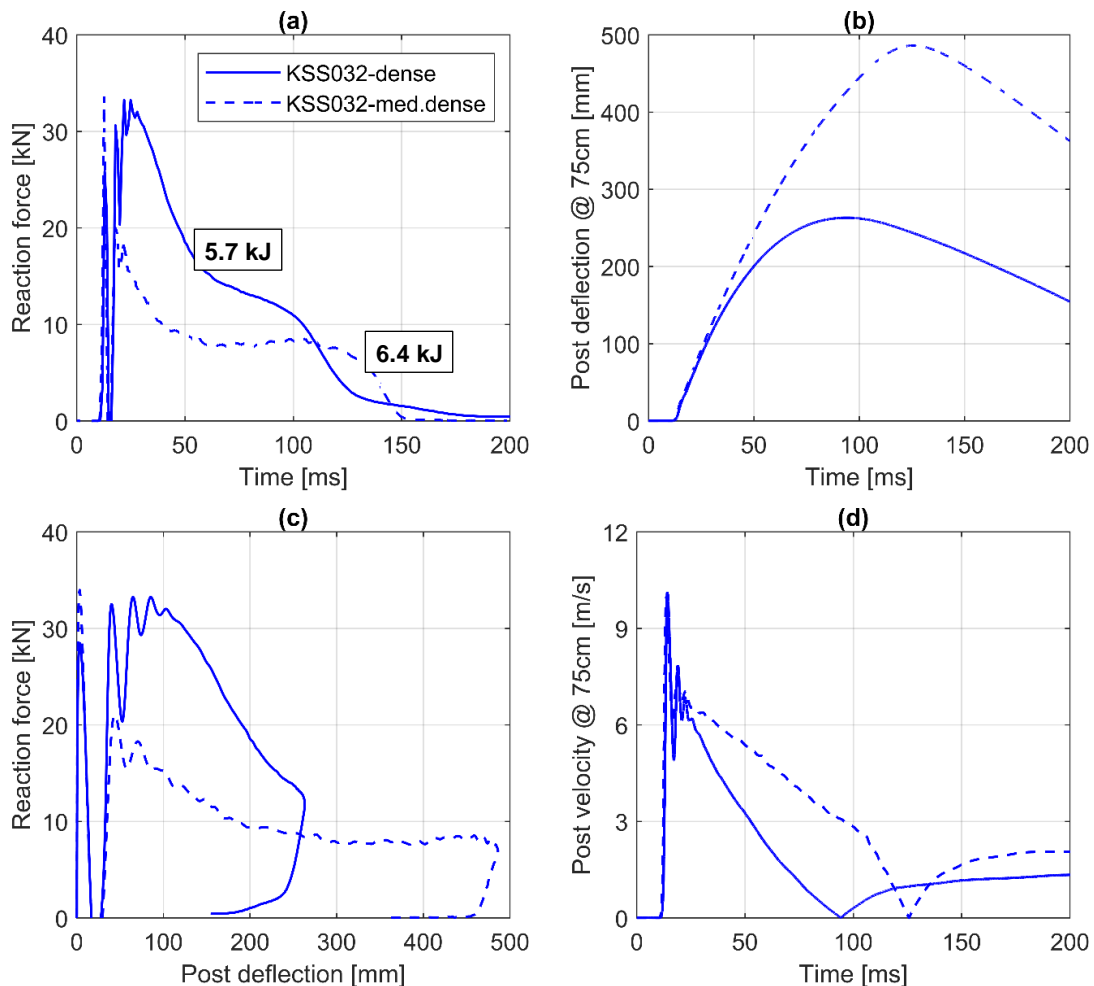


Fig. 3-58: Dynamic test conducted on two IPE120 posts in KSS032 with different relative densities (a) Reaction force time-history (b) Post deflection at the impact height (c) Reaction force-deflection curves (b) Post velocity-time history

The impactor load-displacement curves show nearly a coinciding rate of load increase at the first 7 ms. For the medium dense KSS032, the force then drops rapidly and runs along a plateau of around 20 kN. The displacement increases up to the maximum impactor stroke and then drops abruptly. The maximum displacement is approximately double that measured in the dense KSS032.

The post reaction force was evaluated from the strain gauges. Combining the reaction force and the post lateral deflection, determined from the accelerometer, the post force-deflection curve was constructed (see Fig. 3-58a to Fig. 3-58c). The maximum reaction force is 36% lower than the reference test, while the lateral deflection is 85% higher.




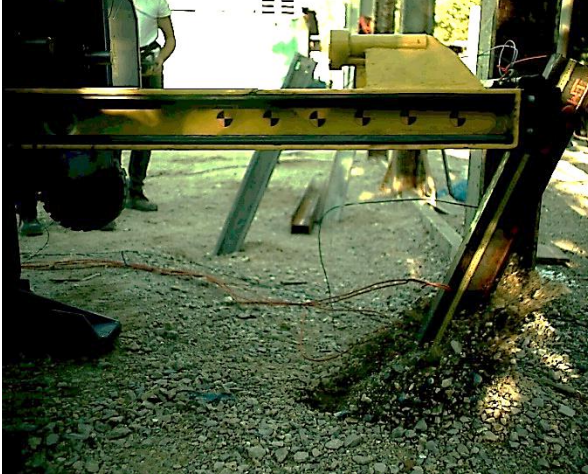
<p>Test No. D20 Impact velocity = 7.7 m/s</p>	<p>Test No. V09 Impact velocity = 8.2 m/s</p>
<p>IPE120, KSS032 dense, strong-axis, Embedment length 100 cm</p>	<p>IPE120, KSS032 medium dense, strong-axis, Embedment length 100 cm</p>
<p>Maximum reaction force t = 25 ms, $u_{post} = 89$ mm, F = 32.60 kN</p>	<p>Maximum reaction force t = 21 ms, $u_{post} = 66$ mm, F = 17.33 kN</p>
	
<p>Maximum post deflection t = 93 ms, $u_{post} = 263$ mm, F = 12.24 kN</p>	<p>Maximum post deflection t = 125 ms, $u_{post} = 486$ mm, F = 7.80 kN</p>
	

Fig. 3-59: Selected frames of the dynamic tests conducted on posts in KSS032 with different relative densities

The post velocity is observed to coincide for both tests in the first peak (Fig. 3-58d). However, the slope of the velocity over time afterwards, i.e. the deceleration, is lower. On average, 85 m/s² for the dense KSS032 and 51 m/s² for the medium dense KSS032. This observation is very important, as it shows the contribution of the soil state on the effectiveness of a VRS, when containing an errant vehicle.

Sequential photographs of both tests, showing the impact phases, are presented in Fig. 3-59. The superficial soil wedge around the post catapulted during the test is larger in the medium dense KSS032 test. This is attributed to the lower soil compaction and the larger deformations at the ground level.

Variation of embedment length

A further variation that was considered in the field tests is the post embedment length. A C125 post with a reduced embedment length of 80 cm was tested in the reference soil condition (dense KSS032) under an impact of 6.5 kJ. The results are compared to the test conducted on a C125 post with 100 cm embedment under 6.2 kJ (see Fig. 3-60). Photographs of the conducted test at the maximum lateral deflection are shown in Fig. 3-61.

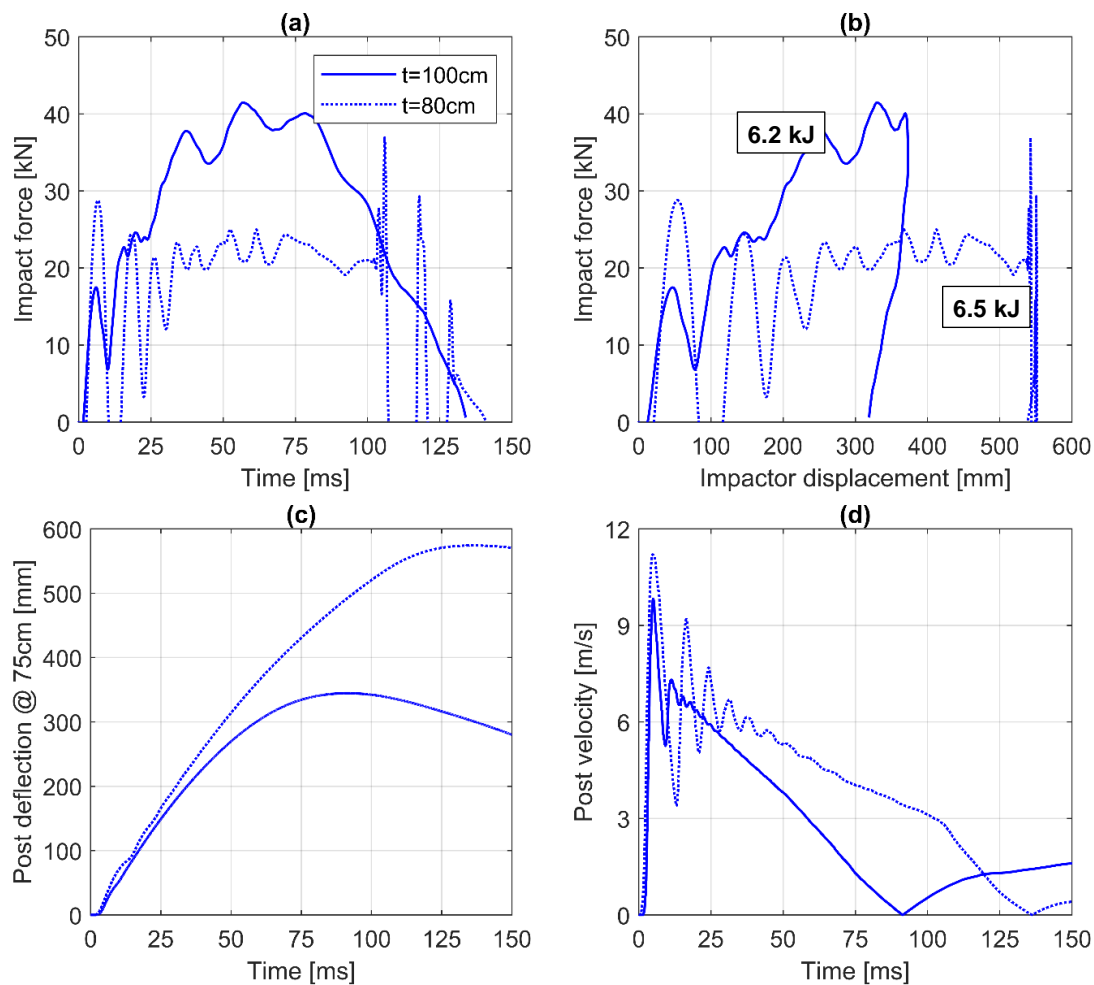


Fig. 3-60: Dynamic test conducted on two C125 posts in dense KSS032 with different embedment lengths under an impact energy of ca. 6.3 kJ (a) Impact force time-history (b) Force-displacement curves (c) Post deflection at the impact height (d) Post velocity-time history

The impactor load-displacement curve has a relatively strong force fluctuation in the first 25 ms. The force then runs along a plateau around 22 kN until reaching the maximum impactor stroke of 550 mm. The curve characteristic is significantly different from the 100 cm embedment post. The post velocity-time history shows on average a lower deceleration of 48 m/s² compared to 89 m/s².



<p>Test No. D31 Impact velocity = 8.05 m/s</p>	<p>Test No. D46 Impact velocity = 8.25 m/s</p>
<p>C125, KSS032 dense, strong-axis, Embedment length 100 cm</p>	<p>C125, KSS032 dense, strong-axis, Embedment length 80 cm</p>
<p>Maximum post deflection t = 91 ms, u_{post} = 345 mm, F_{max} = 41.5 kN</p>	<p>Maximum post deflection t = 135 ms, u_{post} = 574 mm, F_{max} = 25.1 kN</p>
	

Fig. 3-61: Selected frames of the dynamic tests conducted on C125 posts in KSS032 with different embedment length

3.4 Discussion and conclusions

The experimental field tests have shown the influence of the selected factors on the soil-post response under quasi-static and dynamic impact loading. The results of the dynamic tests were compared to the corresponding static tests, and factors were derived in a first trial to correlate the dynamic to the static values. The mechanical behaviour of the posts is further investigated numerically, and the soil-structure interaction is analysed to understand the governing influence factors.

Fig. 3-62 shows the trend of the derived dynamic-to-static factors over increasing impact energy for the tests conducted in the dense KSS032. To compare the dynamic reaction to the static force, an average dynamic impact force was evaluated from the impactor measurements as the impact energy (area under the F-u curve) divided by the maximum impactor displacement. The ratio of the average dynamic impact force to the maximum static force is found to increase linearly (coef. of determination $R^2 > 0.98$) by increasing the impact energy over a range of 3.2 kJ to 9.3 kJ for the tested post-sections (Fig. 3-62a). The factor increases from 1.0 to 2.25 for the IPE-post. The factor decreases by 10% in average for the C-post and increases by 10 to 55% for the HEB120-post.

The initial stiffness was evaluated from the static and dynamic load-deflection curves for deflections up to 15 mm $k_{ini} = \Delta F / \Delta u$. The initial stiffness ratio dynamic-to-static is found to range from 4.6 to 5.0 for the IPE-post, 4.2 to 4.7 for the C-post and 11.8 to 16.8 for the HEB-post (Fig. 3-62b).

A correlation between the maximum dynamic deflection and the static deflection is not meaningful, since, in the static test, the maximum deflection is predefined by the test setup.

The above-mentioned factors were further interpreted for the IPE-post in the soils KSS016 and GB032 (see Fig. 3-63). The initial stiffness factor is nearly equal, with a deviation of $\pm 10\%$ in all soils, over the impact energy range of 3.1 kJ to 6.6 kJ. The average force factor increases by 40 to 60% for the KSS016, compared to the KSS032 and GB032.

The factors interpreted here are based on experimental results and are valid only for the tested materials in the applied impact energy range. Extrapolation of results outside this extent shall be done only based on additional experimental data or numerical analyses.

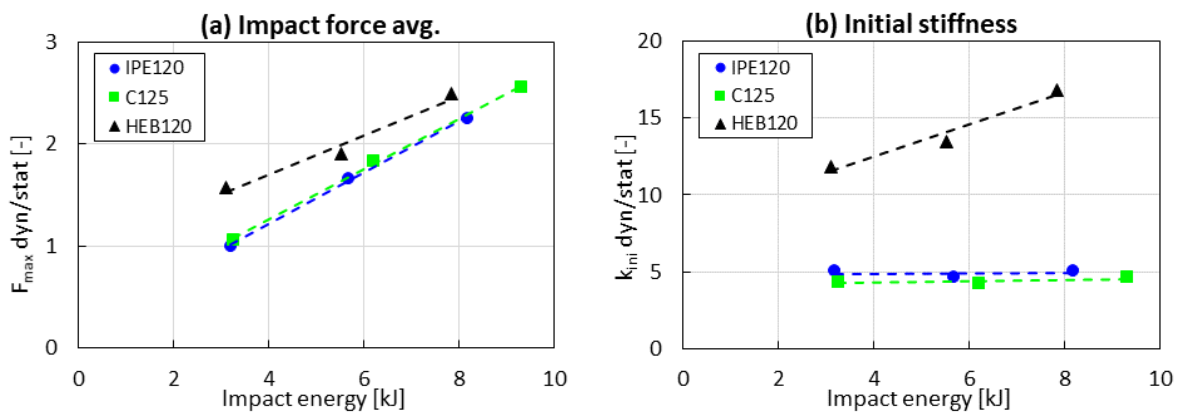


Fig. 3-62: Experimental dynamic-to-static factors for the tested posts in the strong axis in KSS032

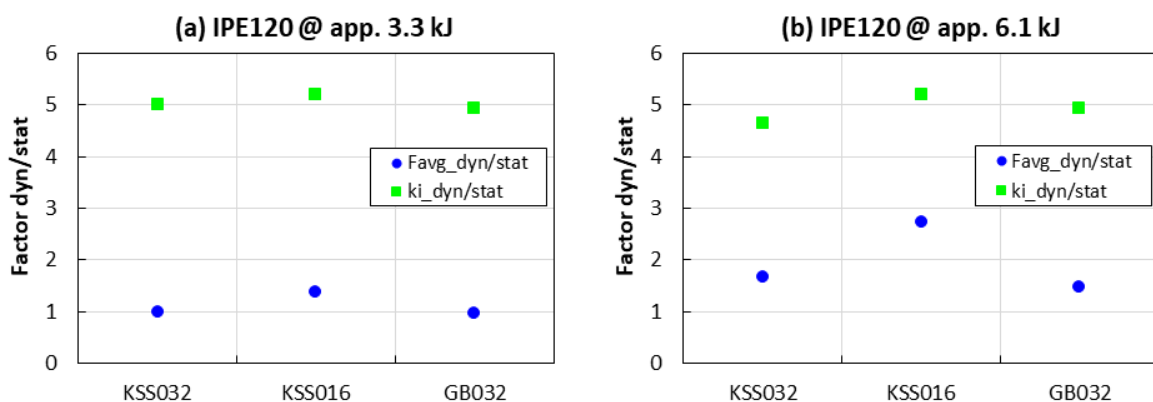


Fig. 3-63: Comparison of the derived dynamic-to-static factors for the tested soil materials under an average impact energy of (a) 3.3 kJ and (b) 6.1 kJ

Based on the experimental results, the following conclusions are drawn [84]:

- For the standard road shoulder materials exhibiting the same relative density, the static reaction force and horizontal stiffness increase with increasing grain strength and decrease with increasing sand content. Under dynamic loading, the effects of these parameters on the post response is negligible.
- The ratio dynamic-to-static force and initial stiffness increases slightly with increasing the sand content in the soil.
- The soil relative density is decisive for the failure mode of the system under static loading; whether the soil reaches the limit state and the post rotates as a rigid body or the soil and post yield together. The experiments show that for posts with an embedment length less than or equal 100 cm in soils with a relative density lower than very dense exhibit a failure controlled by the soil and the post rotates as a rigid body.
- The static reaction force increases linearly with the post embedment length in the range of 80 to 100 cm.
- Under static loading, the C125-section shows a softer behaviour compared to the IPE120 and HEB120 sections. Although the HEB-section exhibits approximately double the width of the IPE, the behaviour of both sections is comparable.
- For standard road shoulder materials under the range of the applied impact loads, the dynamic post reaction force can be estimated using a static test and the dynamic-to-static factors derived in this study.
- The initial stiffness ratio dynamic-to-static depends strongly on the post inertial effects.
- Measuring the impact force directly at the contact between the impactor and the post is susceptible to inertial effects and is highly affected by the contact material properties. Therefore, it is recommended to measure the post reaction force by means of strain gauges positioned below the loading point and above the ground level.

4 Laboratory testing of soil materials

The purpose of the executed laboratory testing programme is to classify the soil materials in terms of soil mechanics and to determine the mechanical material properties. The specimens were classified by means of index properties tests. Additional laboratory tests were carried out to determine the material's mineralogical composition, grain shape, and bearing strength.

In order to investigate the compression and shear behaviour of the material, large oedometer tests, triaxial compression tests and angle of repose tests were carried out. The tests were carried out in the laboratory of the Chair of Soil Mechanics and Foundation Engineering at the Technical University of Munich. The laboratory testing programme was designed to acquire the material parameters required for calibrating the constitutive soil models utilised later for the numerical simulations. The specimens examined were extracted from the road shoulder materials selected for the field tests:

Crushed limestone	0-32 mm	(KSS032)
Crushed limestone	0-16 mm	(KSS016)
Crushed granite	0-32 mm	(GB032)
Silty gravel	0-55 mm	(GU055)

The characteristics and results of the executed laboratory tests are discussed in this chapter. The tests conducted to determine the mineralogical composition and grain characteristics of the soil materials are presented in detail under *3.1 Experimental testing program*.

Classification and identification tests

Several specimens were collected from the different batches received for each material. First, the specimens were examined visually, and a particle size distribution test was conducted to ensure the conformity of the materials to the required materials' specifications. To ensure the homogeneity and representativity of the specimens, each material was mixed in a large container (about 0.4 m³), and the specimen was then extracted. The classifying tests were carried out on the soil specimens according to the standards given in Table 4-1. The grain size distribution curves of the tested materials are shown in Fig. 4-1.

Table 4-1: Soil classification tests

Test	Standard
Grain size distribution (Sieve analysis), dry	DIN EN ISO 17892-4
Soil classification	DIN EN ISO 14688-1
Soil group	DIN 18196
Specific gravity of soil particles	DIN 18124
Determination of the maximum and minimum dry density	DIN 18126
Determination of the maximum dry density and optimum water content (Standard Proctor compaction test)	DIN 18127

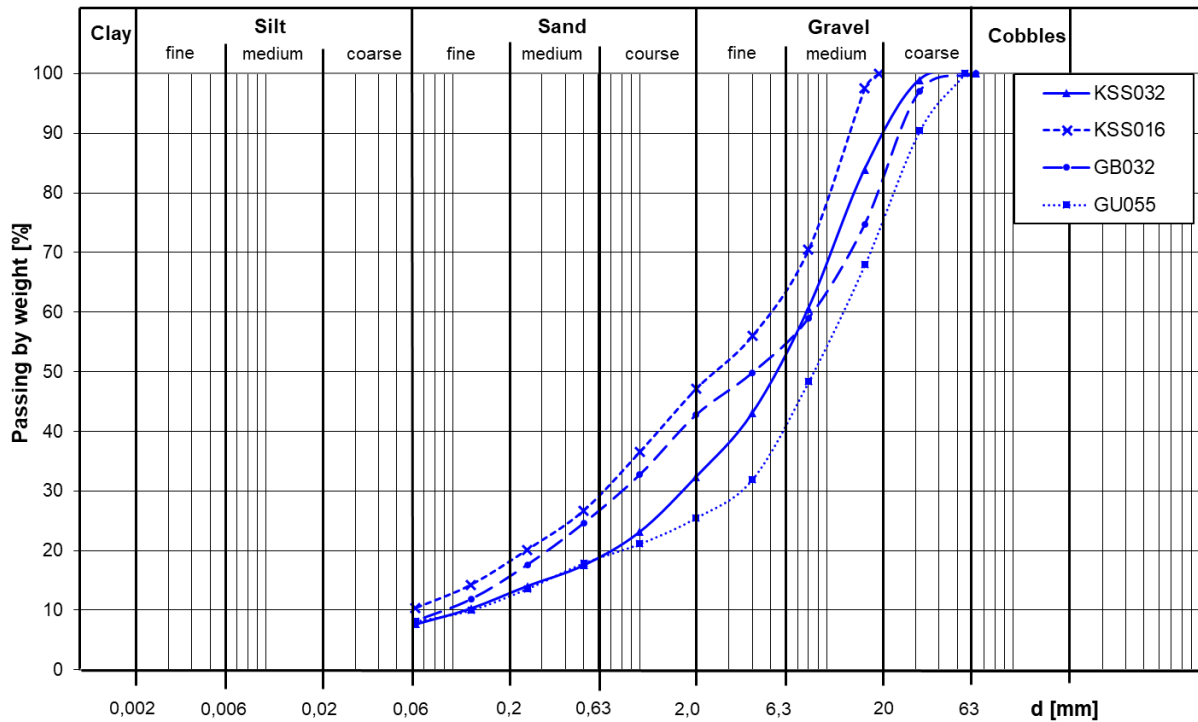


Fig. 4-1: Grain size distribution of the selected road shoulder materials

The results of the classification tests are summarised in Table 4-2. The soil grain density was determined using the air pycnometer according to DIN 18124 [16]. The test is intended to give an average grain density representative for all material particles. Therefore, the specimens were prepared carefully to reflect the characteristics of the grain size distribution. The test was conducted 3 to 4 times, and a mean value of ρ_s was calculated (see Table 4-3).

Table 4-2: Summary of the classification tests

Material		KSS032	KSS016	GB032	GU055
Soil classification		Gr, sa, si*	Gr, sa, si*	Gr, sa, si*	G, u', ms', gs'
Soil group		GU-GT	GU-GT	GU-GT	GU-GT
colour		yellow-beige	yellow-beige	Light - dark grey	brown-grey
Grading	[mm]	0 - 32	0 - 16	0 - 32	0 - 55
<2.00 mm ⁽¹⁾	[%]	43.3	45.0	42.3	25.5
<0.06 mm ⁽¹⁾	[%]	9.7	9.6	8.0	8.1
U _c	[-]	67.2	79.6	89.8	105.8
C _c	[-]	3.2	1.5	0.9	7.0
d ₅₀	[mm]	5.4	2.6	4.1	8.9

⁽¹⁾ mean values

The maximum and minimum dry density $\rho_{d,max}$ and $\rho_{d,min}$ were determined from the standard test as per DIN 18126 [18]. Using these values, the specimen's maximum and minimum void ratio was calculated (see Equ. 4-1). The relative density I_D is then calculated acc. to DIN EN ISO 14688-2 [28] as follows:

$$e = \frac{\rho_s}{\rho_d} - 1 \quad \text{Equ. 4-1}$$

$$I_D = \frac{e_{max} - e}{e_{max} - e_{min}} \quad \text{Equ. 4-2}$$

Based on the I_D value, the relative density of the granular soil material can be described as follows:

I_D [-]	0 – 0.15	0.15 – 0.35	0.35 – 0.65	0.65 – 0.85	> 0.85
Relative density	very loose	loose	med. dense	dense	very dense

The notation D_d or D_r is used for the relative density in the international literature (e.g. ASTM D4254-16), and the value is expressed in percentage. The D_r value is often calculated in terms of density instead of void ratio as follows:

$$D_r = \left[\frac{\rho_d - \rho_{d,min}}{\rho_{d,max} - \rho_{d,min}} \right] \cdot \frac{\rho_{d,max}}{\rho_d} \cdot 100 \quad \text{Equ. 4-3}$$

The relative density values calculated by both methods are identical. However, the range for the relative density classification is different. This study adopts the classification according to DIN EN ISO14688-1 [27].

The Proctor dry density ρ_{Pr} and optimum water content w_{opt} were determined from the standard proctor test as per DIN 18127 [19]. Comparing the dry density values $\rho_{d,max}$ and ρ_{Pr} , the dry density determined from the Proctor test was found to be 1% to 8% higher (see Table 4-3). The Proctor dry density ρ_{Pr} is considered in the calculation of the degree of compaction as follows:

$$D_{Pr}\% = \frac{\rho_d}{\rho_{Pr}} \cdot 100 \quad \text{Equ. 4-4}$$

Compared to the maximum dry density test, the energy applied to compact the specimen in the standard Proctor test is higher. Therefore, the value $\rho_{d,max}$ was considered for the determination of the specimen's relative density to be conform with the standard classification range. The ρ_{Pr} value is considered later for calculating the minimum void ratio in the calibration of the constitutive models as the minimum void ratio that can be achieved for the material (see 5.2 *Material models and parameters calibration*).

Table 4-3: Summary of the experimentally determined material densities and the corresponding void ratios

Material			KSS032	KSS016	GB032	GU055
Specific gravity	ρ_s	[t/m ³]	2.749	2.739	2.701	2.695
Max. dry density	$\rho_{d,max}$	[t/m ³]	2.186	2.111	2.156	2.133
Min. dry density	$\rho_{d,min}$	[t/m ³]	1.703	1.704	1.724	1.666
Proctor density	ρ_{Pr}	[t/m ³]	2.198	2.218	2.139	2.305
Opt. water content	w_{Pr}	[%]	8.0	7.6	8.0	6.0
Proctor void ratio	e_{Pr}	[-]	0.251	0.235	0.263	0.169
Min. void ratio	e_{min}	[-]	0.258	0.297	0.253	0.263
Max. void ratio	e_{max}	[-]	0.614	0.607	0.567	0.618

California bearing ratio tests

The California Bearing Ratio test (CBR-test) was conducted on several specimens to compare the bearing strength of the selected soil materials. As per DIN EN 13286-47 [25], the test gives an indication of the bearing strength of a grain mixture. The test is applied frequently in road construction to evaluate the strength of the unbound road layers. The CBR ratio measures the penetration resistance force F to a specific depth in a compacted material compared to the force F_s measured in a standard crushed limestone:

$$CBR \% = \frac{F}{F_s} \cdot 100 \quad \text{Equ. 4-5}$$

Nevertheless, the test results are not intended to be used for evaluation of the soil stiffness moduli or shear strength parameters. For each material, three specimens were tested. As per standard, the grains larger than 22.4 mm were sieved out. The water content of the specimens was adjusted to the optimum water content and then compacted to the proctor density ρ_{Pr} ($\pm 2\%$). The load-penetration curves and the evaluated CBR ratios of the tested materials are shown in *Appendix [B]: Laboratory test protocols*. The CBR ratios were determined as follows:

Material		KSS032	KSS016	GB032	GU055
CBR min / max	[%]	140 / 165	83 / 100	141 / 187	102 / 138

The GB032 shows the highest CBR value compared to the other materials, which aligns with the fact that granite grains exhibit the highest hardness. The crushed limestone KSS016, with the highest sand content, shows the lowest CBR value. The disassembled samples of the GU055 and KSS032 show cracks in the large grains (see Fig. 4-2). This is attributed to the high stress concentrations under the loading piston, which reaches up to 25 MPa at the end of the test.

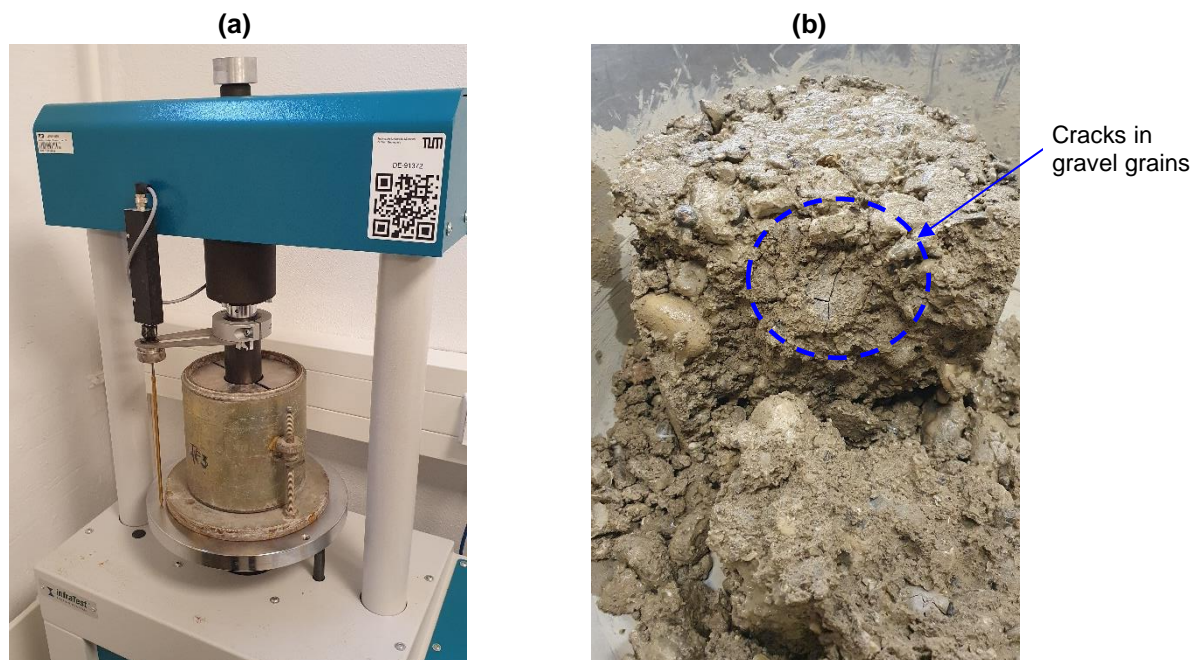


Fig. 4-2: (a) CBR test conducted on road shoulder material (b) disassembled GU055 specimen showing cracks

Large-Oedometer tests

The one-dimensional compression test (also oedometer test) is performed to determine the compressive behaviour of soil under vertical loading and confined conditions. The soil specimen is installed in the rigid oedometer ring and compacted to the required density. The load is then applied in stages with a predefined strain-rate. The test is conducted under drained conditions.

The largest standard oedometer ring exhibits a diameter of 75 mm and a specimen height of 14 to 20 mm. The standard DIN EN ISO 17892-5 [29] specifies the ratio of the specimen height to the maximum grain size to be larger than or equal to 5 [29]. Due to the relatively large grain size of the tested road shoulder materials (≥ 32 mm), the specimens had to be tested in a special oedometer test apparatus fulfilling this requirement. The researchers at Zentrum Geotechnik developed an oedometer apparatus, 'Großödometer', with extra-large dimensions for testing such materials (see Fig. 4-3). With a cell diameter of 300 mm, specimens of up to 200 mm in height and grains size of 60 mm can be tested in this apparatus. The oedometer cell is equipped with porous stone plates at the specimen's top and bottom, allowing for drainage during compression. The large-oedometer apparatus was used successfully in the framework of former research projects to systematically investigate the behaviour of recycled concrete aggregates, steel slags, and road shoulder materials [14].

The oedometer test series was designed with the purpose of calibrating the hypoplastic constitutive soil model, which requires the material stiffness and shear strength properties in the densest and loosest states (see 5.2 *Material models and parameters calibration*). To investigate the compressive behaviour of the materials in different states, the specimens from each road shoulder material were divided into two groups. Each group was installed in the oedometer cell in layers and compacted, analogue to the Proctor test, but with a different target density. The water content of the specimens was set to the corresponding optimum water content w_{Pr} . The initial specimens' height ranged between 140 and 160 mm. The first group

was compacted to 97 to 100% of the Proctor density ρ_{Pr} . The resulting relative density I_D was larger than 0.85, i.e. very dense. The second group was compacted to 75 to 80% of the Proctor density ρ_{Pr} . The resulting relative density I_D was in the range of 0.25 to 0.35, i.e. loose.

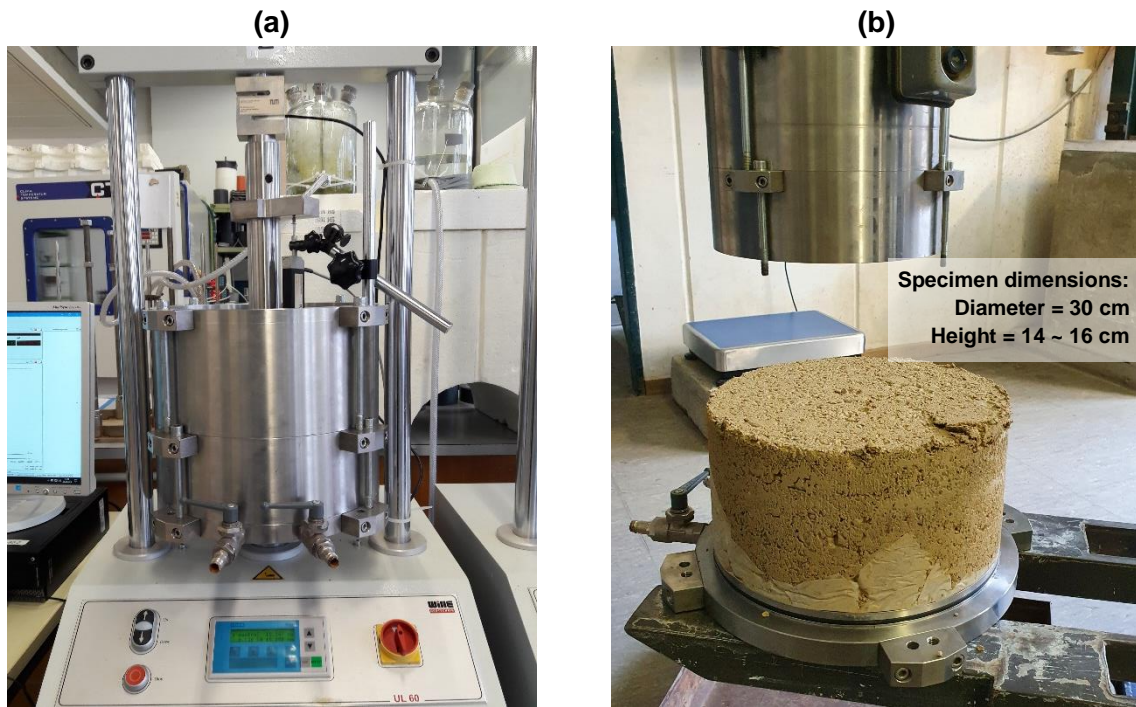


Fig. 4-3: (a) Large-Oedometer test apparatus and (b) soil specimens after testing

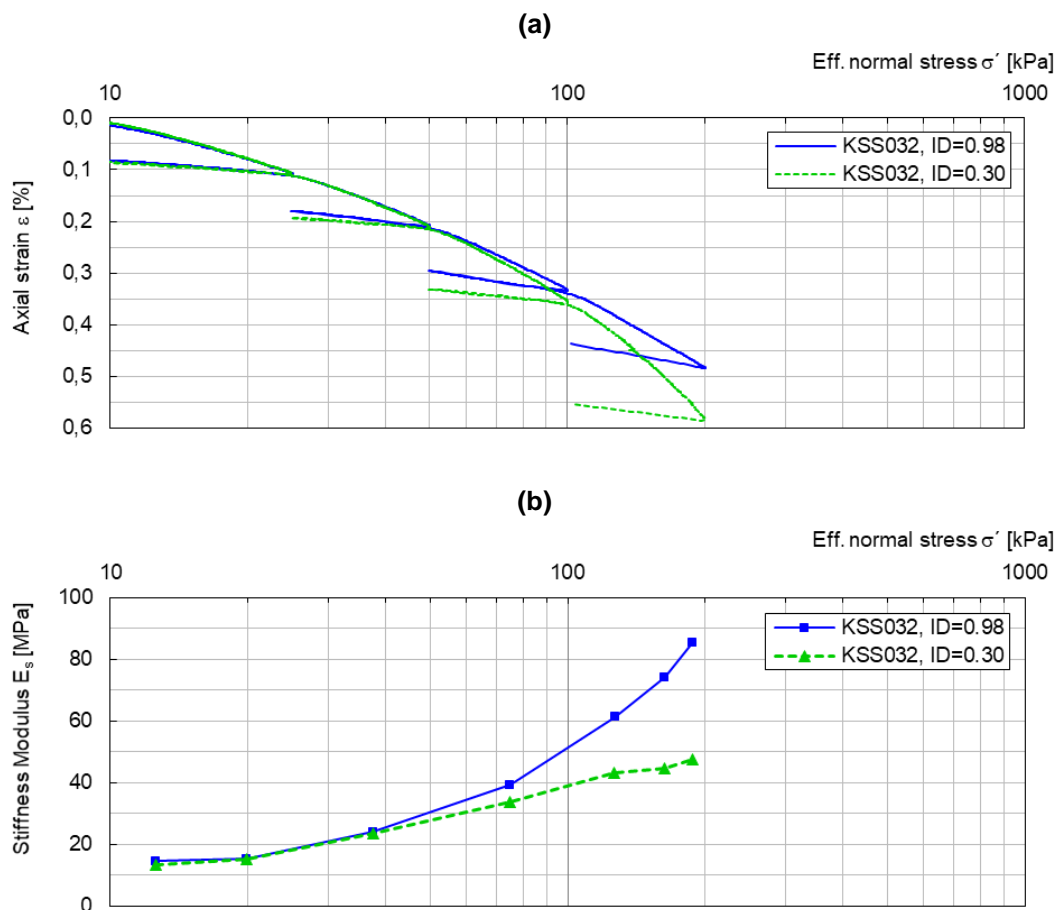


Fig. 4-4: Comparison of the KSS032 compressive behaviour in the very dense and loose state

The specimens were tested to a maximum vertical stress of 200 kPa. To assure drained conditions, the loading rate was set to a very low value of $d\varepsilon/dt = 0.001 \%/min$. Additional unloading phases were added on the loading path at 25, 50, 150 and 200 kPa to evaluate the unloading-reloading stiffness. The variation of the void ratio against the corresponding vertical effective pressure (e -log σ' curves) for each material is presented in *Appendix [B]: Laboratory test protocols*.

A comparison of the stress-strain curves and the evaluated oedometric stiffness modulus E_s for the KSS032 in the very dense and loose state are shown in Fig. 4-4. The results show that the stiffness of both materials is nearly identical up to a vertical stress of ca. 50 kPa. The ratio of the first loading modulus E_s in the very dense to the loose state increases then linearly with the vertical stress to reach 1.8 at 200 kPa. The ratio of the unloading-reloading modulus to the first loading modulus E_{ur} / E_s ranged between 3 and 4 for the very dense specimen and 5 and 6 for the loose specimen. The same ratios were observed for the other tested materials. Except for the GU055, the ratio E_{ur} / E_s ranged between 5 and 6 for the very dense specimen and 6 and 12 for the loose specimen.

Triaxial compression tests

The purpose of the triaxial compression test is to determine the shear strength parameters of a soil specimen. A series of consolidated drained triaxial tests (abbr. CD) were carried out on the selected road shoulder materials according to DIN EN ISO 17892-9 [30]. In contrast to the oedometer test, the specimen is confined in a flexible rubber membrane rather than a rigid ring. This allows for radial deformation and the formation of a failure surface within the specimen. The specimen is supported during the test by the water pressure inside the cell, via which the confinement pressure is applied. The test is performed in three main stages: saturation, isotropic consolidation and then increasing the axial stresses up to shear failure. During the test, the axial load σ_1 , axial strain ε_1 , pore water pressure u_p and the volumetric change ε_v are measured. The test is conducted on at least three samples at different consolidation pressures σ_3 . Constructing the relation between the deviatoric stress $t = (\sigma_1 - \sigma_3)/2$ and the mean normal stress $s = (\sigma_1 + \sigma_3)/2$ for each test, the failure envelope i.e. shear strength parameters can be interpreted for the material [47].

The triaxial test series was designed with the purpose of calibrating the hypoplastic constitutive soil model, which requires the material stiffness and shear strength properties in the densest and loosest states (see 5.2 *Material models and parameters calibration*). Analogue to the oedometer tests, the specimens from each road shoulder material were divided into two groups. Each group was prepared in a 150 mm diameter mould in layers and compacted to the target density. The initial specimen's height ranged between 270 and 280 mm. These dimensions align with the DIN EN ISO 17892-9 [30] requirement of specimen height-to-diameter ratio between 1.8 and 2.5. The standard recommends that the maximum grain size not to exceed 1/6 of the specimen diameter. Therefore, the grains larger than 24 mm were sieved out during specimen preparation. To prevent the granular specimen from collapsing during preparation, the mould walls were lined with geotextile fabric stripes inside the membrane. An additional membrane was pulled over the specimen, the pedestal, and the upper filter plate (see Fig. 4-5) to ensure water tightness under the applied pressure.

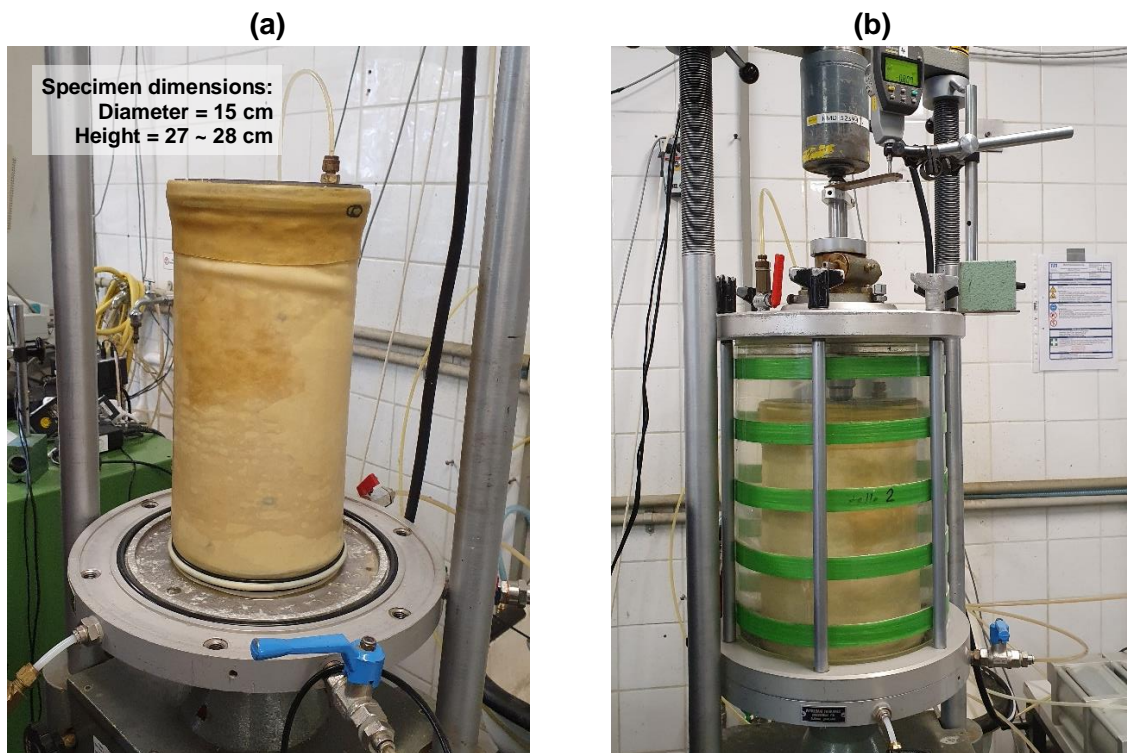


Fig. 4-5: A crushed limestone specimen compacted and enveloped in the rubber membrane (a) before installation in the triaxial cell (b) and during testing

The first specimens group was compacted to 97 to 100% of the Proctor density ρ_{Pr} . The resulting relative density I_D was larger than 0.95, i.e. very dense. The second group was compacted to 75 to 80% of the Proctor density ρ_{Pr} . The resulting relative density I_D was in the range of 0.2 to 0.3, i.e. loose. For each material and relative density, a total of three specimens have been tested. The isotropic consolidation pressure σ_3 was set to 50, 100 and 200 kPa. For the KSS032, an additional test was conducted with $\sigma_3=25$ kPa. The $t' - \varepsilon_1$ and $s' - t'$ diagrams for the KSS032 in the very dense and loose state are shown in Fig. 4-6. The shear strength parameters determined according to the linear Mohr-Coulomb criterion for each material are presented in Table 4-4. The evaluated cohesion values are observed to be high, due to the evaluation of the material shear strength using a linear failure envelope. The application of a curved failure envelope is discussed in section 5.4.

Table 4-4: Summary of the shear strength parameters interpreted from the conducted triaxial tests using linear failure envelope

Material	Relative density	φ'_{peak}	c'
		[°]	[kN/m ²]
KSS032	very dense	50.4	54.9
	loose	42.5	33.9
KSS016	very dense	48.2	52.5
	loose	40.2	0.0
GB032	very dense	48.6	52.9
	loose	41.9	16.1
GU055	very dense	49.2	42.9
	loose	39.5	10.4

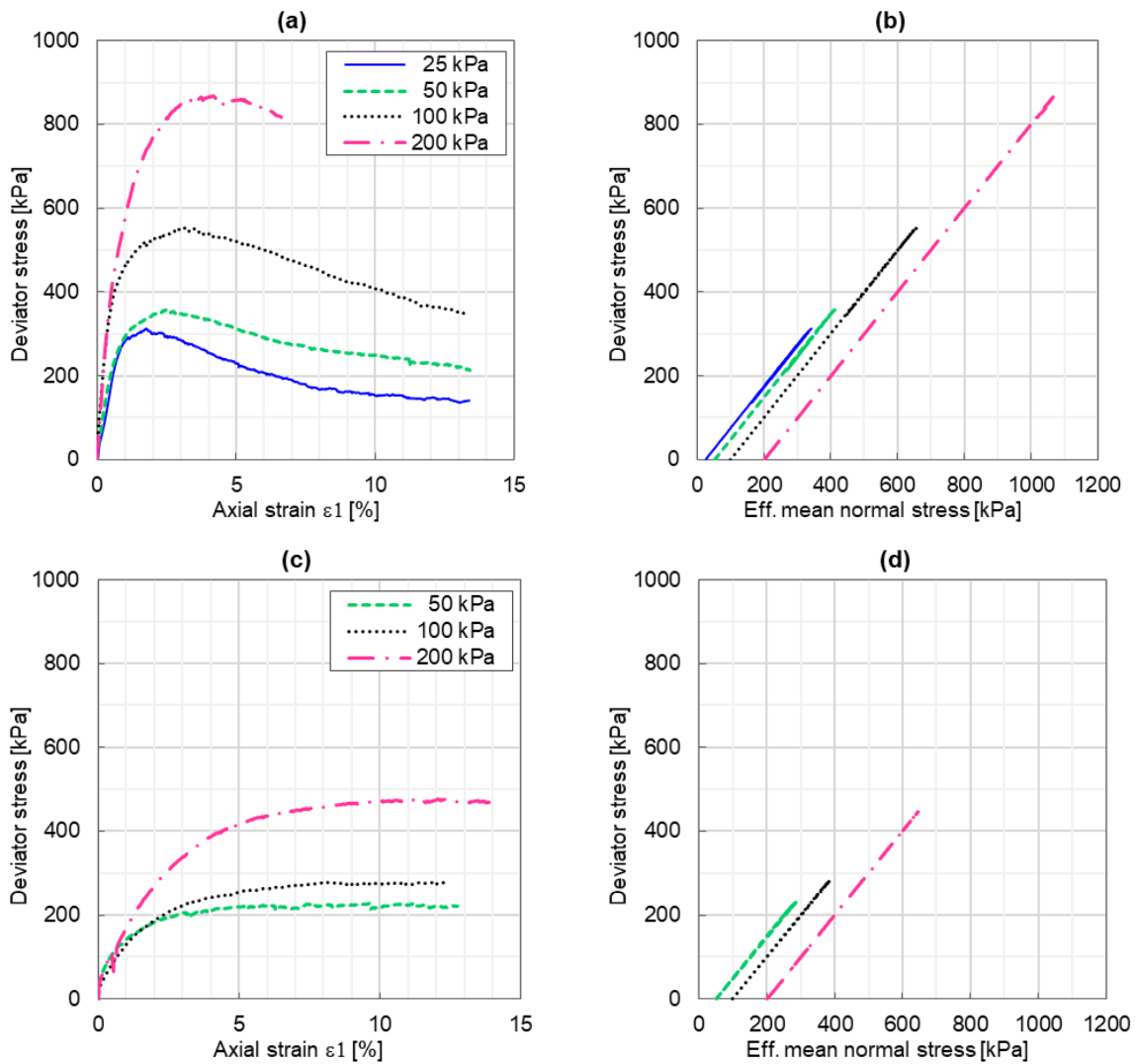


Fig. 4-6: Triaxial test results conducted on KSS032 (a) (b) very dense and (c) (d) loose state

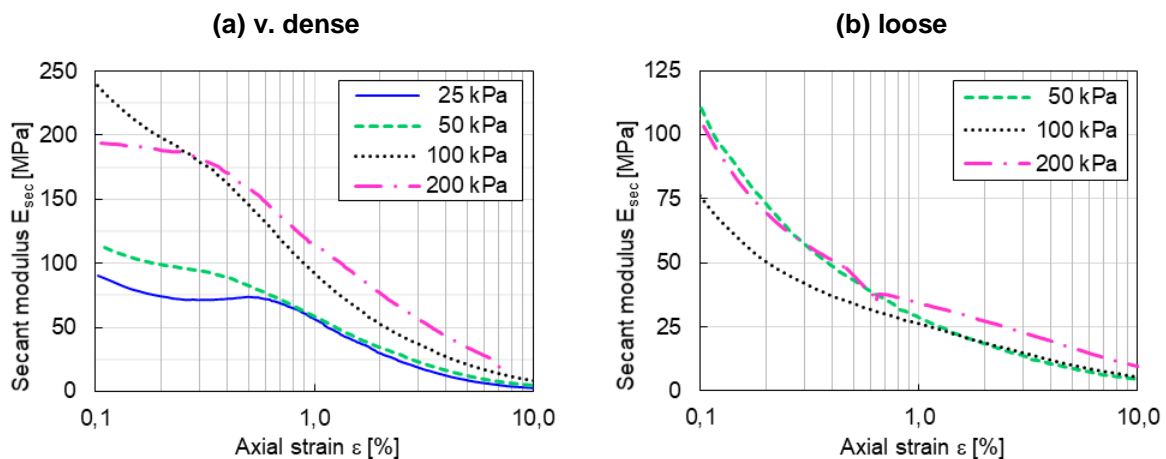


Fig. 4-7: Variation of the secant modulus E_{sec} over axial strain for KSS032 (a) in the very dense and (b) in the loose state

In addition to the shear strength parameters, the stress-strain behaviour of the specimens was evaluated. The secant modulus E_{sec} was interpreted for the KSS032 over the axial strain range of 0.1 to 10% in the very dense and loose state (see Fig. 4-7). E_{sec} is defined as the slope of the straight line connecting the origin and a point on the stress-strain curve and is calculated as follows [47]:

$$E_{sec} = \frac{\Delta(\sigma_1 - \sigma_3)}{\Delta\varepsilon_1} \quad \text{Equ. 4-6}$$

The results show the degradation of the secant modulus E_{sec} with the increase of the axial strain in both states. Comparing the E_{sec} values at 1% axial strain, the very dense specimens range between 57 and 114 MPa, while the loose specimens range between 28 and 34 MPa. The E_{sec} ratio between both states is approximately 3.

Angle of repose tests

The angle of repose test is conducted to estimate the critical friction angle, i.e. the angle of repose of the granular material. The inclination of the conical heap formed by pouring the material at a slow rate out of a funnel corresponds to the critical friction angle φ_c of the soil [55]. Due to the large grain size of the tested materials (up to 55 mm), the specimens' size had to be significantly larger and therefore a special testing setup had to be constructed. Compared to the conventional tests conducted using a relatively small funnel on sand, the tests were conducted using a pipe segment (D=0.4 m, L=1.2 m) lifted up by a crane (see Fig. 4-8). The specimens' weight ranged between 195 and 225 kg.



Fig. 4-8: Conduction of the large-scale angle of repose tests and formation of the soil heap

For each material, the test was conducted at least two times. In each test, the angle of descent relative to the horizontal plane was measured at several locations on the heap's surface. The following table summarises the evaluated critical friction angle:

Table 4-5: Critical friction angle determined from the angle of repose tests

Material			KSS032	KSS016	GB032	GU055
Critical friction angle	φ_c	[°]	35.7	37.0	34.1	31.7

5 Numerical analysis

With the fast-paced development of computer processors nowadays, numerical simulations are becoming increasingly significant in the field of safety hardware crashworthiness as well as in geotechnical engineering. Nevertheless, not only the computational efficiency is decisive for a realistic simulation. Different factors, such as the numerical method, the selection of suitable material models, the calibration of the model parameters, and the definition of the interface between the elements, influence the simulation results.

In this chapter, the focus is applied to the numerical modelling of the soil-structure interaction of a single guardrail post. The post response is analysed using the FEM modelling the soil as continuum elements under quasi-static and impact loading. The advanced hypoplastic constitutive soil relation is introduced for the first time, to the author's best knowledge, to model this boundary value problem. The major advantage of modelling the granular soil behaviour using hypoplasticity, is that it captures the soil non-linearity, stress-dependency of the stiffness and shear strength, loading rate and direction, without explicit distinction between elastic and plastic deformations [52]. Moreover, the material parameters can be calibrated using a straightforward routine from laboratory tests. Using the initial state variables, the model parameters can be set to reflect the in-situ soil conditions.

To investigate the soil-post interaction, FE models were developed to simulate single posts under different lateral loading conditions. The parameters for the hypoplastic soil model were calibrated using the laboratory test results presented under *4 Laboratory testing of soil materials*. The FE models were then validated using the experimental field tests under different loading conditions. In the next step, the validated FE models were used to investigate the influence of the following parameters on the post response:

- Variation of the soil relative density
- Road shoulder subgrade layering
- Variation of the post embedment length
- Variation of the height of the loading point
- Variation of the post section modulus
- Variation of the post-section geometry

The numerical analysis allows for a systematic investigation of factors in a time- and cost-efficient manner compared to the in-situ testing. However, sufficient validation of the numerical model and verification of the output is unconditional to avoid misleading results. The findings of the parametric study are summarised and interpreted to develop correlations between the dynamic and static response of a single post. The significance of the investigated factors on the post response is evaluated. Based on the investigation results, recommendations are formulated for more realistic modelling of the soil-post interaction in the crash test simulations.

The substantial findings of the numerical investigations were published in the peer-reviewed publication SOLIMAN & CUDMANI [83]. Parts of the numerical investigations presented in this chapter have been included in the final report of the research project "Auswirkung des Bodens auf das Verhalten von Fahrzeug-Rückhaltesystemen". The results, text and figures presented in this thesis were created and compiled by the author.

5.1 Finite element model

The numerical simulations were performed with the finite element code ABAQUS v2017 [1] from DESSAULT SYSTEMS using the implicit solver for both quasi-static and dynamic simulations. The dynamic implicit analysis is a powerful numerical technique for solving non-linear engineering problems involving inertial effects. Fundamentally, the dynamic implicit analysis is a time-integration method that solves for the transient dynamic response of the system at discrete time steps using an implicit numerical scheme. The method is characterised by solving for the unknown solution at the next time step by iteratively solving a set of non-linear equations at each time step until convergence. On the other hand, in the dynamic explicit analysis, the solution at the next time step is calculated directly from the solution at the current time step without iterations. Compared to the explicit dynamic analysis, the implicit method is more computationally intensive and requires more memory, due to the need to solve the system of non-linear equations at each time step. This can make it time-consuming to perform dynamic implicit analysis on large or complex models. However, dynamic implicit analysis can be more efficient for problems with very stiff or fast dynamics, where the time step size used in explicit analysis has to be very small in order to maintain stability and accuracy. In these cases, dynamic implicit analysis can handle larger time steps and provide a more computationally efficient solution [1].

Since the soil is modelled using a user-defined hypoplastic material model subroutine “umat” running only under the Abaqus/Standard, the analysis had to be conducted using the implicit solver.

Model geometry and boundary conditions

To simulate the loading test, a three-dimensional FE model was created with a symmetry plane parallel to the loading direction. The geometry of the FE model and the mesh discretization are shown in Fig. 5-1. The model consists of 3 main parts: the post modelled as a beam, the soil block and the transition body between both. The soil block is modelled as a cylindrical volume with a height of 2.0 m and a diameter of 4.2 m. The model radius corresponds to the spacing between the posts in the Super-Rail Eco VRS. The discretization of the soil is done with the first-order C3D8 and C3D6 continuum elements with full integration. First-order solid elements are recommended for problems involving impact or severe element distortions [1]. Full-integration elements are chosen to avoid hourglassing problems under dynamic loading. The soil block is divided into several coaxial zones with finer mesh in the post vicinity and coarser mesh in the outward direction. The element's largest dimension is set to 5 cm in the axial direction around the post and increases with a bias to the outside.

The post is modelled using B31 beam elements as a simplified Timoshenko beam. The beam elements are more efficient for simulating a single post compared to the detailed three-dimensional shell model utilised in crash test simulation. The stiffness and strength properties is assigned to the beam element, which fully represents the cross-sectional properties of the post via the corresponding definition and arrangement of the integration points in the cross-section (see Fig. 5-2). With the help of the integration points, the stress distribution and strains due to normal force, shear force, bending moment, and torsion can be determined in the beam's local axes.

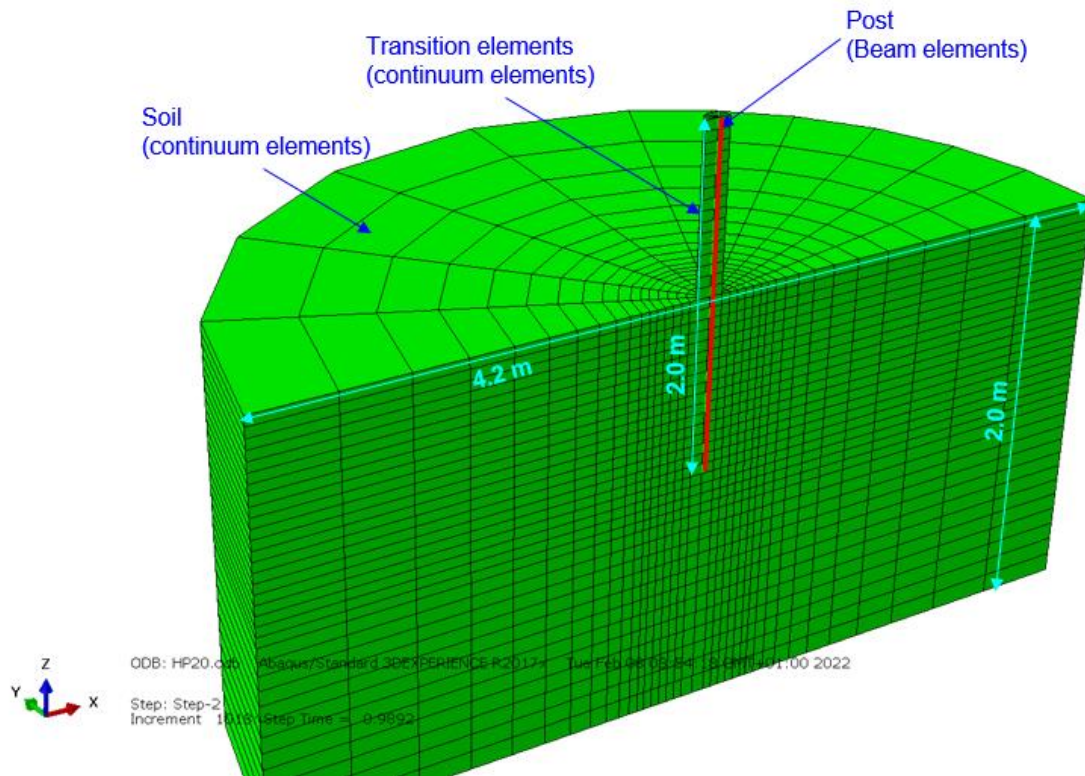


Fig. 5-1: Geometric configuration of the FE model; element types and model dimensions

The beam elements are fully embedded in a cylinder of C3D6 continuum transition elements. The nodes of the transition elements are coupled with the nodes of the beam elements in the post axis. The transition body is defined to avoid the numerical stress concentrations and mesh distortions in the zone around the profile edges. In the current approach, the diameter of the transition elements cylinder has been chosen as an equivalent circle exhibiting an approximate circumference equal to the outer circumference of the post-section.

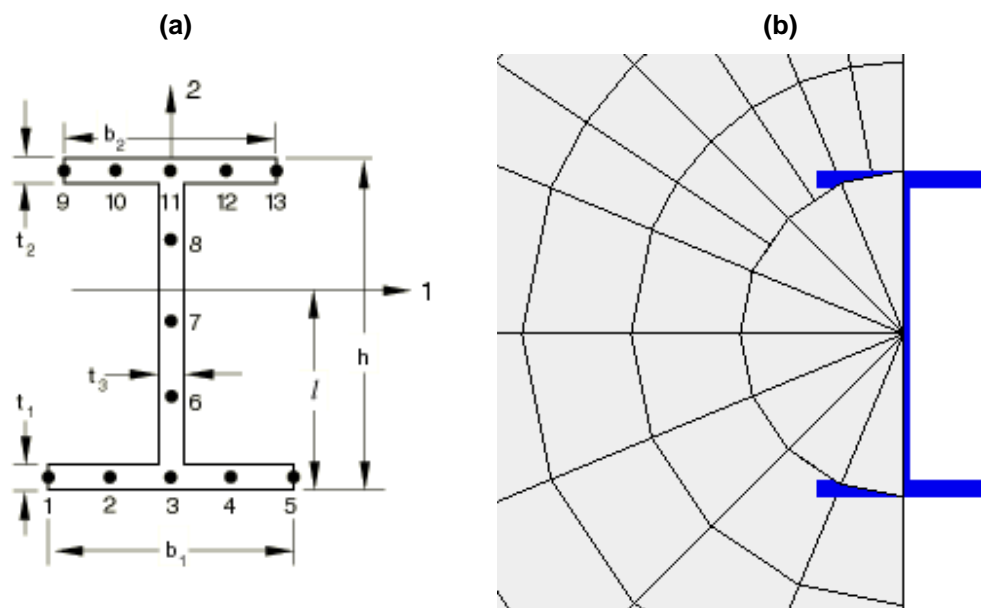


Fig. 5-2: (a) Default beam integration points for I-section in ABAQUS [1], (b) rendered three-dimensional beam element embedded in transition continuum elements

The transition body in the embedment exhibit the soil properties in the unloading-reloading phase. The transition elements above the ground level are modelled weightless, and were defined for continuity of the beam interface. In the dynamic model, the transition body above the ground level was assigned rubber material properties to simulate the impactor's front tyre piece (see 3.3 *Dynamic loading tests*). The impactor was modelled as a rigid body consisting of C3D8 continuum elements.

A contact surface is defined between the transition body and the surrounding soil elements. Applying the transition elements around the post in combination with the contact surface allows for a significantly stable numerical solution under large deformations. In the tangential direction, a node-to-surface contact formulation with a friction coefficient of $\mu = \tan \varphi_{contact} = 0.07$ was used. This value corresponds to a contact friction angle between steel and soil of approximately 10 % of the soil's critical friction angle. The tangential friction was increased to 33% in the dynamic model to prevent the post from oscillating in the unloading phase inside the gap formed in the loading direction. In the normal direction to the transition body, contact with an exponential "pressure-overclosure" relationship was defined for the static and dynamic models. This contact formulation allows for pressure transmission between surfaces once a predefined clearance value in the normal direction is reached. Then, the contact pressure increases exponentially by decreasing the clearance [1]. The clearance value was calibrated to the experimental field test data and was set to a low value of $c_0 = 10^{-2} \text{ mm}$. This value is suitable for modelling posts installed by full soil displacement. Applying higher c_0 values resulted in a softer response of the system until reaching the clearance value, which was not observed in the field tests. Therefore, for posts installed by backfilling the soil around the post, larger clearance values shall be applied in the simulation.

The boundary conditions of the FE model are set as follows. All degrees of freedom are constrained at the lower model boundary. The displacements normal to the outer boundary surface as well as in the symmetry plane, are fixed. The boundary conditions in the symmetry plane resemble conducting the static test using the guidance frame, as deflections out of the plane are restrained. A full symmetric model was used for the dynamic test simulations to allow for eventual deflections in the plane orthogonal to the impact direction. This technique is more realistic, since the guidance frame was not employed to restrain the posts in the dynamic test.

To avoid tension stresses in the top surface elements of the soil block, a uniform surcharge load of 0.5 to 1.0 kN/m² was applied. In the contact surface between the transition elements and the ground, a radial surface pressure of 0.5 kN/m² was defined to model the supporting force of the apparent cohesion during the gap opening behind the post, thus improving the numerical convergence. Reducing the radial surface pressure to zero led to severe distortion of the soil elements in the opened gap and premature abort of the simulation.

The horizontal stresses in the soil are calculated at the beginning of the simulation with an earth pressure coefficient at-rest of $K_0 = 1.1$. This value, which is higher than the common geotechnical practice ($K_0 = 1 - \sin \varphi \approx 0.5$), accounts for the compaction pressure in the shallow road-shoulder material layer. Fig. 5-3a shows a schematic illustration of the increase of the horizontal pressure in the compacted soil layers under a strip surface load, i.e. compaction equipment (after LANG et al. [48]). This pattern was also observed in the heavy dynamic probing DPH logs (see *Appendix [A]: In-situ soil testing*). In each placed layer of 30 cm thickness, the blow counts show a peak in the upper third and a decrease over the rest of the layer thickness.

The additional horizontal pressure in each depth can be estimated from the elastic half-space theory after BOUSSINESQ as follows:

$$\Delta\sigma_h = K_0 \cdot I \cdot q \tag{Equ. 5-1}$$

where, σ_h is the horizontal pressure, I is an influence factor, and q is the equipment's vertical pressure. However, this approach requires the compaction pressure under the equipment and the contact area, which are unknown.

As an approximation, LANG [48] proposes an earth pressure coefficient \bar{K}_0 considering the compaction effect as the reciprocal of K_0 . However, this approximation results in very high horizontal pressure values, app. 5-folds of the vertical pressure, which is not realistic.

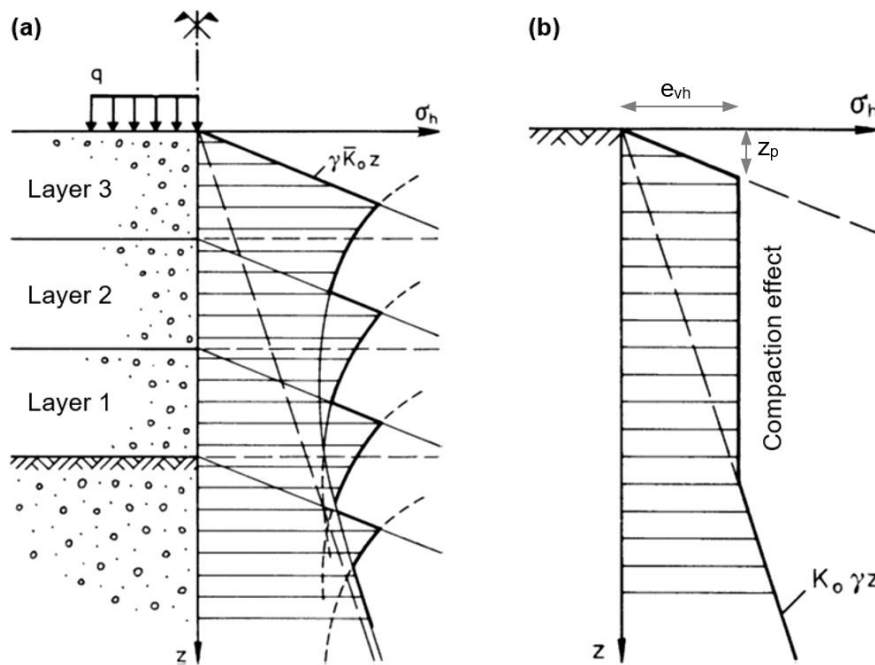


Fig. 5-3: (a) Increase of the earth pressure at-rest due to compaction of the placed soil layers after LANG et al. [48] (b) estimation of the additional horizontal compaction pressure as per DIN 4085 [21]

The German standard DIN 4085 [21] recommends the estimation of the additional horizontal pressure due to compaction as follows (see Fig. 5-3b):

$$z_p = \frac{e_{vh}}{\gamma \cdot K_{pgh}(\delta=0)} \tag{Equ. 5-2}$$

where, $e_{vh} = 25 \text{ kN/m}^2$ is the additional horizontal pressure induced by a compaction equipment heavier than 0.25 tons, on a backfill area width larger than 2,5 m behind a rigid wall. z_p is the influence depth of the compaction pressure, γ is the soil unit weight and $K_{pgh}(\delta=0)$ is the passive earth pressure coefficient for a smooth wall.

The test field was fully excavated up to a depth of 1 m before placement of the road-shoulder material layers. The excavation sides were stable, and no shoring system was required. Therefore, the field can be considered as a basin with rigid sides in this state. The soil material

layers were then placed on the test field with the full area and compacted. Which can be considered as an infinite half-space compared to the compaction equipment area. Based on these observations, the horizontal deformations in the soil during compaction can be neglected, and hence, no active earth pressures were induced. The earth pressure coefficient can then be calculated as an equivalent out of the earth pressure at-rest K_0 and the lateral compaction pressure as per DIN 4085 [21], acting on a rigid excavation support at a given depth.

The resulting earth pressure force, i.e. the integration of the earth pressure distribution over depth, was calculated for the depth of 2.0 m, corresponding to the lower boundary of the soil continuum in the FE model. Assuming a linear increase of earth pressure over depth, the area was approximated to a triangle and the equivalent earth pressure coefficient \bar{K}_0 was determined to be 1.1.

Calculation phases

In the first calculation step in the FE model, the equilibrium of the post embedded in the soil is calculated under the own weight and surcharge loads (initial stress state). The Installation phase of the post driving has not been simulated explicitly (instead, the so-called "wished-in-place" method). However, the installation effects were considered indirectly by increasing the stiffness modulus of the transition elements compared to the surrounding soil block to simulate a reloading phase of the soil. Moreover, the lateral earth pressure coefficient is adapted as described earlier to consider the compaction pressure. Further, the contact clearance in the interface was set to a very low value to allow for full contact force transmission starting from the very beginning of loading.

In the static test simulation, a second step is defined, in which a prescribed horizontal displacement of 40 cm is applied at a height of 75 cm above ground level. This height corresponds to the load application point during the in-situ tests. The resulting reaction force versus post deflection is evaluated at the same point.

In the dynamic test simulation, the impactor was modelled as a rigid body with an initial velocity moving on a horizontal path to hit the post at a height of 75 cm above ground level (see Fig. 5-4). This phase was subdivided into two steps; the first is the acceleration of the impactor to reach a steady velocity, and the second step is the unforced free motion of the impactor. The impactor is allowed to collide with the post and recoil freely afterwards. The rigid body is restrained using boundary conditions from rotation and from deviating out of a linear path orthogonal to the post. These settings resemble the impactor frame structure.

In the field experiments, the impactor was equipped with a front tyre strip to avoid the high amplitude vibrations due to collision between the steel impactor frame and the post. This part is simulated in the model by a weightless rubber cylinder, i.e. transition elements wrapping the post above ground. This approximation has no effect on the results, since decisive is only the contact area properties between the impactor and post and not the element carrying those properties. Moreover, this approach has the advantage of using the same post model geometry from the static test without modification.

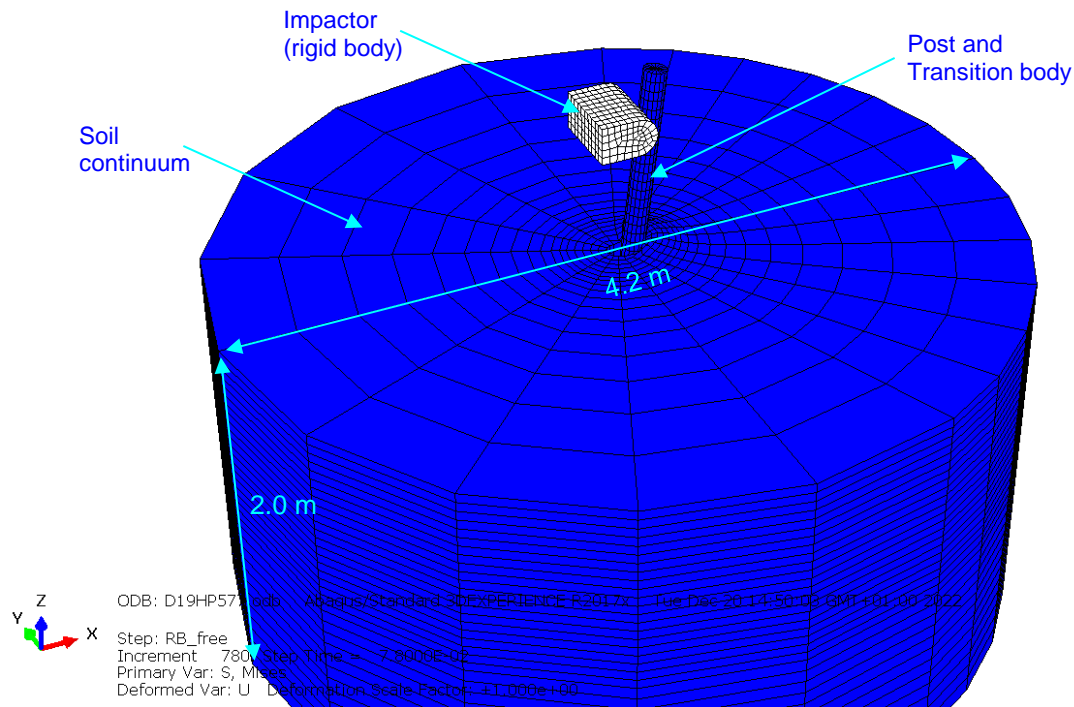


Fig. 5-4: Configuration of the full model used for the dynamic test simulations

To avoid the numerical problem of hourglass modes (also known as zero-energy modes) in the dynamic simulations, only fully integrated elements have been used. In the case of using reduced-integration elements, the elements may form a regular pattern like hourglass rows under dynamic loading, which may lead to unrealistic excessive element distortions and consequently the model fails to converge [59]. To avoid this problem when using reduced-integration elements, the model discretization has to be very fine, which requires a higher computational effort. Or a numerical hourglass stabilization technique has to be applied and the required artificial strain energy has to be inspected [1] [59].

The chosen first-order fully integrated continuum elements are generally vulnerable to shear and volumetric locking, which may lead to overestimating the element stresses. Shear locking occurs in elements subjected mainly to bending stresses. This behaviour is excluded in the simulated guardrail post problem, since the soil elements are subjected mainly to compression and shear stresses. A further undesirable behaviour that may arise with the fully integrated continuum elements is volumetric locking. The elements exhibit a false too stiff behaviour under pressure stresses, if the material is nearly incompressible. This problem can be avoided by choosing first-order elements with full integration. Moreover, the soil material properties are relatively compressible [1].

To include the large-deformation effects in the model, the non-linear geometry option is activated in all calculation steps. To assure satisfying accuracy and resolution of the results, the duration of the initial time step was set in the dynamic analysis after a convergence study to 0.1 ms.

5.2 Material models and parameters calibration

Selecting a suitable constitutive model for the simulation of a particular application is generally a challenging task for engineers. In geotechnical engineering, the mechanical behaviour of soils can be simulated using different models at various degrees of sophistication and accuracy. Depending on the engineering application or the problem modelled, as well as the simulation purpose, a constitutive soil model can be selected. The constitutive soil model has to capture the fundamental material features to be capable of simulating the complex soil behaviour adequately. However, the degree of sophistication of the soil model is reflected in the number of parameters required and the laboratory testing effort needed for the calibration process. Therefore, the engineer or the researcher has to balance between the essential soil features that are unconditionally to be considered for a realistic simulation and the availability of the required calibration data.

The simulation of the guardrail post behaviour requires the consideration of specific mechanisms and soil features. The quasi-static tests exhibit non-linear load-deflection curves, indicating the non-linearity of the soil response. No explicit transition was observed between the reversible and irreversible deformation phases. Under impact loading, the reaction force increased significantly due to the soil and post mass inertial effects and damping. Large deformations and soil heave in front of the post were observed under both loading conditions. The soil is observed to reach the limit state after a certain deflection range. The steel section showed plastic deformations after reaching the yield stress. However, the yield strength seems to increase under dynamic loading, since the posts did not yield under higher forces experienced in the impact test. The tyre material between the impactor and post contributed to damping the high-frequency amplitudes due to impact.

Based on these observations from the experimental field tests, the suitable constitutive model for each material was chosen. The selected constitutive models, as well as the parameters determination process, are described in this section.

Hypoplastic soil model

Many researchers utilised the hypoplastic constitutive model developed by VON WOLFFERSDORF [93] to model the soil in static and dynamic boundary value problems. The application of the hypoplasticity theory for modelling the geomaterials' behaviour was proposed and handled by many researchers independently (e.g. KOLYMBUS 1985, BAUER 1996, NIEMUNIS 1996, HERLE & GUDEHUS 1998). The advanced hypoplastic material model is capable of simulating the non-elastic behaviour as well as the non-linear stress-strain response of granular soils efficiently. It captures the main characteristic properties of soil behaviour, such as contraction and dilation, the critical state, and the dependency of both stiffness and shear strength on the stress state and relative density.

With the extension of the model with the intergranular strain properties (IGS) introduced by NIEMUNIS & HERLE [60], the material stiffness is adjusted for first loading and unloading-reloading phases. Moreover, the intergranular strain properties capture the hysteretic material behaviour and accumulative effects under cyclic loading. Compared to the common constitutive soil models, no distinction is drawn in the hypoplastic constitutive relation between elastic and plastic strains. The rate formulation of the stress-strain behaviour implemented in the model makes it numerically more stable despite the consideration of material non-linear behaviour [52]. The constitutive equation is written as a tensor-valued function.

The hypoplastic relation can be abbreviated as follows:

$$\dot{\sigma} = H(\sigma', e, \dot{\epsilon}, \delta) \quad \text{Equ. 5-3}$$

where; $\dot{\sigma}$, $\dot{\epsilon}$ and δ are the stress-rate tensor, the strain-rate tensor and the intergranular strain tensor, respectively. Depending on the present stress state σ' and void ratio of the soil e , the hypoplastic relation is capable of simulating the soil compaction and dilatancy realistically.

The hypoplastic material model is not available as a material model in ABAQUS and is implemented with a user-defined subroutine "umat". The hypoplastic user-defined subroutine developed by NIEMUNIS (version 2003) was used for the simulations. This version was developed for implicit analysis.

The model parameters are subdivided into material parameters and state variables. The material parameters include the critical state friction angle φ_c , the maximum and minimum void ratios, the pycnometric α and barometric β exponents and the granulate hardness h_s . The state variables include the void ratio, the effective stress and the intergranular strain. The material model parameters were calibrated and optimised using the data from the laboratory tests conducted on specimens of crushed limestone KSS032 (see 4 Laboratory testing of soil materials). The determined model parameters are summarised in Table 5-1.

The calibration procedure proposed by HERLE & GUDEHUS [41] was followed for the determination of the model parameters. First, the limiting void ratios were determined. The initial critical void ratio e_{c0} defines the density of the soil specimen in the critical state under zero pressure. This value was identified using the standard test as per DIN 18126 [18]. The upper bound void ratio e_{i0} was estimated as recommended by WICHTMANN [91] by the factor $1.15 \cdot e_{c0}$. The initial minimum void ratio e_{d0} , which defines the lower bound, was identified from the standard proctor test as per DIN 18127 [19]. The dependency of the void ratio on the mean pressure is described by the equation from BAUER [41] (see Fig. 5-5).

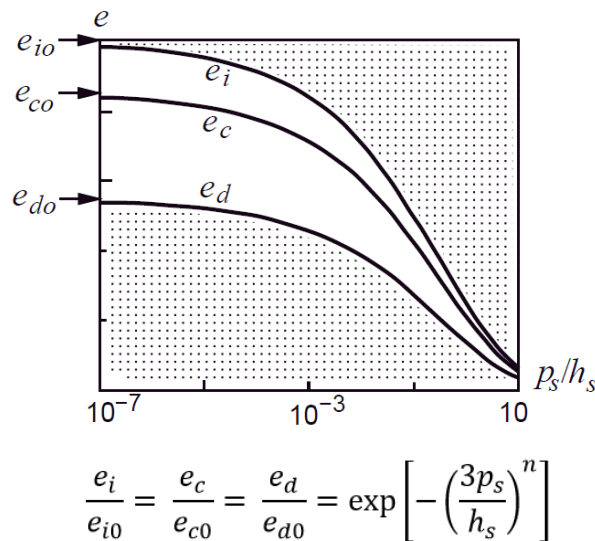


Fig. 5-5: Evolution equation of the limiting void ratios with the increasing mean effective pressure p_s after BAUER [41]

The critical state friction angle φ_c i.e. angle of repose was estimated as a mean value from several tests. Due to the large grain size of the material, a special setup was used instead of the conventional funnel (see 4 *Laboratory testing of soil materials*).

In the next step, the granulate hardness h_s and the exponent n , which control the shape of the limiting void ratio curves, were assessed through curve fitting to oedometer test data (see Fig. 5-6). Two oedometer tests were conducted on very dense specimens ($I_D \approx 95\%$) and two oedometer tests were conducted on loose specimens ($I_D \approx 32\%$). The tests were executed using a specially customised oedometer test equipment for large specimens of granular materials. The specimen's dimensions ($D = 30\text{ cm}$ and $H = 14 - 16\text{ cm}$) fulfilled the requirements of the DIN EN ISO 17892-5; specimen diameter larger than 1/5 of the maximum grain size and the ratio D/H smaller than 2.5.

To determine the pycnometry exponent α , two series of consolidated drained triaxial compression tests were executed on very dense ($I_D \approx 98\%$) and loose ($I_D \approx 28\%$) specimens, respectively (see Fig. 5-7). The exponent α , which controls the dependency of the peak friction angle and dilatancy on the relative soil density, was calculated using the set of equations given by WICHTMANN [91]. The equations require the peak deviator stress q_p and void ratio e_p at the specimens mean pressure at failure p_p from the experimental data of the specimen in the dense and loose states. The barometry exponent β controls the influence of the relative density and mean pressure on the soil stiffness. This parameter was derived from the comparison of the oedometric stiffness of the specimens in the dense and loose state. The equations followed for the determination of α and β are described in detail by WICHTMANN [41] [91].

The hypoplastic relationship is extended using the "intergranular strain" state parameter to account for the change in stiffness due to the change in loading path. A change in the deformation direction, e.g. unloading after monotonic loading, leads to an increase in stiffness in granular soils [41]. The model parameters controlling the intergranular strain feature R, m_T, m_R, β_r and χ can be determined from dynamic laboratory tests on soil samples e.g. resonant column or cyclic shear tests. The parameter R defines the range in which the soil response is elastic. The elastic strain range considers the small strain response of the soil exhibiting the maximum shear modulus. The stiffness ratio after a change in loading direction by 90° and 180° is defined by m_T and m_R respectively. The exponents β_r and χ are the parameters controlling the evolution equation of the intergranular strain tensor. The IGS parameters were assumed in the range given in the literature for comparable soils [52] and by fitting them to the laboratory test data. The ratio m_R/m_T is set equal 2.0 as recommended by WICHTMANN [91].

Using the determined material parameter set, the experimental oedometer and triaxial tests were simulated for verification. The parameters were then optimised slightly to achieve the best reproduction of the experimental data. The final material parameter set used for modelling the soil in different states is presented in Table 5-1. In the field test simulations, the initial void ratio e_0 is set to 0.328 equivalent to the in-situ relative density of $I_D = 0.80$. In the laboratory test simulations, the initial void ratio was set to the respective relative density of the specimen.

Table 5-1: Material parameters of the hypoplastic soil model for the KSS032

Description	Parameter		Value
Critical state friction angle	φ_c	[°]	35.7
Poisson's ratio	ν	[-]	0.35
Granulate hardness	h_s	[MPa]	42E+03
Exponent gran. hardness	n	[-]	0.22
Initial minimum void ratio	e_{d0}	[-]	0.251
Initial critical void ratio	e_{c0}	[-]	0.614
Initial maximum void ratio	e_{i0}	[-]	0.706
Pycnotropy exponent	α	[-]	0.108
Barometry exponent	β	[-]	1.10
Max. value of intergranular strain	R	[-]	1.0E-04
Stiffness multiplier (180°)	m_R	[-]	4.0
Stiffness multiplier (90°)	m_T	[-]	2.0
Exponent IGS	β_r	[-]	0.1
Exponent IGS	χ	[-]	1.0
Initial void ratio (in-situ)	e_0	[-]	0.328

The simulations of the oedometer tests and the triaxial shear tests using the determined model parameters are presented in Fig. 5-6 to Fig. 5-7. The stress-strain curve in the oedometer test could be well reproduced with the calibrated parameter set for the specimens with high relative density ($I_D = 94\% - 96\%$). For the loose specimens ($I_D = 30\% - 34\%$), a softer behaviour is obtained in the higher stress levels compared to the laboratory test result. This deviation is insignificant for the simulation of the field tests due to the predominant dense soil condition.

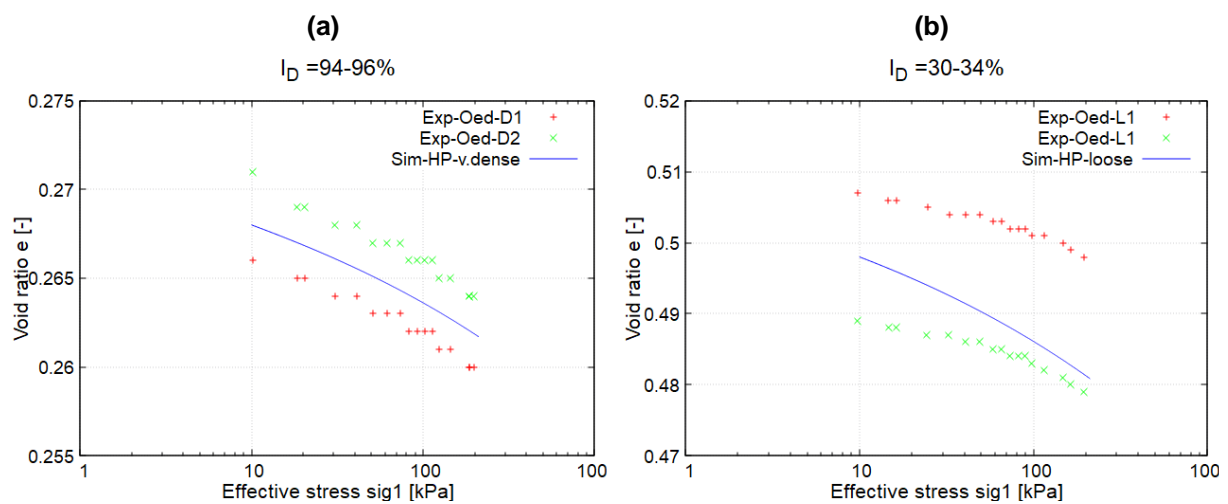


Fig. 5-6: Simulation of the Oedometer tests conducted on KSS032 specimens (a) very dense and (b) loose

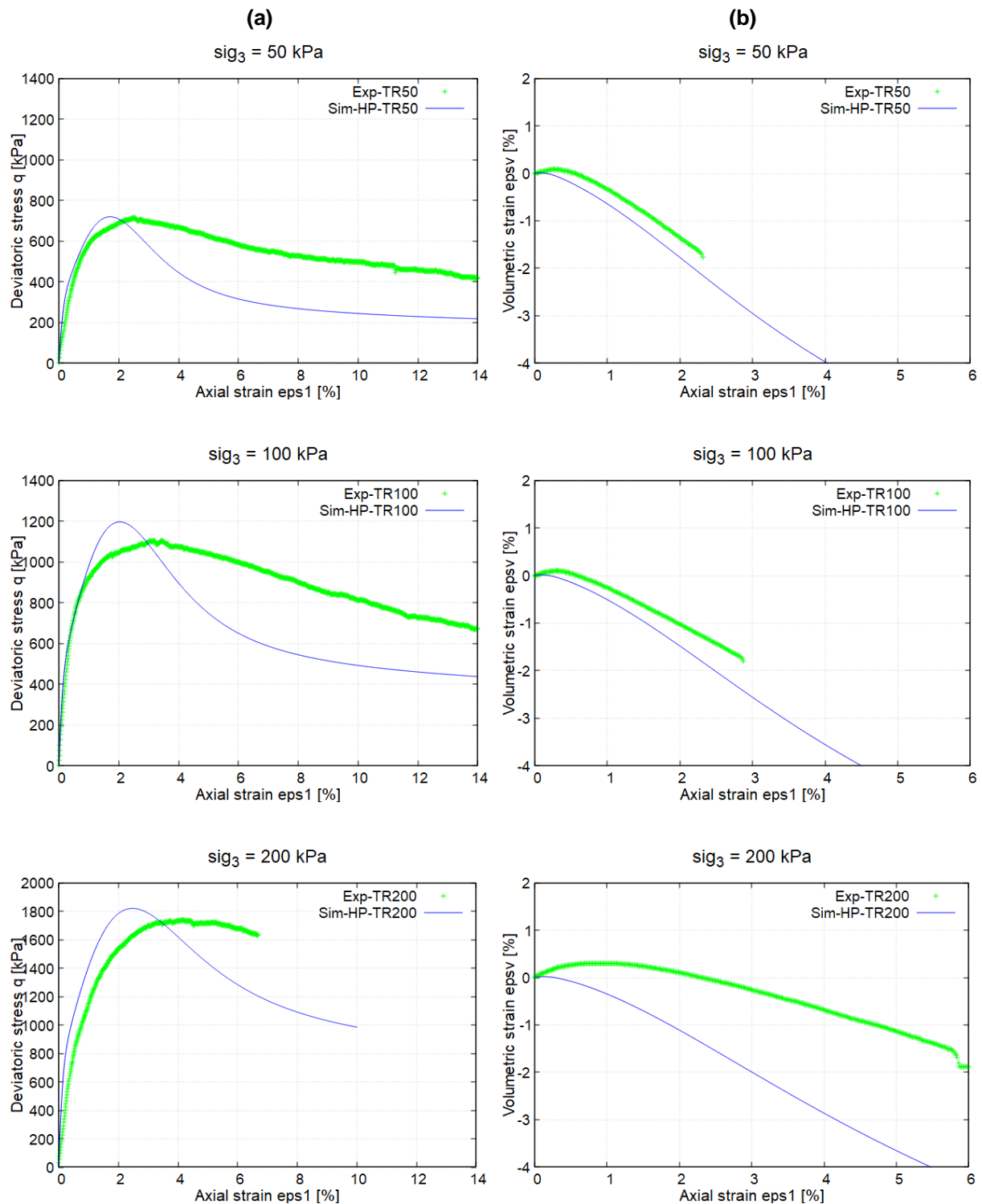


Fig. 5-7: Simulation of the drained triaxial compression test conducted on very dense KSS032 specimens under confinement pressures of 50, 100 and 200 kPa (column a) stress-strain curves (column b) volumetric strain over vertical strain

The simulation of the deviatoric stress ($q = \sigma_1 - \sigma_3$) over axial strain ϵ_1 in the triaxial shear test shows a good agreement with the measured values up to the peak stress, for the specimen with the consolidation stress 50 kPa. With the further increase in the axial strain beyond the peak stress, a simulated softer behaviour is observed, and the deviatoric stress is slightly underestimated. For the specimens with consolidation stress 100 and 200 kPa, the simulated peak stress is 9% and 6% higher than the measured values, respectively. However, this deviation is not decisive for the simulations, as the prevailing overburden stresses in the

embedded zone do not exceed 25 kPa. The simulation of the volumetric strain for both specimens shows a deviation of a maximum of 20% from the measured values. A higher deviation in the volumetric strain simulation was reported by WICHTMANN [91] for the calibration of the “Karlsruher Sand” parameters, which was described as acceptable.

The relative density of the soil is defined in the material model as an initial state variable in the form of the initial void ratio e_0 . This value was determined from the in-situ tests carried out to determine the dry soil density ρ_d using the nuclear densometer (see *Appendix [A]: In-situ soil testing*). Since the soil was placed and compacted in 3 layers, the dry density was calculated as an average value over the depth. The initial void ratio e_0 was then calculated using the experimentally determined specific weight and the average dry density (Equ. 4-1).

Steel and rubber material models

The steel cross-section of the post was modelled with an elastoplastic material model with isotropic hardening. The yield stress and the stress-strain behaviour of the material were calibrated to the tensile testing results conducted by TÜV-SÜD on specimens from the post material. The experimental stress-strain data represent the nominal (also engineering) values. During the tensile testing, especially in the plastic range, the specimen cross-section area contracts significantly compared to the original cross-section area. The stress then becomes higher as the tensile force is distributed over a smaller area. This is known as the true stress. The true strain is less than the nominal strain and is equal to the natural log of the quotient of the current length during testing over the original length. For the numerical modelling of the plasticity of ductile materials at large deformations like steel, the true stress-strain relationship is required [1].



Fig. 5-8: Nominal versus true stress-strain values of the steel material applied for the post model

The nominal stress-strain values were converted to the true values as follows:

$$\sigma_T = \sigma_N \cdot (1 + \varepsilon_N) \tag{Equ. 5-4}$$

$$\varepsilon_T = \ln(1 + \varepsilon_N) \tag{Equ. 5-5}$$

where, σ_N and ε_N are the nominal stress-strain values and σ_T and ε_T are the true stress-strain values.

The true stress-strain curve of the post material derived from the experimental data is presented in Fig. 5-8. The experimental data show a degradation of the material strength after ca. 15% strain (equivalent to 19.5% true strain). This behaviour was modelled using material damage criteria, defined by an initiation failure strain and an exponential softening function. The elastic modulus and the Poisson's ratio of the steel material were assumed in the typical range for steel to $E = 210 \text{ GPa}$ and $\nu = 0.28$ (see Table 5-2).

It has been proven in many studies that the steel yield strength increases with increasing strain rate. The yield stress under impact loading, i.e. high strain rate, can increase up to 2-folds compared to the quasi-static value [94]. The power function suggested by COWPER & SYMONDS describes the relation between the yield stress and the strain rate [13]:

$$R = 1 + \left(\frac{\dot{\varepsilon}}{D}\right)^{1/n} \quad \text{Equ. 5-6}$$

$$R = f_{y \text{ dyn}} / f_{y \text{ stat}} \quad \text{Equ. 5-7}$$

where, R is the yield stress ratio (dynamic to quasi-static), $\dot{\varepsilon}$ is the strain rate, D and n are the material constants of the constitutive model.

The COWPER-SYMONDS model was used to simulate the strain rate dependency of the steel post under impact loading. The values of the coefficients D and n were adopted as per COWPER & SYMONDS [13] for mild steel (see Table 5-2). These values have been investigated by WRIGHT & RAY [94] were compared to and have shown a good agreement with the experimental results conducted by themselves.

Table 5-2: Material model parameters of the steel and rubber material

Description	Parameter		Steel post S355	Rubber Tyre
Elasticity modulus	E	[MPa]	210.0E+03	30.0E+03 ($\varepsilon=0\% - 26\%$)
Poisson's ratio	ν	[-]	0.28	0.45
Density	ρ	[g/cm ³]	7.85	0.001
Yield stress	f_y	[N/mm ²]	416	-
Ultimate stress	f_u	[N/mm ²]	520	-
Strain-rate multiplier	D	[s ⁻¹]	40.4	-
Strain-rate exponent	n	[-]	5.0	-

In the quasi-static test simulation, the transition elements around the beam along the embedment length were modelled as linear-elastic with a modulus of elasticity corresponding to the stiffness modulus of the soil for unloading-reloading at a mean stress level of 25 to 50 kPa ($E_{\text{transition}} = 75 \text{ MPa}$ evaluated from laboratory soil testing). This stiffness value was multiplied in the dynamic model by a factor of 15 to simulate the dynamic stiffness of the transition elements. The ratio of the dynamic to static stiffness modulus was investigated by WICHTMANN & TRIANTAFYLLIDIS [92]. For well graded gravelly sand, the ratio $E_{s \text{ dyn}} / E_s$

was determined experimentally between 10 and 20 for soils exhibiting a stiffness modulus between 10 to 20 MPa. This factor is applied to consider the influence of the small strain magnitude on the stiffness, not the loading rate. The factor $E_{s\ dyn} / E_s = 15$ was applied constant in the impact simulations to the transition elements independent of the impact energy. The simulations with the stiffness $E_{\text{transition}} = 75$ MPa, analogue to the static test simulation, results in a post resistance of approximately 10% less. This value is also acceptable for the validation under dynamic loading, and is even closer to the measured values (see section 5.3). However, the impact simulations with $E_{\text{transition}} = 75$ MPa terminated shortly after reaching the maximum resistance, due to excessive distortions in the transition body's lower bound elements. Therefore, the stiffness factor was applied to achieve a higher numerical stability.

In the dynamic model, the transition elements around the beam above the ground level were modelled as rubber tyre material. Rubberlike solids are modelled in the practice as hyperelastic materials, e.g. using OGDEN material model [64]. As no experimental tests have been conducted on the tyre piece of the impactor, the material was modelled as a non-linear elastic material for simplicity. The stress-strain behaviour of the rubber material was fitted to experimental compression test data conducted on solid rubber tyre specimens by PHORMJAN & SUVANJUMRAT [65]. The material is approximately linear up to a strain of 26% (see Fig. 5-9). For higher strains, the stiffness increases exponentially. The behaviour was simplified in the simulation to a continuous multilinear curve.

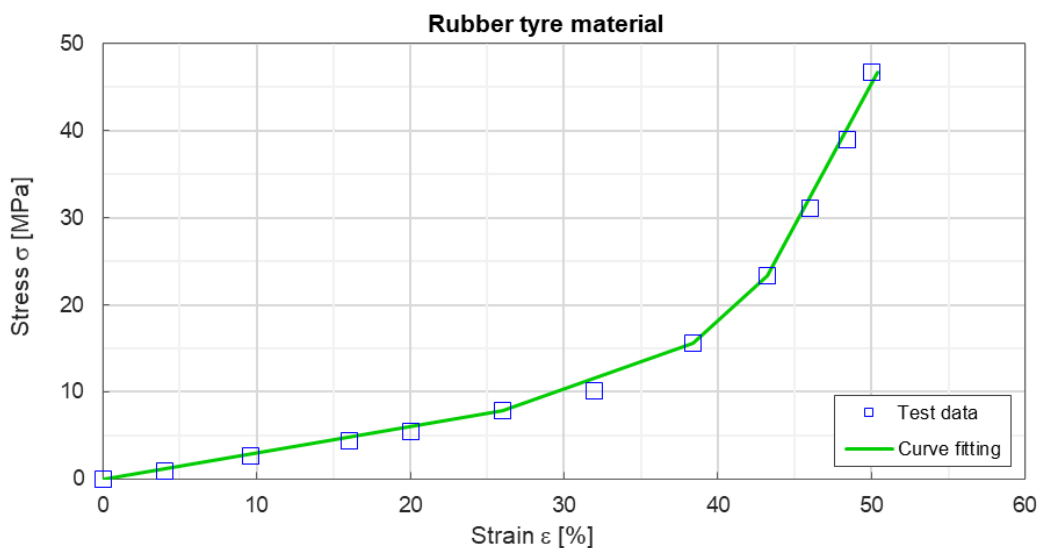


Fig. 5-9: Calibration of the rubber tyre material stress-strain curve to experimental data after PHORMJAN & SUVANJUMRAT [65]

The damping properties of the rubber tyre were considered by assigning Rayleigh damping to the material. No specific damping coefficient was found in the literature for the tyre material applied for the impact purpose considered in this study. Therefore, the mass and stiffness proportional coefficients were assumed $\alpha = 5.0E-04$ and $\beta = 1.0E-04$, respectively. These values are equal to the standard values assigned to steel material, which is a conservative assumption. To quantify the influence of the chosen rubber damping parameters on the simulated resistance, the calculation was rerun without these factors. The results show a negligible increase of the force and acceleration peaks in the respective time histories of maximum of 3.5%.

5.3 Validation of the FE model

The FE model was validated using the reference field tests conducted on IPE120 posts installed in dense KSS032 with an embedment length of 100 cm. First, the results of the FE simulations using the hypoplastic soil model for the quasi-static test conducted in the strong and weak axis are used for validation. Then, the influence of the mesh discretisation and the model geometry on the numerical solution are investigated. In the next step, the dynamic FE model is validated under different impact intensities.

Further, selected field tests were simulated using an elastoplastic soil model, and the results were compared to the FE simulations using the hypoplastic soil model.

In order to quantify the agreement of the simulations to the experimental data, the coefficient of determination R^2 and a performance metric W were calculated for the simulated reaction force. The coefficient of determination indicates for the force-displacement curve the proportionate amount of variation of the simulation from the field test. An R^2 value of 1.0 means totally coinciding curves.

$$R^2 = 1 - \frac{\sum (F_{i\ Exp} - F_{i\ Sim})^2}{\sum (F_{i\ Exp} - \bar{F}_{Exp})^2} \quad \text{Equ. 5-8}$$

The performance metric W gives an indication of the agreement of the total work done by the applied load (integral of the force over displacement at the loading point) in the simulation and the field test.

$$W = 1 - \frac{\int_0^{u_{max}} |F_{Exp} - F_{Sim}| du}{\int_0^{u_{max}} F_{Exp} du} \quad \text{Equ. 5-9}$$

where;

$F_{i\ Exp}$: maximum reaction force measured from the experimental field test

\bar{F}_{Exp} : mean value of the reaction force measured from the experimental field test

$F_{i\ Sim}$: reaction force from the simulation at a given displacement

u_{max} : maximum deflection of the post at the loading point. In case of simulations terminated before reaching 40 cm deflection, the last deflection value is used for assessment.

The metrics R^2 and W were used by SASSI & GHRIB [79] for the evaluation of the guardrail posts simulation performance compared to experimental field tests.

Simulation of the quasi-static loading tests

The simulation results of the quasi-static test conducted in the strong axis using hypoplasticity show very good agreement with the experimental data (see Fig. 5-10). The simulation load-deflection curve (Sim-HP) is compared to the executed tests under the same conditions (Exp-P01 to P03). The maximum reaction force shows a deviation of a maximum of 1.5 kN (ca. 10%) from the corridor formed by the experimental data. The calculated coefficient of determination for the simulation is $R^2 = 0.93$ and the performance metric is $W = 0.94$. This slight deviation can be attributed to the idealisations in the numerical model, e.g. transition body geometry, contact surface properties, as well as the calibrated soil material parameters. Moreover, features like soil cracking and grains rearrangement in the influence zone in front of the post cannot be considered, therefore the results are acceptable for simulating the soil using continuum elements.

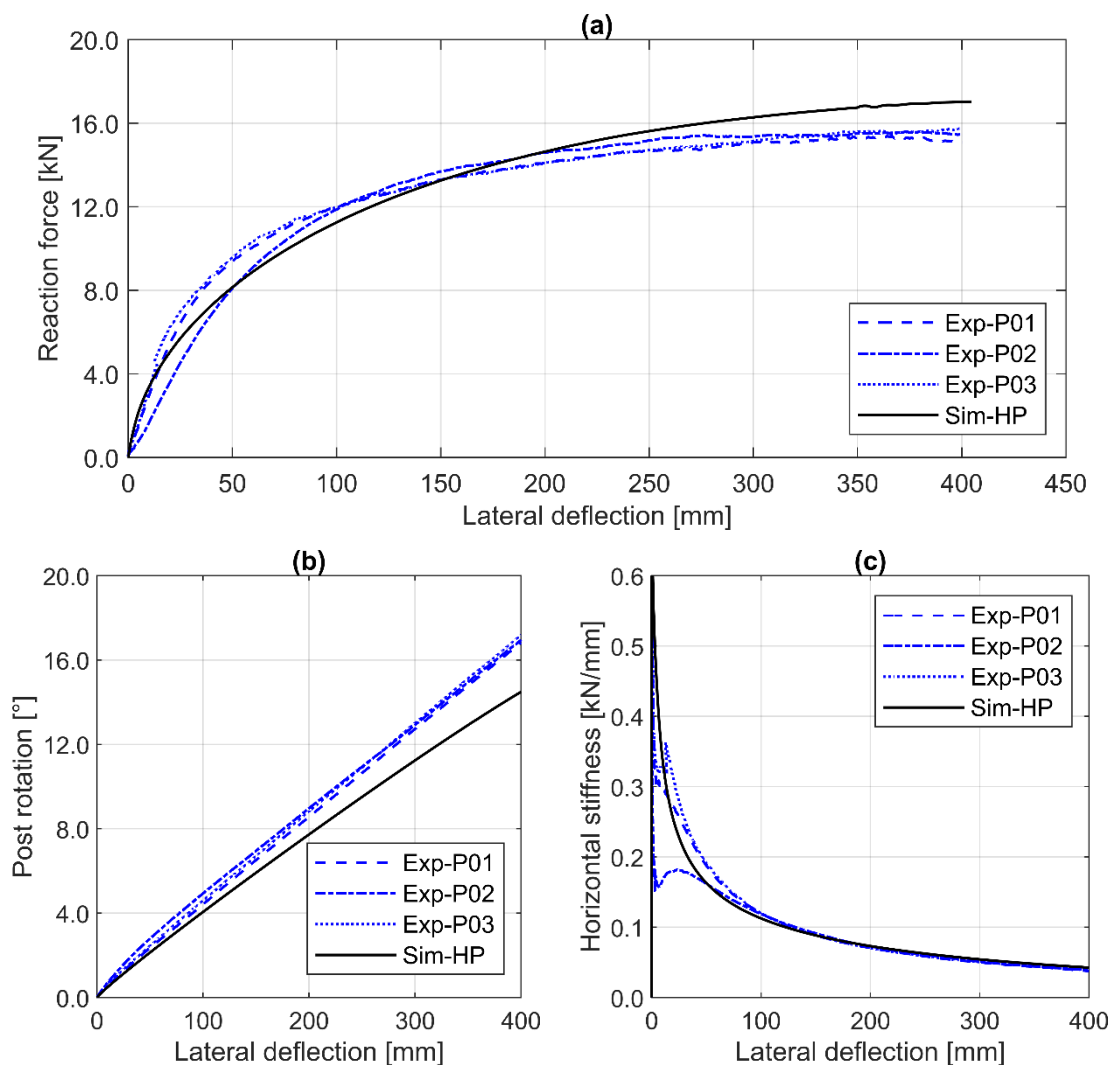


Fig. 5-10: Comparison of the simulated reference static test and the field tests results in the strong axis (a) load-deflection curves at the loading height (b) rotation over lateral deflection of the loading point (c) Linear stiffness of the system evaluated at the loading point.

The post rotates under lateral loading as a rigid body (Fig. 5-10b), and no plastic deformations occur. The excavated posts in the field test also exhibited no signs of yielding. The horizontal stiffness of the system (Fig. 5-10c), assuming a single degree of freedom, lies in the range of the field test results.

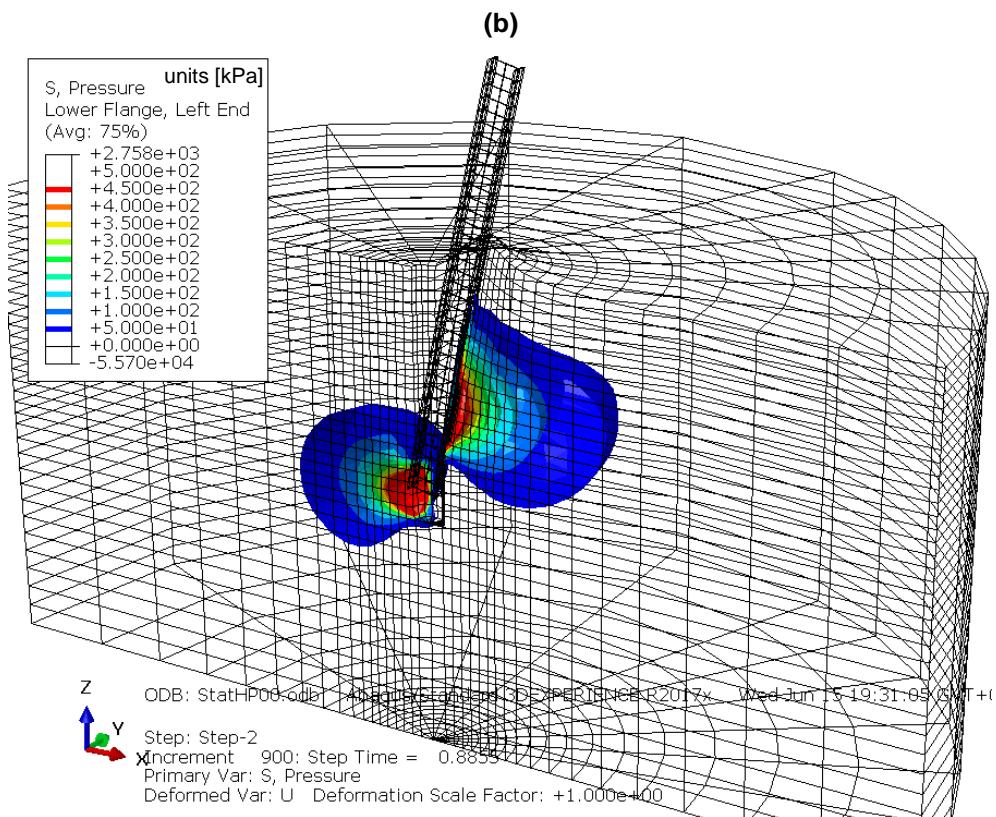
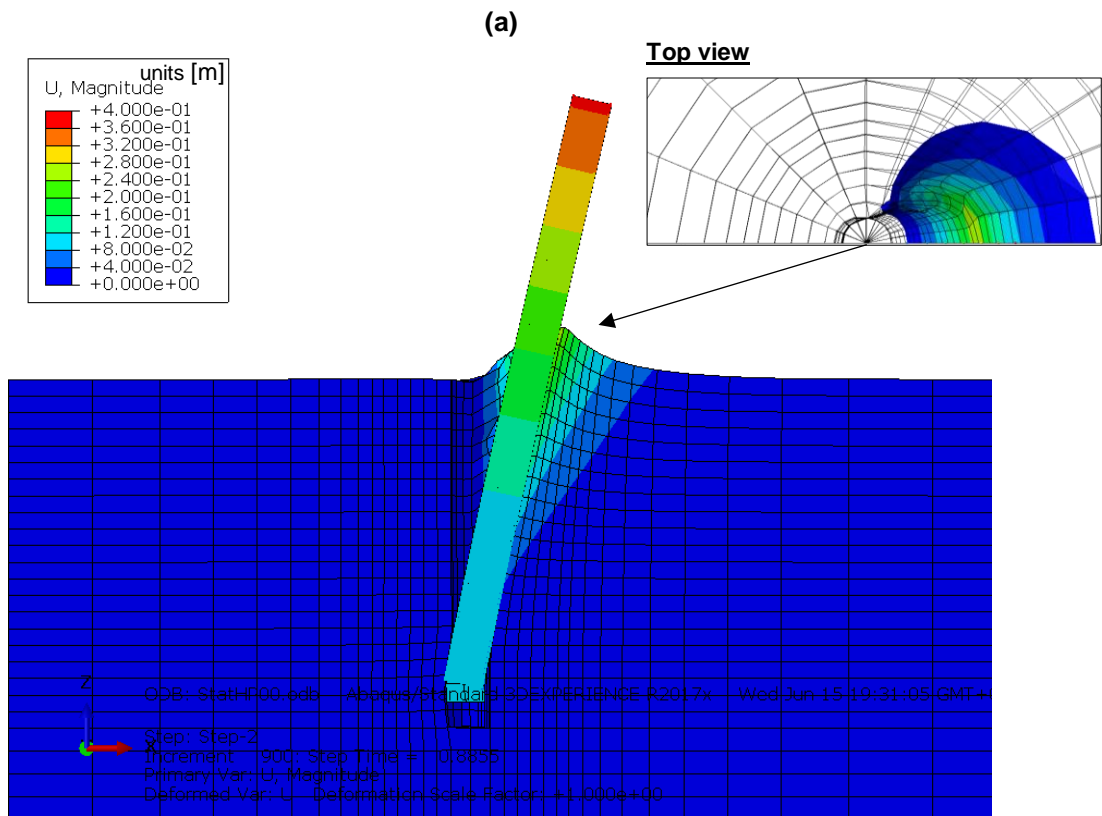


Fig. 5-11: Results of the reference static test simulation in the strong axis at the maximum reaction force (a) soil deformation contours (b) mean pressure distribution

The post rotation is observed to increase approximately linearly with the deflection. However, comparing the post rotation development with the reaction force, the relationship is disproportionate (2.5° at 50% F_{max} and 15° at 100% F_{max}). These results coincide with the field test observations (see 3.2 *Reference test results*).

Fig. 5-11a shows the deformed contour of the soil at the maximum force and the mean effective stress distribution around the post. A soil heave of 15 cm is formed in front of the post in the vicinity of approximately 60 cm. Behind the post, a gap is opened along the contact surface. During loading, the post is pulled upwards by a total of 4 cm at 40 cm deflection. The simulated soil and post deformations coincide with the field test observations. No increase in the mean stress is evident near the surface from the beginning of loading to the maximum force (see Fig. 5-11b). The locally increased mean stress at 0.5 m and 0.9 m below ground level builds the force couple resisting the applied lateral load. The stress bulb of mean pressure extends to a maximum of 77 cm in front of the post and 62 cm behind the post, with a width of 76 cm.

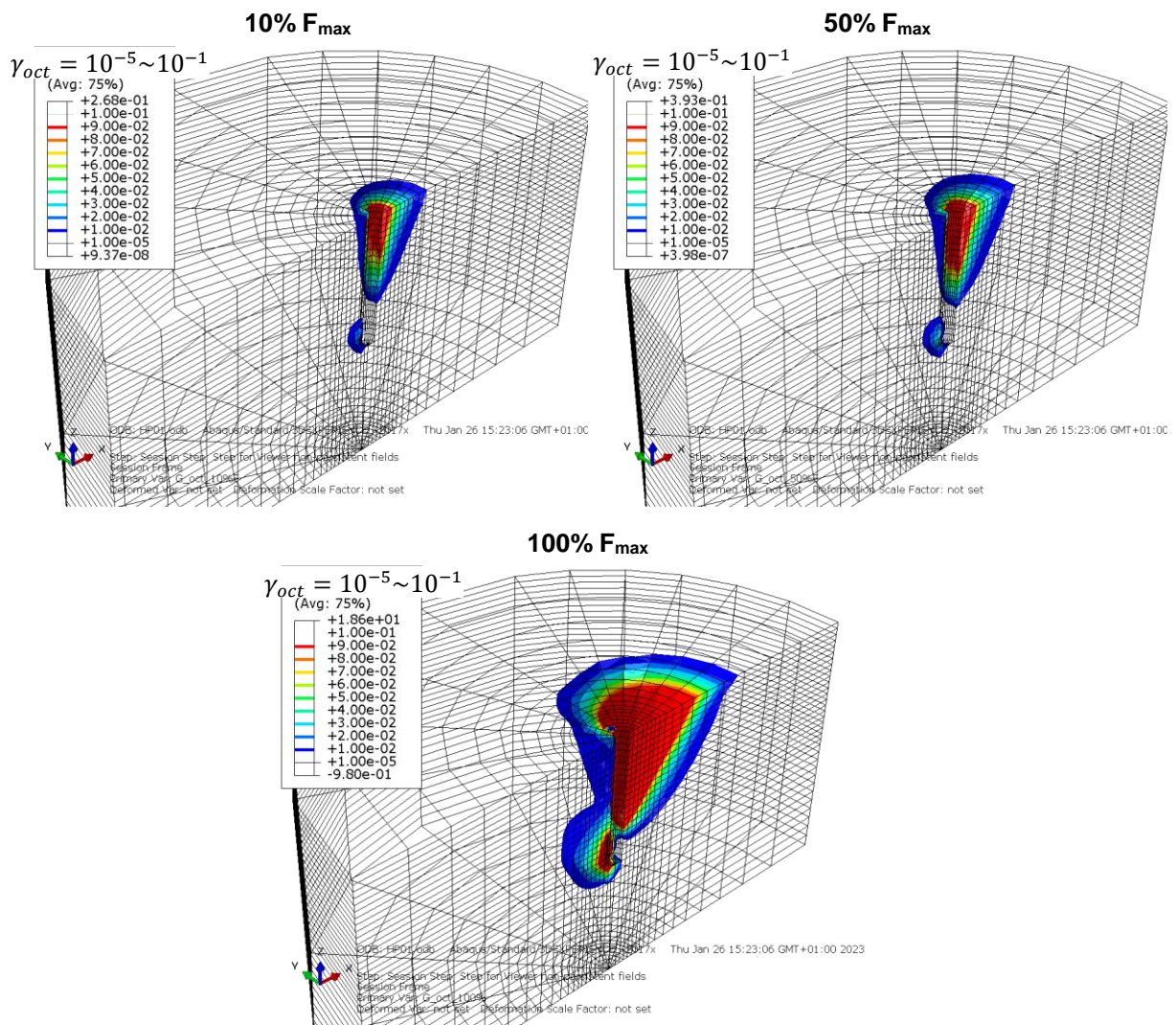


Fig. 5-12: Shear strain contours in the post vicinity evaluated at 10%, 50% and 100% of the maximum reaction force

As a measure for the shear strains induced in the soil continuum, the octahedral shear strain $\gamma_{oct} = \frac{2}{3} * \sqrt{((\epsilon_1 - \epsilon_3)^2 + (\epsilon_2 - \epsilon_3)^2 + (\epsilon_3 - \epsilon_1)^2)}$ was evaluated in each soil element, as described by LADE [47]. The shear strain contours assessed at 10%, 50% and 100% of the

maximum reaction force F_{max} show the evolution of the influence zone around the post during loading (see Fig. 5-12). As per the German Recommendations for Soil Dynamics [35], the small shear strain amplitude for gravel and sand can be assumed $\gamma < 10^{-5}$. By defining a lower bound for the shear strain of $\gamma = 10^{-5}$, the contours show values in the influence zone reaching up to $\gamma = 2 * 10^{-1}$. This indicates that the shear strains in the elements resisting the post deflection lie in the range of large deformations. Consequently, the shear modulus governing the soil behaviour is much lower than the maximum shear modulus $G < G_{max}$ and shows degradation with the increasing post deflection.

The same model of the static test in the strong axis is used for the validation in the weak axis. Only the local axis of the beam elements is inverted to apply the load in the orthogonal direction. The simulation results are compared to two field tests as shown in Fig. 5-13. The post strain and the mean stress distribution around the post at a lateral deflection of 35 cm are shown in Fig. 5-15. In the simulation as well as in the field test, the post shows yielding of the steel cross-section at a deflection of 8 to 10 cm. The depth of the plastic hinge formed is between 20 cm and 30 cm below ground level. The maximum reaction force reached at 35 cm deflection is 7.1 kN in the simulation versus 7.2 to 7.6 kN in the field test.

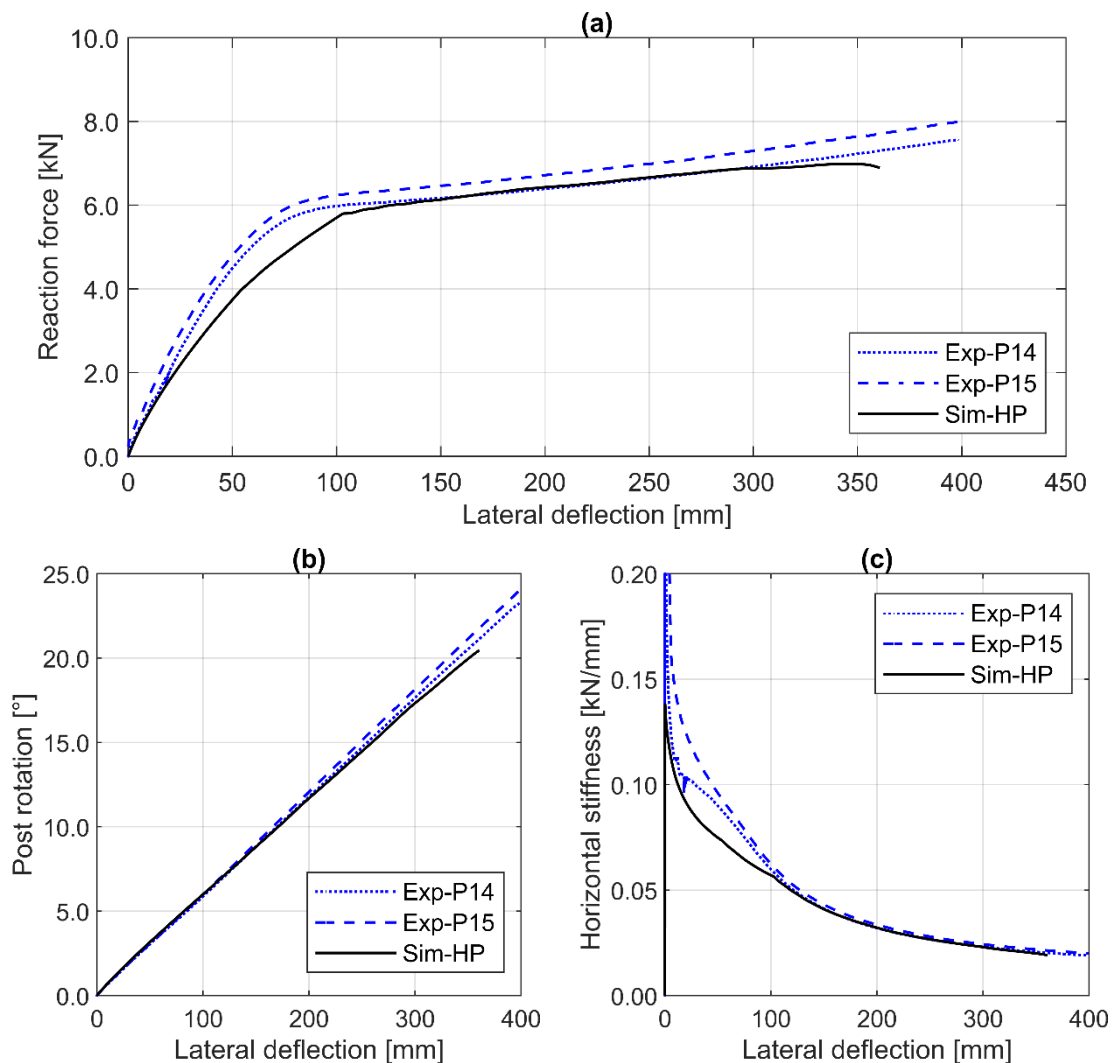


Fig. 5-13: Comparison of the simulated reference static test and the field tests results in the weak axis (a) load-deflection curves at the loading height (b) rotation over lateral deflection of the loading point (c) Horizontal stiffness of the system evaluated at the loading point.

With the achieved performance coefficients of $R^2 = 0.95$ and $W = 0.96$, the simulation is in very good agreement with the experimental field tests. The initial stiffness in the simulation is slightly lower than the field test. This value is a combination of the stiffness of the soil material and the post section before yielding. However, the maximum reaction force in the weak axis is governed by the yield strength of the post material.

Comparing the post resistance in the strong and weak axis, a ratio can be derived for the post resistance. Fig. 5-14 shows the development of the reaction force ratio and the linear stiffness ratio over post deflection. Both ratios start at a value of app. 3.9 and decreases to reach 1.5 to 2.0 at the point of post yielding. This proves that the system stiffness is not only governed by the soil and post material properties, but also with the post section modulus acting in the loading direction. Afterwards, the reaction force ratio runs nearly asymptotic around 2.0, while the linear stiffness ratio jumps to a mean value of 5.2 after the full yielding of the post section. The ratio of the linear stiffness in this phase is observed to be equal to the quotient of the IPE120 elastic section modulus in the strong axis and the plastic section modulus in the weak axis ($W_{el,y} / W_{pl,x} = 53.0 / 9.92 = 5.3$). This observation indicates that the behaviour in this phase is governed mainly by the post material and section properties.

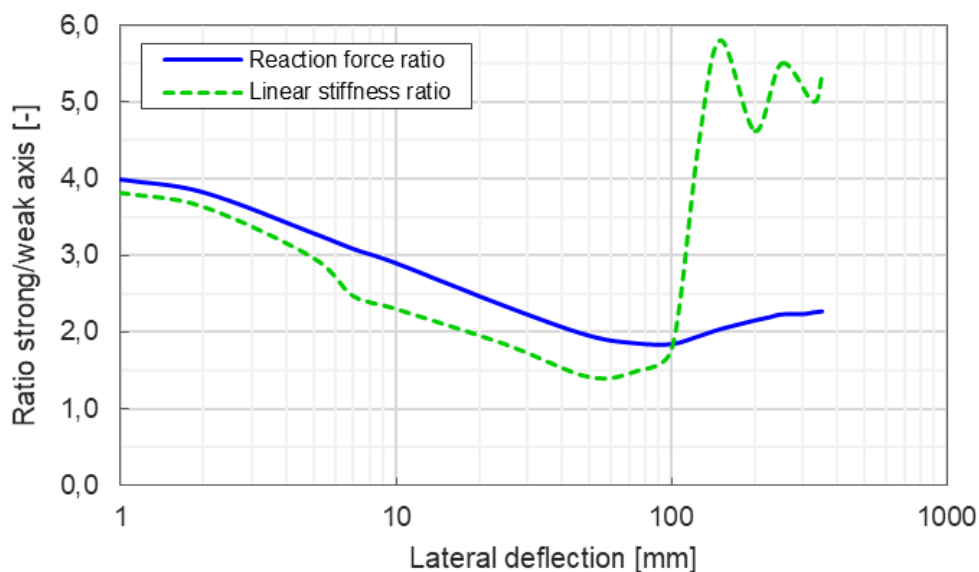


Fig. 5-14: Ratio of the post resistance in the strong to weak axis; reaction force and linear stiffness

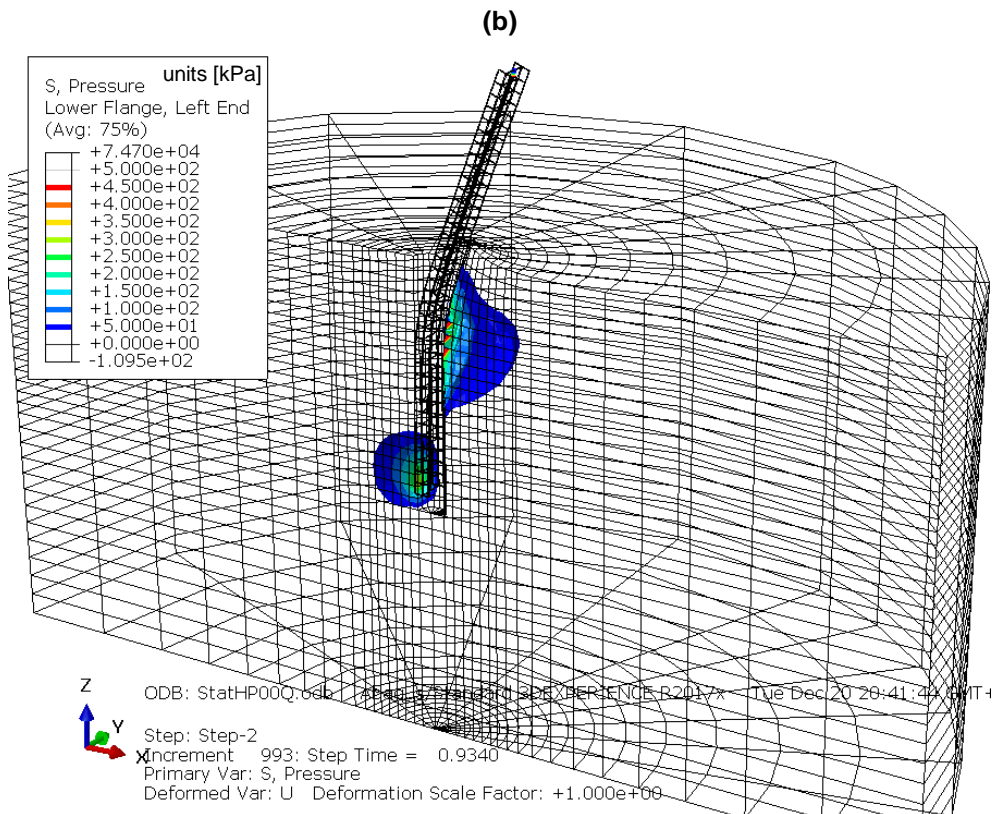
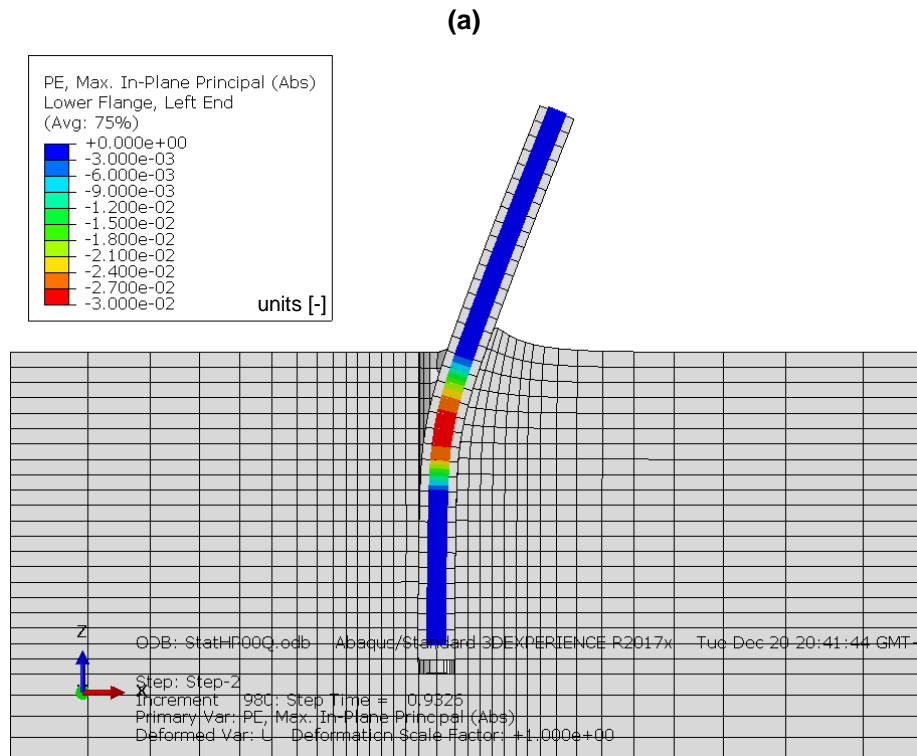


Fig. 5-15: Simulation of the quasi-static reference test in the weak axis (a) Plastic strains of the post section and formation of a plastic hinge (b) mean pressure distribution in kPa

Influence of the mesh discretisation

To investigate the influence of the mesh discretization on the numerical solution, further simulations were performed with various mesh fineness. In the near-field of the post, the discretization is governed by two contrasting arguments. On the one hand, a fine mesh is required to adequately represent the high stress and deformation gradients anticipated around the post. On the other hand, with very fine elements and large deformations in the near-field, the elements can become numerically unstable as a result of the induced distortions, and thus the calculation no longer converges. With larger elements, this problem can be avoided at the cost of a coarser representation of the local stress and strains.

Since there is always a mesh dependency of the numerical solution, especially when utilizing constitutive models with a plasticity criterion, adjusting or calibrating the element size is necessary to fit the numerical results to the experimental data. This approach is essential for most geotechnical FE simulations of soil-structure interaction [59].

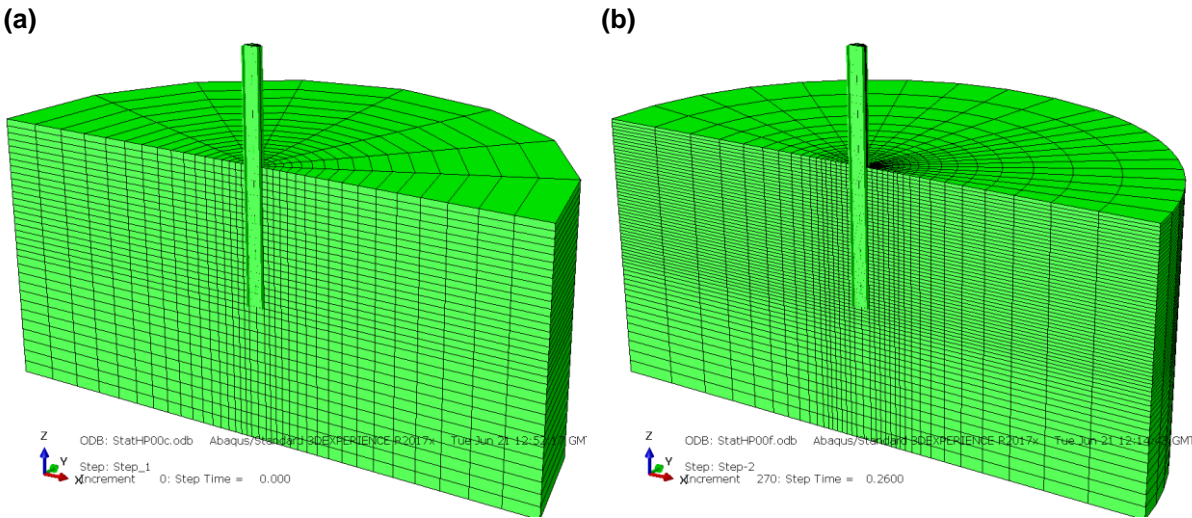


Fig. 5-16: Comparison models for the investigation of the mesh discretization effect on the results (a) coarse mesh with 4.916 elements (b) fine mesh with 24.536 elements

The model for the reference test consists of a total of 6.635 elements and 7.737 nodes. A finer model with a total of 24.536 elements and 27.073 nodes, as well as a coarser model with 4.916 elements and 5.901 nodes, were created (see Fig. 5-16). All boundary and loading conditions were kept unchanged. The results of all three models show only a negligible deviation of ± 0.2 kN in the maximum reaction force (see Fig. 5-17). In the finer model, the calculation terminated prematurely due to convergence problems caused by excessive distortion of individual soil elements in the flanks of the transition body. The post rotation and the derived linear stiffness coincide with the simulation results utilising the reference element fineness.

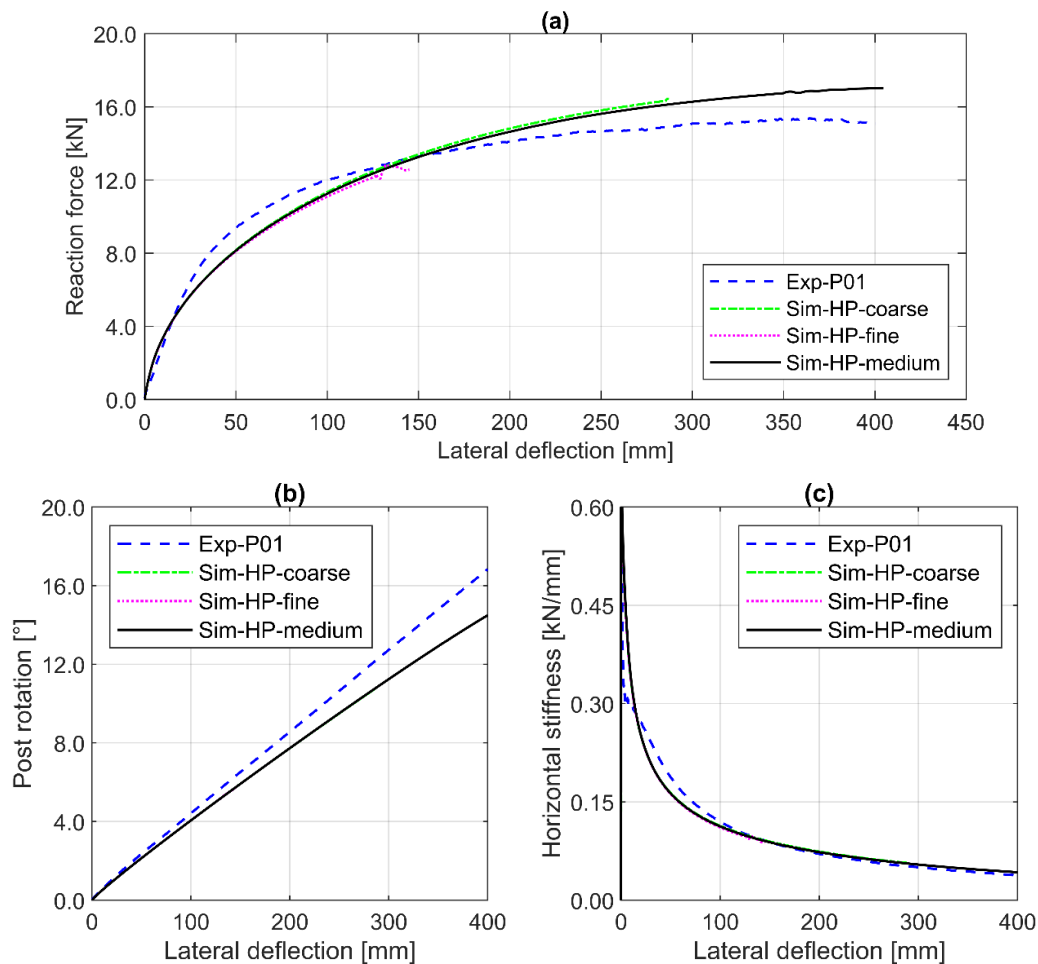


Fig. 5-17: Static test simulation using different mesh discretization (a) load-deflection curves at the loading height (b) rotation over lateral deflection (c) linear stiffness of the system.

Influence of the transition body geometry

To investigate the influence of the transition body cross-section geometry, i.e. post projection in the loading direction, two further models were created with different geometries based on the reference model. The first model exhibits an elliptical cross-section, while the second model exhibits a rectangular cross-section with chamfered edges (see Fig. 5-18). The circumference of the transition body was kept equal to that of the circle cross-section in the reference model. The soil block is discretised as a radial offset of the transition body shape. The long dimension of the soil block is set to 4.2 m. The mesh fineness in the vertical direction was kept unchanged compared to the reference model. The results of both simulations were compared to those of the reference model and the experimental data (see Fig. 5-19). The elliptical and the rectangular models failed to converge at relatively large post deflections, due to the excessive distortion of individual soil elements in the corners and flanks of the transition body. The reaction force and the derived horizontal stiffness of the elliptical and rectangular sections lie in the same range as the circular section, with a maximum deviation of 7 to 18%. The post rotation is nearly coinciding with the reference model results. Consequently, the transition body shape can be considered to play a subordinate role in modelling the post. The approximation of the transition body shape and the resulting minor deviation of the post resistance can be accepted for the required numerical stability. Therefore, the models created for further numerical investigations adopted a circular cross-section for the transition body and the soil block.

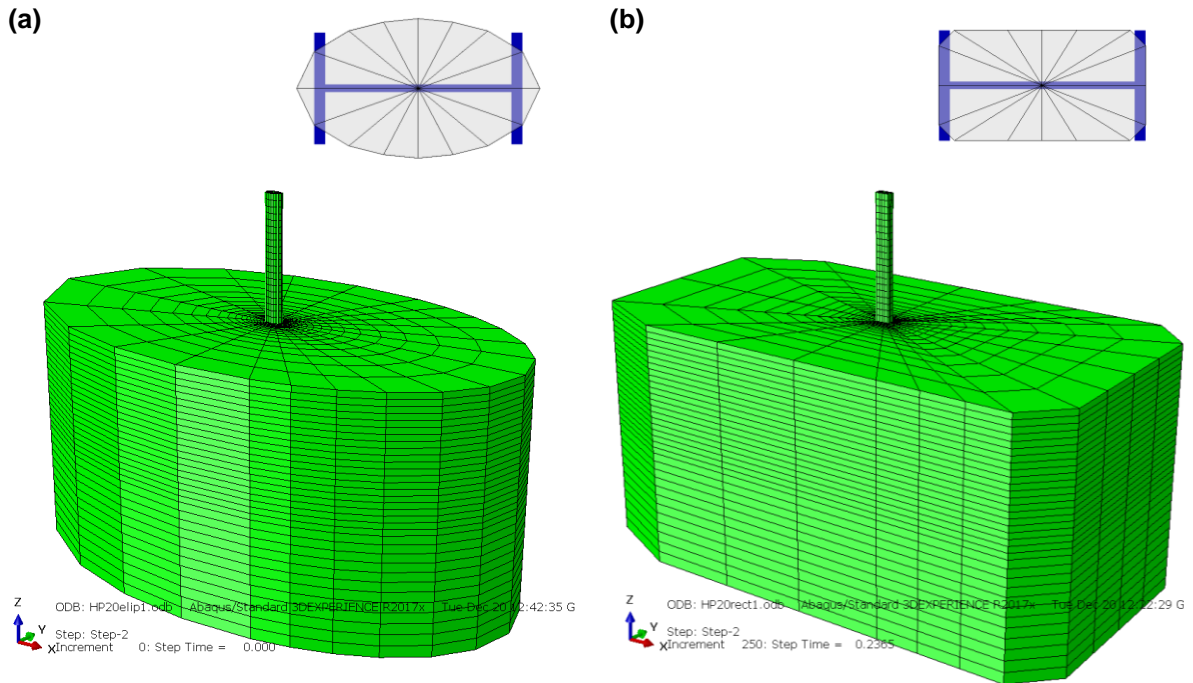


Fig. 5-18: Comparison models for the investigation of the transition body shape on the results (a) elliptic cross-section (b) rectangular cross-section

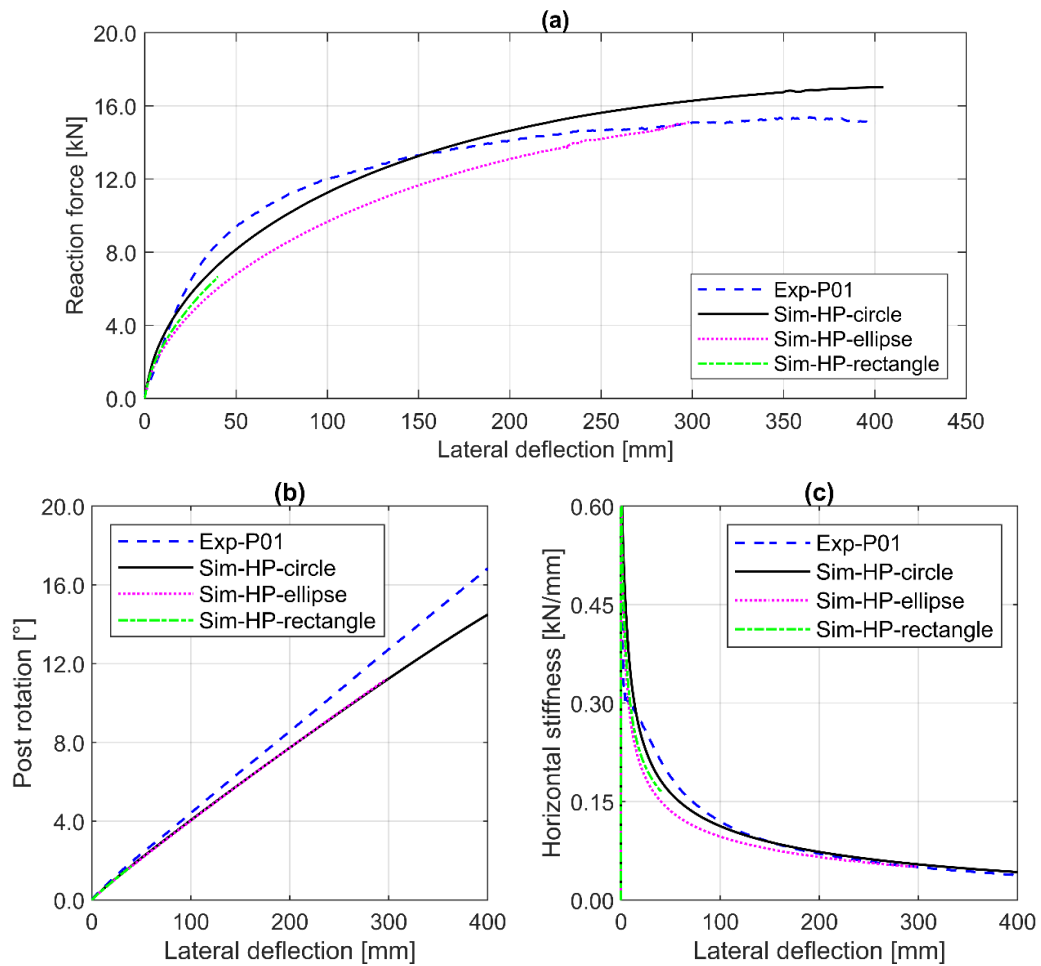


Fig. 5-19: Static test simulation using different transition body shape (a) load-deflection curves at the loading height (b) rotation over lateral deflection (c) linear stiffness of the system.

Simulation of the impact loading tests

In this section, the model for impact tests, which was developed based on the validated quasi-static model, is validated. The dynamic impact is simulated using a rigid body, i.e. an impactor colliding with the test post at 75 cm above the soil surface. In contrast to the static test, the velocity and acceleration are relevant and have to be considered in the validation. Moreover, to ensure that the model can simulate different impact intensities adequately, the same model was run with various impactor velocities. The validation includes running simulations with the same model for different impact intensities, which were simulated by varying the impactor velocities according to the values measured in the field tests.

The simulation results of the dynamic test executed under reference conditions (KSS032 dense, IPE120 strong axis) under an impact energy of 3.2 kJ ($v_{\text{imp}} = 5.77$ m/s) are presented in Fig. 5-20 and Fig. 5-21. The simulations agree with the experimental data in terms of maximum force, lateral deflection, and velocity. The impact force evaluated as an integration of the contact stress at the collision surface is compared to the impact force measured using the load cell (Fig. 5-20a). The maximum force simulated is 24.9 kN ($t = 16$ ms), while the measured force is 23.1 kN ($t = 14$ ms). The influence of the mass inertia is clear on the force-time history, especially in the first 25 ms. This is the time range in which the post acceleration amplitude is at its maximum (Fig. 5-20d). The force dip of -2.6 kN measured at 2 ms in the field test did not appear in the simulation, as the impactor is modelled as a rigid body. This indicates that the impactor head construction and connection with the load cells have an effect on the measured force.

Afterwards, the force declines rapidly to reach a plateau (13.4 to 14.5 kN) at 40 ms and continues to 71 ms, where the time point of recoil is reached. The force in this time range is ca. 90% of the maximum quasi-static reaction force. The time point of separation between the post and impactor is reached at 103 ms, i.e. zero contact force. Comparing the impact force to the reaction force in Fig. 5-20g, the simulation shows less inertial effects and a higher agreement with the experimental data. The reaction force is evaluated from the simulation as the net shear force in the post acting above ground level. The maximum reaction force simulated and measured are 24.4 and 21.9 kN, respectively. The reaction force reached in the plateau, i.e. at low velocity before recoil, is 97% of the static reaction force.

The lateral deflection of the post and the impactor displacement could be simulated with a maximum deviation of 0.5 cm and 1.5 cm, respectively (see Fig. 5-20b and Fig. 5-20e). The post rotation in the simulation is slightly overestimated by 2.5° at the maximum deflection (see Fig. 5-20f). The post velocity-time history shown in Fig. 5-20c nearly coincides with the measured values. The rate of change of velocity is approximately linear after the first 20 ms to the point of recoil, which indicates a nearly constant deceleration. The energy absorbed by the post, i.e. integration of the reaction force over post deflection, shows a good agreement with the experimental data with a maximum deviation of 0.4 kJ at the maximum deflection. This deviation can be attributed to the energy loss in the impactor head's mechanical parts and the tyre piece's deterioration, which were not considered in the simulation.

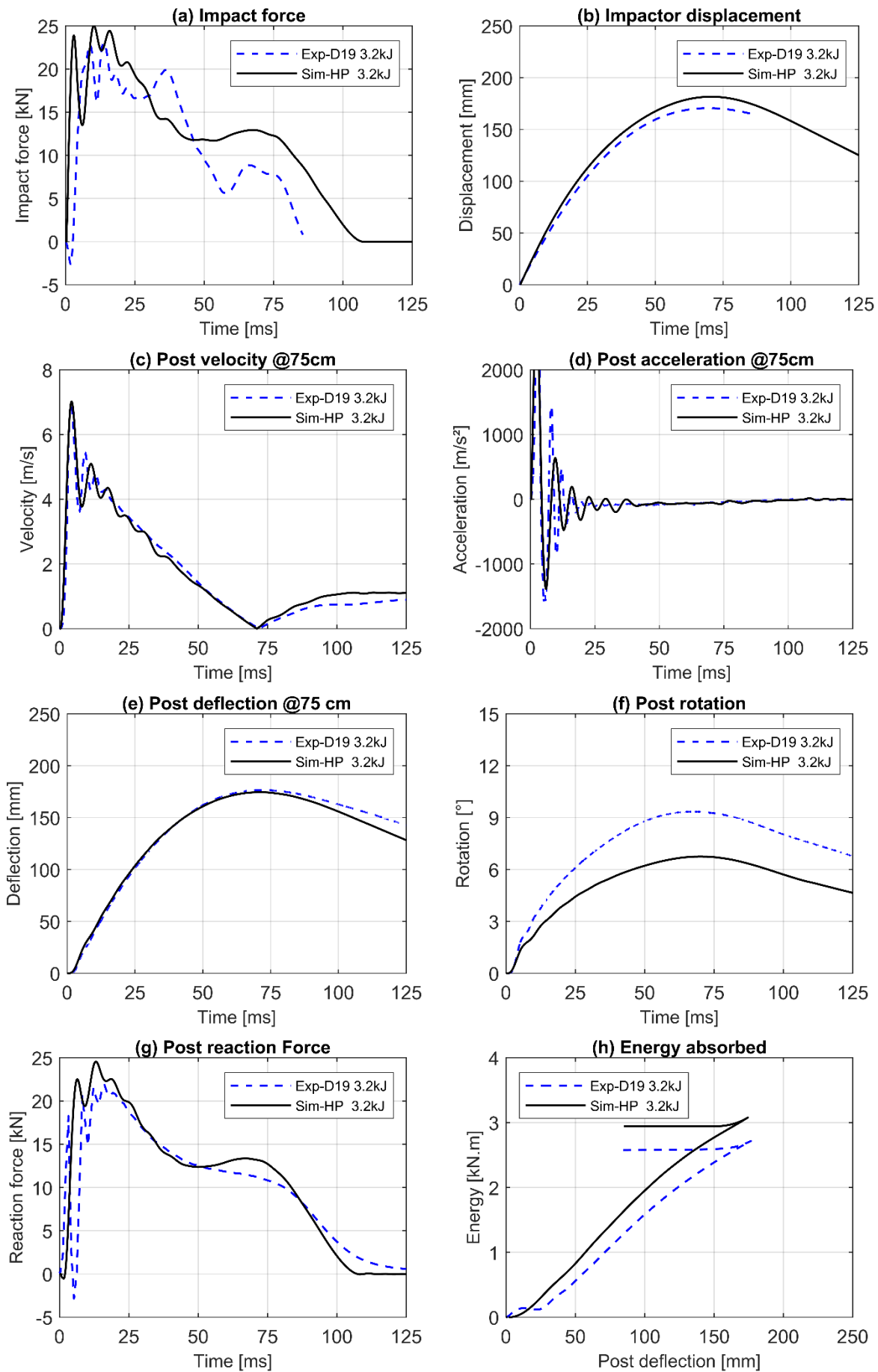


Fig. 5-20: Simulation results of the dynamic impact test under an impact energy of 3.2 kJ

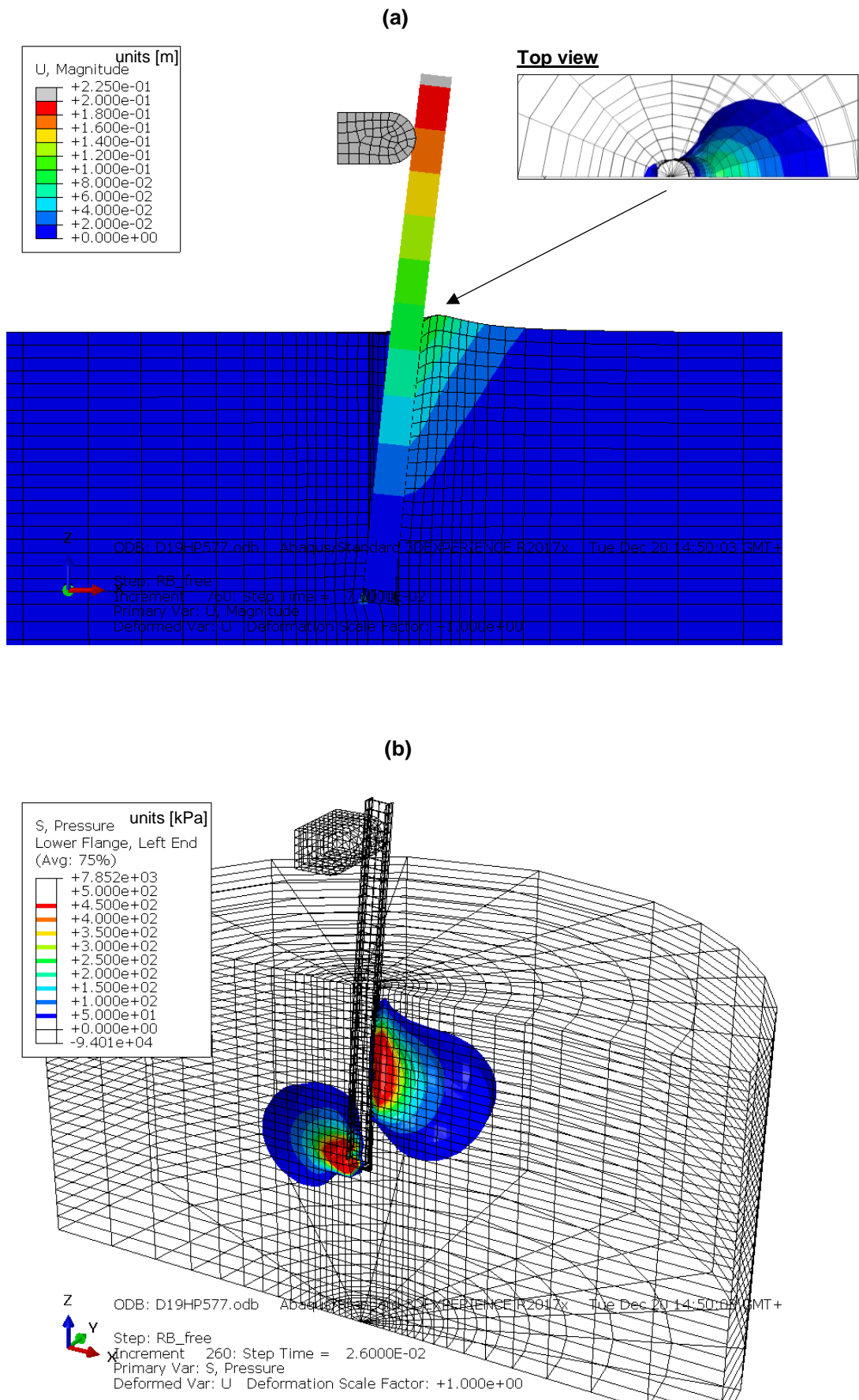


Fig. 5-21: Results of the reference dynamic test simulation in the strong axis (a) soil deformation contours at the maximum deflection (b) mean pressure distribution at maximum reaction force

The deformed contour of the post and soil block at the maximum deflection is shown in Fig. 5-21a. The post rotates during the impact as a rigid body, and no yielding of the post occurs. The rotation point travels from 20 cm to 65 cm under ground level during impact. The soil heaves during impact up to 7 cm in front of the post in the vicinity of 55 cm length and 50 cm width. This coincides with the experimental observations. However, in the field test, a handful mass of grains was catapulted away from the post, which cannot be simulated by continuum elements. The mean pressure distribution along the post at the point of maximum force is shown in Fig. 5-21b. Compared to the static test, a higher soil pressure is reached with smaller post deflection. However, the vicinity where the stress increases is approximately the same as in the static test. The stress bulb of mean pressure extends to a maximum of 77 cm in front of the post and 64 cm behind the post, with a width of 70 cm. In the simulation, the depth of the soil reaction in front of the post was found to move deeper (from 20 cm to 55 cm under ground level) as the post deflection increased. Due to the large strains in the upper soil layer, the material dilates and reaches the limit state. Therefore, the contribution of the upper layer to the soil reaction is negligible at large deflections.

Analogue to the static test simulation, the octahedral shear strain γ_{oct} induced in the soil continuum was evaluated from the FEA. The shear strain contours evaluated at the maximum reaction force F_{max} and the maximum post deflection u_{max} show the evolution of the influence zone around the post during loading (see Fig. 5-22). By defining a lower bound for the shear strain of $\gamma = 10^{-5}$, the contours show values in the influence zone reaching up to $\gamma = 5 * 10^{-1}$. This indicates that the shear strains in the elements resisting the post deflection lie in the range of large deformations. Consequently, the shear modulus governing the soil behaviour at these time points is lower than the maximum shear modulus $G < G_{max}$.

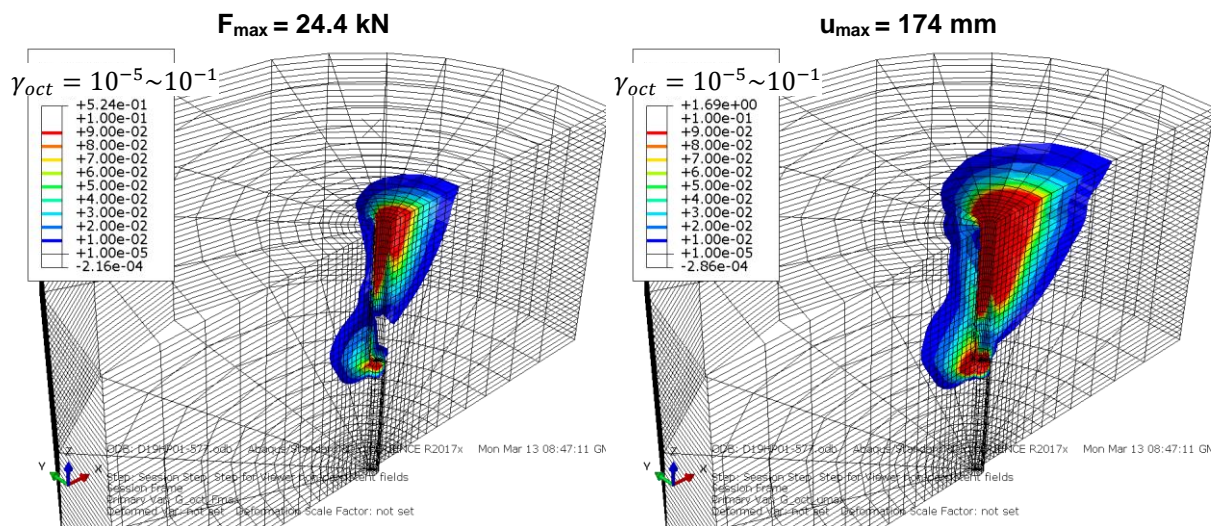


Fig. 5-22: Shear strain contours in the post vicinity evaluated at the maximum reaction force F_{max} and the maximum post deflection u_{max}

In the next step, the velocity of the impactor was varied in three models to simulate the impact intensities applied in the field tests ($v_{imp} = 7.69, 9.23$ and 10.48 m/s, corresponding to $E_{imp} = 5.7, 8.2$ and 10.5 kJ). All other system properties were kept unchanged. The simulation results are shown in Fig. 5-23 and Fig. 5-25. The maximum impact force increases in the first 25 ms in all simulations due to the inertial effects. Then, the force decreases and runs along the same value of ca. 90% of the maximum quasi-static reaction force. The simulations fail to converge and abort after reaching this time point.

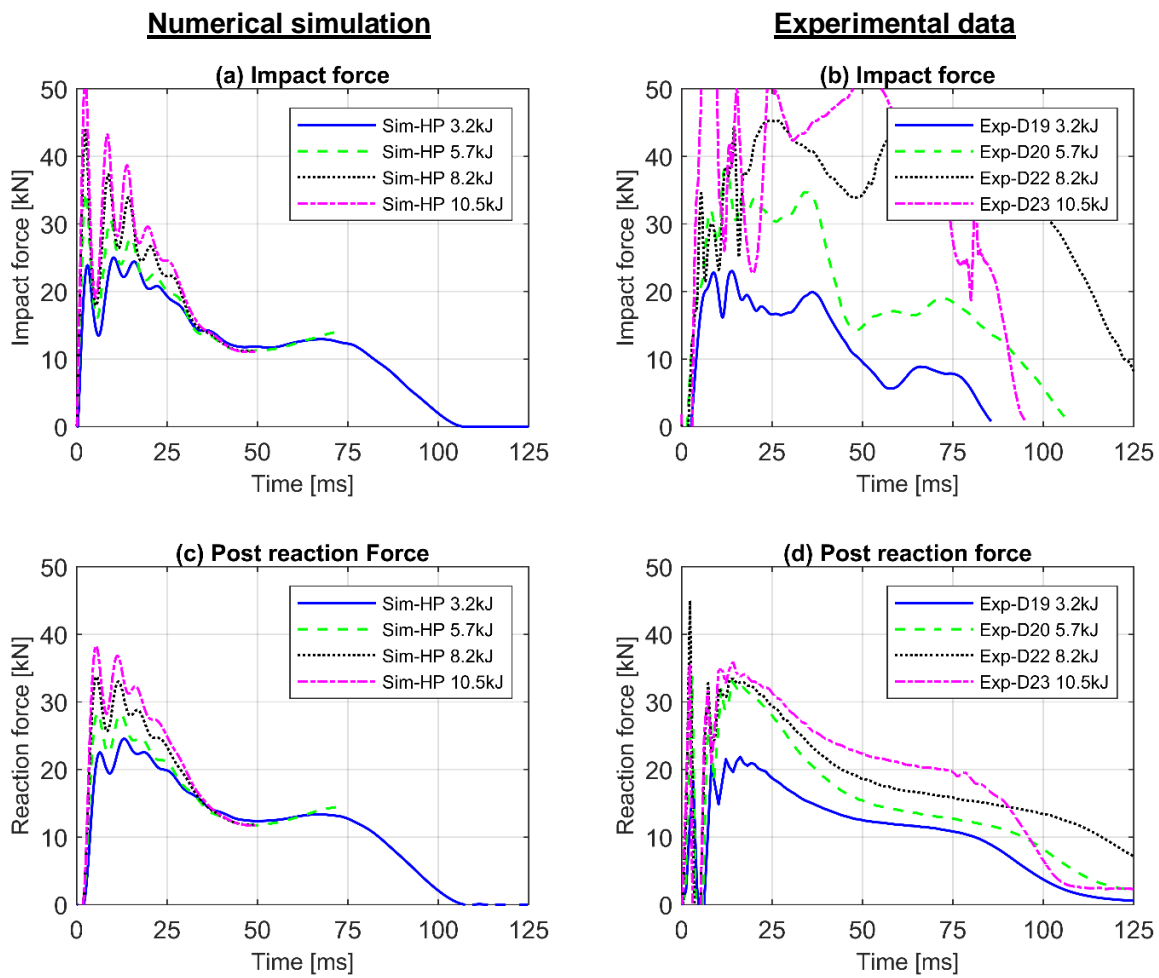


Fig. 5-23: Comparison of the simulated forces in the dynamic impact test (left) to the experimental data at different impact intensities (right)

(a) Sim-HP 8.2 kJ

(b) Sim-HP 10.5 kJ

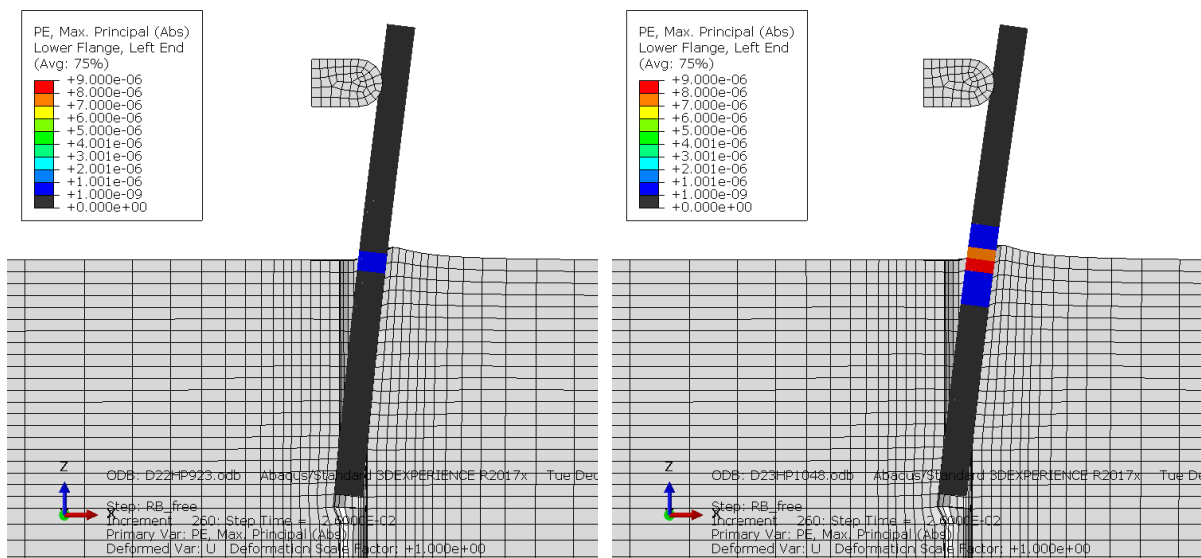


Fig. 5-24: Yielding of the post section and formation of a plastic hinge at the maximum force (a) simulation impact 8.2 kJ (b) simulation impact 10.5 kJ

The velocity-time histories exhibit the same characteristic with a linear deceleration after the first 20 ms, which coincides with the field test measurements. The load-deflection curves agree with the experimental data when comparing the maximum force and trend after the peak. The

simulations confirm the experimental observations, stating that increasing the impact intensity beyond the ultimate soil resistance does not lead to a further increase in the post reaction force. The simulations with 8.2 and 10.5 kJ show nearly the same reaction force. Since the simulations aborted before the end of impact, the maximum deflection could not be evaluated. The higher impact levels simulations at 8.2 and 10.5 kJ show a slight plastic deformation of the post at 5 to 10 cm under ground level (see Fig. 5-24). These observations coincide with the field test observations, as the extracted posts were slightly curved. The stress bulb of mean pressure extends in front of the post to maximum 80, 94 and 104 cm for the impact intensities 5.7, 8.2 and 10.5 kJ, respectively. Which indicates the contribution of a larger soil mass to the inertial effects.

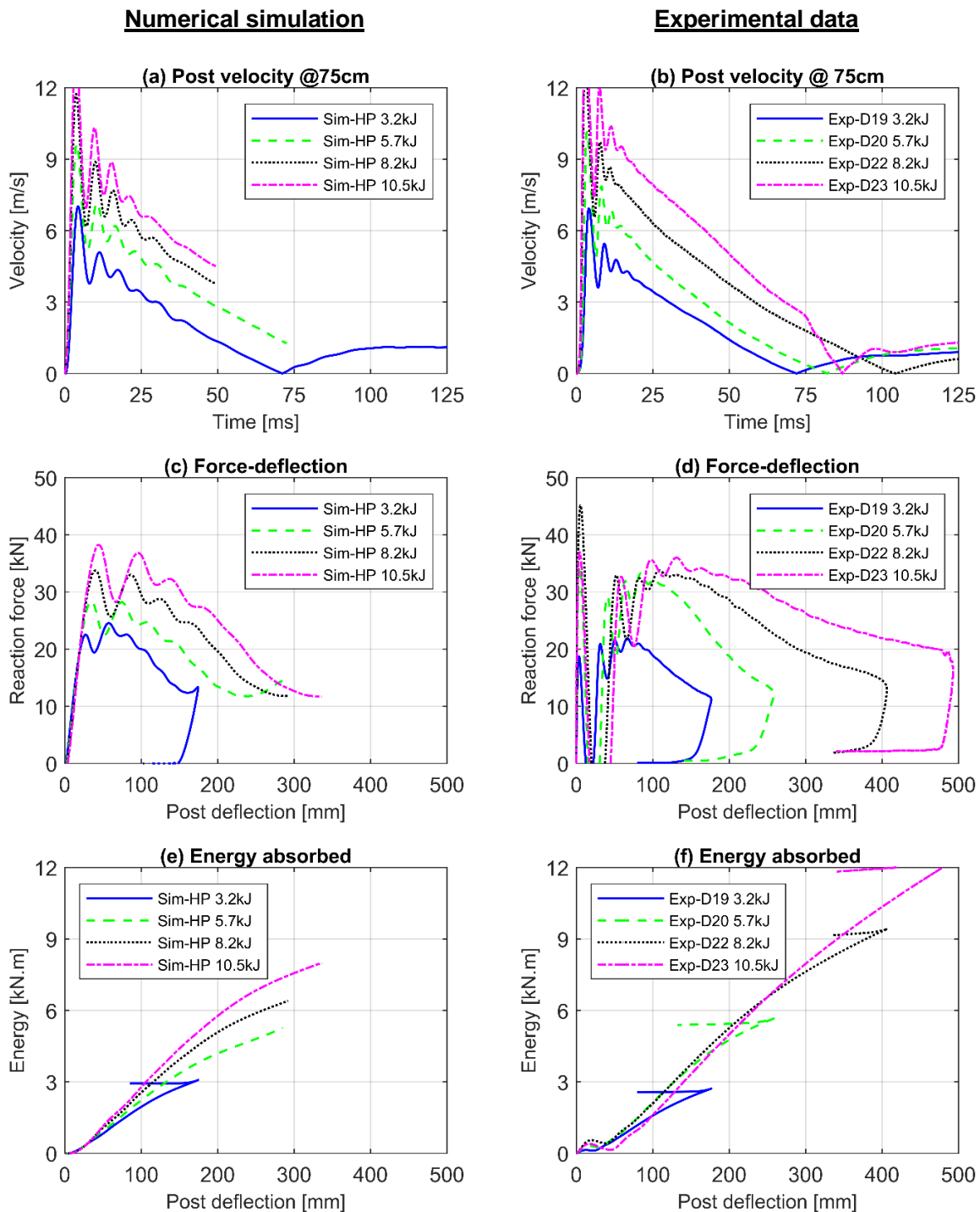


Fig. 5-25: Comparison of (left column) the simulation results of the dynamic impact test to (right column) the experimental data at different impact intensities

Influence of model boundary extent

Generally, in dynamic problems, a quiet boundary condition is defined to simulate the energy dissipation due to wave propagation in unbounded domains, e.g. soil medium. This approach is commonly applied in seismic analysis to prevent the applied waves, i.e. energy, from being trapped inside the model. Another approach to prevent the reflection of the waves propagating outwards from the excitation source can be increasing the extent of the modelled medium. The medium dimensions are chosen to be large enough so that the reflecting waves do not interfere with the studied zone of interest.

These approaches are applied basically in problems where the soil is defined as an elastic medium or the applied dynamic excitation is not expected to induce large deformations, i.e. plastic strains in the medium. The boundary value problem of the guardrail post under impact loading involves relatively large deformations compared to the conventional dynamic analysis under harmonic loading. This leads to more energy dissipation in the deformation of the soil and post rather than in the wave propagation.

The quiet model boundaries can be modelled in the FE code ABAQUS using infinite elements defined as an additional non-reflecting layer around the soil block. However, the infinite elements are only silent for shear and compression waves in an elastic space [1], but not for surface waves or a non-linear half-space [1]. In ABAQUS, the neighbouring finite elements must be assigned the same material behaviour. Since the soil is modelled here using a non-linear user-defined model, the application of infinite elements boundary is technically not an alternative to avoid wave reflections. Moreover, it adds complexity to the model and does not necessarily contribute to the result's accuracy.

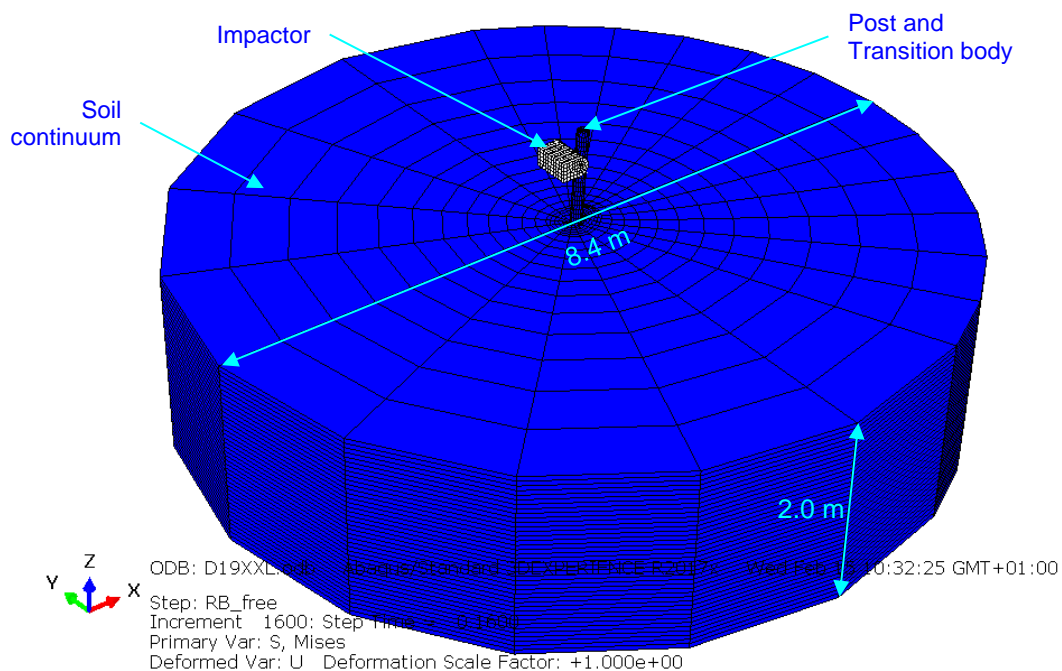


Fig. 5-26: Geometry of the dynamic test model used for examining the Influence of the model boundary extent

To examine the influence of the model boundary extent on the simulated results, the FE model for the impact test 3.2 kJ was simulated using a larger soil domain. The diameter of the soil block is doubled to 8.4 m (see Fig. 5-26). The mesh discretization is kept unchanged in the inner zone of 52 cm around the post.

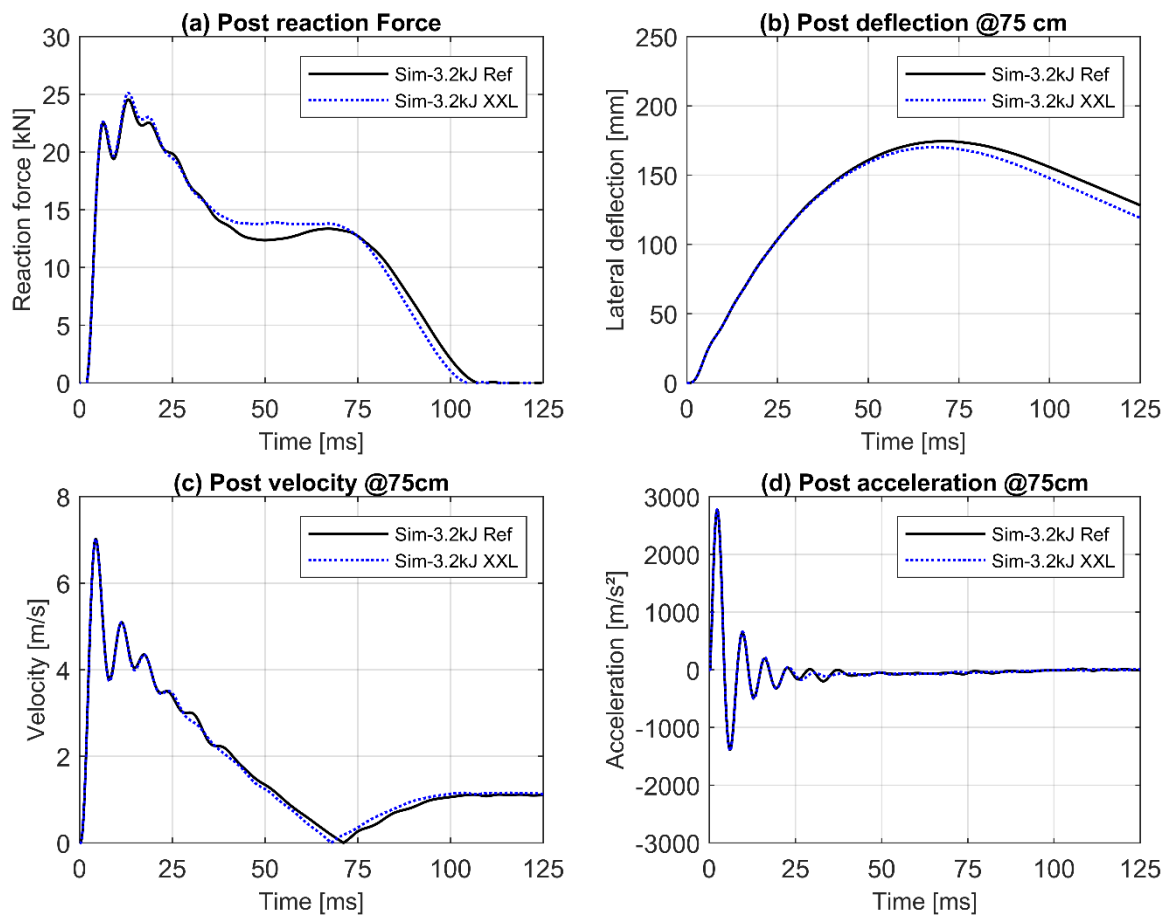


Fig. 5-27: Simulation of the impact test 3.2 kJ using a larger model exhibiting double the soil block diameter, (black) reference model (blue) larger model

The effect of the model extents is evaluated by comparing the parameters of interest, namely, maximum reaction force, post velocity, and deflection, to the reference model results. The simulated maximum reaction force shows a minor deviation of 1.5%. The plateau at 50 ms shows a maximum deviation of 1 kN. The post velocity and acceleration time histories are nearly coinciding. The recoil time point is shifted by -3 ms. The post deflection curve is coinciding with the reference model curve up to the maximum deflection, afterwards an increasing deviation of maximum 1 cm is observed.

Further, the velocity of selected soil nodes is evaluated to quantify the influence of the wave reflection at the boundary on the soil motion. The soil nodes are selected at 5 cm below ground level at the distances shown in Fig. 5-28a. The soil velocity beyond a distance of 1.1 m away from the post is less than 0.1 m/s. The velocity time history from the large model, as well as the reference model, show practically no effects of wave reflection in the post vicinity (see Fig. 5-28b and Fig. 5-28c). The maximum velocity in the soil continuum (2.02 m/s) is reached at the beginning of loading at 5 to 20 ms and then diminishes rapidly till the time point of post recoil. The velocity at the lateral boundary of the large and reference model are 0.02 and 0.07 m/s, respectively.

(a) Contours of the maximum soil velocity

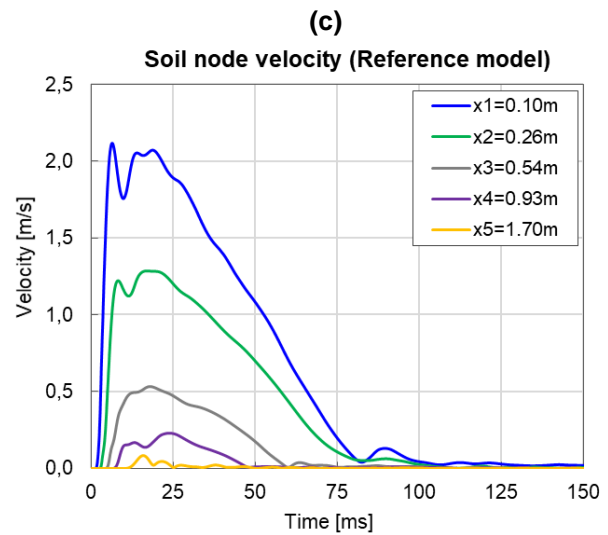
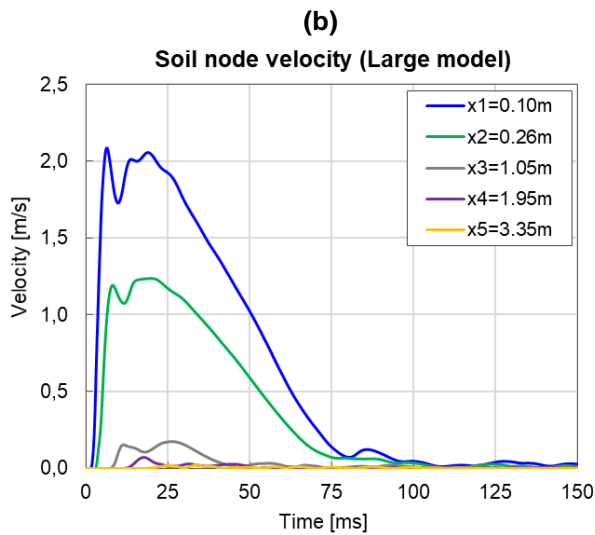
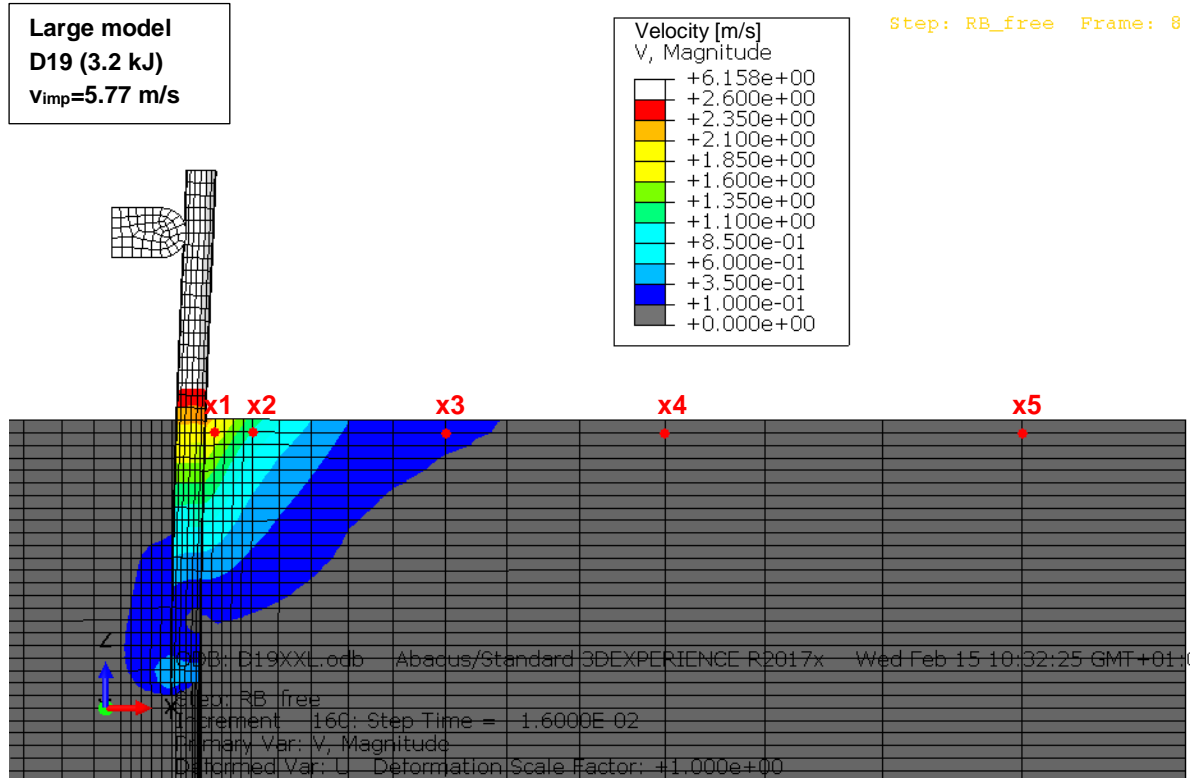


Fig. 5-28: Comparison of the velocity of selected nodes in the soil continuum in the large and the reference FE models

The results show that the chosen model dimensions are adequate to simulate the post response under impact loading without additional quiet boundaries. The influence of wave reflections at the boundaries on the post response and soil motion in the vicinity of the post can be neglected.

5.4 Simulations using an elastoplastic soil model

In order to test the suitability of a common simple material model for simulating the loading tests, further simulations were carried out using an elastoplastic material model with a Mohr-Coulomb failure criterion. In contrast to the simulations with the hypoplastic model and due to the formulation of the material model without explicit consideration of the soil state conditions during loading, the material parameters must be adjusted depending on the initial state and the state changes. Since the in-situ soil, in which the loading tests were performed, exhibited a relative density of $I_D = 0.8$, the material parameters from the laboratory tests (very dense $I_D \approx 0.95$ and loose $I_D \approx 0.32$) could not be used directly to simulate the loading test.

Therefore, two sets of soil parameters were calibrated for the aforementioned laboratory specimens. The shear strength parameters φ' and c' were determined from the drained triaxial shear tests conducted on three specimens with different consolidation stresses 50, 100 and 200 kPa. Based on the results of the conducted oedometer tests, the initial stiffness modulus could be evaluated at different vertical stress values. The initial stiffness profile over depth was implemented using the power function after OHDE 1939, calibrated with the oedometer test results at higher stresses:

$$E_s = v \cdot \sigma_{at} \left(\frac{\sigma_z}{\sigma_{at}} \right)^\omega \quad \text{Equ. 5-10}$$

where; v and ω are the material dependent OHDE constants defining the initial shape of the increase of stiffness with the effective overburden stress σ_z . The atmospheric reference pressure is assumed $\sigma_{at} = 100 \text{ kPa}$. The stress-dependency of the stiffness modulus during loading cannot be considered in this material model formulation. The determined parameter sets are listed in Table 5-3.

Table 5-3: Material parameters of the elastoplastic Mohr-Coulomb soil model for the KSS032

Description	Parameter		v. dense specimen	loose specimen	in-situ (calibrated)
Peak friction angle	φ_p'	[°]	50.4	42.5	53.5
Dilatancy angle	ψ	[°]	17.0	15.4	2.0
Cohesion	c'	[kPa]	54.9	33.9	0.1
Poisson's ratio	ν	[-]	0.35	0.35	0.35
Stiffness modulus	E_s^*	[MPa]	1.5 - 16.0	1.4 - 13.7	7.6 - 80.1
Stiffness modulus ratio	$E_s / E_{s_{v,dense}}$	[-]	1.0	0.9	5.0

*Stiffness modulus range over the post embedment depth 5 to 100 cm below ground level

The calibrated parameter sets (very dense and loose) were then used to simulate the quasi-static loading test. The force-deflection curves of the post were compared to the experimental results (see Fig. 5-29). The results of simulations with both parameter sets (curves 3 and 4) show an almost linear increase of the reaction force up to 26 kN without reaching the limit state, which does not represent the behaviour of the post in the field test. In the case of the very dense specimen parameters, a plastic hinge is developed at a depth of 0.2 m below ground level at 20 cm lateral deflection. In the case of the loose specimen parameters, a plastic

hinge was formed in the same depth at 32 cm lateral deflection. These results do not agree with the field test observations, since no plastic deformations of the post cross-section occurred in the quasi-static reference test (see 3.2 *Static loading tests*). These results conclude that the soil's strength is considerably overestimated with the applied approach for parameter calibration.

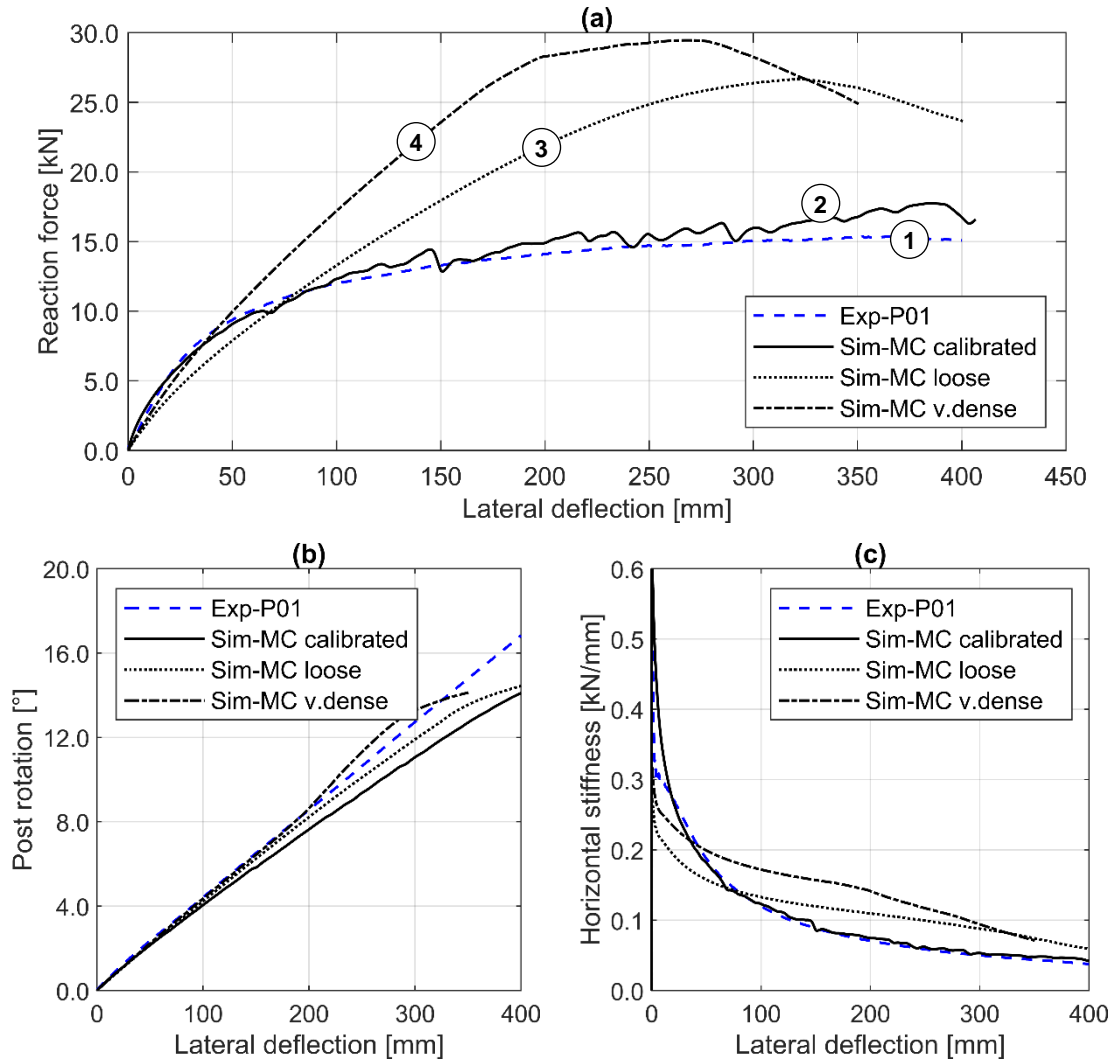


Fig. 5-29: Simulation results of the quasi-static reference test using an elastoplastic soil model

LADE [47] investigated the linear Mohr-Coulomb failure envelope for the determination of the soil shear strength parameters in shallow depths. He concluded that the failure envelope in the low-stress range is concave rather than linear. At higher stress levels, the failure envelope is observed to become convex and straighten out to become linear with a constant slope. The common method of applying a linear failure envelope over the whole stress range results in an overestimated intercept, i.e. cohesion, especially for granular soils. Which leads to an overestimation of the shear strength at low mean stress levels.

Based on these findings, a curved failure envelope described by the power function proposed by LADE was fitted to the triaxial test data from the very dense and loose specimens as follows:

$$\tau = a \cdot p_{ref} \cdot \left(\frac{\sigma + d \cdot p_{ref}}{p_{ref}} \right)^b \tag{Equ. 5-11}$$

where; a , b and d are dimensionless fitting constants and $p_{ref} = 100 \text{ kPa}$ atmospheric pressure. The fitted failure envelope for each state is shown in Fig. 5-30.

The shear strength was then calculated at an effective stress of $\sigma = 20 \text{ kPa}$, corresponding to the overburden pressure at the post-toe. Assuming nil cohesion by applying $d = 0$, the peak friction angle was calculated for each specimen. The peak friction angle was then interpolated for the in-situ relative density of 80% and was found $\varphi_p = 54.7^\circ$ (see Table 5-4).

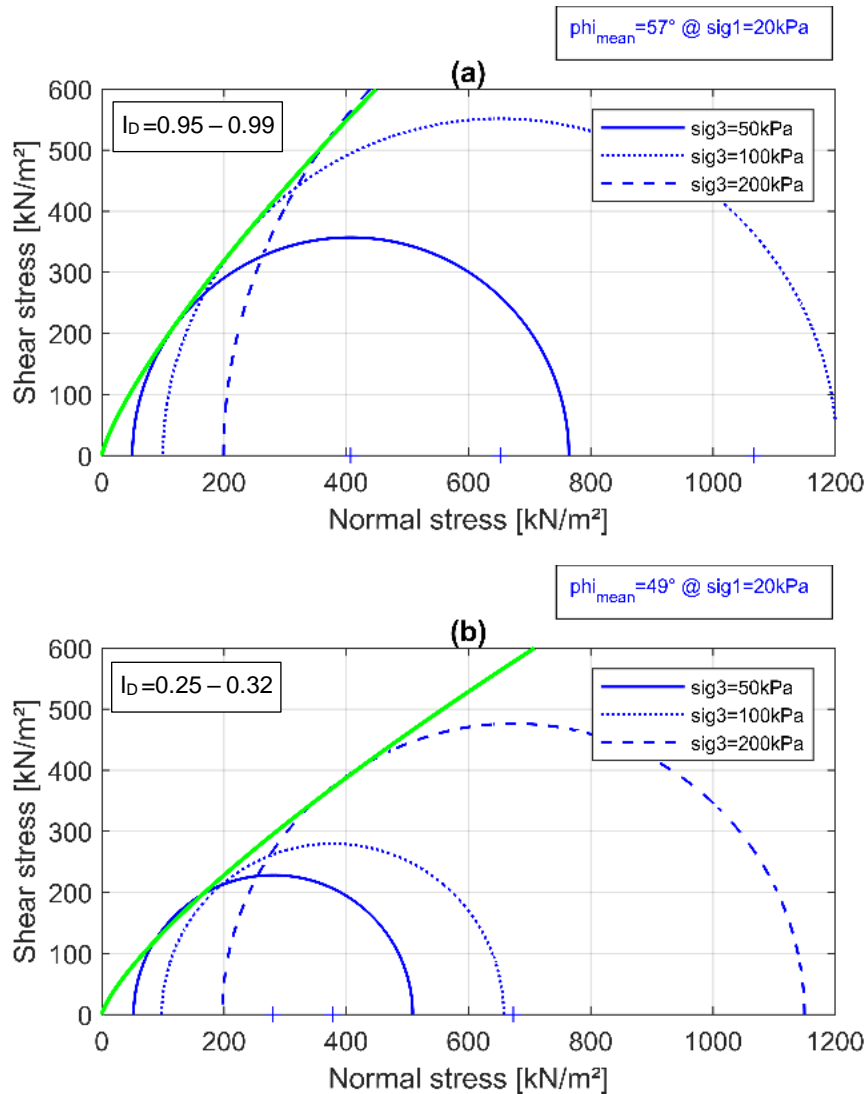


Fig. 5-30: Curved failure envelope fitted to the triaxial compression tests conducted on KSS032 (a) very dense specimens (b) loose specimens

BOLTON [7] discussed the correlation between the peak friction angle φ_p , the critical state friction angle φ_c , the relative soil density and the effective stress. He derived the following relationship based on an extensive experimental testing program on granular materials:

$$\varphi_p' = \varphi_c + \Delta\varphi \cdot I_D \left[Q - \ln \frac{p'}{p_{ref}} \right] - R \quad \text{Equ. 5-12}$$

where; $\Delta\varphi = 3^\circ$ is a constant, I_D is the relative density, Q and R are material grain type dependent factors, p' is the mean stress at failure. This approach was applied to determine φ_p of the KSS032 at the in-situ relative density of 80% and an average overburden pressure of 20 kPa.

First, the factors Q and R were calibrated using the triaxial test data from the very dense and loose specimens and were estimated to $Q = 14$ and $R = 3^\circ$, respectively. With $\varphi_c = 35.7^\circ$ and assuming no cohesion for the granular material, the peak friction angle was calculated to $\varphi_p = 53.3^\circ$. It is worth mentioning that the estimated peak friction angle is sensitive to the constants used for the curve fitting and the factors calibrated for the grain type.

Table 5-4: Peak friction angle interpreted for KSS032 under a normal stress of 20 kPa

Dry density ρ_d [t/m ³]	Relative density I_D [%]			Peak friction angle* φ_p [°]
2.20	99.8	very dense	specimen	57 (58)
1.80	26.4	loose	specimen	49 (41)
2.07	80.0	dense	in-situ	55 (53)

* φ_p determined as per LADE 2016, and the corresponding value (in brackets) determined as per BOLTON 1986.

For the simulations, a mean value for the peak friction angle from both approaches of $\varphi_p = 53.5^\circ$ was applied, and an apparent cohesion of 0.1 kPa was considered for numerical stability. The dilatancy angle was chosen through a parametric study to $\psi=2.0$, as lower values have led to early abort of the simulation. The value of the stiffness modulus E_s was also estimated through a parametric study. It was found that E_s had to be increased by a factor 5 compared to that of the very dense oedometer specimen ($I_D = 98\%$). This is attributed to the fact that the stiffness of the soil is stress-dependent, and the stresses in the near-field of the post increased significantly compared to the initial stresses during the loading test. The simulation results using the calibrated parameters are shown in Fig. 5-29 curve 2.

In the next step, the validated model for dynamic impact loading was used in conjunction with the elastoplastic soil model. The parameters listed in Table 5-3 (last column) were applied for the simulation. The post was simulated under the same impact energy levels applied in the reference field tests $E_{imp} = 3.2, 5.7$ and 8.2 kJ. The results are shown in Fig. 5-31 in the left column. Compared to the experimental measurements (see 3.3 *Dynamic loading tests*), the maximum post reaction force is underestimated by 15 to 20%. The maximum post deflection at the loading point is in the range of the measured experimental measurements $\pm 5\%$. The force deflection curves are relatively flat with a significant increase of the reaction force before recoil.

To fit the simulation results to the experimental data, the stiffness of the soil material had to be increased by a factor of 2. All other parameters were kept unchanged. The simulation results are presented in Fig. 5-31 in the right column.

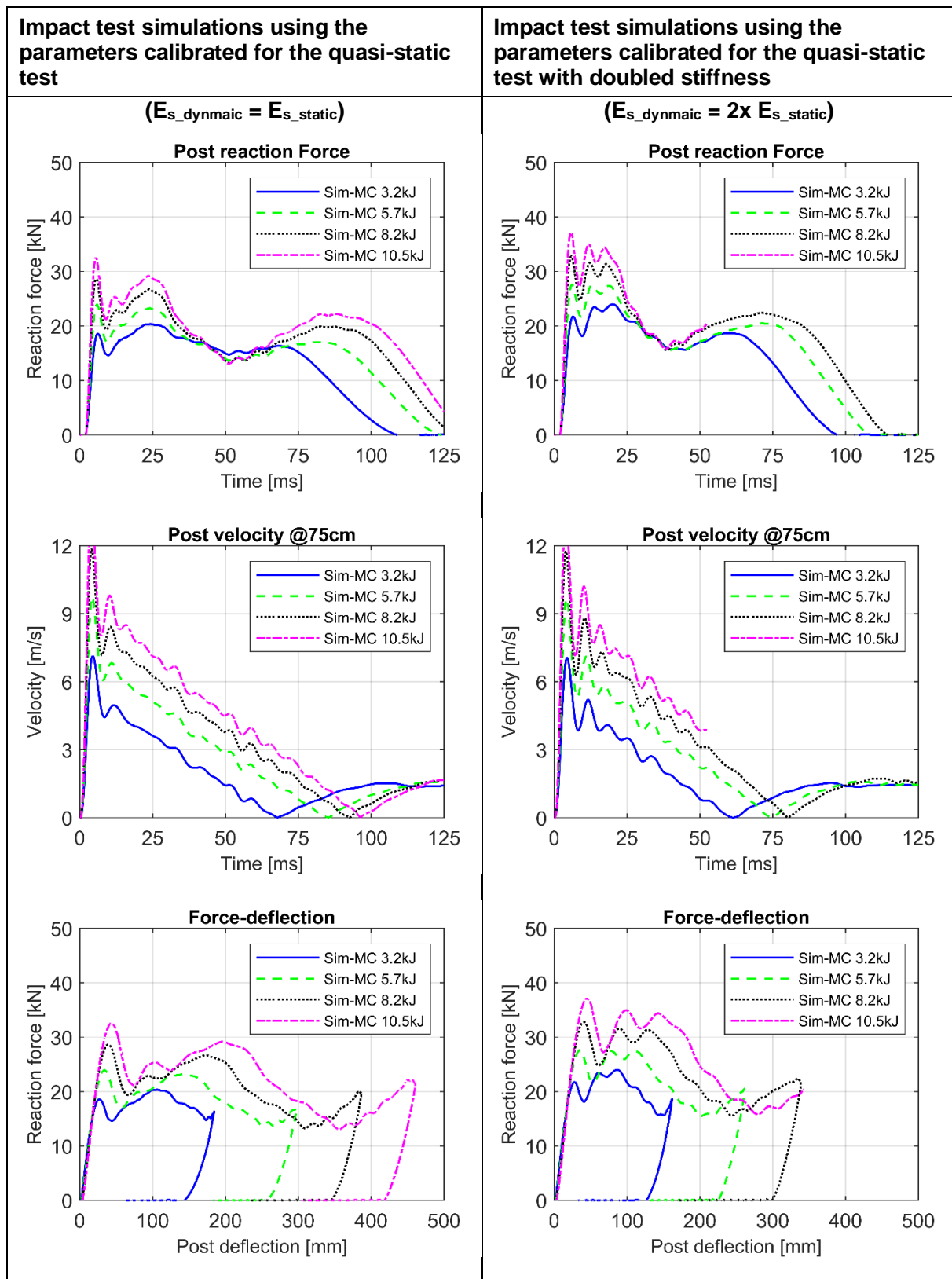


Fig. 5-31: Influence of the stiffness on the simulated post response under different impact energy levels

The force-time history curves show an increase in the reaction force and a decrease in the impact duration due to doubling the soil stiffness. The simulated reaction force matches the measured experimental reaction force. However, the increased stiffness reduces the post deflection by ca. 10 to 15%. The force-deflection curve characteristic is closer to the

experimental data. The post velocity-time history is approximately linear up to the recoil time point in both simulations, with higher oscillations in case of higher stiffness.

The hypoplastic model and an elastic-ideal plastic model were utilised to simulate the guardrail post response by means of FEA. The hypoplastic model exhibits a major practical advantage regarding estimating the model parameters. Using one parameter set calibrated to laboratory soil tests, the post behaviour could be simulated under quasi-static and impact loading with acceptable accuracy. Moreover, the calibrated parameter set can be applied for simulations using the same material with a different relative density.

In contrast, the elastic-ideal plastic model had to be customized with much effort to deliver comparable results. First, the parameters could not be determined directly from conducted laboratory tests. The parameters for the quasi-static simulation could only be determined by a laborious procedure comprising curve fitting and calibration to the quasi-static field test data. The stress level, in which the parameters are determined, significantly affects the results. The parameters calibrated for the quasi-static test failed to simulate the post response under dynamic impact loading without additional customization. An adjustment factor is required to fit the stiffness modulus to compensate for the absent stress-dependency of the soil stiffness in the model.

5.5 Parametric study

In this section, the finite element method is applied to analyse the influence of different parameters on the response of a single post under quasi-static and impact loading. A systematic investigation of the behaviour of the system is conducted under variation of selected parameters. This study aims to gain insight into how the system behaves under different conditions and identify the optimal parameter combination for a given set of performance criteria. The simulation results are used to understand the relationships between the soil and post parameters and to determine the factors governing the soil-post interaction. The parameters investigated in this study are summarised in Table 5-5.

In general, the performance of a process or a system is influenced by two types of factors: controllable and uncontrollable variables, as defined by MONTGOMERY [57] for the design and analysis of experiments. The purpose of an experimental program or a parametric study is to determine the most influential controllable variables on the system performance. Then, the domain of the controllable variables that fulfils the required performance is determined. The uncontrollable variables are investigated to determine their range, which minimises the deviation from the optimum system performance.

Table 5-5: Influence factors investigated in the systematic parametric study

Parameter		Steps	Quasi-static loading	Dynamic impact loading
Soil relative density	$I_D [-]$	0.3, 0.6, 0.8, 0.85, 0.9, 0.95, 0.99	Lateral deflection up to 400 mm	2.5 kJ, 5.0 kJ, 10.0 kJ
Soil Layering	$d [m]$	Loose layer (0.2 m steps from top)	Lateral deflection up to 400 mm	-
	$d [m]$	Very dense layer (0.2 m steps from top)	Lateral deflection up to 400 mm	-
Embedment length	$t [m]$	0.70, 0.80, 0.90, 1.00, 1.10, 1.20	Lateral deflection up to 400 mm	2.5 kJ, 5.0 kJ, 10.0 kJ
Loading height	$h [m]$	0.40, 0.55, 0.65, 0.75, 0.85, 0.90	Lateral deflection up to 400 mm	2.5 kJ, 5.0 kJ, 10.0 kJ
Section modulus	$W [cm^3]$	20.0 (IPE80), 34.0 (IPE100), 53.0 (IPE120), 77.3 (IPE140), 109.0 (IPE160)	Lateral deflection up to 400 mm	2.5 kJ, 5.0 kJ, 10.0 kJ
Post-section	$[-]$	IPE120, C125, HEB120	Lateral deflection up to 400 mm	-

Applying this concept on the investigation of the single guardrail post performance, the study aspects can be described as follows. The controllable variables are the post properties (embedment length, section geometry, section modulus and steel grade) and the soil properties (material type and relative density). These represent the design parameters of the system. The VRS design parameters, including the post spacing, rails, connectors and anchorage, are excluded when considering the single post. The uncontrollable variables include the vehicle type (mass and impact height), the impact angle, the vehicle deformability (defining the per cent of impact energy dissipated in the VRS) and the load distribution between the posts. All these variables can be lumped into the impact energy applied on the post, which is considered here as the input for the system. The system performance can be assessed based on the maximum reaction force, maximum deflection and whether the post material reaches the yield strength. The strategy of experimentation applied is selecting one controllable variable at a time and varying it over its anticipated range, while keeping all other variables constant. The effect of the variation of each variable on the post response is presented. The interaction of selected variables is further examined for some cases.

Variation of soil relative density

The simulation results of the influence of soil relative density on the single post response are presented in this section. The simulations are performed using the reference model, whether static or dynamic, with the reference conditions (IPE120 post, embedded 1.0 m in KSS032, loaded in the strong axis). The soil is modelled using the hypoplastic constitutive relation. In the first series of simulations, the soil block is assumed to exhibit homogenous soil conditions along and below the post embedment length. The soil relative density I_D is varied through the initial void ratio e_0 , which is an input state parameter for the hypoplastic model. The soil unit weight is adjusted and changed subsequently. The varied simulation parameters are listed in Table 5-6.

Table 5-6: Parameters array for the variation of the soil relative density

Simulation	Relative density		Initial void ratio	Dry density	Moist unit weight ⁽¹⁾
	I_D		e_0	ρ_d	γ
	[-]		[-]	[t/m ³]	[kN/m ³]
ID=0.30	0.30	loose	0.507	1.824	18.79
ID=0.60	0.60	med. Dense	0.400	1.963	20.22
ID=0.80 ⁽²⁾	0.80	dense	0.328	2.070	21.32
ID=0.85	0.85	dense - v. dense	0.310	2.099	21.55
ID=0.90	0.90	very dense	0.294	2.125	21.89
ID=0.95	0.95	very dense	0.276	2.155	22.19
ID=0.99	0.99	very dense	0.262	2.179	22.44

(1) assuming a moisture content of 3% as in the field tests

(2) parameters of the reference model Sim-P01_ID=0.80

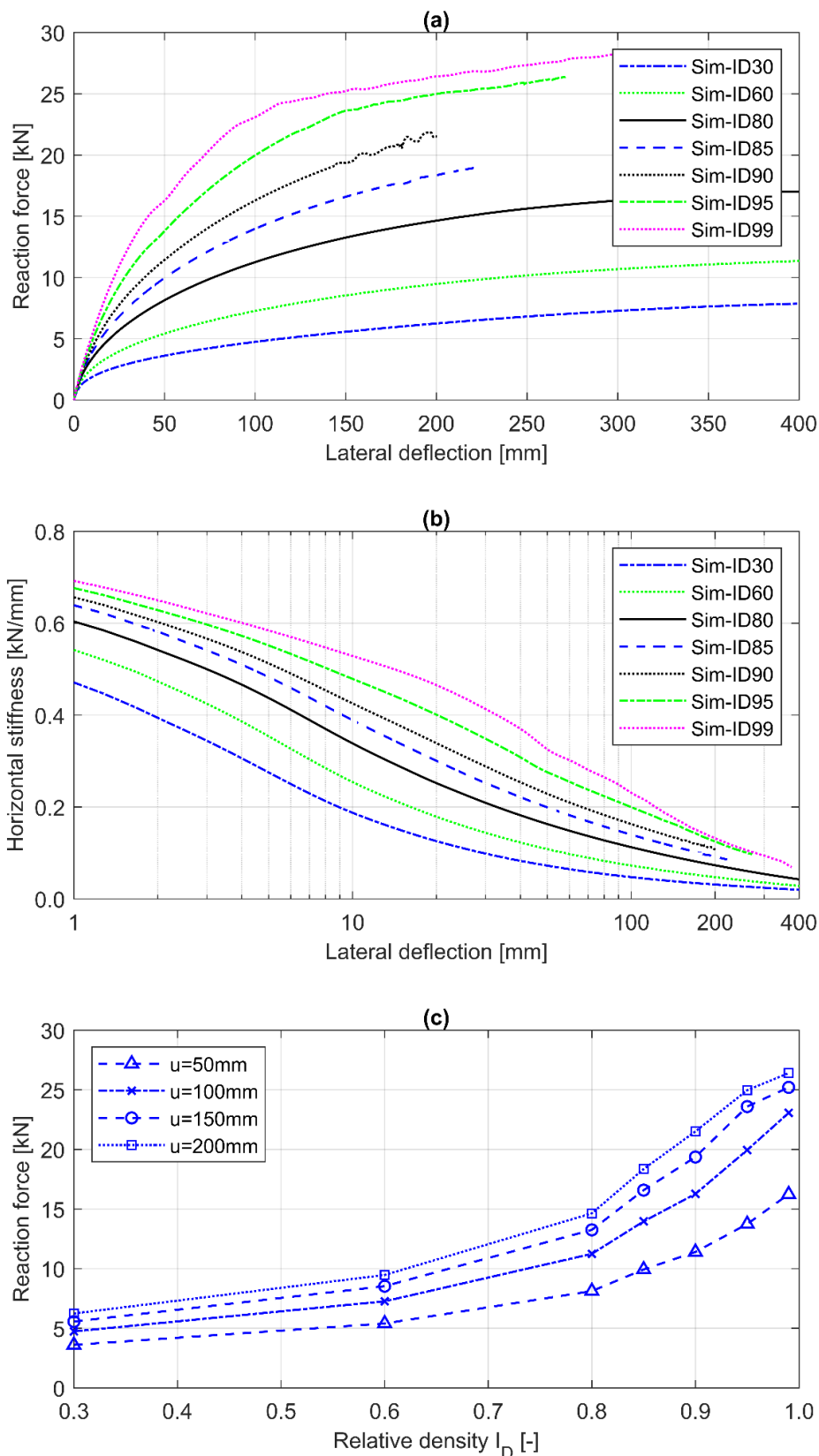


Fig. 5-32: Effect of variation of the relative density on the reaction force under quasi-static loading (a) load-deflection curves (b) system stiffness (c) influence of relative density variation on the reaction force at selected deflection values

The load-deflection curves of the quasi-static simulations evaluated at the loading height of 75 cm are presented in Fig. 5-32a. The reaction force decreases approximately linearly by decreasing the soil relative density below $I_D = 0.80$. A reduction of I_D from 0.80 to 0.30 leads

to a reduction of 50% of the reaction force. In the simulations with $I_D < 0.80$ the post rotates as a rigid body and shows no signs of steel yielding. On the other hand, increasing I_D above 0.80 leads to an increase of the reaction force by a much higher factor. An increase of I_D from 0.80 to 0.95 leads to an increase of 65% of the reaction force. The post section shows yielding at a lateral deflection of 189, 122 and 90 mm for the simulations $I_D = 0.90, 0.95$ and 0.99 , respectively. A plastic hinge is formed at a depth of 0.40 m in the simulation with a relative density $I_D = 0.90$. The plastic hinge is formed at a shallower depth for the higher relative densities (0.35 m for $I_D = 0.95$ and 0.30 m for $I_D = 0.99$). The characteristic of the load-deflection curve at $I_D = 0.99$ and 0.95 can be compared to the experimental field test conducted in the very dense silty gravel GU055 (refer to Fig. 3-33 curve No. 3).

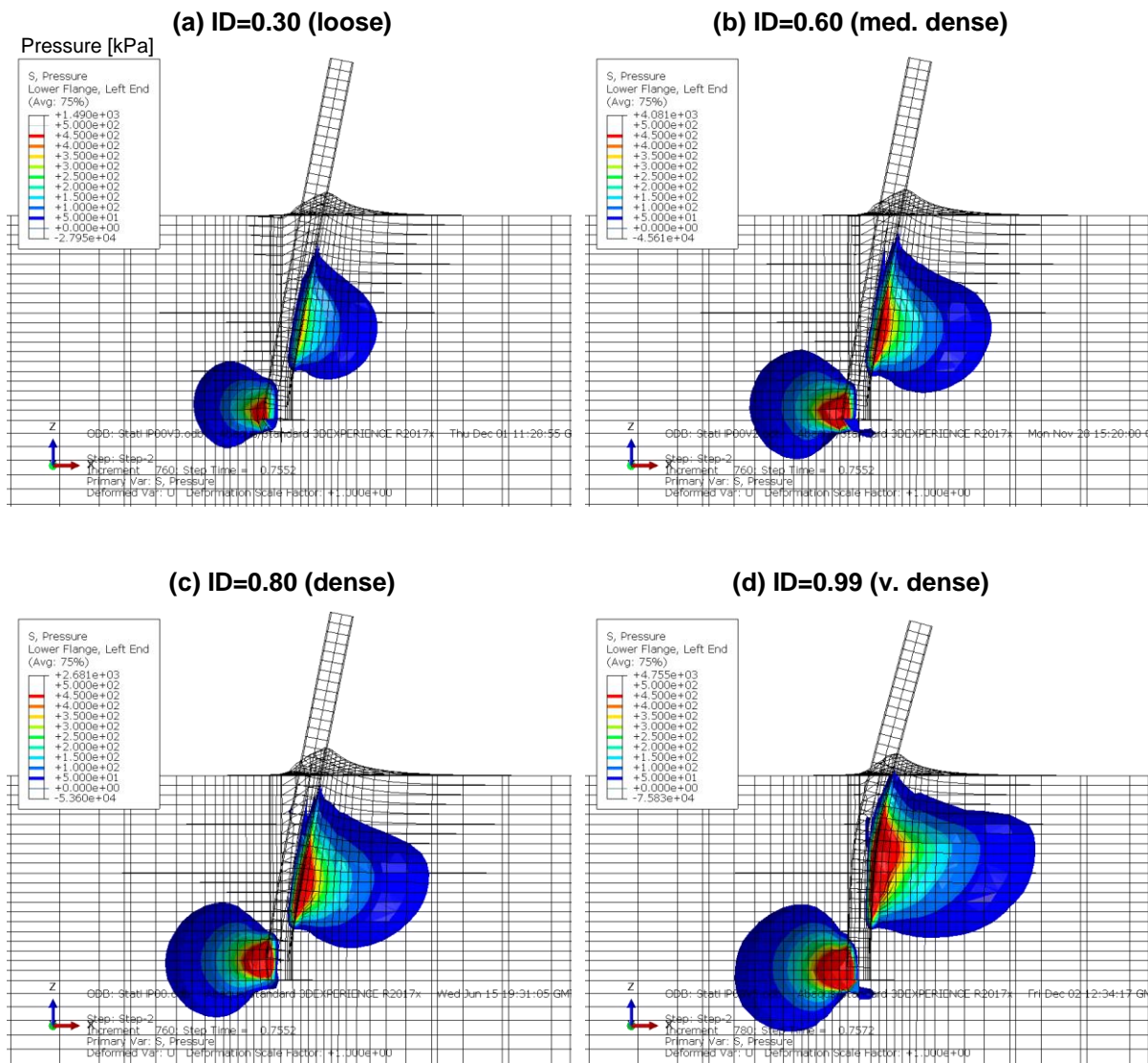


Fig. 5-33: Mean pressure distribution around the post at a deflection of 300 mm under variation of the soil relative density

The load-deflection behaviour can rather be considered bilinear, consisting of two phases. The reaction force increases approximately linearly with a high stiffness until reaching the plastic steel section capacity, and then the system stiffness drops significantly.

Fig. 5-32b presents the development of the horizontal system stiffness with lateral deflection. The horizontal stiffness is evaluated as a secant stiffness modulus equal to the ratio of the difference in the reaction force to the corresponding lateral deflection. For all simulations, the

horizontal stiffness shows a degradation with increasing lateral deflection reaching up to 80% to 90% of the initial value at 200 mm. The comparison of the reaction force variation at deflection values up to 200 mm builds a corridor of a maximum 5% range for $I_D < 0.85$ and a maximum 50% range for denser soils (see Fig. 5-32c). The distribution of the mean pressure around the post evaluated at a deflection of 300 mm is shown in Fig. 5-33. The acting point of the force couple component in front of the post lies shallower for the denser soil (0.60 m for $I_D = 0.30$ and 0.38 m for $I_D = 0.95$). The mean pressure increases in the vicinity of 48, 55 and 90 cm in the simulations $I_D = 0.30$, $I_D = 0.60$ and $I_D = 0.95$, respectively. The soil heaves in front of the post, and a gap is opened at the back along the contact surface.

Further, the relative density variation is simulated under an impact of 2.5 kJ (impactor mass 192 kg and impact velocity 5.1 m/s). The results are shown in Fig. 5-34. Compared to the reference test, the soil's relative density highly affects the load-deflection curve characteristic. For medium dense and loose soils, the post reaches the maximum reaction force at ca. 20 cm deflection, and then drops to the limit state reaction force. The lateral deflection increases without any increase in the reaction force. No signs of yielding were observed for the relative density $I_D \leq 0.85$.

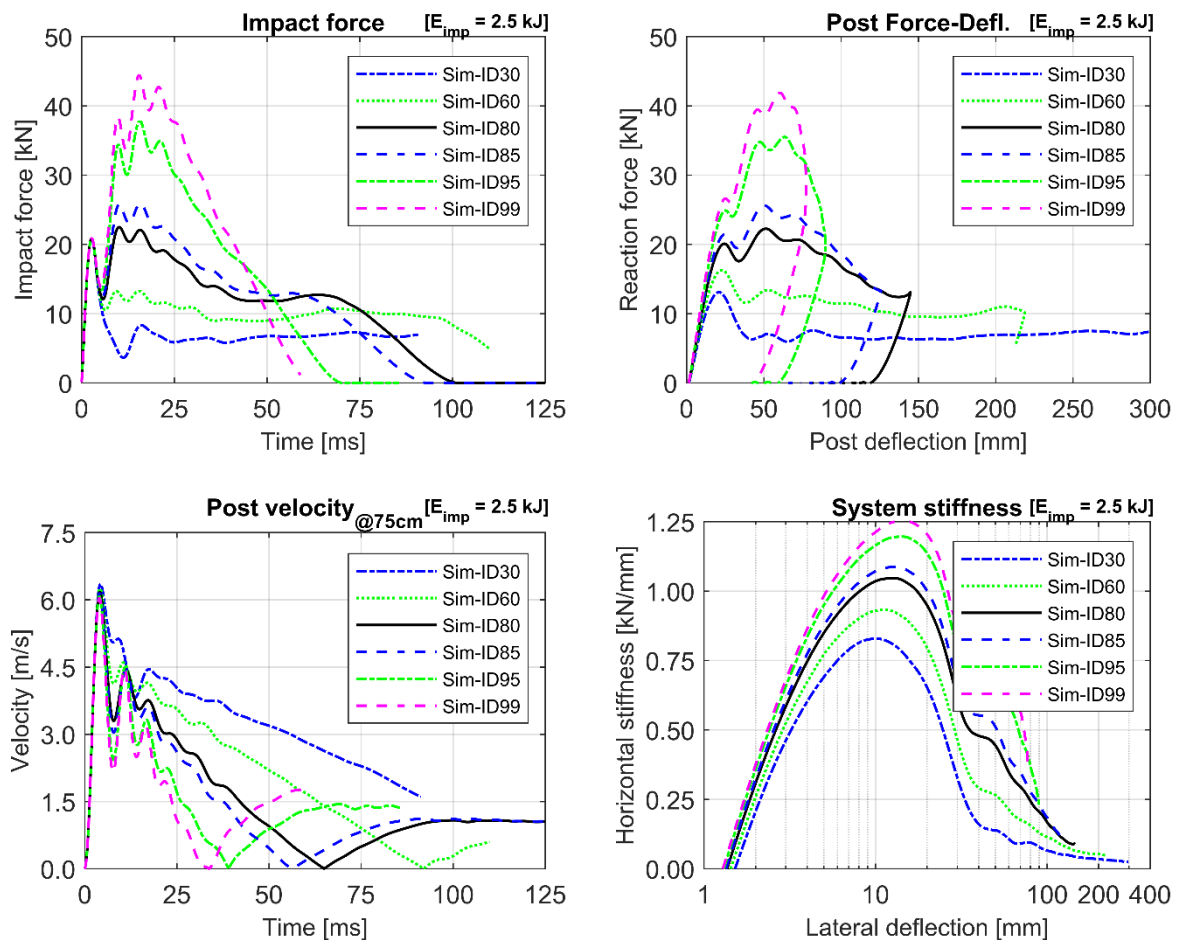


Fig. 5-34: Effect of variation of the relative density on the post response under a dynamic impact of 2.5 kJ

The very dense variation shows yielding of the post at 5 cm below ground level when reaching the maximum reaction force. The reaction force drops abruptly without any further increase (no plateau is formed). This behaviour indicates that the steel section material governs the post response, and the soil acts as a fixation. The maximum horizontal stiffness is reached for

all simulations at 10 to 15 cm lateral deflection. The value ranges between 0.8 and 1.25 kN/mm for the loose and the very dense soil, respectively. The stiffness decreased then significantly to less than 25% of the maximum value at a deflection of 8 cm.

The post velocity-time history shows the influence of the relative density on the deceleration of the colliding body. The denser the soil material, the shorter the required time to stop the colliding body, which means higher deceleration. Comparing the medium dense to the very dense state, the system requires 3-folds the time required to reach the recoil point.

For each relative density variation, the impact energy was increased in additional simulations by a factor 2 and 4. The mass of the impactor is kept constant, and the impact velocity is increased to 7.22 and 10.21 m/s to induce 5.0 kJ and 10.0 kJ, respectively. The influence of the relative density under variation of the impact energy on the post reaction and deflection is shown in Fig. 5-35. The rate of increase of the maximum reaction is approximately linear under $I_D = 0.80$. Afterwards, the force increases with a higher rate up to 5.0 kJ. Due to the relatively early yielding of the post at 10.0 kJ, the rate decreases after $I_D = 0.85$.

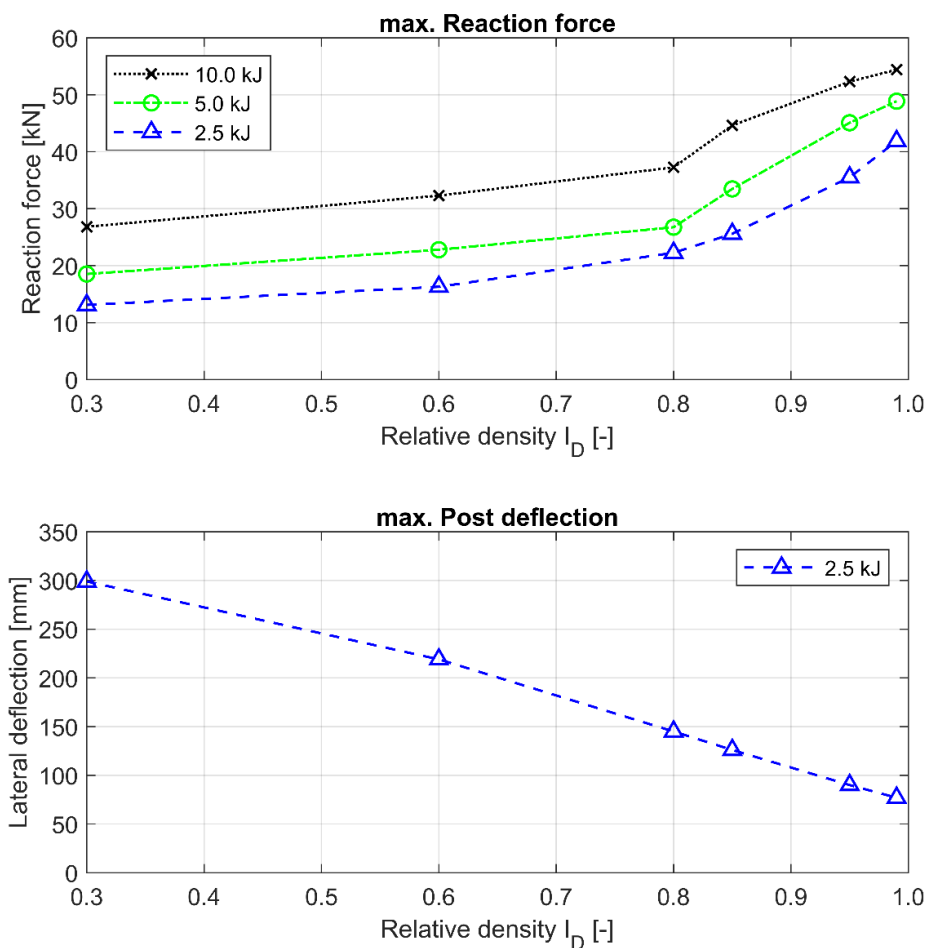


Fig. 5-35: Influence of the relative density on the maximum reaction force and maximum post deflection under impact loading

The maximum post deflection decreases linearly with increasing the relative density at 2.5 kJ. The maximum deflection could not be evaluated for the higher impact energy levels, since the simulations failed to converge shortly after reaching the maximum force.

Effect of Layering: Loose layer

Additional simulations have been conducted to investigate the influence of soil layering on the post-response. The effect of layering is investigated exemplarily under quasi-static loading. In this series of simulations, the effect of an inadequately compacted soil layer on the post response is investigated. A loose soil layer with a relative density of $I_D = 0.30$ is assumed to exist along the post embedment length. The layer thickness is increased in steps of 20 cm from the ground level to the post-toe level (see Fig. 5-36). The soil beneath the loose layer is assigned dense soil properties $I_D = 0.80$. The parameters applied for the respective layers are listed in Table 5-6.

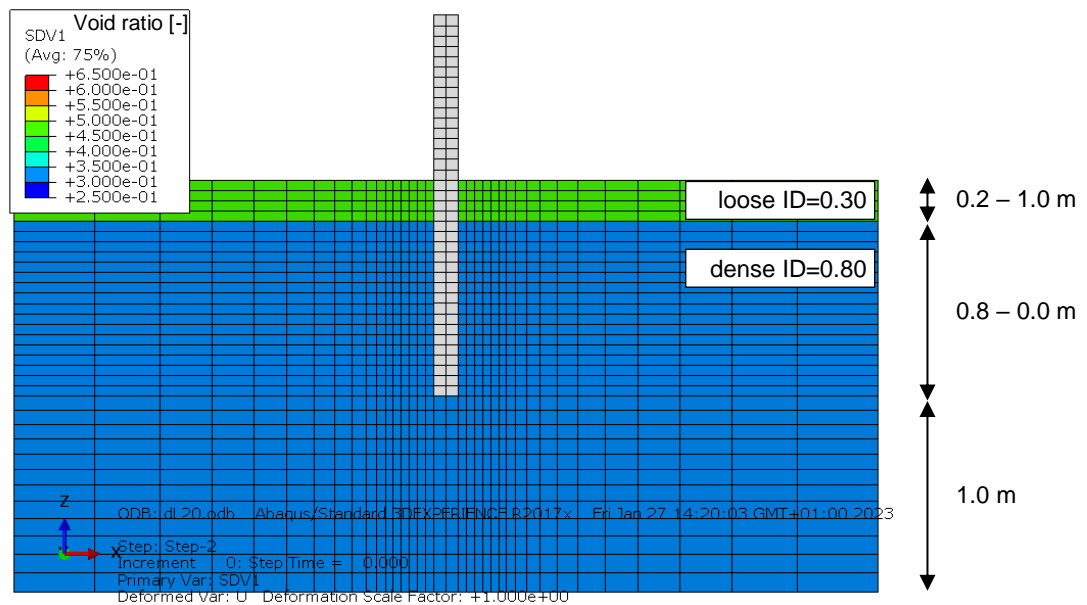


Fig. 5-36: Configuration of the soil layers for the study of the effect of a loose soil layer on the post behaviour

The simulation results are presented in Fig. 5-37. The introduction of a loose layer of 20 cm leads to a reduction of the reaction force by 8 to 10%. Increasing the loose layer thickness to 1.0 m, i.e. the full embedment length, decreases the reaction force by 50 to 56%. The simulation with 1.0 m loose layer shows a slightly higher reaction force of 7% compared to the simulation of the full soil block with loose soil. This is attributed to the higher drag force at the post-toe due to the existence of the dense soil beneath. The comparison of the reaction force reduction at different deflection values builds a relatively narrow corridor of a maximum 5%. In all simulations, the post rotates as a rigid body and no yielding of the cross-section is observed.

The results show that the effect of a loose layer is most significant, if it exists in the upper 60 cm. This is the vicinity above the rotation point, where the passive earth pressure component in front of the post is mobilised.

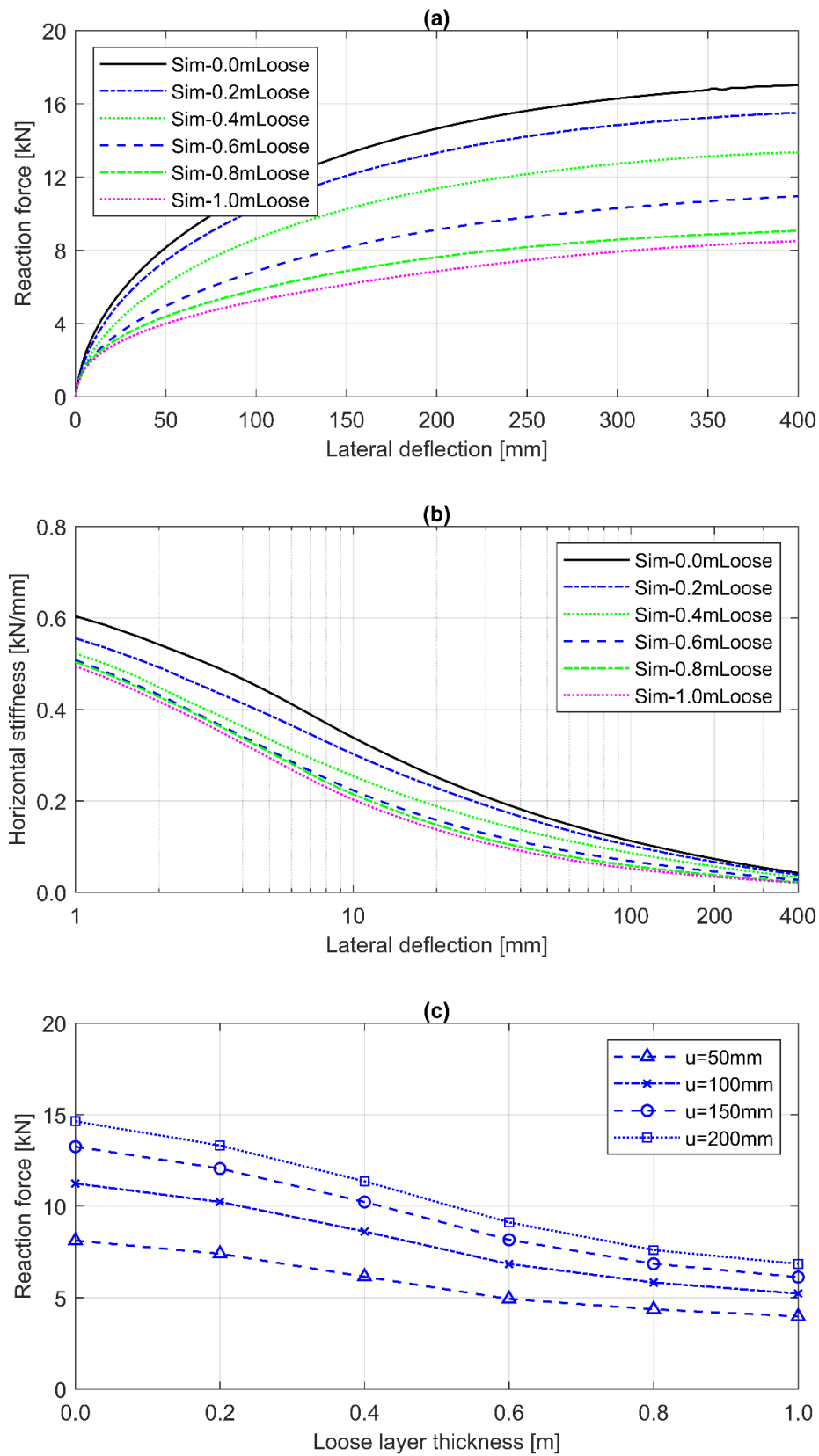


Fig. 5-37: Effect of the existence of a loose layer along the post embedment under quasi-static loading (a) load-deflection curves (b) system stiffness (c) influence of layer thickness on the reaction force at selected deflection values

Effect of Layering: very dense layer

In this series of simulations, the effect of a highly compacted soil layer on the post response is investigated. A very dense soil layer with a relative density of $I_D=0.99$ is assumed to exist along the post embedment length. The layer thickness is increased in steps of 20 cm from the ground level to the post-toe level (see Fig. 5-38). The soil beneath the very dense layer is assigned dense soil properties. The parameters applied for the respective layers are listed in Table 5-6. The effect of the very dense layer is investigated exemplary only under quasi-static loading.

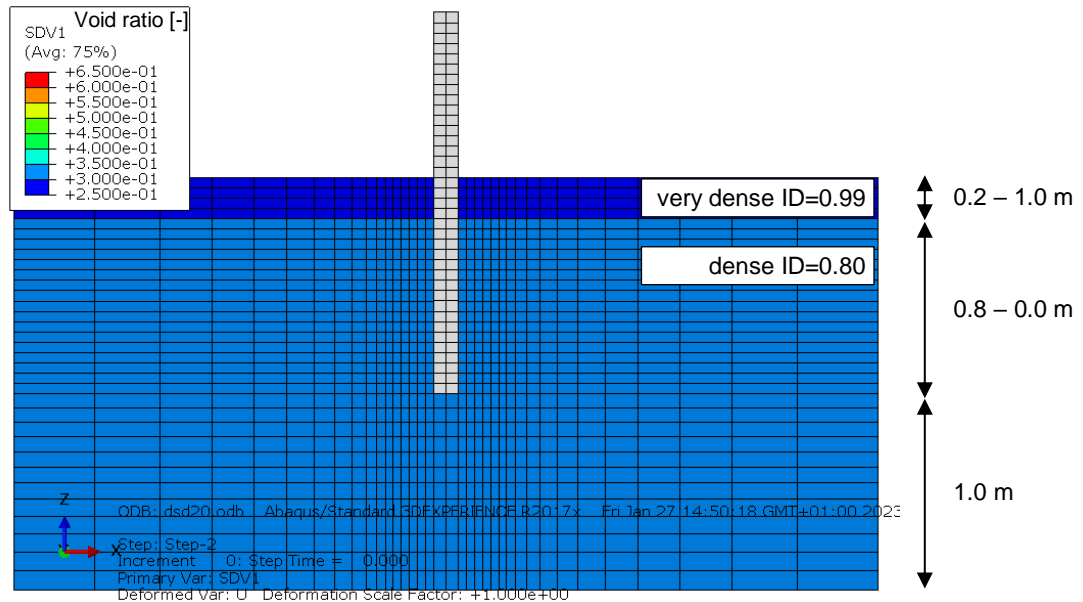


Fig. 5-38: Configuration of the soil layers for the study of the effect of a very dense soil layer on the post behaviour

The simulation results are presented in Fig. 5-39. The introduction of a very dense layer of 20 cm at the top leads to high stress concentration in the upper elements, and the soil reaches the limit state. Subsequently, the reaction force is not affected significantly. By increasing the very dense layer thickness to 60 cm, the reaction force increases by 45 to 50%. A further increase of the very dense layer thickness has a relatively lower effect on the reaction force (less than 10%). This is attributed to the yielding of the post section. In the simulations with a very dense layer thickness of less than 60 cm, the post rotates as a rigid body without any signs of yielding. For larger very dense layer thickness, a plastic hinge is formed at a depth of 0.4 m at a lateral deflection of 100 to 150 mm. The simulation with 1.0 m very dense layer shows a lower reaction force of 8% compared to the simulation of the full soil block with very dense soil. This is attributed to the lower drag force at the post-toe due to the existence of the dense soil beneath.

The results of this simulation series show that the effect of a very dense layer is most significant, if it exists in the upper 20 to 60 cm. In this range, the passive earth pressure component in front of the post is mobilised. A further layer thickness increase has no significant effect on the reaction force, as the post forms a fixation in the soil. The properties of the steel section material govern the post response in this case.

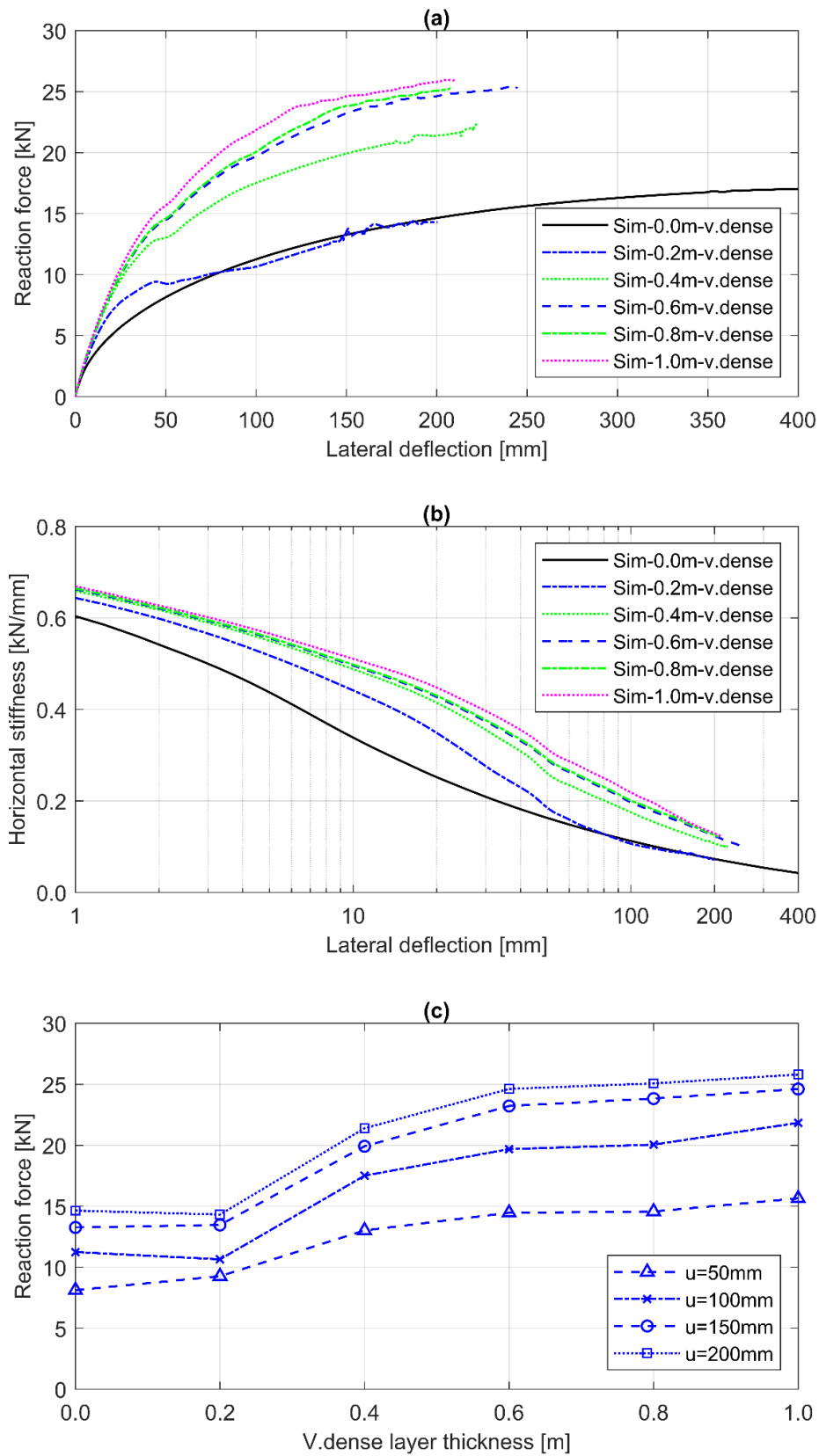


Fig. 5-39: Effect of the existence of a very dense layer along the post embedment under quasi-static loading (a) load-deflection curves (b) system stiffness (c) influence of layer thickness on the reaction force at selected deflection values

Variation of embedment length

The influence of the embedment length on the post response is discussed in this section. The quasi-static test was simulated using the reference FE model ($I_D=0.80$) under variation of the post embedment between 70 and 120 cm. The distribution of the mean pressure around the post due to the reduction of the embedment length from 100 to 70 cm is shown in Fig. 5-40. The posts rotate under lateral loading as a rigid body without any signs of yielding. The pressure distribution is comparable; however, the influence zone extent decreases by reducing the embedment length.

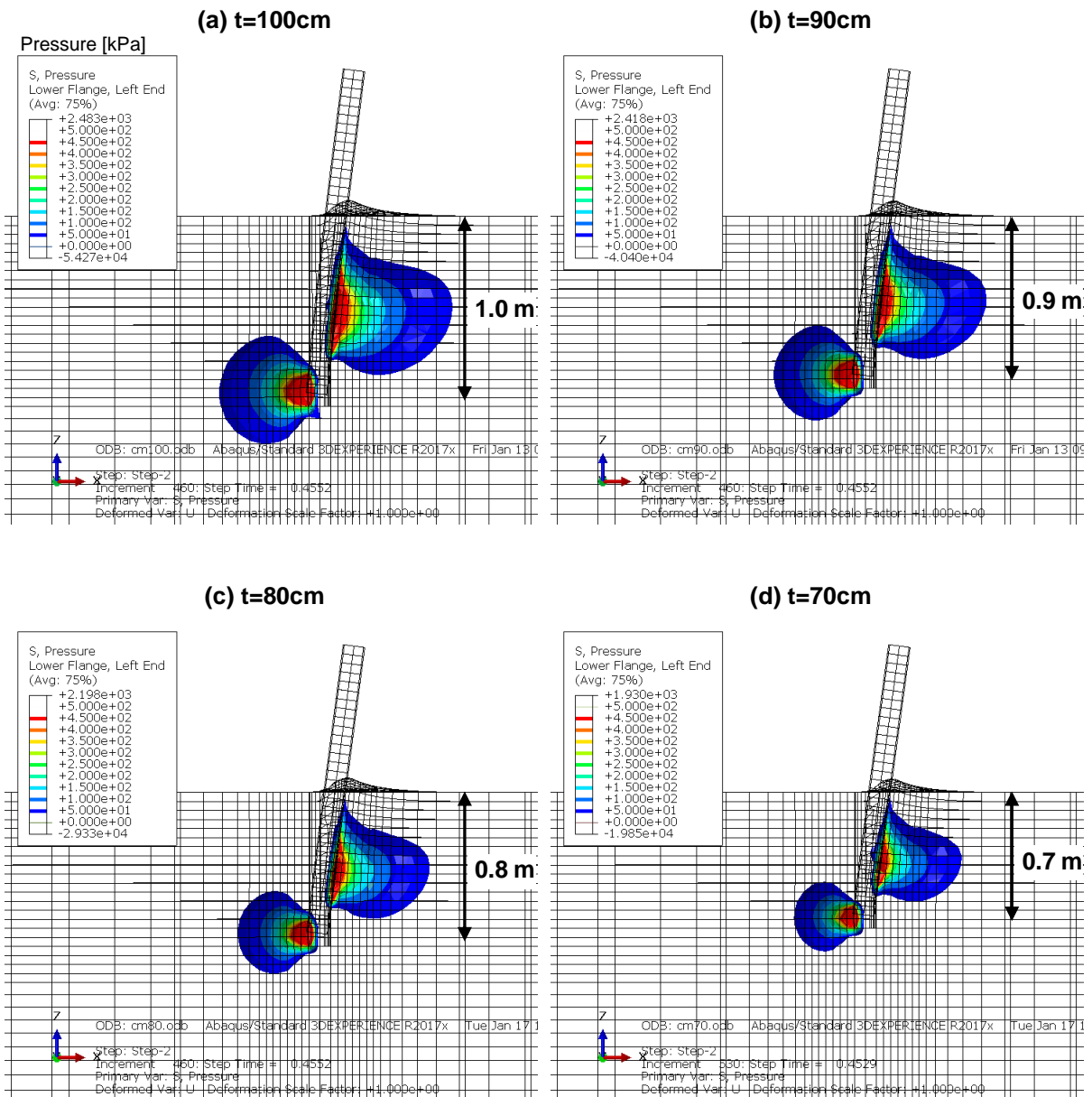


Fig. 5-40: Mean pressure distribution around the post at a deflection of 180 mm under variation of the post embedment length under quasi-static loading (dense soil $I_D=0.80$)

Increasing the embedment length to 110 and 120 cm leads to yielding of the post section starting from a lateral deflection of 205 and 132 mm, respectively. The yield zone increases with the increased loading to form a plastic hinge, as shown in Fig. 5-41. The plastic zone is located at 45 to 50 cm below ground level for both variations.

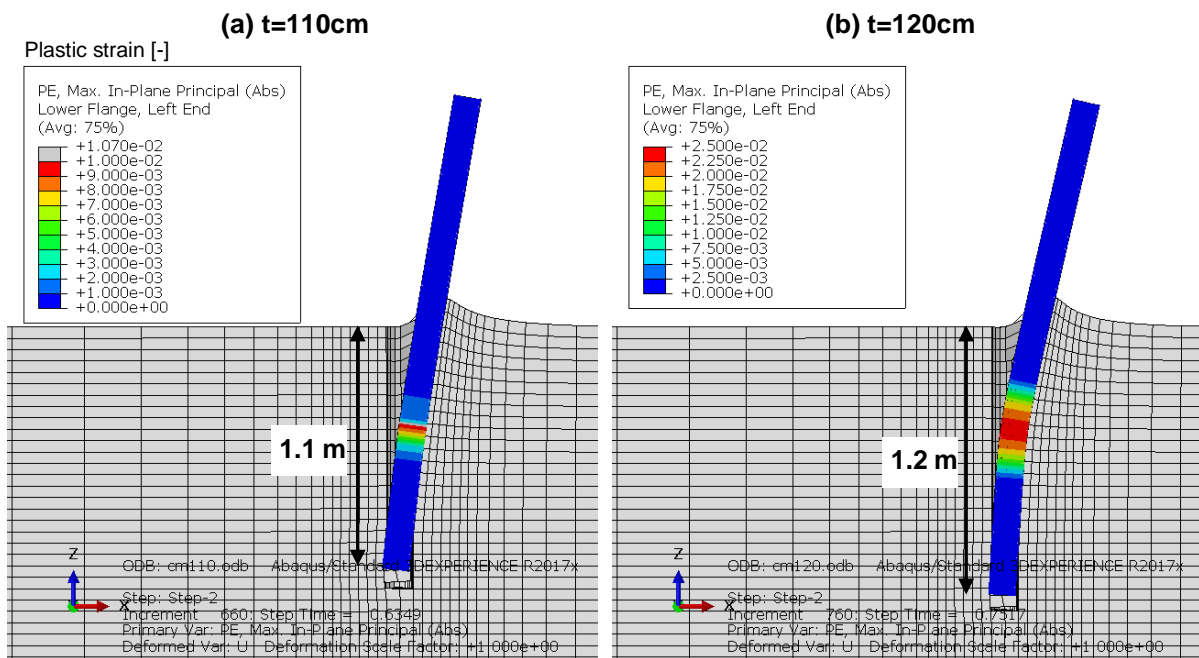


Fig. 5-41: Yielding of the post section under variation of the embedment length (in dense soil $I_D=0.80$) at (a) 250 mm for embedment=110cm and (b) formation of a plastic hinge at a deflection of 300 mm for embedment=120cm

The load-deflection curves and the derived horizontal stiffness of the simulated variations are presented in Fig. 5-42. The load-bearing behaviour is comparable for all variations up to a deflection of 20 cm. With further loading, the variations 70 and 80 cm reach the limit state at 210 mm deflection, while the variations 90, 100 and 110 cm reach the limit state at ca. 350 mm deflection. The variation 120 cm shows a bend at 22 kN in the load-deflection curve due to the formation of the plastic hinge.

The reaction force can be described to increase non-linearly with increasing the embedment length for the relative density $I_D = 0.80$ as shown in Fig. 5-42c. To investigate whether this relation is valid under variation of the relative density, the post embedment was varied from 70 to 120 cm in a very dense soil ($I_D = 0.95$). The results are shown in Fig. 5-43. As expected, the posts reached the limit state earlier compared to the dense soil. The post section shows yielding with an embedment of 100 cm. The horizontal stiffness is 10 to 15% higher, and the degradation rate is lower. The relation between the reaction force and the embedment length in the very dense soil can be rather described as multi-linear (see Fig. 5-43c). As soon as the section yields, no significant increase in the reaction force is observed.

The results of the impact loading simulations with 2.5 kJ under variation of the embedment length in dense soil $I_D = 0.80$ are shown in Fig. 5-44. Compared to the reference test, the load-deflection curves become flatter by reducing the embedment length, i.e. lower reaction force and larger deflections, and vice versa when increasing the embedment length. The variation in the system stiffness is more significant for the embedment reduction. With an embedment of 70 cm, the post recoils after 68% longer time duration compared to the reference test. The maximum post velocity coincides for the simulated variations. No signs of post yielding were observed under 2.5 kJ.

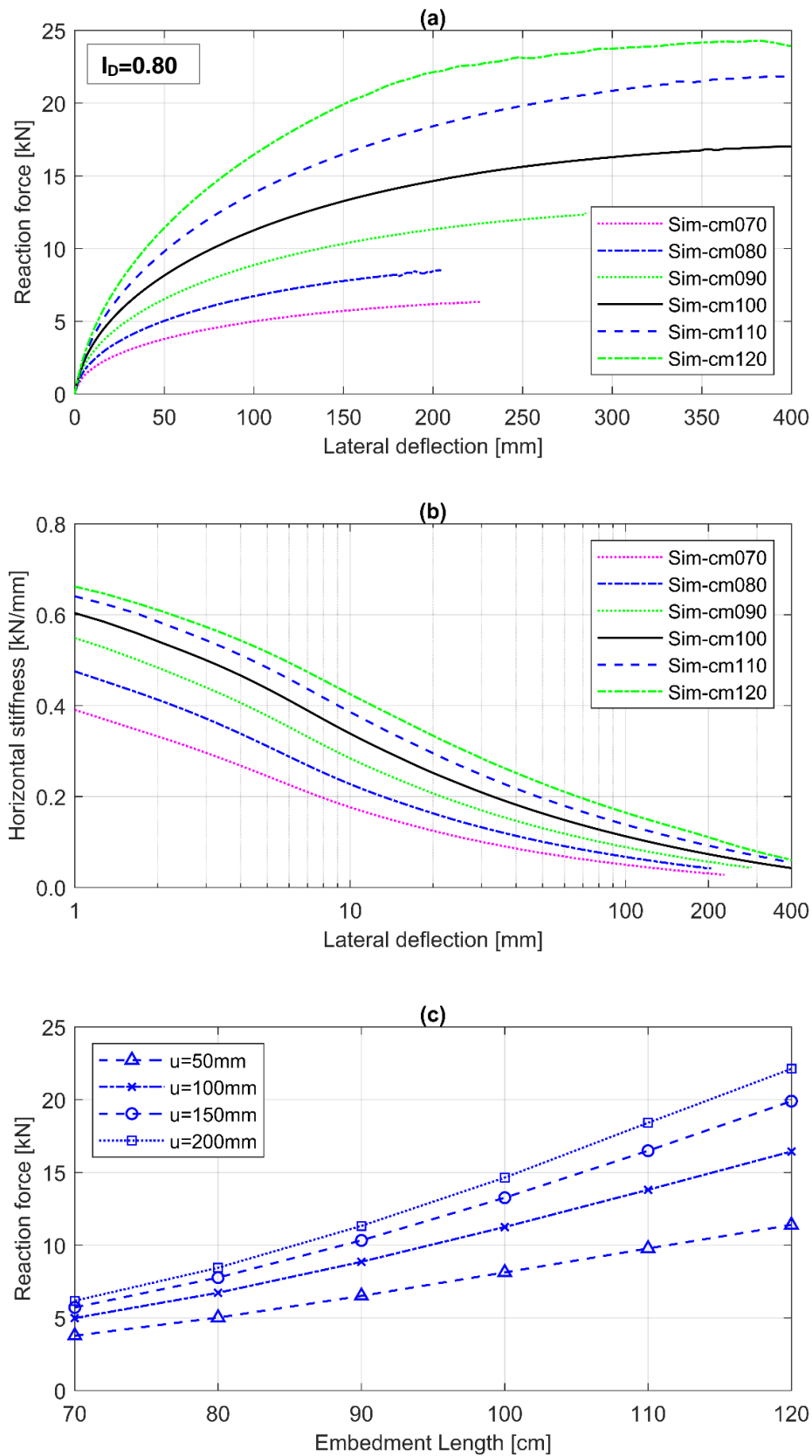


Fig. 5-42: Variation of the post embedment length in dense soil ($I_D=0.80$) under quasi-static loading (a) load-deflection curves (b) system stiffness (c) reaction force versus embedment length

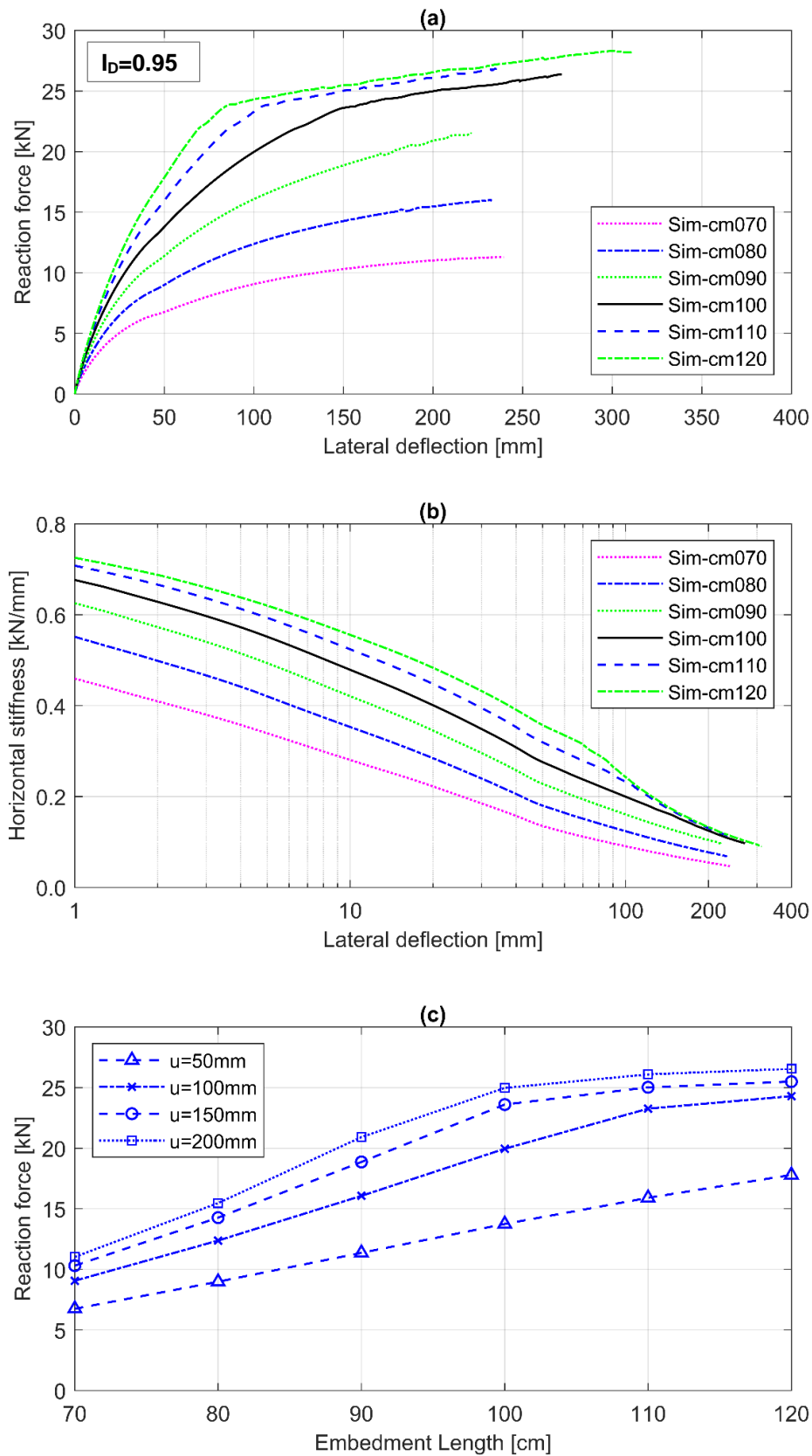


Fig. 5-43: Variation of the post embedment length in very dense soil ($I_D=0.95$) under quasi-static loading (a) load-deflection curves (b) system stiffness (c) reaction force versus embedment length

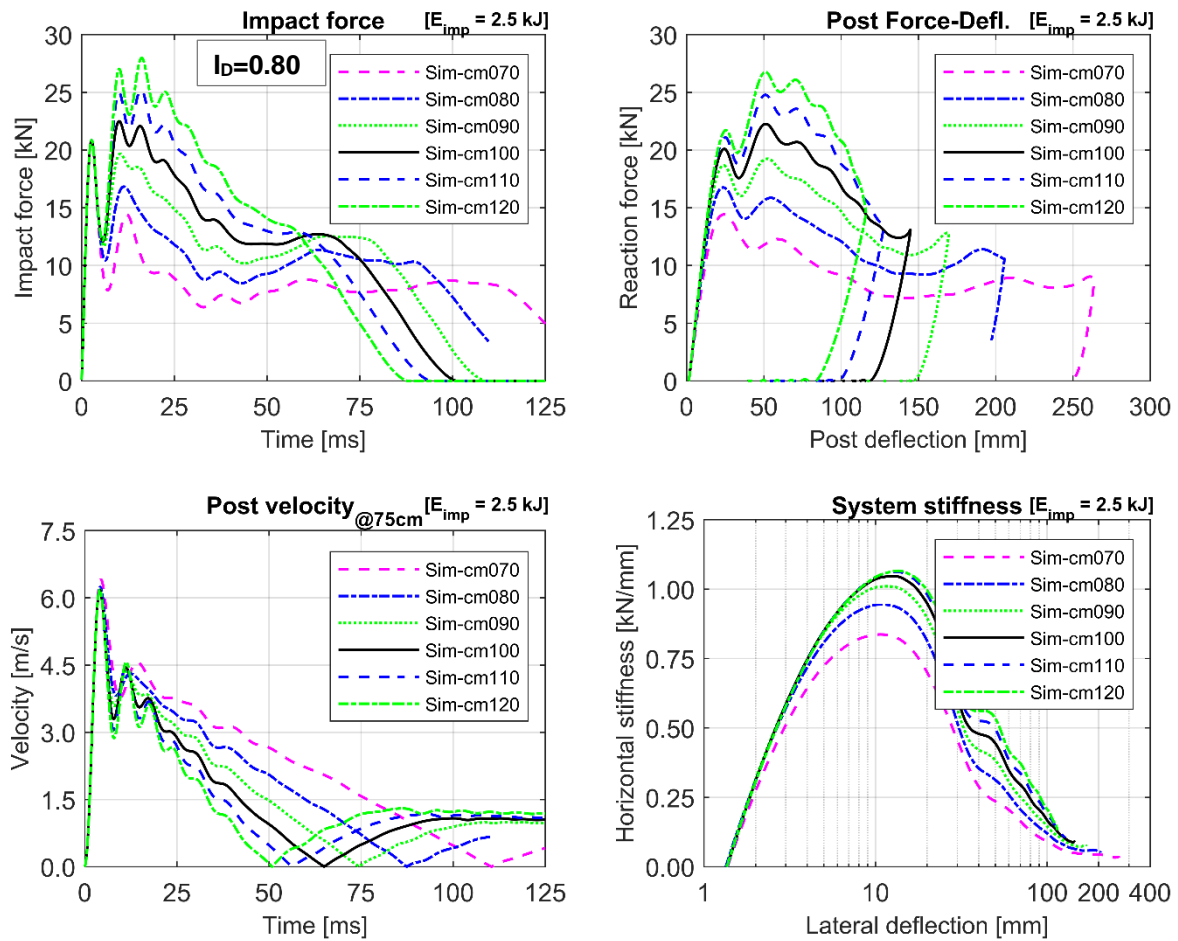


Fig. 5-44: Effect of variation of the embedment length on the post response under a dynamic impact of 2.5 kJ

To check whether these observations are valid for higher impact levels, the embedment length variations in dense soil ($I_D = 0.80$) were simulated under 5.0 kJ and 10.0 kJ. The simulation results are summarised in Fig. 5-45. The maximum reaction force is observed to increase linearly with increasing the embedment length independent of the impact energy. By increasing the impact energy by 2- and 4-folds, the maximum reaction force increases by 25 and 75% respectively.

Under an impact of 2.5 and 5.0 kJ, the maximum post deflection decreases non-linearly with increasing the embedment length. The maximum deflection could not be evaluated for the higher impact energy level 10.0 kJ, since the simulations failed to converge shortly after reaching the maximum force. The deflection increases by 78% on average when doubling the impact energy from 2.5 to 5.0 kJ.

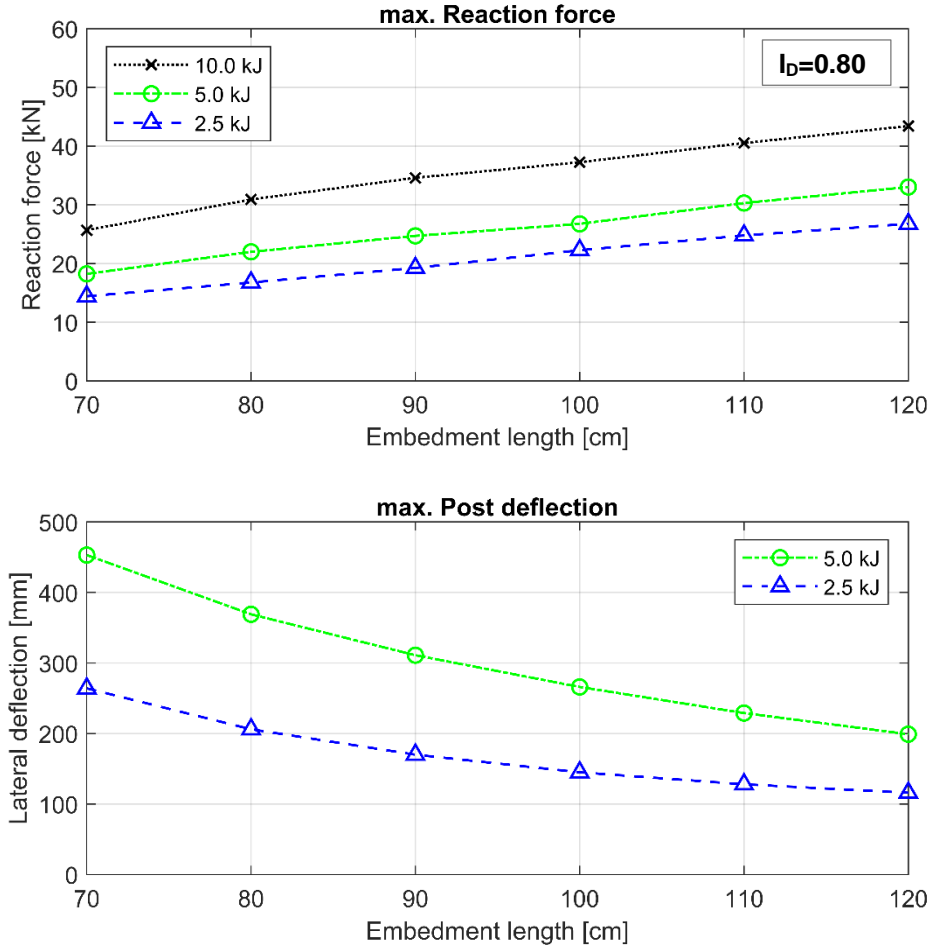


Fig. 5-45: Influence of the post embedment length on the maximum reaction force and maximum post deflection under impact loading

Variation of loading height

The influence of the height of the loading point on the post response is discussed in this section. The quasi-static test was simulated using the reference FE model (IPE120, KEE032, $I_D=0.80$, embedment length 1.0 m) under variation of the load application height. Fig. 5-46 shows the dimensions of the Super-Rail Eco post and the location of the guardrail and box beam in the vertical direction. In a crash event, the vehicle comes first in contact with the guardrail beam. The impact force is then transferred from the guardrail beam to the posts through the deformation brackets, which are bolted to the posts in two points at 49 and 60 cm height. During impact, the bracket tends to fold and shift the impact point upwards. Moreover, the box beam acts as a bracing for the posts, which further shifts the action point of the impact load above the centreline of the guardrail beam and brackets. Based on these observations, the loading point for the reference model was chosen at 75 cm, corresponding to 5 cm above the bracket upper edge and equal to the lower edge of the box beam. In a crash event, the impact force can act on the post at a height ranging from the lower bolt holding the bracket to the post head, depending on the vehicle type and crash severity. Further geometric conditions may also lead to altering the impact point height, e.g. resurfacing of the roadway.

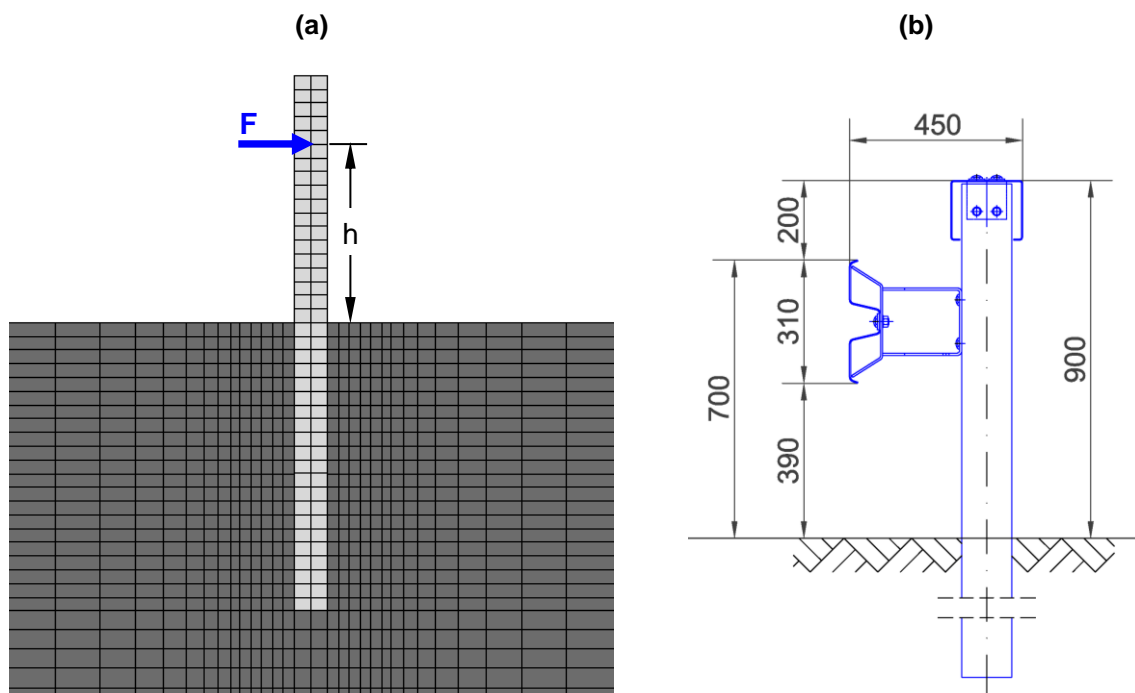


Fig. 5-46: (a) Configuration of the post profile under variation of the loading height (b) Dimensions of the Super-Rail Eco post and location of the longitudinal beams

In this series of simulations, the loading point is varied between 40 and 90 cm above ground level to investigate the effect of the shear and bending moment on the post response. The simulated load-deflection curves evaluated at the loading point are presented in Fig. 5-47a. The results show that increasing the height of loading from 75 to 90 cm has a negligible effect on the post response. The reaction force shows a maximum reduction of 6% from the reference test. The initial stiffness is in a narrow range of 0.48 to 0.60. On the other side, lowering the loading point increases the reaction force (e.g. 33% for 40 cm loading height). The initial stiffness jumps to 0.74 to 1.21 for the variations 65 to 40 cm. The reaction force decreases linearly by increasing the loading height. No yielding of the post section was observed in the simulations.

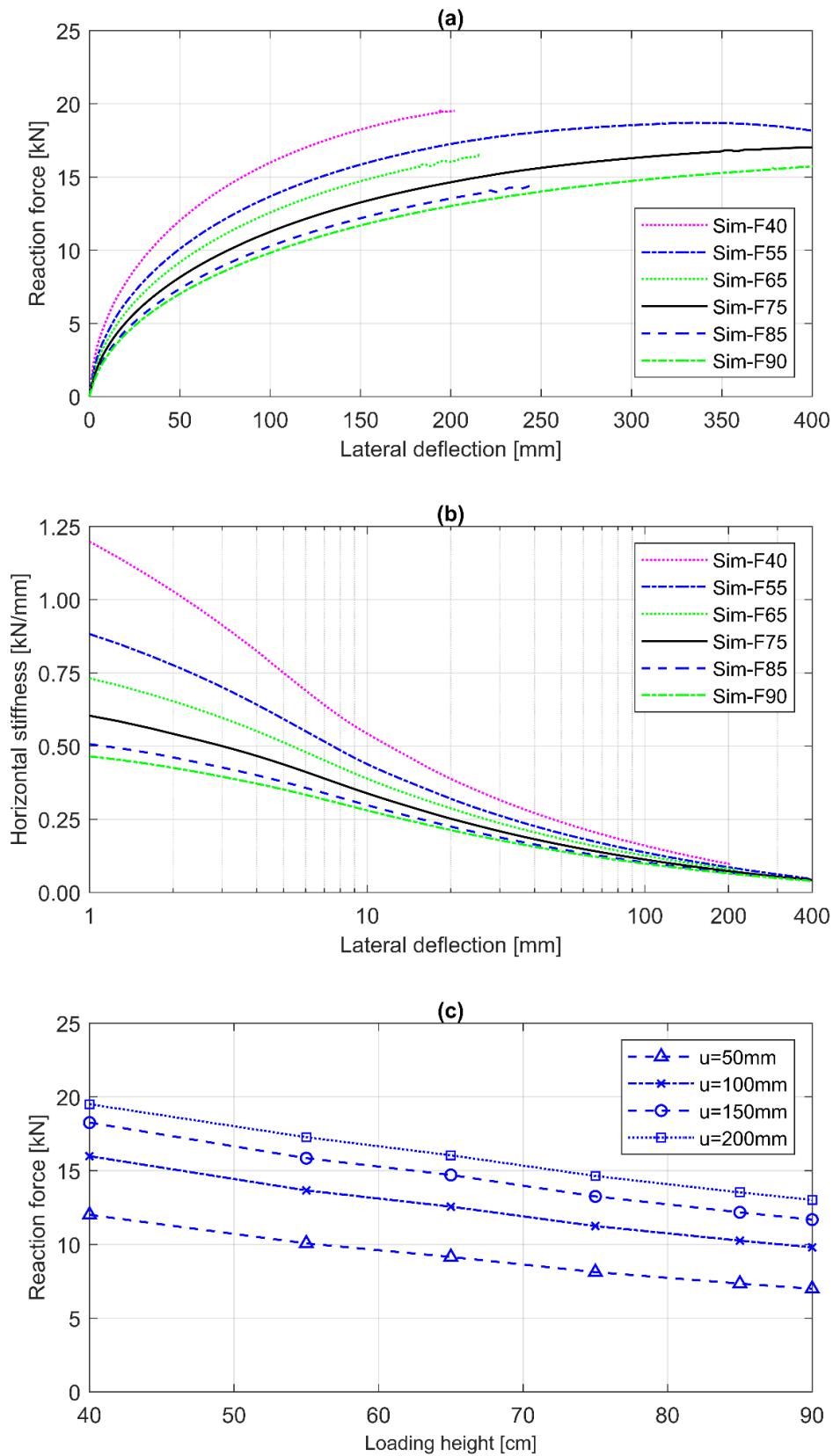


Fig. 5-47: Variation of the load application height under quasi-static loading (a) load-deflection curves (b) influence on lateral deflection

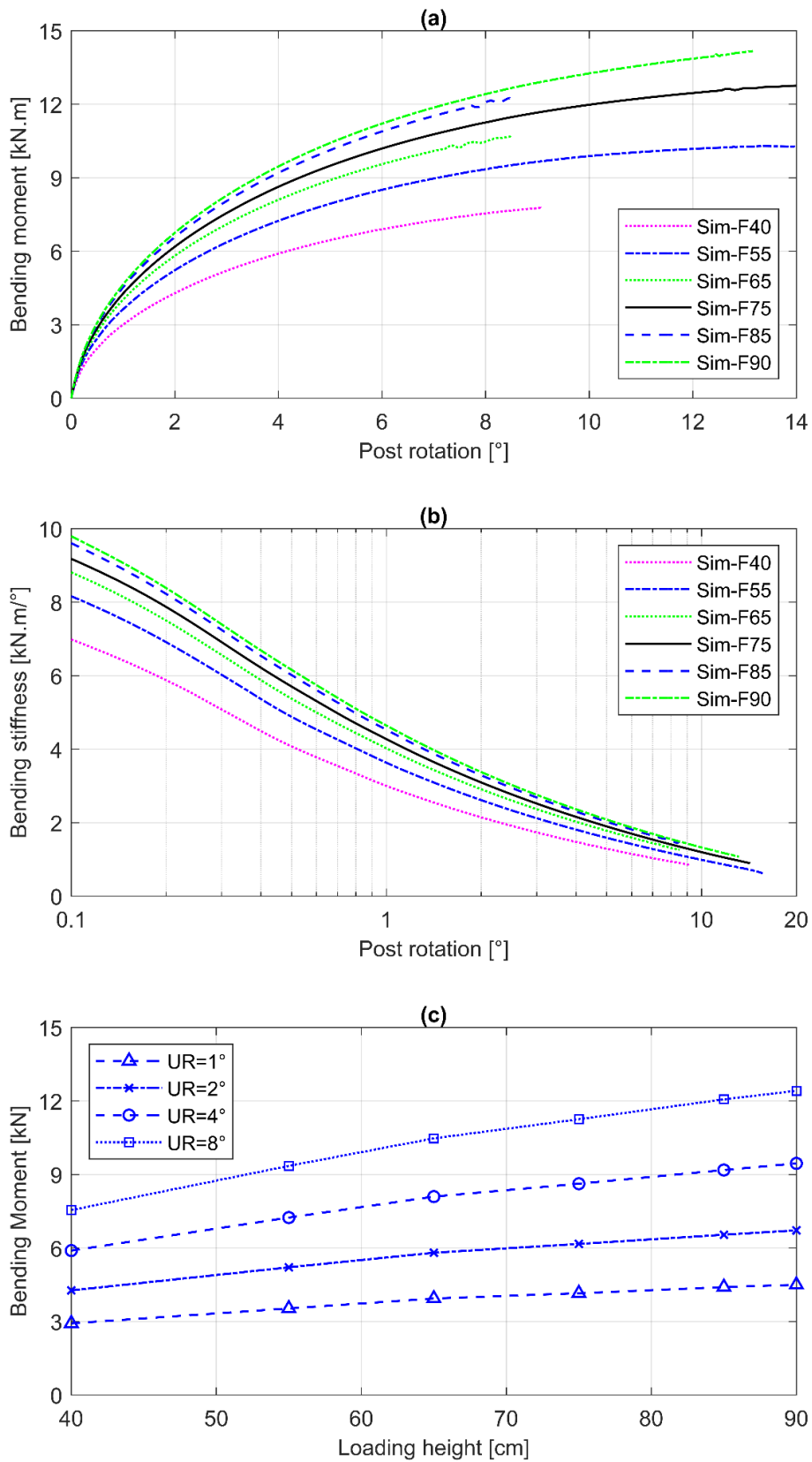


Fig. 5-48: Variation of the load application height under quasi-static loading (a) Moment rotation curves at ground level (b) rotational stiffness (c) influence on the post rotation

The bending moment was analysed with respect to the post rotation (see Fig. 5-48). Increasing the loading height yields a higher bending moment and a larger post rotation. Substituting the soil and post by a rotational spring, the bending stiffness of the system can be derived, as shown in Fig. 5-48b. The initial bending stiffness at 0.1° ranges between 7 and 10 kN.m per degree. The bending stiffness shows a degradation with further loading to ca. 15% of its value at 10° .

The influence of the loading height on the post response under impact loading was investigated. The results of the simulations under 2.5 kJ are shown in Fig. 5-49. By increasing the loading height, the reaction force decreases and the lateral deflection increases. The relation can be described as linear for both parameters (see Fig. 5-50). The deflection values determined for $h=85\text{cm}$ and 90 cm are lower compared to the maximum values, since the simulation failed to converge before the recoil point.

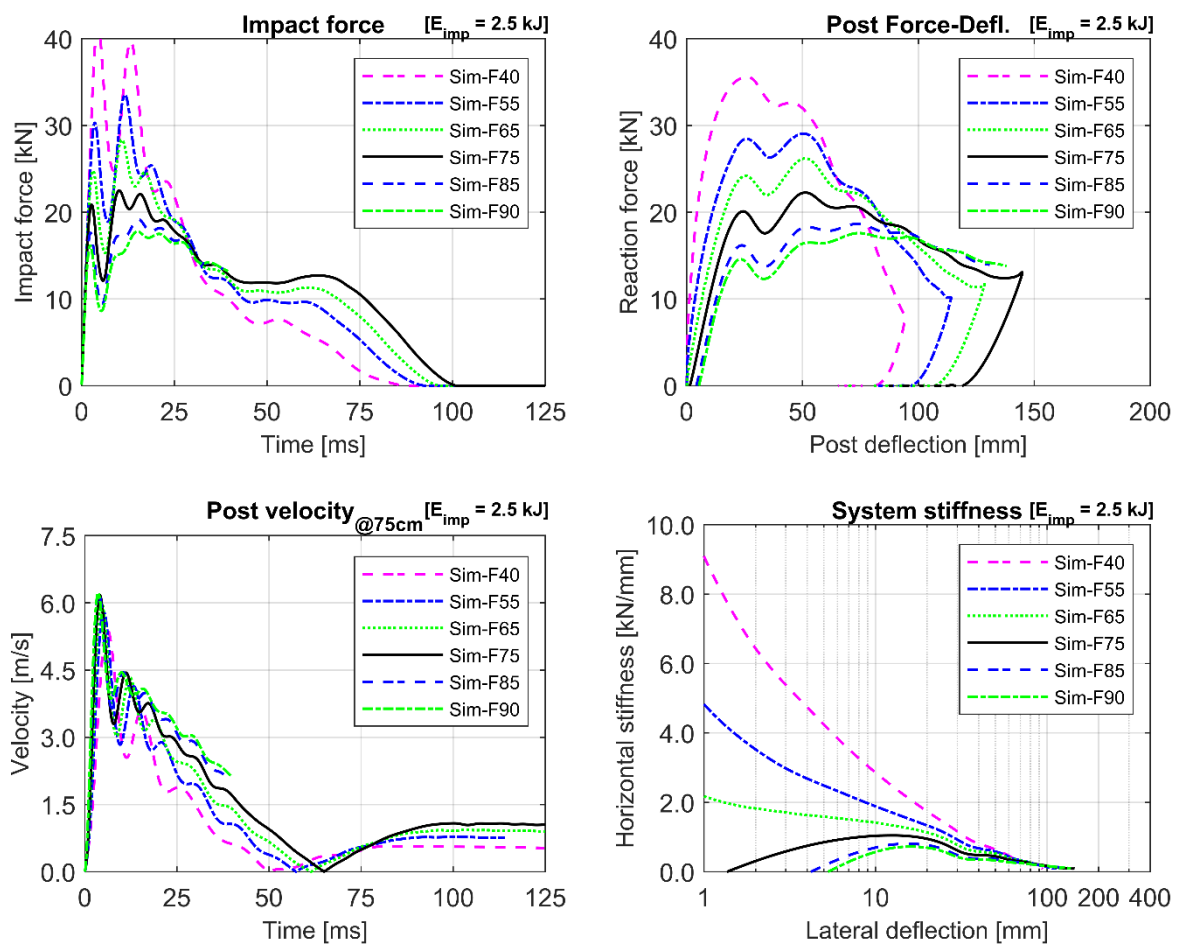


Fig. 5-49: Effect of variation of the load application height on the post response under a dynamic impact of 2.5 kJ

The development of the horizontal stiffness with lateral deflection shows a different characteristic compared to the reference test. For the variation $h=40\text{cm}$, the stiffness shows an exponential degradation from 9.1 to 0.2 over a deflection of 90 mm. The same characteristic is observed for the variations $h=55\text{cm}$ and 65 mm . For the lower loading height variations, the stiffness starts with a negative value due to the first dip in the reaction force due to the inertial effect of the post mass above ground level. By lowering the loading point close to the centre of mass of the upper post segment, the inertial effect of the post mass diminishes. The loading

height is observed to have no significant effect on the deceleration of the impactor. The recoil time point is shifted by a maximum of 14 ms for the variation $h=40\text{cm}$.

The post response was investigated under higher impact levels of 5.0 kJ and 10.0 kJ. As shown in Fig. 5-50, the maximum reaction force increases by increasing the impact energy. On average, the maximum force increased by 28% and 76% upon increasing the impact energy by a factor of 2 and 4, respectively. The post section shows slight plastic deformations at the ground level for the variations $h=40\text{cm}$ to 65 cm at the impact levels 5.0 kJ and 10.0 kJ.

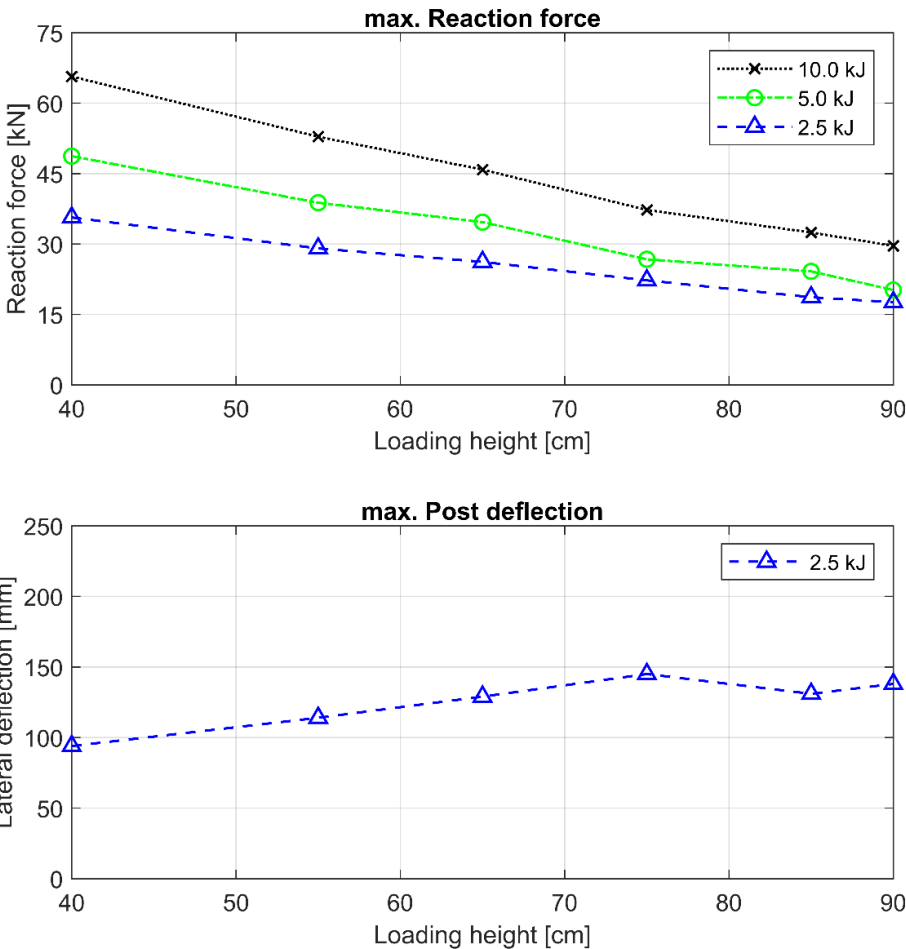


Fig. 5-50: Influence of the load application height on the maximum reaction force and maximum post deflection under impact loading

Variation of section modulus

The influence of the section modulus on the post response under lateral loading is discussed in this section. In general, the section modulus of a beam (W) in a given axis is calculated as the second moment of area (I) divided by the distance from the neutral axis to the section's extreme edge. By increasing the section modulus, the flexural rigidity of the beam (EI) increases consequently. In this series of simulations, the effect of increasing the post flexural rigidity, while keeping the cross-sectional shape and steel grade constant is investigated. The simulations are conducted using the reference model with reference conditions (KSS032, $I_D = 0.80$, embedment 1.0 m, loading at 75 cm above GL) under variation of the section properties from IPE80 to IPE160.

Compared to the reference IPE120 post, the IPE80 exhibits 62% lower elastic section modulus $W_{el,y}$, while the IPE160 exhibits a 106% higher $W_{el,y}$. The post section dimensions and parameters are listed in Table 5-7. The diameter of the transition body cylinder enclosing the beam elements in the FE model is adjusted to an equivalent circle exhibiting an approximate circumference equal to the outer perimeter of the post-section, analogue to the approach adopted for the reference model.

Table 5-7: Parameters and schematic presentation for the variation of the post section modulus

Post section	Dimensions height/width h/w [mm]	Sec. Area A [cm ²]	Weight per meter M [kg/m]	Steel grade [-]	Second moment of area		Section modulus	
					strong axis I_y [cm ⁴]	weak axis I_x [cm ⁴]	elastic $W_{el,y}$ [cm ³]	plastic $W_{pl,y}$ [cm ³]
IPE80	80/46	7.6	6.0	S355	80.1	8.49	20.0	23.2
IPE100	100/55	10.3	8.1	S355	171.1	15.90	34.0	39.4
IPE120	120/64	13.2	10.7	S355	318.0	27.70	53.0	60.7
IPE140	140/73	16.4	12.9	S355	541.0	44.90	77.3	88.3
IPE160	160/82	20.1	15.8	S355	869.0	68.30	109.0	124.0

The schematic diagrams show the cross-sections of five IPE profiles. From left to right: IPE160 (height 160 mm, width 82 mm, flange thickness 7.4 mm, web thickness 5.0 mm); IPE140 (height 140 mm, width 73 mm, flange thickness 6.9 mm, web thickness 4.7 mm); IPE120 (height 120 mm, width 64 mm, flange thickness 6.3 mm, web thickness 4.4 mm); IPE100 (height 100 mm, width 55 mm, flange thickness 5.7 mm, web thickness 4.1 mm); and IPE80 (height 80 mm, width 46 mm, flange thickness 5.2 mm, web thickness 3.8 mm).

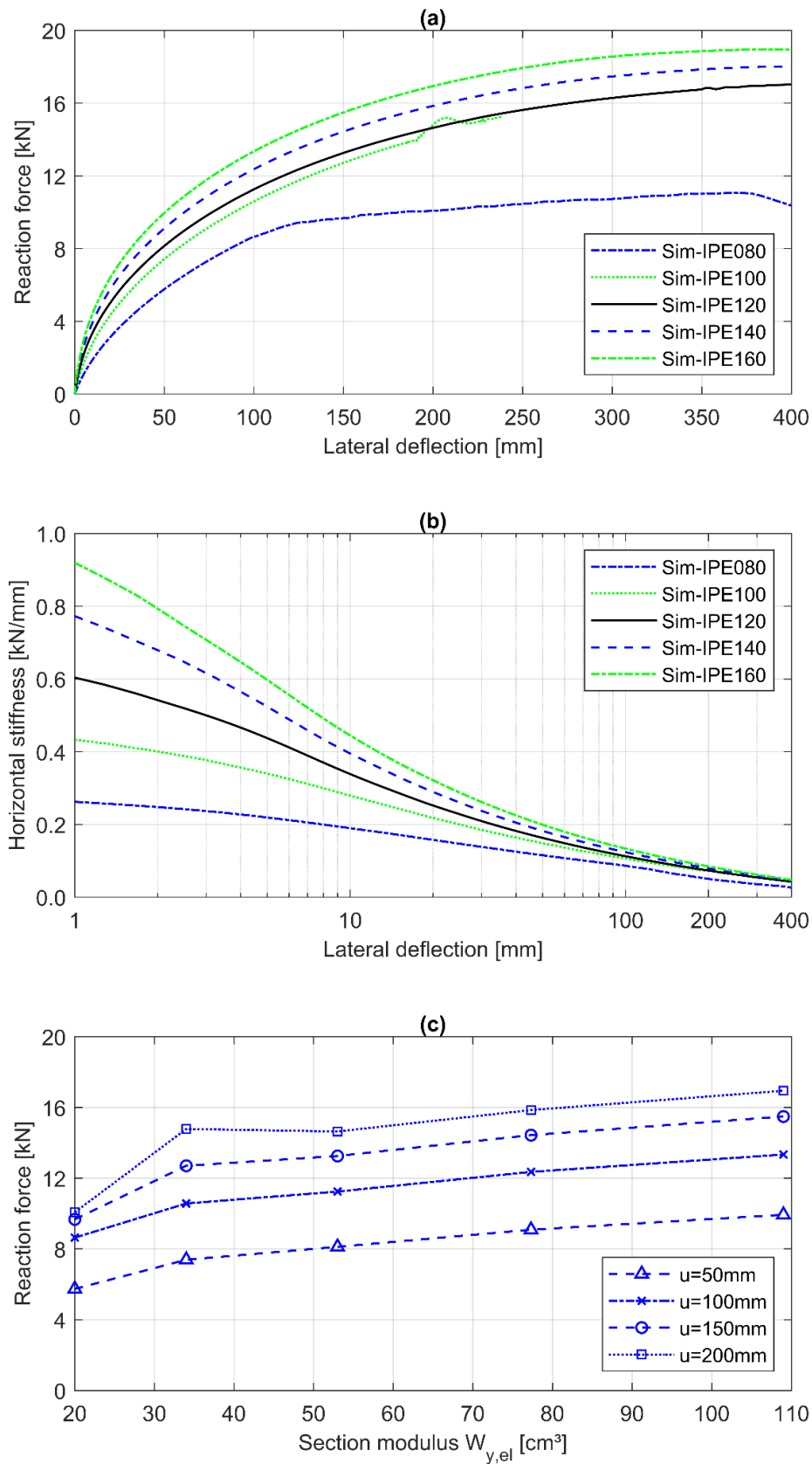


Fig. 5-51: Variation of the section modulus under quasi-static loading (a) load-deflection curves (b) system stiffness (c) influence of section modulus variation on the reaction force

The load-deflection curves and the derived system stiffness under quasi-static loading are shown in Fig. 5-51. Except for the IPE80, the curve characteristic is very comparable to the reference test. The IPE80 section shows an early yielding at 105 mm deflection. A plastic hinge is formed at a depth of 35 cm below ground level. The IPE100 section shows a slight plastic yielding at the same depth. The sections IPE120 to IPE160 rotated as a rigid body without any signs of yielding. The initial stiffness of the investigated sections ranges between 0.28 to 0.92 kN/mm. The stiffness then shows a degradation up to 10% to 5% of the initial value at a deflection of 300 mm. Apart from the IPE180, the reaction force increases linearly with the increase of the elastic section modulus $W_{el,y}$.

Analogue to the former variations, the post response was investigated under three impact intensities: 2.5 kJ, 5.0 kJ and 10.0 kJ. The simulation results for the simulations under 2.5 kJ are presented in Fig. 5-52. The lighter sections IPE80 and IPE100 show stronger vacillations compared to the other sections. This is obvious in the force-time and velocity-time histories. By increasing the section modulus, the reaction force increases and the lateral deflection decreases. For the simulation 2.5 kJ, increasing the section modulus by a factor 2 (IPE120 to IPE160) leads to an increase of the reaction force by 33%. For the impact intensities 5.0 kJ and 10.0 kJ, the increase of the reaction force jumps to 54% and 63%, respectively (see Fig. 5-53).

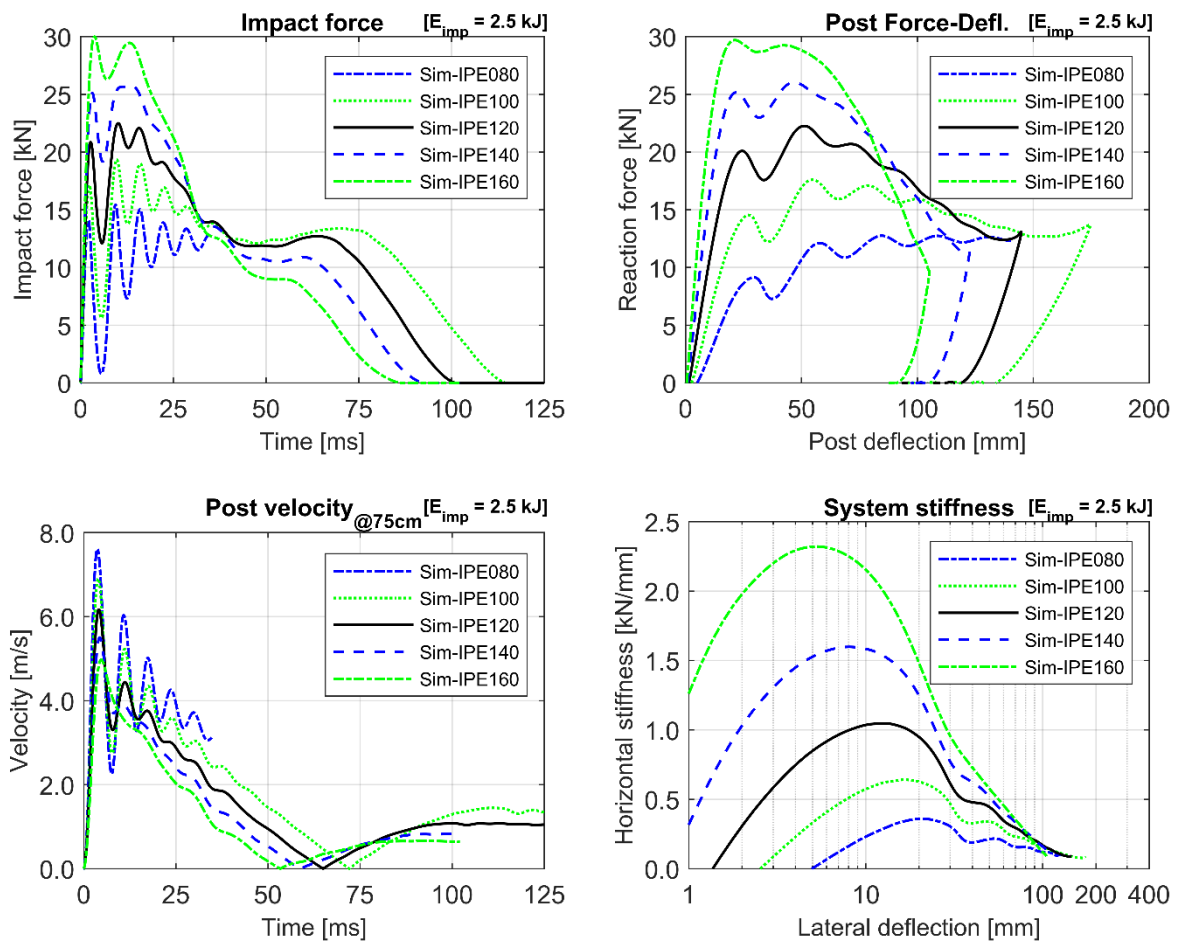


Fig. 5-52: Effect of variation of the section modulus on the post response under a dynamic impact of 2.5 kJ

The maximum horizontal stiffness increases by increasing the section modulus. The initial stiffness derived at 1 mm deflection shows that the heavier sections are stiff enough to mobilise the reaction force at very low post deflection. In contrast, the IPE80 for example, requires 5 mm to mobilise the soil resistance. This can also be attributed to the post-flange dimension, which is wider for the heavier sections (see Table 5-7).

The relation between the maximum reaction force and the section modulus is approximately linear for the investigated impact intensities, as shown in Fig. 5-53. Increasing the impact energy by a factor of 2 leads to an increase of the reaction force by 25% to 40%. Increasing the impact energy by a factor of 4 leads to an increase of the reaction force by 53% to 105%. The maximum post deflection decreases by increasing the section modulus and increases by increasing the impact energy. Based on the deflection values evaluated from the successful calculations, the curve characteristic can be described as approximately linear. However, the curve points are not enough to derive a correlation.

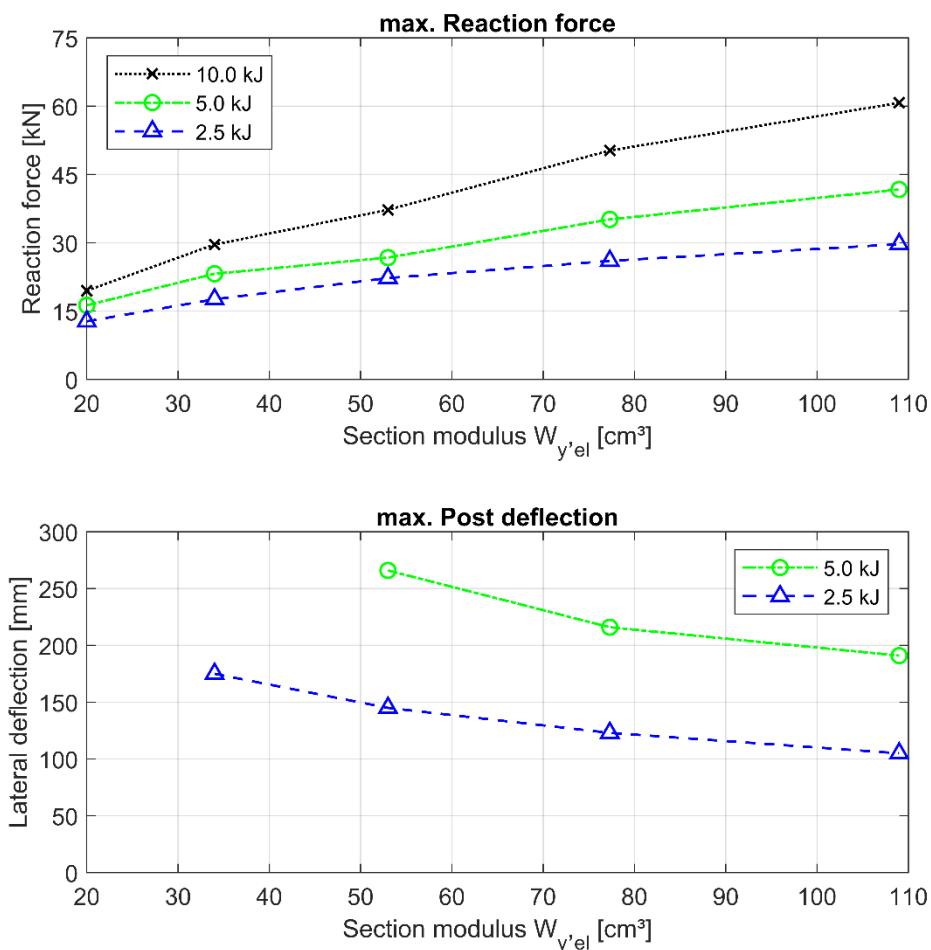


Fig. 5-53: Influence of the post section modulus on the maximum reaction force and maximum post deflection under impact loading

Variation of post-section

The influence of the section geometry on the post response is discussed in this section. The quasi-static test conducted on the post-sections HEB120 and C125 in the strong axis was simulated under the reference conditions (KSS032, $I_D = 0.80$, embedment 1.0 m). The properties of the simulated sections are presented in Table 5-8. First, the simulation results are compared to the field test data for validation (see Fig. 5-54). Then, the simulation results are compared to the reference IPE120 section simulation (see Fig. 5-55).

Table 5-8: Parameters and schematic presentation for the variation of the post-section geometry

Post section	Dimensions height/width	Sec. Area A [cm ²]	Weight per meter M [kg/m]	Steel grade [-]	Second moment of area		Section modulus	
	h/w [mm]				strong axis I_y [cm ⁴]	weak axis I_x [cm ⁴]	elastic $W_{el,y}$ [cm ³]	plastic $W_{pl,y}$ [cm ³]
HEB120	120/120	34.0	27.4	S355	864.0	318.0	144.0	165.0
IPE120	120/64	13.2	10.7	S355	318.0	27.70	53.0	60.7
C125	125/62.5	13.4	10.74	S355	309.9	78.7	49.6	57.5

The HEB120 section exhibits a larger outer perimeter (48 cm) compared to the IPE120 (36.8 cm) and C125 (37.4 cm) sections. Therefore, in the FE model, the diameter of the transition body was increased to 150 mm (circumference = 47.1 cm), to fit to the section outer dimensions. Compared to the experimental data, the model can simulate the reaction force with a deviation less than 1.0 kN, before reaching the maximum force. Afterwards, the deviation increases to a maximum of 2 kN. This deviation can be attributed to an eventual inhomogeneity of the soil at the post location. The characteristic of the load-deflection curve is comparable for the simulation and the experimental data. The maximum force is reached with lower lateral deformations compared to the IPE and C-posts. Nevertheless, the maximum force mobilised by the HEB and IPE sections is approximately equal in the simulations and the field test (refer to 3.2 *Static loading tests*).

The HEB120 exhibits a 51% higher initial stiffness than the IPE120 post. However, the degradation of the horizontal stiffness over lateral deflection is similar for all simulations. At a deflection of 140 mm, the horizontal stiffness drops to a mean value of 0.1 kN/mm for all sections.

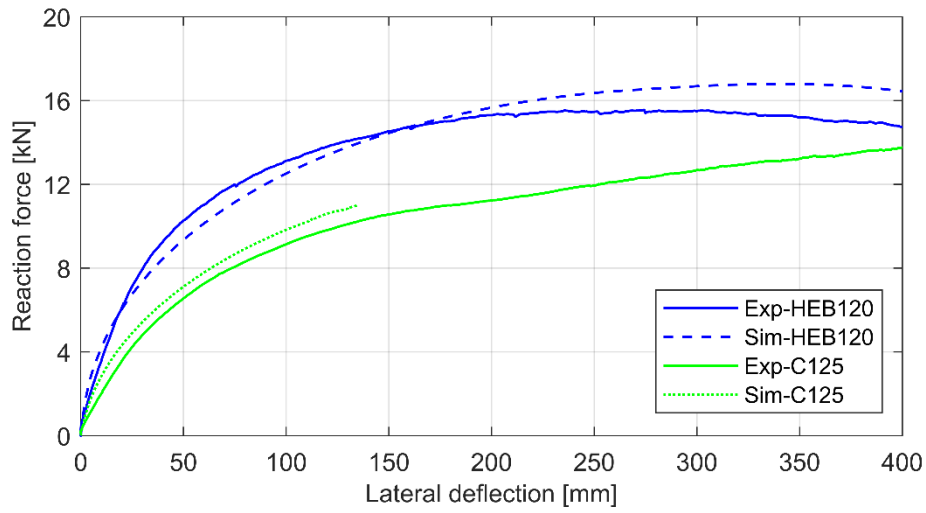


Fig. 5-54: Validation of the HEB120 and C125 simulations against quasi-static field test data

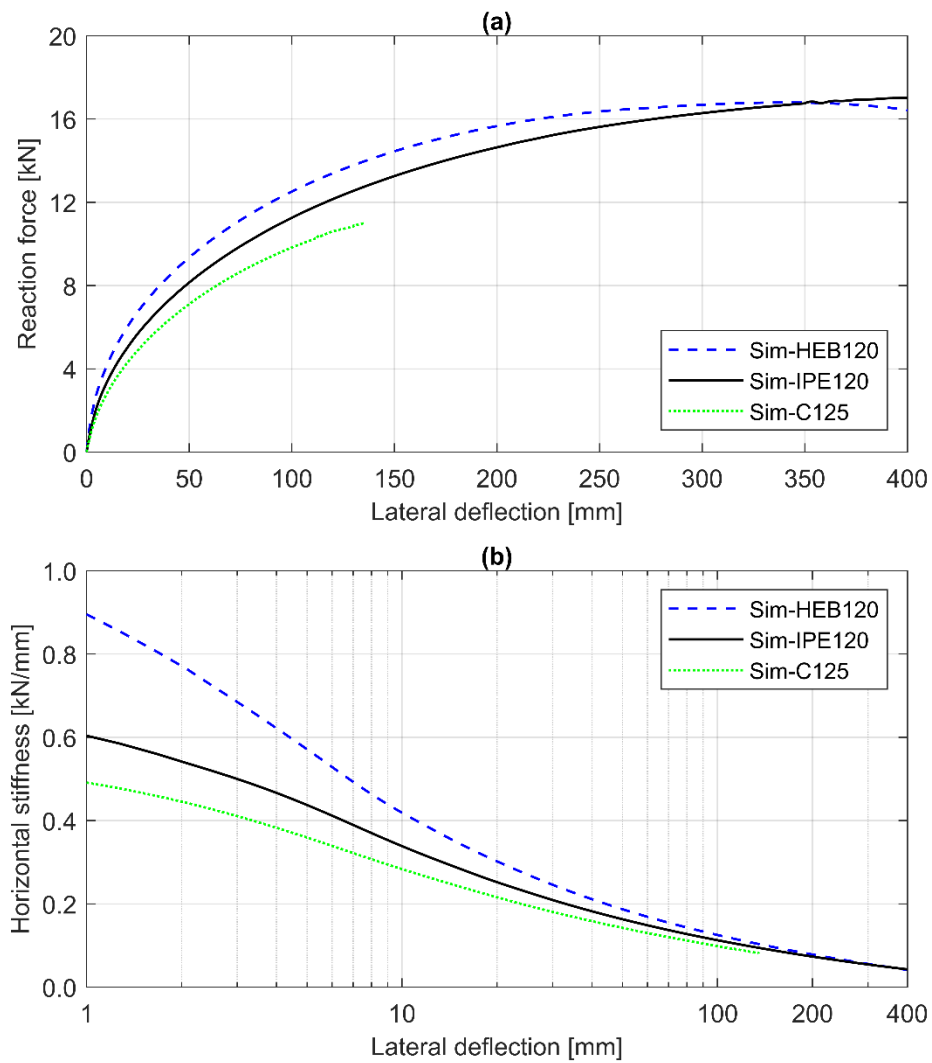


Fig. 5-55: Variation of the post-section under quasi-static loading (a) load-deflection curves (b) system stiffness

The C125 simulation shows good agreement with the experimental data as shown in Fig. 5-54. The reaction force increases non-linearly up to a lateral deflection of 115 mm. Afterwards, the reaction force tends to increase linearly with the deflection, which indicates reaching the limit state. This behaviour coincides with the experimental test data. The initial stiffness is 16% lower than the IPE120 post. Although the elastic section modulus of the C125 is only 6.8% less than the IPE120 (53.0 and 49.6 cm³ respectively), the maximum reaction force is 27% lower. This is attributed to the torsional effects under lateral loading. The centroid (centre of area) and the shear centre of the asymmetrical C125-section do not coincide in the strong axis (see Fig. 5-56). The lateral load acting on the post does not act through the section's shear centre and, therefore produces a twisting moment, i.e. torsion at the unconstrained elevations. The twisting moment is equal to the lateral load multiplied by its eccentricity with respect to the shear centre. ABAQUS [1] recommends modelling thin-walled open section beams in space using the B31OS beam elements, which consider warping of the section, i.e. axial strains, under lateral loading. Using a regular beam element type to model an open section leads to underestimation of the section torsional stiffness.

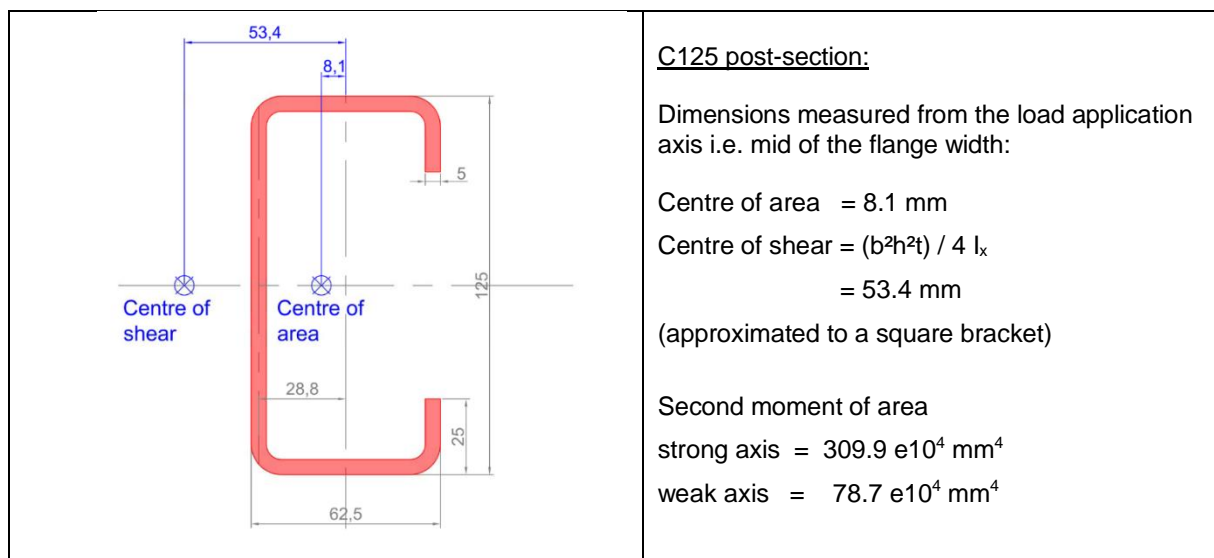


Fig. 5-56: Location of the centre of shear and centre of area for the C125 post-section

To consider the torsional effects in the C125-section simulation, the rotation about the beam axis was released below the guidance frame level and along the embedment length. The last node at the pile toe is constrained against rotation for stability. The beam is modelled using the 2-node B31OS elements. The torsional moment (SM3) and the rotation of the post-section (UR3) at a lateral deflection of 140 mm are shown in Fig. 5-57. The reaction force reached at this point is $F=11.08 \text{ kN}$. The simulation results show that the maximum torsional moment occurs in the segment above ground level and ranges between 0.75 and 0.40 kN.m. The torsional moment can be calculated analytically as follows:

Torsional moment = Lateral force * eccentricity = $11.08 * 0.0534 = 0.59 \text{ kN.m}$. The calculated value lies in the range of the simulated maximum torsional moment.

The variation of the post-section under quasi-static loading shows that, for sections symmetric in the loading direction, mainly the soil properties govern the post response as long as steel yielding does not occur. This is obvious from the IPE and HEB simulation results. The C-section exhibits a softer response due to twisting during loading. Which leads to rotation of the section and resisting the load with a section modulus less than the value in the strong axis.

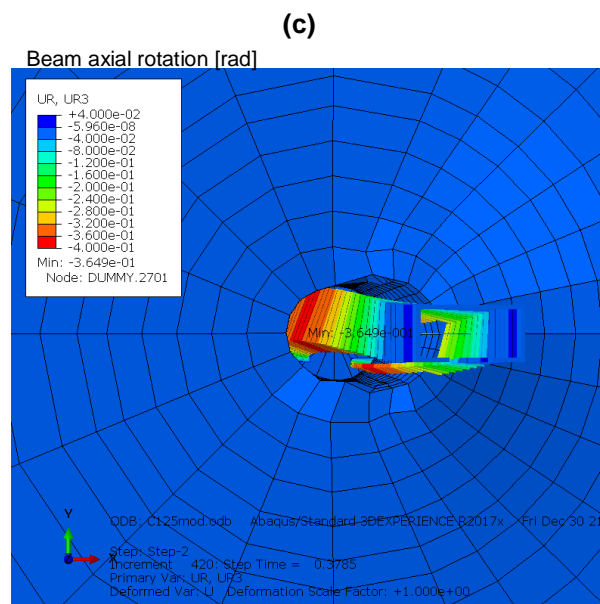
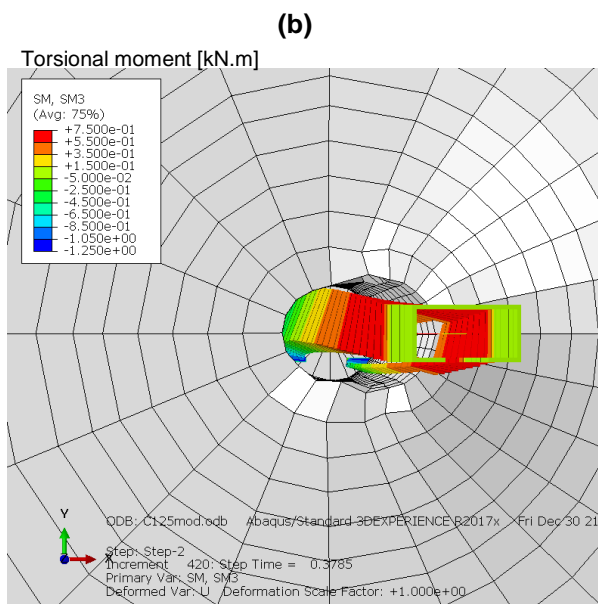
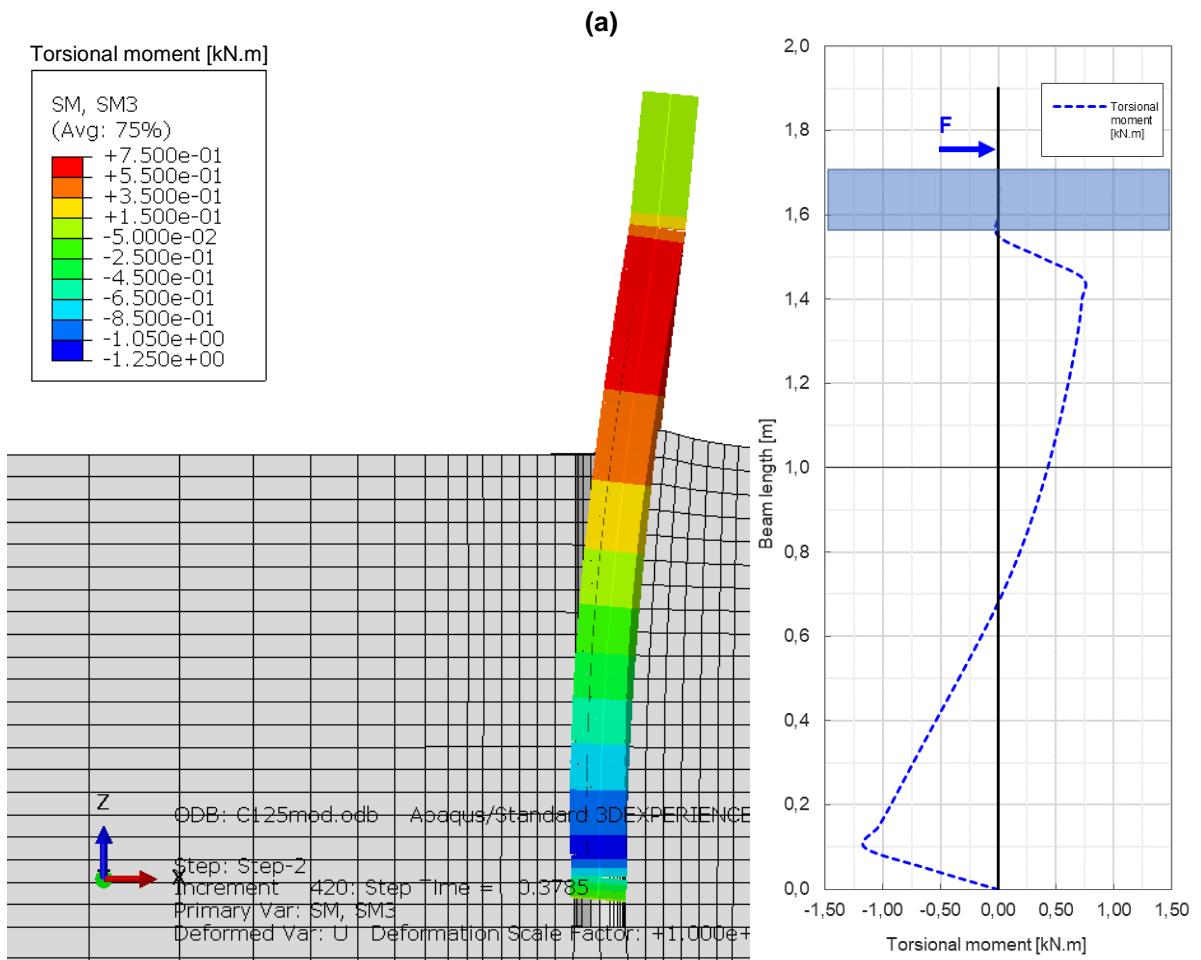


Fig. 5-57: Torsional moment and rotation around the beam axis of the C125 post-section at a lateral deflection of 150 mm (a) torsional moment profile (b) plan view (c) rotation around beam axis

5.6 Discussion and conclusions

In this chapter, the guardrail post response was investigated under different loading conditions by means of FEA. A FE model was created, considering the aspects distinguishing the investigated boundary value problem, e.g. shallow soil depth and large deformations. The soil was modelled using hypoplasticity with intergranular strains. The required material parameters were calibrated from the conducted laboratory test data. Using the experimental full-scale reference test data, the FE model was validated under quasi-static and impact loading for different impact energies. The same hypoplastic parameter set was utilised for both loading conditions.

The modelling technique applied has proven to be efficient for the guardrail post simulations. The post is modelled using beam elements enclosed in a circular transition body. The diameter of the transition body is determined based on the post outer perimeter. Compared to modelling the post using shell elements or as a rectangular body, this approach avoids stress concentrations and excessive mesh distortions in the corners. The interface definition between the transition body and the soil continuum allows for large post deflections, which have to be considered in the guardrail post problem. The compaction pressure in the shallow soil layer, has to be considered in the determination of the initial horizontal stress.

The hypoplastic soil model enables the simulation of the quasi-static and impact loading test with one parameter set. The material parameters can be determined from laboratory test data and the state parameters from in-situ soil testing. No further calibration to the post loading test is required. This feature of the soil model allows for systematic simulation of the soil in different states using the same material parameters. Further simulations were conducted using an elastic-ideal plastic constitutive model, to examine the applicability and usefulness of such a common model for the simulation of the guardrail post behaviour. The analyses have shown that the stress-dependency of the soil stiffness is very crucial for the simulations. The stiffness increase with soil depth has also to be considered. Since the post embedment is in a low-stress depth, the shear strength parameters had to be estimated using a non-linear yield criterion. The Mohr-Coulomb relationship with the shear parameter obtained from laboratory does not lead to realistic results. An adaption of the stiffness and strength parameters was necessary to obtain a good agreement between the experimental and numerical post loading test results. The determined parameter set is not unique.

In the next step, a parametric study was conducted to investigate the influence of the post and soil properties on the post response. The validated FE models were utilised for the study. In each simulation series, a single parameter was varied in the anticipated range, and the influence on the post response was observed. The most important findings of the parametric investigation are summarised as follows:

- The soil relative density is found to have a significant influence on the system's horizontal stiffness of the system as well as on the deceleration of the colliding body.
- The soil relative density also defines the failure mode of the post. A very dense soil acts as a fixation for the post, and the steel section yields and forms a plastic hinge under quasi-static loading. In contrast, the post rotates as a rigid body in a dense, medium dense or loose soil without any signs of section yielding.

- The failure mode under impact loading depends on the impact intensity and the soil relative density. For the tested intensity range 2.5 kJ to 10 kJ, a high impact energy in a dense soil can induce section plastic strains exactly like a low impact energy in a very dense soil.
- The inadequate or over-compaction of soil layers during road shoulder installation can lead to forming stiffness contrasts along the post embedment. The effect of this stiffness contrast or layering is most significant on the post response, if this layer exists in the upper 20 to 60 cm of the post embedment length.
- A very important design parameter of the VRS is the post embedment length. Each centimetre post length reduction has a positive economic and logistic effect. However, the reduction of the post embedment length can significantly worsen the system performance. The variation of the post embedment length has shown that under quasi-static loading, posts with embedment ≥ 1.1 m exhibit section failure in dense soils. While in very dense soils, posts with embedment ≥ 0.9 m yield under quasi-static loading. This indicates that the failure mode is mainly governed by the relative density and the embedment length, assuming a constant section modulus. This behaviour feature is known for laterally loaded piles, and is the base for the differentiation between long and short piles. The post embedment length was found also decisive for the deceleration under impact loading.
- Increasing the section modulus increases the system stiffness significantly and consequently the reaction force. However, no substantial effect is observed on the deceleration of the colliding body. Under impact loading, increasing the weight of the post per unit length increases the maximum reaction force due to the effect of the post inertia. By decreasing the section modulus, the section is more susceptible to developing plastic strains and failing earlier.
- The influence of the loading height shows that the combination of the shear and bending moment acting on the post is decisive for the failure mode. Increasing the loading height leads to decreasing the post reaction force.

To quantify the influence of each investigated parameter on the post response, unified performance criteria had to be defined for all variations. Ultimately, in a crash test simulation, the performance of the VRS is evaluated based on the capability to absorb impact energy in conjunction with the acceleration severity index (*ASI*) and the dynamic deflection. A VRS is efficient, if it can absorb high impact energy, with a low *ASI* in a limited deflection range [22]. This means the VRS exhibits a high containment level of the colliding vehicles, as well as less deceleration rate jeopardizing the occupants' safety, and can be installed safely in the vicinity of road structures.

In the following section, the influence of the system parameters on the performance of the post is analysed. Thereby, only those parameters exhibiting the most substantial influence on the post response; which are the soil relative density, post embedment length, post section modulus and the loading height, are considered.

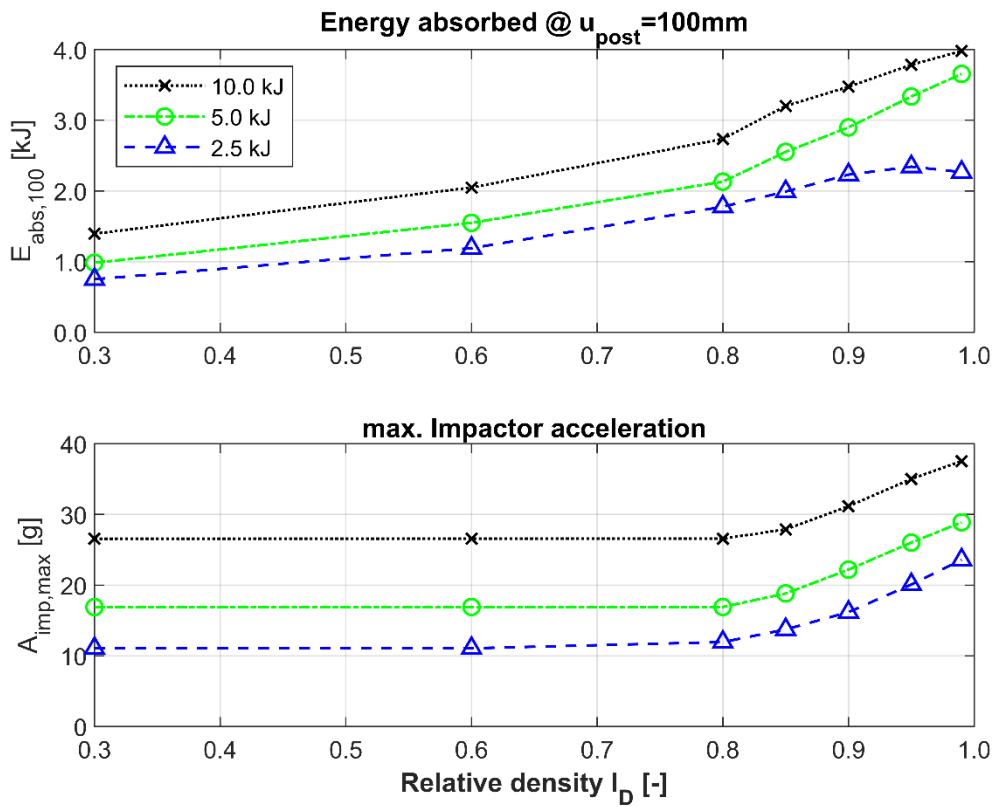


Fig. 5-58: Evaluation of the post performance as a function of the soil relative density

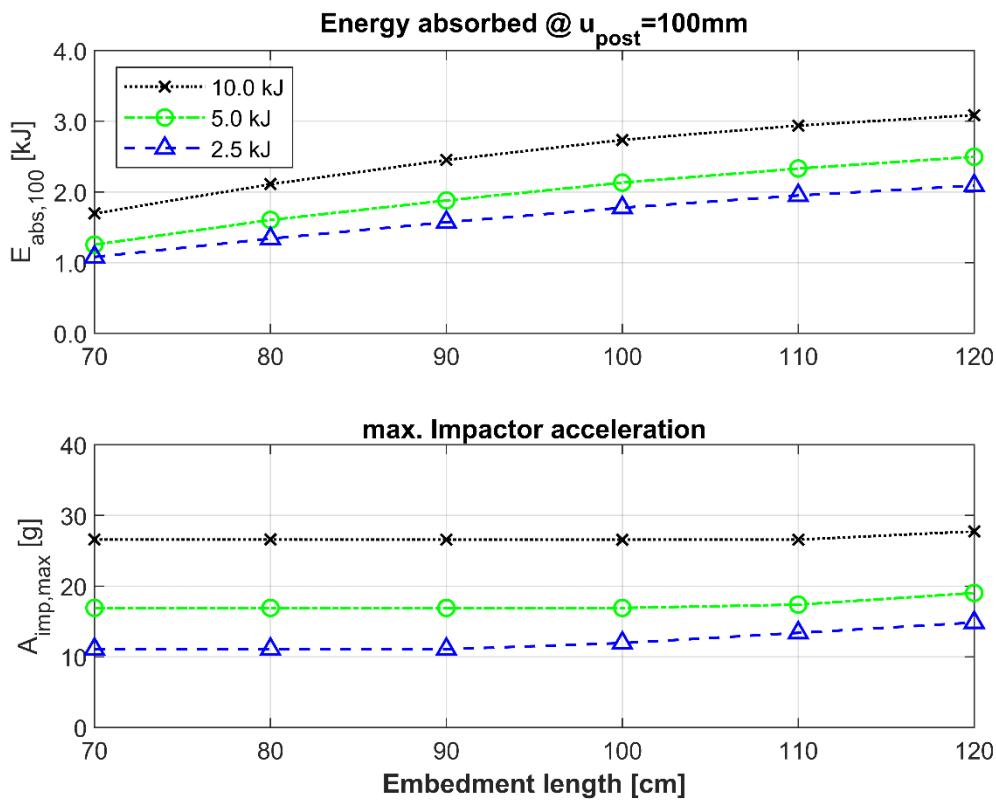


Fig. 5-59: Evaluation of the post performance as a function of the embedment length

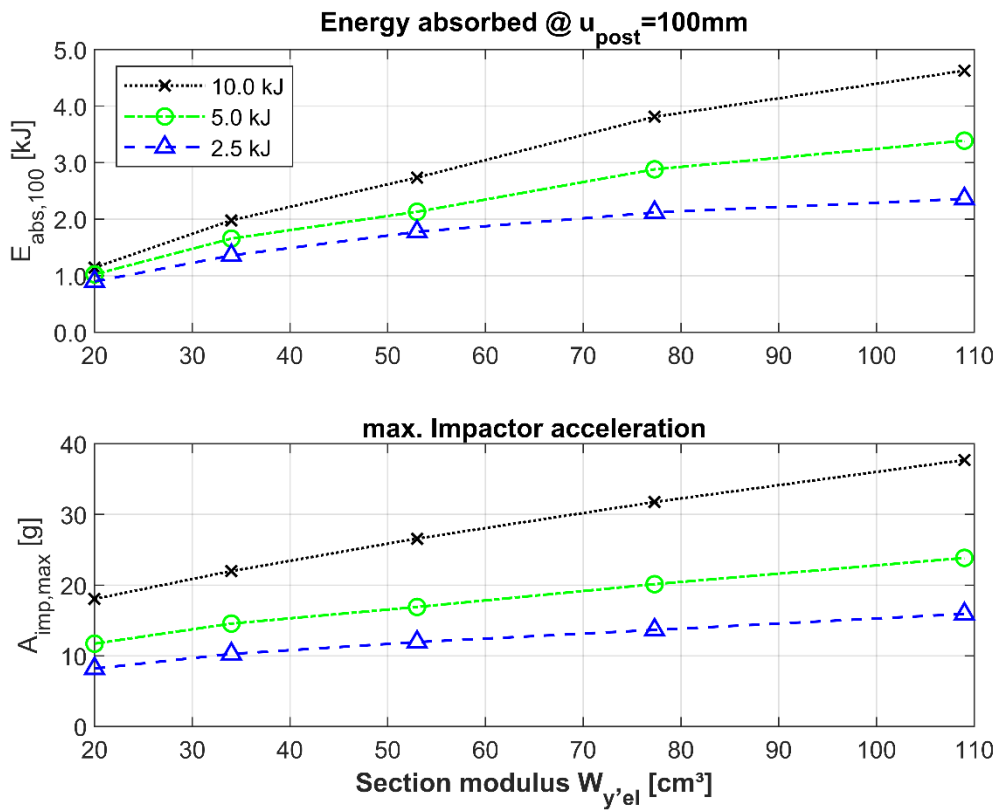


Fig. 5-60: Evaluation of the post performance as a function of the post section modulus

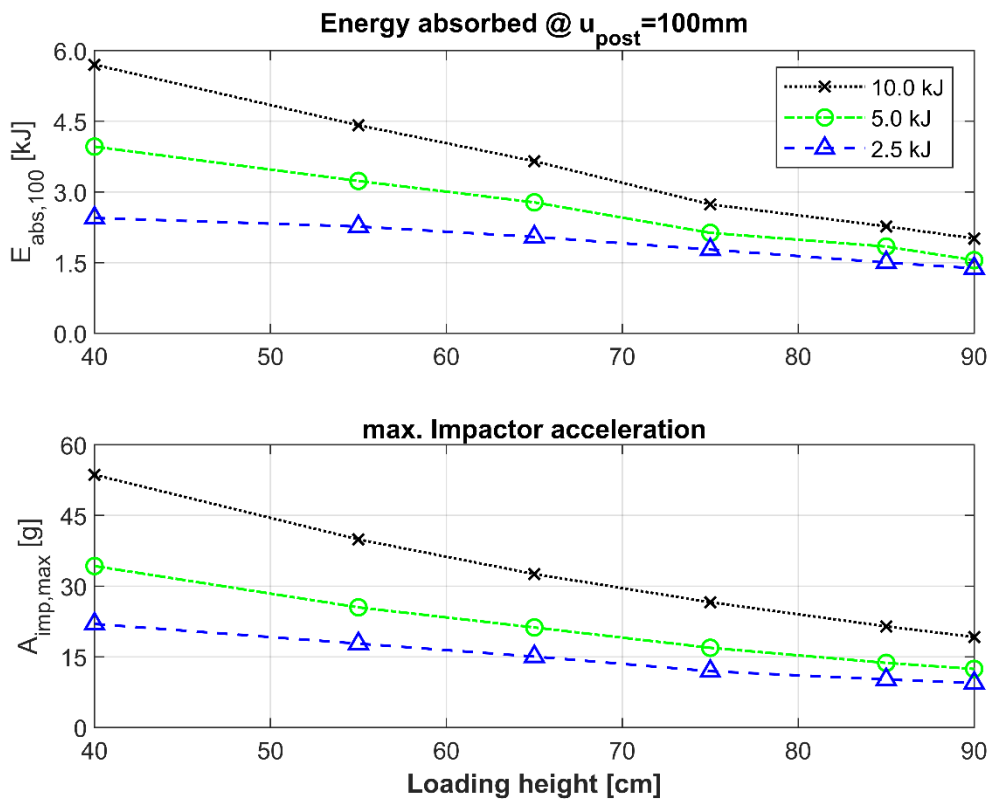


Fig. 5-61: Evaluation of the post performance as a function of the height of loading point

To evaluate the performance of a single post, the following parameters equivalent to the VRS performance criteria are defined [83]:

- $E_{abs\ 100}$: The energy absorbed by the post up to a lateral deflection of 100 mm. The threshold of 100 mm was selected based on the analysed system horizontal stiffness through the parametric study. It has been observed that at 100 mm deflection value, the system stiffness has already dropped to less than 20% of its initial value. Which indicates that the increase of the system resistance beyond this deflection value is not significant.

The value of $E_{abs\ 100}$ is determined as the integration of the post load-deflection curve at the loading point up to 100 mm lateral deflection, and is given in kJ.

- $A_{imp\ max}$: The maximum acceleration measured on the impactor, i.e. colliding body. The maximum impactor acceleration defines the impact force measured at the contact between the post and impactor. Worth mentioning is that the impactor is modelled as a rigid body, which is not the case for a real vehicle. However, the $A_{imp\ max}$ value can give an indication of the relative post-soil response and is not intended for direct comparison with ASI .

The value of $A_{imp\ max}$ is extracted directly from the FEA and is given as a multiple of the gravitational acceleration [g].

The evaluated parameters $E_{abs\ 100}$ and $A_{imp\ max}$ for each variation are presented in Fig. 5-58 to Fig. 5-61. The influence of multiple variables on the absorbed energy $E_{abs\ 100}$ was evaluated at the mean impact intensity of 5.0 kJ by linear interpolation. The interpreted isoline diagrams are shown in Fig. 5-62.

Based on the aforementioned performance analysis results, the following conclusions can be drawn [83]:

- The range of relative density $I_D = 0.8$ to 0.9 is observed to be optimum for the post performance, since the absorbed energy is relatively high and the impactor acceleration is still low in this range.
- Increasing the post embedment length beyond 1.0 m leads to a minor increase in the absorbed energy. The acceleration is nearly unaffected by the embedment length in the investigated range.
- Increasing the section modulus for the IPE post leads to an increase of the absorbed energy as well as the impactor acceleration.
- Lowering the height of the loading point results in increasing the absorbed energy as well as the impactor acceleration. This effect is more significant when increasing the impact energy level.

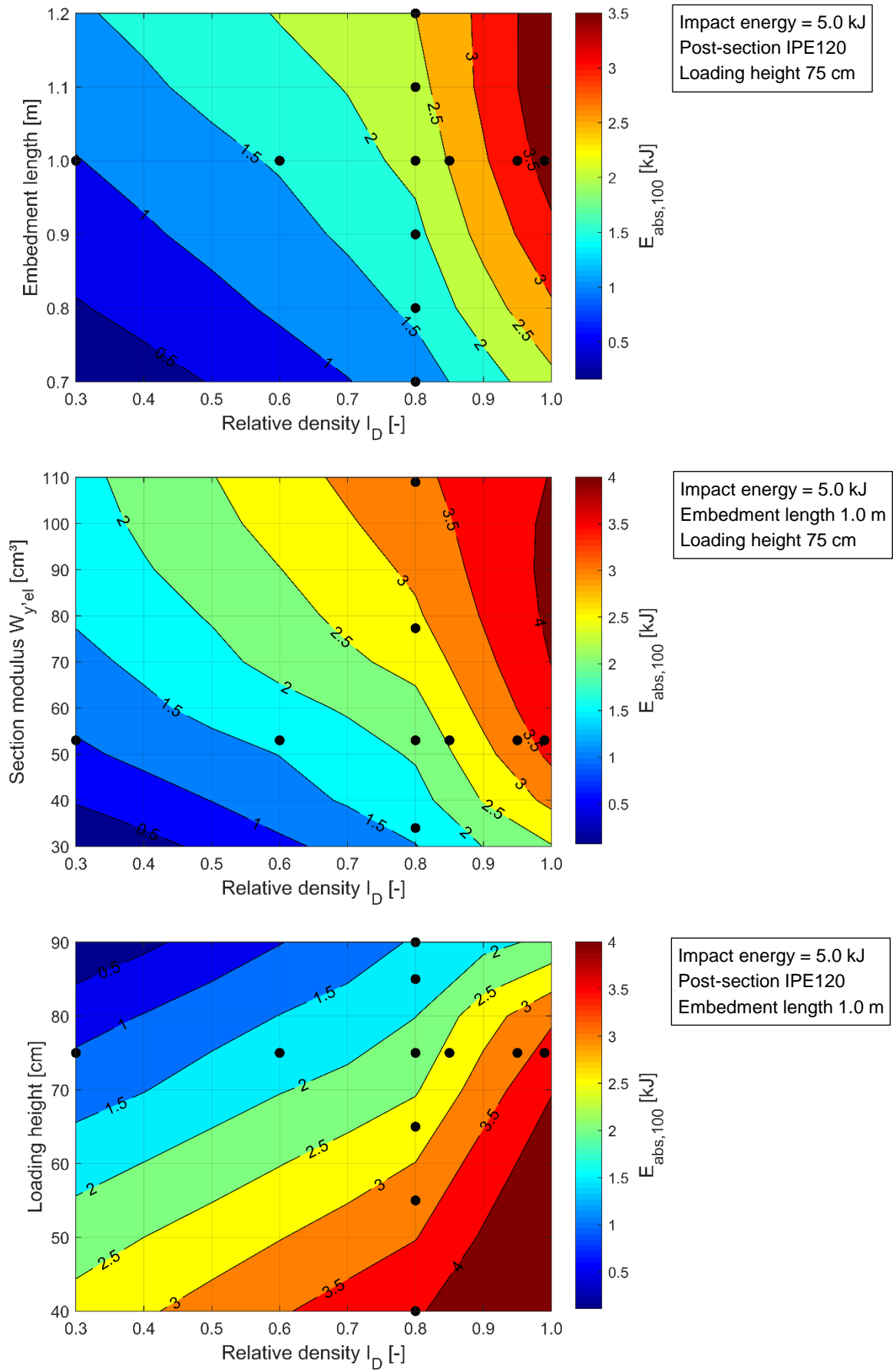


Fig. 5-62: The influence of multiple variables on the absorbed energy $E_{abs,100}$ under an impact energy of 5.0 kJ

6 Analysis of soil-post interaction by means of LPM

In this chapter, the soil-structure interaction of the single guardrail post is simulated and analysed using a two-dimensional mechanical model in which the post is modelled as a beam and the soil resistance with a lumped-parameter model (abr. LPM). The model is developed and implemented using the FE-code ABAQUS for the simulation of the post response under quasi-static and impact loading. The model considers the non-linear soil properties, as well as the soil relative density. A procedure is proposed for the determination of the model parameters from laboratory soil testing. The model assumptions rely on well-established geotechnical engineering literature and standards. The model is intended to accurately simulate the post response with much less computational effort than the FEA with the soil as continuum. The author disseminated the developed LPM and the parameters calibration procedure in the peer-reviewed publication SOLIMAN & CUDMANI [83].

The post strains measured in the full-scale field tests are used to derive the lateral load-transfer curves, i.e. p-y curves. The p-y curves are an experimental evidence utilised for the development and validation of the LPM. Therefore, the derivation of the p-y curves is discussed in the first section. The post response obtained using the LPM is compared to the quasi-static and dynamic impact field tests. The quasi-static results are further compared to the approaches available in the literature for laterally loaded piles.

6.1 Experimental p-y curves

In the loading tests, the posts were instrumented with strain gauges mainly for the purpose of the analysis of the soil-post interaction at each loading step. The post instrumentation included additional sensors attached at the loading point and at a point near the ground level to determine the total lateral displacements. More details regarding the post instrumentation are presented in chapter 3 *Full-scale testing of single posts*. Using the strain gauge readings combined with the force measurements, the lateral load-transfer curves can be assessed along the post embedment length. The derivation of p-y curves from instrumented laterally loaded posts can be concluded in four steps. The equations used in each step are listed in a flow chart form in Table 6-1. The following procedure is only valid in the elastic range of the post material [85] [82]:

- (a) Determination of the curvature versus depth profile from the measured strain data.

The bending strains ε_{Mb} are measured at discrete sections along the post and the section curvature κ is calculated as the bending strain divided by the section height (Equ. 6-6 and Equ. 6-7). A continuous curvature profile $\kappa(z, t)$ is deduced by means of piecewise polynomial curve fitting (Equ. 6-8). Above the ground level, the curvature profile is linear between the loading point and the strain gauge section at 5 cm above GL. The curvature above the loading point is equal to zero. Below the ground level, the curvature profile is fitted using a 5th-order polynomial. For this assumption, two further curvature values are required besides the four measured sections. The first value is $\kappa = 0$ at the post-toe and the second value is extrapolated from the linear segment above GL to the ground line at $z = 0$.

- (b) Derivation of the pile deflection versus depth profile using double integration of the curvature versus depth profile.

First, the piecewise polynomial curvature profile is integrated once to get the elastic rotation profile $\theta_{el}(z, t)$. The total rotation $\theta_t(z, t)$ is equal to the sum of the elastic section rotation around the neutral axis $\theta_{el}(z, t)$ and the rigid body rotation of the post $\theta_{rb}(z, t)$. The rigid body rotation of the post $\theta_{rb}(z, t)$ can be assumed linear, as long as the post section does not reach plasticity. $\theta_{rb}(z, t)$ is calculated as the difference between the lateral post displacement measured at the loading point and the point at 5cm above GL (Equ. 6-4 and Equ. 6-5). The total rotation profile versus depth $\theta_t(z, t)$ is then integrated to get the total lateral deflection profile $y_t(z, t)$ (Equ. 6-3). In general, the lateral deflection of the post can be deduced as double integration of the section curvature over depth.

$$y(z, t) = \iint_{z=0}^{z=L} \kappa(z, t) dz \quad \text{Equ. 6-1}$$

- (c) Derivation of the net soil resistance profile along the embedment length using double differentiation of the moment versus depth profiles.

The piecewise polynomial curvature profile is multiplied by the post flexural rigidity $E_p I_p$ to determine the moment versus depth profile $M(z, t)$ (see Equ. 6-9 to Equ. 6-11). The post material is assumed to be homogenous and exhibit uniform section modulus along its length. The moment distribution is differentiated once to obtain the shear force distribution $V(z, t)$ and differentiated twice to get the line load profile i.e the soil reaction per unit length $p(z, t)$ of the embedment

$$p(z, t) = \frac{d^2}{dz^2} (E_p I_p \cdot \kappa(z, t)) \quad \text{Equ. 6-2}$$





- (d) Formulation of the soil reaction-deflection curves at discrete depth increments

The soil reaction profile and lateral deflection profile versus depth are derived for each time increment. Combining these data in a matrix form, the soil pressure and lateral deflection pairs for a given depth increment can be plotted for each time increment to construct the load transfer curves at different depths.

Since the posts are loaded mainly in the lateral direction, the effect of the normal forces acting in the post axis are neglected in this approach.

The p-y curves derived from the quasi-static reference test measurements (IPE120, KSS032, $I_D = 0.8$) are presented in Fig. 6-1. The depth increment is chosen to $z = 0.1 m$. The curves show a characteristic that can be compared to a hyperbolic function. The set of curves on the right-hand side are those derived for the post segment above the rotation point. The set of curves on the left-hand side are those derived for the post segment below the rotation point, and therefore presented as negative deflections. The initial stiffness lies nearly in the same range of 0.5 to 0.6 kN/mm with a slight increase with depth. This range coincides with the post horizontal stiffness determined at the loading point from the field test and the FEA in chapter 5 (see Fig. 5-10c). The straight segment, representing the elastic range of the soil before yielding, shows an increase with depth.

Table 6-1: Relationships used for the development of the p-y curves from the measured strain values

Variable	Description	Formula	Units	Equation
Deflection	Total lateral deflection incl. rigid body displacement	$y_t(z, t) = \int \theta_t(z, t) dz$	[m]	Equ. 6-3
Total rotation	Total post rotation incl. rigid body rotation	$\theta_t(z, t) = \theta_{el}(z, t) + \theta_{rb}(z, t)$	[rad]	Equ. 6-4
Elastic rotation	Section rotation around neutral axis	$\theta_{el}(z, t) = \int \kappa(z, t) dz = \frac{dy}{dz}$	[rad]	Equ. 6-5
 Integration 				
Strain measurements	Bending strain measured discrete values	$\varepsilon_{Mbi} = \frac{ \varepsilon_{1i} + \varepsilon_{2i} }{2}$	[$\mu m/m$]	Equ. 6-6
Curvature	Curvature calculated discrete values	$\kappa_i = \frac{\varepsilon_{Mbi}}{h} = \frac{d^2y}{dz^2}$	[rad/m]	Equ. 6-7
Curvature function	Piecewise polynomial function	$\kappa(z, t) = f(\kappa_i)$	[rad/m]	Equ. 6-8
Bending moment	Continuous bending moment function	$M(z, t) = E_P I_P \cdot \kappa(z, t)$ $= E_P I_P \cdot \frac{d^2y}{dz^2}$	[kN.m]	Equ. 6-9
 Differentiation 				
Shear force	First derivative of the bending moment function	$V(z, t) = \frac{d}{dz} M(z, t)$ $= E_P I_P \cdot \frac{d^3y}{dz^3}$	[kN]	Equ. 6-10
Soil reaction	Second derivative of the bending moment function	$p(z, t) = \frac{d}{dz} V(z, t)$ $= E_P I_P \cdot \frac{d^4y}{dz^4}$	[kN/m]	Equ. 6-11

where;

$E_P I_P$: is the post flexural rigidity

z : is the post length increment

t : is the time increment

h : is the post-section height

$\varepsilon_1, \varepsilon_2$: are the strains measured on the outer sides of the flanges

Index el : for elastic deformations

Index rb : for rigid body displacement

The ultimate soil resistance is also observed to be depth-dependent. The ultimate soil resistance reached is 105 kN/m at 0.5 m below GL and 141 kN/m at the post-toe. The soil resistance increases approximately linearly after reaching the yielding point, without a softening phase, except at the post-toe, where a short softening phase before unloading is observed.

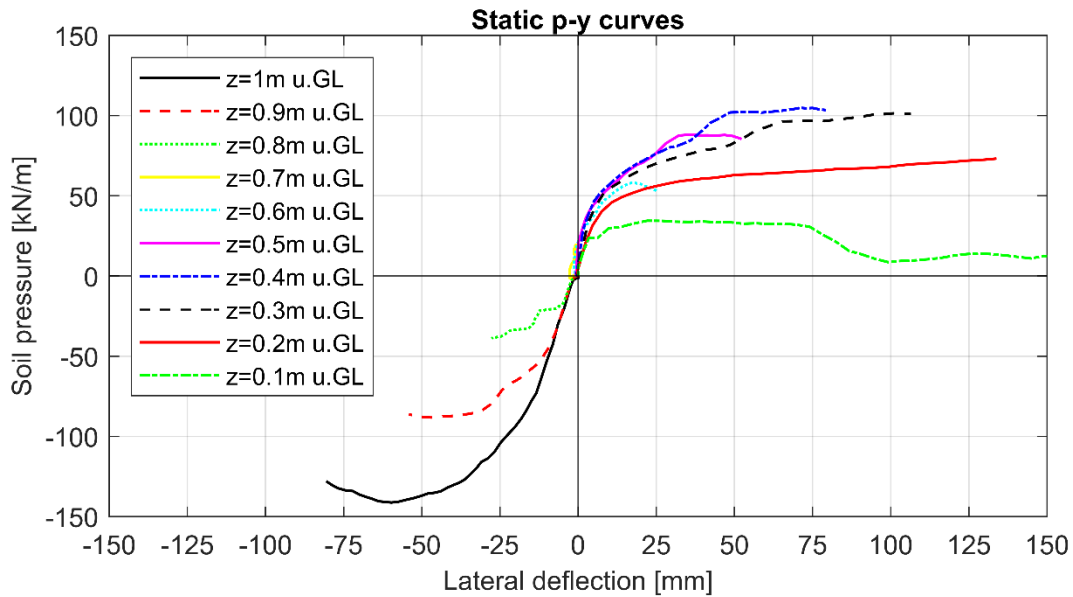


Fig. 6-1: p-y curves derived from experimental data for the reference test under quasi-static loading

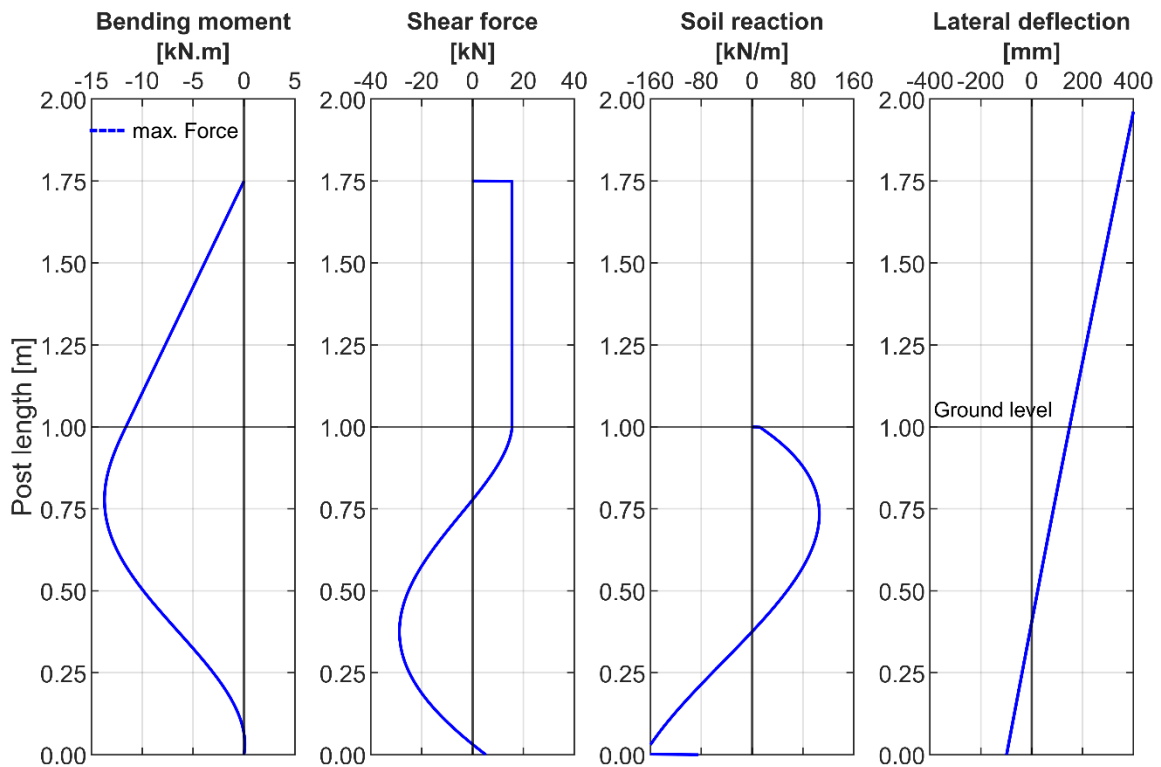


Fig. 6-2: Experimental results at 340mm lateral deflection ($F_{max}=15.3kN$); post straining actions and deflection profile under quasi-static loading

The bending moment, shear force, soil resistance and lateral deflection profiles derived from the measured strains at reaching the maximum reaction force are shown in Fig. 6-2. The maximum bending moment is reached at a depth of ca. 0.22 m below GL, which is the point of zero shear force. At this elevation, the posts loaded in the transversal direction was observed to develop a plastic hinge due to the stress concentrations. The post rotation point is located at 0.62 m below ground level.

Under static loading conditions in the elastic range of the material, and assuming no axial force acting on the post, P_{stat} is described by the Bernoulli beam equation as follows:

$$EI \frac{\partial^4 y(z)}{\partial z^4} - P_{stat} = 0 \quad \text{Equ. 6-12}$$

$$EI \frac{\partial^4 y(z)}{\partial z^4} - \mathbf{k}(y, z) \cdot \mathbf{y}(z) = 0 \quad \text{Equ. 6-13}$$

where; $\mathbf{k}(y, z) \cdot \mathbf{y}(z)$ is the spring resistance.

Under impact loading conditions, based on the Bernoulli beam equation and considering the inertial and damping effects, the system reaction components to lateral transient loading $F(t)$ can be written as follows:

$$EI \frac{\partial^4 y(z, t)}{\partial z^4} - [M(z) \frac{\partial^2 y(z, t)}{\partial t^2} + k(y, z) \cdot y(z, t) + c(z) \cdot \frac{\partial y(z, t)}{\partial t}] = 0 \quad \text{Equ. 6-14}$$

$$EI \frac{\partial^4 y(z, t)}{\partial z^4} - [P_{dyn}] = 0 \quad \text{Equ. 6-15}$$

where the sum of the inertial force $M(z) \frac{\partial^2 y(z)}{\partial t^2}$, the non-linear spring resistance $\mathbf{k}(y, z) \cdot \mathbf{y}(z)$ and the damping component $c \cdot \frac{\partial y(z)}{\partial t}$ forms the dynamic soil reaction. The spring resistance is assumed to be independent of the loading rate. This assumption is verified later in the LPM model's validation process.

The p-y curves derived from the dynamic impact test measurements under reference conditions (IPE120, KSS032, $I_D = 0.8$) are presented in Fig. 6-3. Here, the p-y curves are derived for the impact energy of 3.2 kJ. The depth increment is chosen to $z = 0.1 \text{ m}$. The derived pressure values include inertial and damping effects. Therefore, these unit load-displacement curves depend on the impact intensity and are presented here only for comparison with the quasi-static curves. The curves show a linear behaviour in the first phase up to a deflection of ca. 10 mm. This is nearly the same range in which the static p-y curves are linear. Compared to the results of the FEA, these values correspond well to the horizontal stiffness calculated from the load-deflection curves (see Fig. 5-25c under 5.3 *Simulation of the impact loading*). The curve derived at the first 0.1 m shows unexpectedly a higher resistance and a sudden drop, which can be attributed to the observed catapulting of the soil grains at the ground surface. The ultimate soil resistance reached is 132 kN/m at 0.4 m below GL and 164 kN/m at the post-toe.

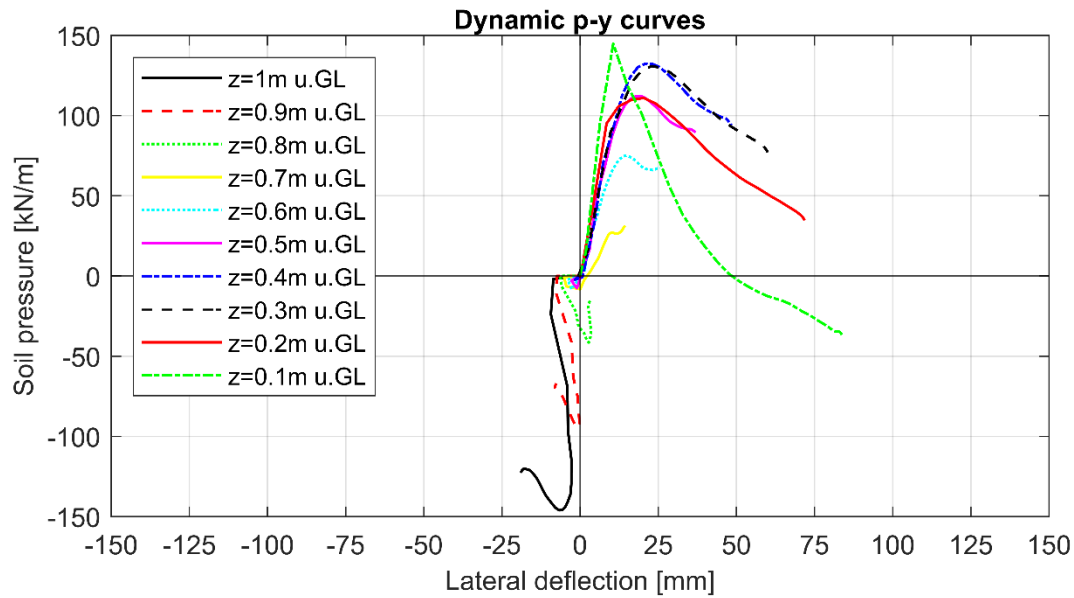


Fig. 6-3: p-y curves derived from experimental data for the reference test under impact loading with 3.2 kJ

Under impact loading, the maximum force is reached at a time point earlier before reaching the maximum post deflection. Therefore, the bending moment, shear force, soil resistance and lateral deflection profiles were derived at two time points: maximum impact force and maximum deflection (see Fig. 6-4). The maximum bending moment is reached at a depth between 0.20 and 0.25 m below GL. At this elevation, the posts loaded with higher impact intensities were observed in the field test to develop plastic deformation. The post rotation point is located between 0.60 and 0.75 m below ground level.

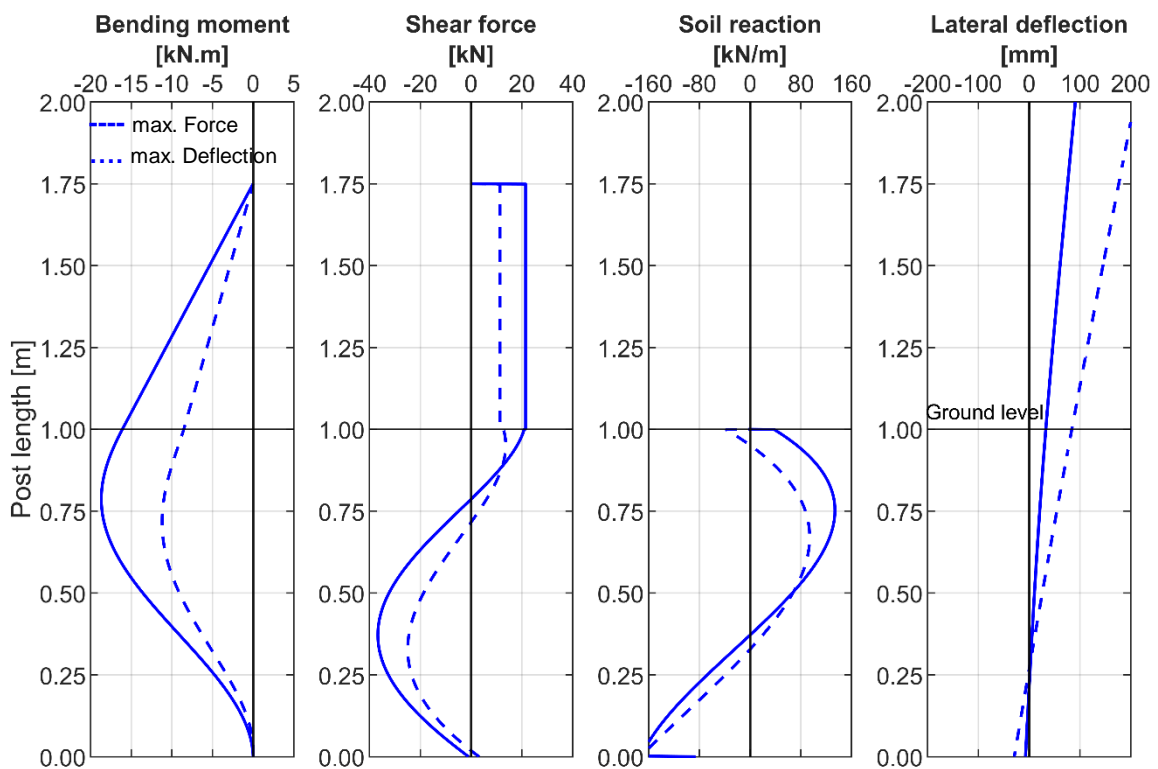


Fig. 6-4: Experimental results under impact loading with 3.2 kJ; post straining actions and deflection profile at maximum lateral deflection ($u_{max}=176\text{mm}$) and at maximum impact force ($F_{max}=21.9\text{kN}$)

6.2 Lumped-Parameter model for guardrail posts

The post-soil system is modelled using a MDOF lumped-parameter model, based on the horizontal subgrade method. The post is modelled as a two-dimensional beam laterally loaded in one axis. The soil along the embedment length is substituted by a series of discrete non-linear elastoplastic springs to model the soil reaction. This approach is also known in the literature as 'Beam on non-linear Winkler foundation'. Without further modifications, this model can calculate the bearing behaviour of the posts under quasi-static loading. The model is extended to simulate the post behaviour under impact loading. To include the damping effects, i.e. energy dissipation in the surrounding soil, dashpot elements are added in parallel to the springs. The inertial effect of the soil mass is modelled as discrete lumped mass points at the elevations of the springs. A schematic representation of the proposed LPM is shown in Fig. 6-5.

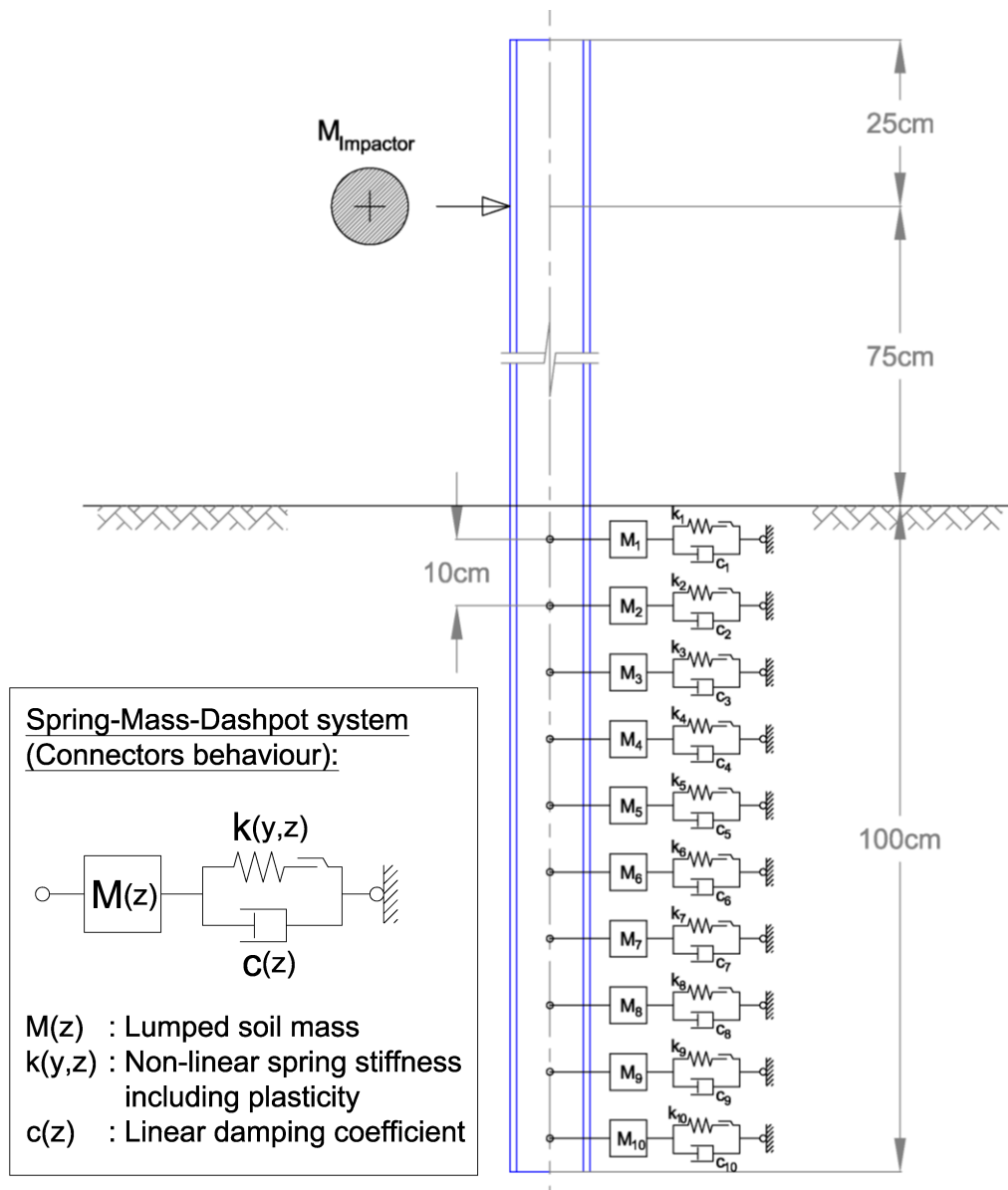


Fig. 6-5: Proposed lumped-parameter model for the simulation of the soil-post interaction

The LPM can be used to estimate the reaction force and post deflection with less computational effort compared to the FEA, in which the soil is modelled as continuum. The simulation of the post response using a spring-mass-damper system has been investigated by several scholars for different applications, e.g. SASSI & GHRIB [79] for guardrail posts and ASADOLLAHI & BRIAUD [56] for in-line pile group barriers. In these studies, the model parameters had to be partially estimated either through calibration to a field test or a FEA. Moreover, these models were developed to simulate only the impact loading case.

The proposed model is envisaged to simulate the post response under quasi-static and impact loading using one set of input parameters. The required parameters for standard road shoulder materials can be determined from a simple laboratory test program comprising relative density, oedometer and angle of repose tests.

The model is implemented in ABAQUS v2017 and run using the implicit solver for both, quasi-static and dynamic simulations. The beam is modelled using B23 elements and an elastic-perfectly plastic steel material. The rate-dependent steel strength is modelled using the power law by COWPER & SYMONDS (for further details, see 5.2 *Steel and rubber material models*).

The soil is discretised in 10 cm segments along the embedment length of 100 cm. The soil stiffness and damping properties can be modelled either using non-linear elastic SPRING2 and DASHPOTA elements or CONNECTOR elements. The CONNECTOR elements allow for definition of several constitutive behaviour properties for an element connecting two nodes.

Both approaches have been applied and found to deliver equivalent results under the first loading. However, the irreversible soil deformations could only be simulated in ABAQUS using CONNECTOR elements. Thus, the soil response is modelled in each segment using CONNECTOR elements connected to a hinged node on the post. The connector non-linear elasticity is defined by force and displacement couples for the positive and negative deflection direction. The soil plastic limit is defined as the depth-dependent ultimate soil resistance. After reaching this limit, the developed deflections afterwards are irreversible. A linear damping behaviour is defined for the connectors to allow for energy dissipation, due to elastic wave propagation outside the plastic zone. The soil mass is defined using additional point MASS elements attached to the post in each segment. The mass of the post is considered automatically through the steel material density.

For the case of quasi-static loading, a prescribed displacement is applied at the loading point. For dynamic loading, the impactor is simulated by a rigid mass colliding with the post with a predefined velocity. The loading height is set to 75 cm above ground level. The same model with the same CONNECTOR behaviour parameters is applied for both loading cases.

Components of the soil resistance model

The applied approach, model assumptions and determination of the input parameters are discussed in this section:

- **Non-linear spring model**

The depth-dependent relationship between the lateral soil-pile resistance and the lateral deflection can be described by empirical load-transfer curves, so-called p-y curves, which need to be calibrated either to full-scale field or model tests [73]. However, in an attempt to eliminate the necessity of lateral loading tests, load-transfer functions have been proposed in the literature, whose parameters are directly correlated to soil properties. For cohesionless soil, the non-linear p-y curves can be described, for example by a piecewise linear function (SCOTT 1980), a hyperbolic function (KONDNER 1963) or a combination of linear and parabolic segments (REESE et al. 1974). The piecewise approaches require a predefinition of the transition deflections, which consequently requires additional empirical parameters or calibration factors valid for a specific deflection range. In contrast, besides its simplicity of implementation, the hyperbolic function exhibits one continuous function for the full deflection range.

The hyperbolic function proposed by KONDNER [43] has the advantage of incorporating the initial soil stiffness k_{ini} and ultimate soil resistance P_{ult} without any further empirical factors to estimate the soil reaction per unit length P_{stat} :

$$P_{stat} = \frac{y}{\frac{1}{k_{ini}} + \frac{y}{P_{ult}}} \quad \text{Equ. 6-16}$$

This function is chosen for the characterisation of the non-linear spring stiffness under quasi-static as well as impact loading.

- **Initial subgrade reaction modulus**

Adopting the subgrade reaction modulus approach recommended by the EAP [36], the initial soil stiffness k_{ini} can be estimated as a function of the oedometric soil modulus E_s :

$$k_{ini} = E_s / D_{equ} \quad \text{Equ. 6-17}$$

where; D_{equ} is an equivalent circular post diameter calculated based on the post outer perimeter. The distribution in the oedometric stiffness modulus over the embedment length can be estimated using the power function after OHDE 1939:

$$E_s = v \cdot \sigma_{ref} \left(\frac{\sigma_z}{\sigma_{ref}} \right)^\omega \quad \text{Equ. 6-18}$$

where; v and ω are the material-dependent OHDE constants defining the initial shape of the increase of stiffness with the effective overburden stress. The coefficients v and ω were calibrated to the conducted odometer test on the KSS032.

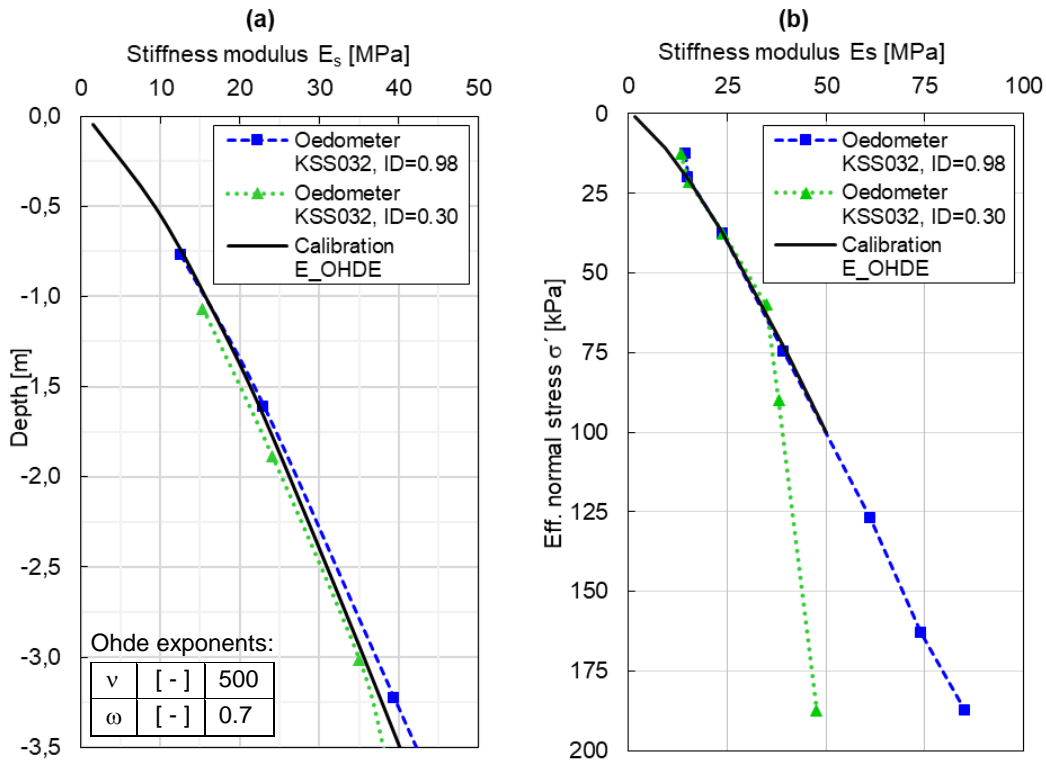


Fig. 6-6: Calibration of the soil stiffness modulus to the experimental data (a) variation over depth (b) variation over effective normal pressure

The distribution of the calibrated stiffness modulus is shown in Fig. 6-6. The calibrated coefficients were found to be in line with the values recommended by the committee for "Waterfront Structures, Harbours and Waterways" EAU 2012 [34] for silty gravel. So, in the absence of large oedometer tests, the coefficients ν and ω can be assumed accordingly.

• Ultimate soil pressure

The mobilised soil resistance values and distribution play a governing role in estimating the total post reaction force, especially for a shallow embedment length. In the case of a short laterally loaded pile, the ultimate pressure mobilised in front of the post above the rotation point and behind the post below the rotation point cannot exceed the three-dimensional passive earth pressure. This is assuming that the drag force in the pile toe is minor and can be neglected. As per the German standard DIN 4085 [21], the horizontal three-dimensional passive earth-pressure force per meter E_{pgh} can be calculated for a non-cohesive soil as:

$$E_{pgh} = \frac{1}{2} \cdot \gamma \cdot z^2 \cdot K_{pgh} \cdot \mu_{pgh} \quad \text{Equ. 6-19}$$

where K_{pgh} is the passive earth pressure coefficient due to own weight of soil, μ_{pgh} is a shape factor considering the narrow pile width. This factor was developed mainly for the calculation of the soil resistance in front of soldier pile wall beams. For beam width-to-height ratio t/D less than 0.3, the shape factor is given by:

$$\mu_{pgh} = 0.55 \cdot (1 + 2 \cdot \tan\varphi') \cdot \sqrt{t/D} \quad \text{Equ. 6-20}$$

The mobilization of the full passive earth pressure requires a relatively large displacement of the laterally loaded element. At the beginning of loading, the lateral deflection is not enough to mobilise the full passive pressure. Therefore, the earth pressure coefficient to be applied ranges between the earth pressure coefficient at-rest K_0 and the passive earth pressure coef. K_{pgh} . According to DIN 4085 [21], the partially mobilised passive earth pressure E^*_{pgh} can be estimated as follows:

$$E^*_{pgh} = (E_{pgh} - E_{0gh}) \cdot \left[1 - \left(1 - \frac{y}{y_p} \right)^b \right]^c + E_{0gh} \quad \text{Equ. 6-21}$$

where y/y_p is the ratio of the element displacement to the displacement required for the mobilisation of the full passive earth pressure. For $y < y_p$ the mobilised earth pressure E^*_{pgh} is between E_{0gh} and E_{pgh} . For $y \geq y_p$, full E_{pgh} is mobilised. The exponents b and c are constants and are given by 1.5 and 0.7 for non-cohesive soils.

The value of y_p depends on the deflection form of the element, whether rotation at the pile head, at pile toe or parallel displacement. The reference values of y_p recommended in DIN 4085 for granular soils exhibiting $I_D > 0.3$ are expressed as follows:

$$y_p = \begin{cases} z \cdot (-0.08 \cdot D + 0.12) & \text{Rotation at pile toe and parallel displacement} \\ z \cdot (-0.05 \cdot D + 0.09) & \text{Rotation at pile head} \end{cases} \quad \text{Equ. 6-22}$$

For simplicity, a mean value of y_p is assumed for the post above and below the rotation point, since the rotation point depth is unknown in advance. Moreover, the experimental field tests have shown that the location of the rotation point changes with increasing lateral deflection.

As discussed earlier, the shear failure envelope is curved rather than linear in the low overburden pressure range [47]. Moreover, the shear strength parameters of the granular material depend mainly on its relative density. The formula developed by BOLTON [7] correlates the peak friction angle φ' to the critical state friction angle φ_c , the relative soil density I_D and the mean effective stress at failure p' :

$$\varphi' = \varphi_c + \Delta\varphi \cdot I_D \left[Q - \ln \frac{p'}{p_{ref}} \right] - R \quad \text{Equ. 6-23}$$

where $\Delta\varphi = 3$, $Q = 14$ and $R = 3$ are material grain type dependent factors estimated through experimental testing by BOLTON for limestone. Using this relationship, the peak friction angle can be determined and is assumed to be constant along the post embedment.

Considering all the above-discussed aspects, the distribution of the mobilised earth pressure over depth for laterally loaded posts can be calculated as follows:

$$P_{ult} = \mu_{pgh} \cdot K^*_p \cdot D_{equ} \cdot \gamma' \cdot z^n \quad \text{Equ. 6-24}$$

$$K^*_p = (K_p - K_0) \cdot \left[1 - \left(1 - \frac{y}{y_p} \right)^b \right]^c + K_0 \quad \text{Equ. 6-25}$$

$$K_p = \frac{1 + \sin \varphi'}{1 - \sin \varphi'} \quad , \quad K_0 = 1 - \sin \varphi' \quad \text{Equ. 6-26}$$

where, the compaction pressure influence is considered indirectly through the exponent n .

As discussed in section 5.1 *Finite element model*, the compaction pressure leads to an increase of the lateral pressure in the upper soil zone. By introducing a factor $n = 0.5$, the ultimate soil pressure increases in the very shallow layers significantly and approaches the unadapted earth pressure values at the post-toe at the depth $z = 1.0\text{m}$. This assumption fits very well to the derived experimental static p-y curves (see Fig. 6-1 versus Fig. 6-7). This approach was also applied by TAK & KIM et al. [86] for the characterisation of static load-transfer curves for shallow embedded laterally loaded model piles in sands. The static p-y curves generated using the above-mentioned approach are shown in Fig. 6-7. Comparing the computed maximum soil reaction to the experimental values shown in Fig. 6-1 at different depths, the values are very close (at $z = 0.1\text{m}$: $\frac{\text{computed}}{\text{experimental}} = \frac{43}{36} \text{ kN/m}$ and at $z = 1.0\text{m}$: $\frac{\text{computed}}{\text{experimental}} = \frac{138}{141} \text{ kN/m}$).

The input parameters used for the generation of the static p-y curves are listed in Table 6-2. The damping parameters are described in the following section.

Table 6-2: Input parameters for the Lumped-parameter model

Description	Parameter		Value
p-y curves			
Critical state friction angle	φ_c	[°]	35.7
Relative density	I_D	[-]	0.80
Soil effective weight	γ'	[kN/m ³]	21.3
Equivalent post diameter	D_{equ}	[m]	0.12
Ohde coefficient	ν	[-]	500
Ohde exponent	ω	[-]	0.7
Reference pressure	σ_{ref}	[kN/m ²]	100
Depth exponent	n	[-]	0.5
Passive pressure mob. exponents	b/c	[-]	1.5/0.7
Damping coefficient			
Poisson's ratio	ν	[-]	0.35
Soil unit weight	ρ	[t/m ³]	2.13
Small-strain stiffness ratio	G_{max}/E_s	[-]	4.5
Novak damping parameter	S_{u2}	[-]	2.0
Damping reduction factor	x	[-]	0.01

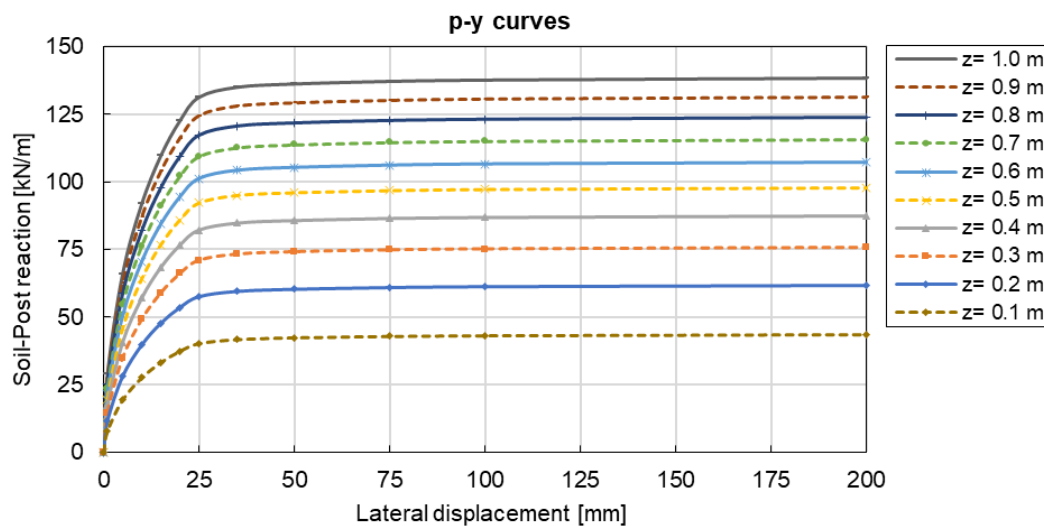


Fig. 6-7: Generated static soil resistance-displacement curves for IPE posts in reference soil conditions

- **Modelling irreversible soil deformations**

Since the soil undergoes irreversible deformations during quasi-static and impact loading of the posts, the plasticity feature of the soil cannot be neglected. This material behaviour is also very important to be considered when simulating the overall response of the VRS under collision. Otherwise, modelling the post-soil system with pure elastic behaviour underestimates the plastic strain energy and leads to full recovery of the post original location, which is not realistic. The irreversible soil deformations were also observed in the experimental field tests under both loading cases (see *sections 3.2 and 3.3*).

The applied CONNECTOR elements enable the definition of a plastic behaviour. The plastic behaviour is assumed to begin, when the deflection y_p required to mobilise the full passive resistance at each depth is reached.

- **Soil damping**

The main mechanisms responsible for dissipation of energy in the case of laterally impacted posts are material damping in the soil and post materials in form of plastic work as well as mechanical wave radiation in the soil domain. In general, the main sources of damping considered in soil-structure interaction problems include [45]:

- **Material damping:** This type of damping arises due to the inherent viscous and frictional characteristics of the soil particles. The rearrangement of soil particles, e.g. due to a stress wave propagating through the medium, results in energy dissipation due to the intergranular friction, the pore-fluid viscosity and the grain structure rearrangement. The dissipated mechanical energy is converted into heat. This phenomenon can be observed in the hysteretic stress-strain response of soils under cyclic loading. In the post material, damping results from the movement and dislocations within the crystalline structure of the steel, which generates heat due to friction.
- **Radiation damping:** (also known as geometric damping) This type of damping occurs due to the spreading of the stress wave energy over a larger volume of material. For boundary value problems, where the excitation source is finite, e.g., an earthquake epicentre or a vibrating machine placed on a foundation, radiation damping is dominant compared to

material damping. Further damping types that are also categorised as external damping include mechanical energy dissipation at joints, contact points or supports of the system elements due to relative motion. For large deformation problems, the material damping through plastic strains is much more significant than radiation damping.

The determination of the damping properties of a dynamically loaded system is complex due to the superposition of different phenomena, e.g., viscosity, interface properties, and the problem's geometric conditions. For engineering applications, the different energy dissipation effects in the system can be lumped in a damping parameter to help represent the system in a convenient mathematical way. However, the damping elements' properties and arrangement depend on the studied problem. NOGAMI et al. [61] considered two concentric zones around the pile for the pile dynamic lateral response analysis. In the vicinity of the pile, i.e. the near-field, the material damping is defined by non-linear dashpots. In the far-field the radiation damping is considered through a linear dashpot coefficient, where the soil is assumed to exhibit an elastic behaviour. For non-cohesive soils, the near and far-field can be summed up in one element representing mainly radiation damping.

The determination of the damping coefficient c for foundations under harmonic vibration has been studied by many researchers, e.g. NOVAK [62] and MAKRIS & GAZETAS [50]. The damping coefficient, which is derived from closed solutions of the elasticity theory or FEA, is frequency-dependent and cannot be applied directly in the time-domain analysis of the posts under impact loading. The applied force for a post in a crash event is not given in advance, and consequently the excitation frequency is unknown. Therefore, the post response must be analysed in the time-domain, where the frequencies and displacement amplitudes are replaced by incremental time quantities [61].

In 1978, NOVAK et al. [63] proposed an expression for the determination of the dynamic stiffness and the damping coefficient for an embedded cylindrical body, assuming plane strain of the domain under harmonic loading. In terms of viscoelastic behaviour, the viscous damping coefficient was formulated as follows:

$$c = \frac{2 \cdot G_{max} \cdot r_0 \cdot S_{u2}}{V_s} \quad \text{Equ. 6-27}$$

where; G_{max} is the small-strain shear modulus of the soil, r_0 is the near-field influence zone and S_{u2} is the damping factor. The shear wave velocity V_s is determined from the shear modulus and the soil unit weight ρ .

$$V_s(z) = \sqrt{G_{max}(z)/\rho} \quad \text{Equ. 6-28}$$

Substituting in Equ. 6-19, the damping coefficient can be written as follows:

$$c(z) = 2 \cdot \sqrt{G_{max}(z) \cdot \rho} \cdot r_0 \cdot S_{u2} \quad \text{Equ. 6-29}$$

The shear modulus G depends on the shear strain amplitude γ (see Fig. 6-8). For a range of γ up to approximately 10^{-5} to 10^{-2} , granular materials exhibit their maximum shear modulus $G = G_{max}$. With increasing shear strain, the shear modulus decreases significantly. Therefore, G_{max} is also known as the dynamic stiffness, due to its application in small-strain vibration problems [45].

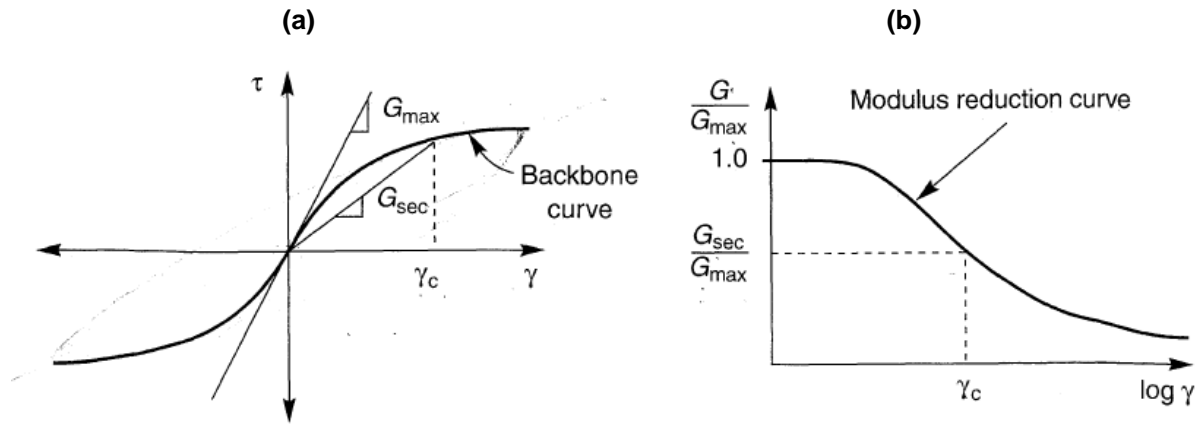


Fig. 6-8: (a) Definition of the secant shear modulus G and (b) the modulus degradation with shear strain amplitude after KRAMER [45]

The correlation between the large-strain oedometric modulus E_s and the small-strain stiffness modulus $E_{s\ dyn}$ and shear modulus G_{max} was investigated experimentally by WICHTMANN & TRIANTAFYLLIDIS [92]. The study findings were adopted by the German committee for Soil dynamics "EA-Baugruddynamik" [35]. For a gravelly well graded sand ($C_u = 4.5, d_{50} = 0.52\text{mm}$), the factor $\eta = G_{max} / E_s$ ranges between 3 and 6 for an oedometric modulus of $E_s = 10\sim 20\text{ MPa}$. For the same E_s range, the ratio $E_{s\ dyn} / E_s$ lies between 10 and 20.

The large-strain shear modulus G can be determined according to the elasticity theory as follows:

$$G = \frac{E_s(1 - 2\nu)}{2(1 - \nu)} \quad \text{Equ. 6-30}$$

where, ν is Poisson's ratio. Applying the small-strain correlations discussed above, the maximum shear strain modulus can be estimated by one of the following equations:

$$G_{max} = \left(\frac{E_{s\ dyn}}{E_s}\right) \cdot E_s \cdot \frac{(1 - 2\nu)}{2(1 - \nu)} \quad \text{Equ. 6-31}$$

$$G_{max}(z) = \eta \cdot E_s(z) \quad \text{Equ. 6-32}$$

The stiffness modulus $E_s(z)$ distribution calibrated from the Oedometer test (see Fig. 6-6) is used for the calculation of $G_{max}(z)$. Applying mean values for $E_{s\ dyn} / E_s = 15$ and $\eta = G_{max} / E_s = 4.5$, both approaches give very close values.

The S_{u2} parameter can be estimated from the correlation developed by NOVAK et al. [63] for horizontal dynamic damping. The S_{u2} parameter is a function of ν and the dimensionless frequency $a_o = r_o \cdot \omega / V_s$. For the observed impact duration of 100 to 140 ms, the loading frequency can be estimated to be ranging from 7 to 10 Hz. Assuming a mean shear wave velocity of $V_s = 150\text{ m/s}$ and a near-field radius r_o equal to the activated wedge extent at each level, a_o ranges between 0.1 and 0.2. For this range S_{u2} is approximately equal 2.0 to 2.5.

The damping coefficient calculated using this approach overestimated the reaction force and underestimated the lateral deflection. This observation has been encountered by other researchers investigating posts under lateral impact [54] [56] [79]. The damping coefficient had to be determined by curve fitting either to experimental or numerical data. This is attributed to the fact that all the established approaches for damping in soils are developed for vibrations in a viscoelastic medium, ignoring the soil's irreversible deformations.

Since, the guardrail posts undergo large lateral deflections and the granular road shoulder material exhibits negligible loading-rate dependency, the material damping in the form of plastic yielding dominates. A small component of the input energy is dissipated by radiation damping. By definition, radiation damping is not an inherent material property and depends on the geometric conditions of the problem. However, the radiation damping increases with increasing shear modulus and density of the material. Therefore, the damping coefficient c , estimated according to the above-discussed viscoelastic approach, had to be significantly reduced. Hence, the damping coefficient c is adjusted by a reduction factor of $x = 0.01$ to fit to the test data (see Table 6-3).

- **Lumped soil mass**

The influence of the mobilised soil mass on the post response cannot be neglected under impact loading. However, the determination of the soil mass and distribution at each depth requires some interpretation. The experimental field tests show soil heaving in front of the post during impact loading. The analysis of the video frames shows vertical vibration of points at ground level extending to ca. 60 cm (see Fig. 6-9).

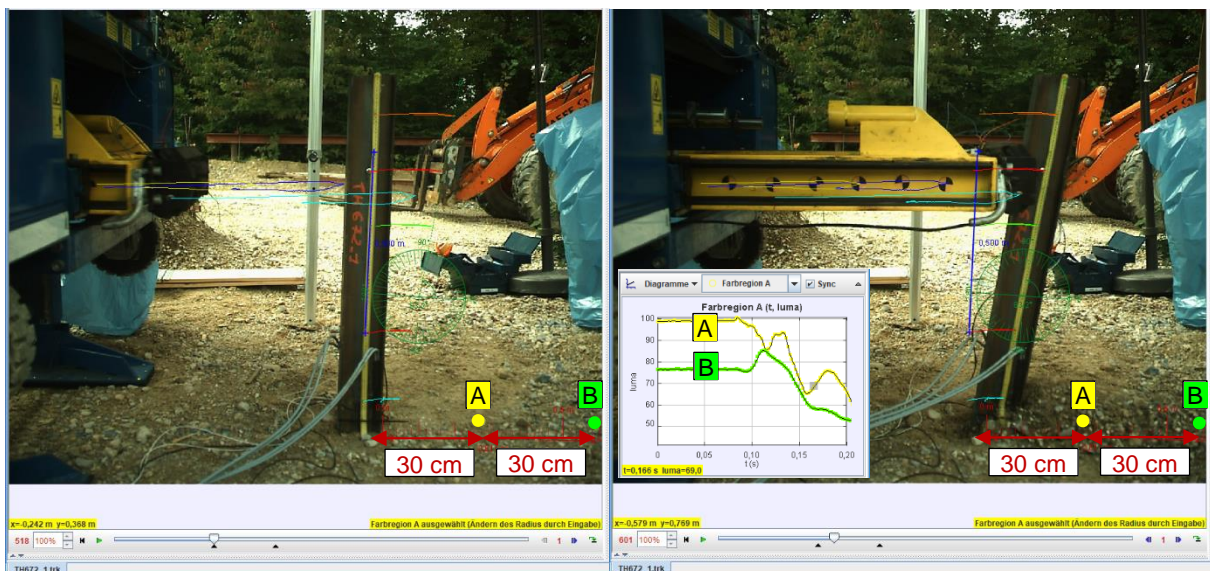


Fig. 6-9: Tracking the vibrations of two points at 30 cm and 60 cm away from post under an impact of 3.2 kJ; (left) position before impact (right) at maximum lateral deflection

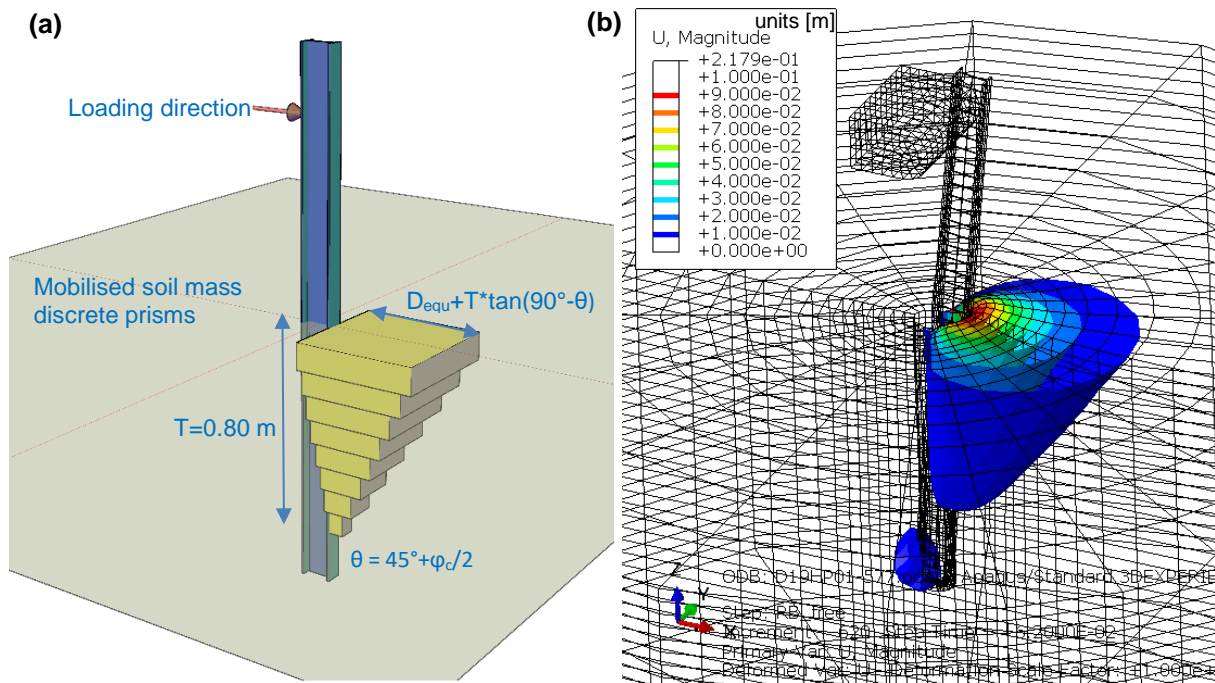


Fig. 6-10: (a) Schematic view of the mobilised mass under impact loading considered for LPM (b) mobilised soil wedge simulated using FE continuum model

This observation is confirmed by the FEA (see 5.3 *Simulation of the impact loading*). The dimensions of the soil wedge contributing to the impact resistance can be estimated based on the FEA by defining a deformation threshold (see Fig. 6-10b). Here, the threshold is assumed to a displacement of 1 cm. The extent of the soil wedge mobilised at ground level was found to range between 55 and 75 cm, depending on the impact intensity. The wedge cross-section in front of the post is approximately circular, with a slightly larger width in the transversal direction. The depth of the wedge below ground level extends to the post rotation point. The inclination angle of the failure surface measured from the horizontal plane is ca. 60° . The wedge length at the rotation point is approximately equal to the equivalent post diameter D_{equ} .

Based on the estimated dimensions, the shape of the soil wedge can be discretised to right prisms with a square base in each depth, as shown in Fig. 6-10a. The prisms have a side dimension of $D_{equ} + (T - z_i) * \tan(90^\circ - \theta)$, and a height of 10 cm. Where, T is the maximum depth of the rotation point. The lumped mass is calculated using the estimated prism volume in each depth and the soil density as $M(z) = \rho * h_i * (D_{equ} + (T - z_i) * \tan(45^\circ - \frac{\phi_c}{2}))^2$.

The calculated lumped mass points and damping coefficients in each depth increment are presented in Table 6-3.

Table 6-3: Lumped soil mass points and linear damping coefficient evaluated along the post embedment length

Depth under ground level	Lumped soil mass	Linear damping coef.
z	$M(z)$	$c(z)$
[m]	[kg]	[kN.s/m]
0.1	59.9	3.47
0.2	48.9	4.06
0.3	39.0	4.22
0.4	30.2	4.14
0.5	22.5	3.89
0.6	16.0	3.51
0.7	10.6	3.02
0.8	6.2	2.44
0.9	3.1	1.79
1.0	1.0	1.07

LPM performance under quasi-static loading

The developed LPM is used to simulate the post response under quasi-static loading. The model configuration is shown in Fig. 6-11.

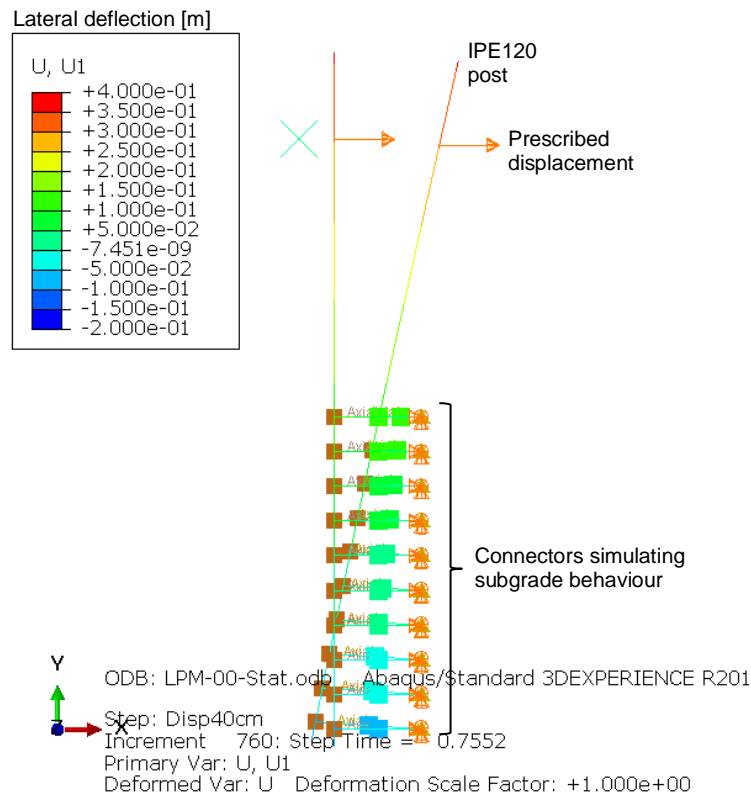


Fig. 6-11: LPM configuration and post deflection under quasi-static loading at 300 mm prescribed displacement of the loading point

The simulation results are compared to the full-scale field data as shown in Fig. 6-12. The results show a very good agreement with the experimental data, regarding the horizontal stiffness, maximum reaction force and post deflection. The performance metrics (described under 5.3 *Validation of the FE Model*) were evaluated for the LPM simulation load-deflection curve and were found equal to $R^2 = 0.94$ and $W = 0.95$. The maximum reaction force exhibits a deviation of maximum 0.5 kN compared to the average experimental value. The maximum force of 14.8 kN is reached at app. 300 mm and increases slightly with the deflection to reach 15.0 kN at 400 mm. The simulated section strains show a maximum deviation of 16% compared to the strain gauge measurements (see Fig. 6-12d). Though the rough conditions in which the strain gauges are installed in-situ, the low deviation indicates that the field experiments and simulations successfully estimated the soil pressure distribution.

The simulated bending moment, shear force, soil resistance and lateral deflection profiles at the maximum reaction force (ca. 300 mm lateral deflection) are shown in Fig. 6-13. The maximum bending moment is reached at a depth of ca. 0.25 m below GL, which is the point of zero shear force. The rotation point is located at 0.70 m below ground level. The results exhibit a good agreement with the measured post deflection and straining actions shown in Fig. 6-4 in section 6.1.

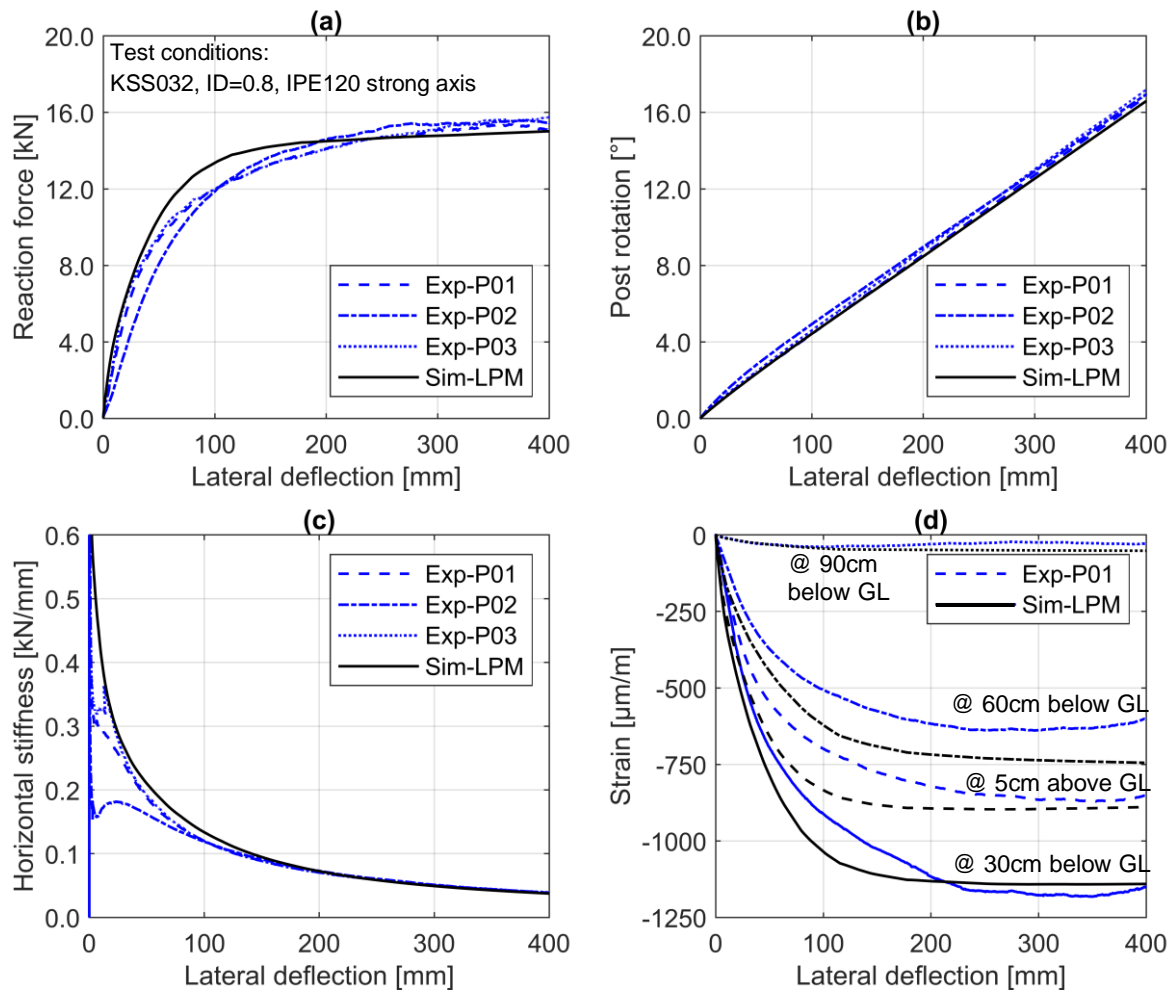


Fig. 6-12: Comparison of the LPM simulation results to the experimental quasi-static field test; (a) reaction force, (b) post rotation, (c) horizontal stiffness at loading point and (d) strain values

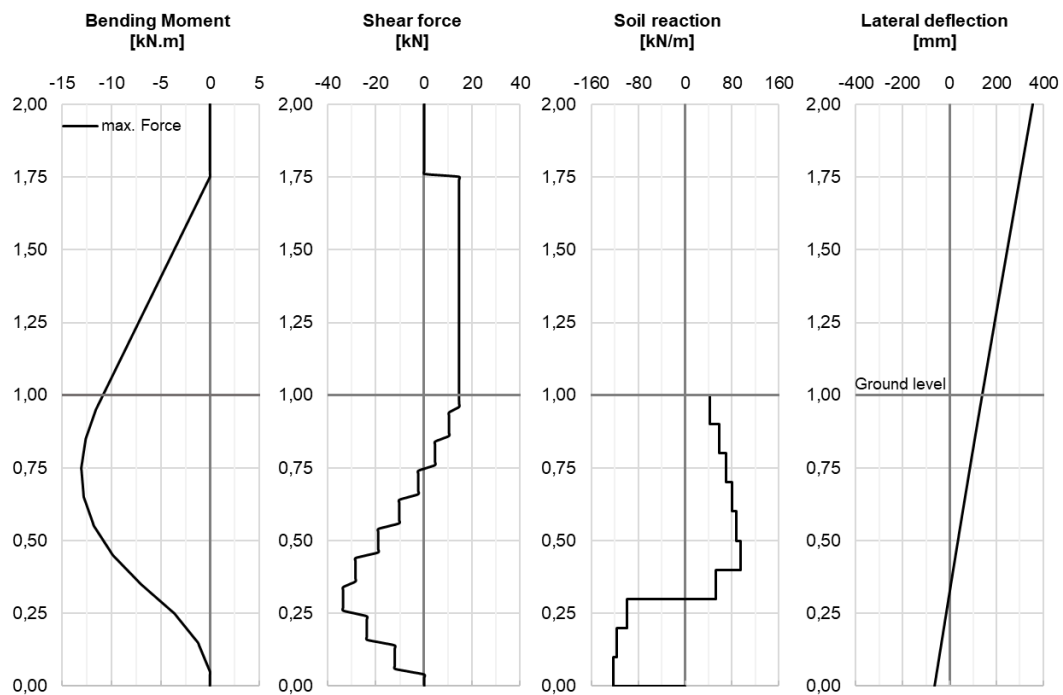


Fig. 6-13: LPM simulation results under quasi-static loading at 300mm lateral deflection ($F_{max}=14.8kN$); straining actions and deflection profile

Comparison to the design methods for laterally loaded piles

To evaluate the performance of the developed p-y curves, the results obtained using the LPM under quasi-static loading are compared to selected pile analysis methods available in the literature. First, the post response is calculated using the ultimate capacity method (after BROMS 1964 for short piles) and the subgrade reaction method as per the German recommendations EAP. The reference test is further calculated by incorporating the p-y curve approach according to API and REESE. The software PYPILE v.9.4 and GGU-LATPILE were used for the laterally loaded pile analysis. Both programs utilise the finite difference method to solve the differential equation for an embedded beam. The pile analysis methods applied here are explained in detail under *2 Literature review*.

The LPM simulation results are compared to the calculated post response in terms of maximum reaction force, the corresponding deflection at the loading point and the work done by the acting force. The acting loads are simulated by a lateral load applied incrementally in each step. To simulate the loading point above ground level analogue to the reference test, a moment is applied at the pile top equal to the lateral load multiplied by a lever arm of 75 cm.

In all calculations, the shear strength parameters determined for the LPM after BOLTON are applied ($\varphi_p = 54^\circ$, $c' = 0$). These correspond to the parameters estimated earlier for the elastoplastic FE simulations using Mohr-Coulomb failure criteria (see *5.4 Simulations using an elastoplastic soil model*). The soil unit weight is set equal $\gamma = 21.3 \text{ kN/m}^3$ in all calculations.

The load-deflection curves calculated using the considered methods for an IPE120 post in KSS032 with relative density $I_D=0.8$ are shown in Fig. 6-14. The calculation results are summarised in Table 6-4.

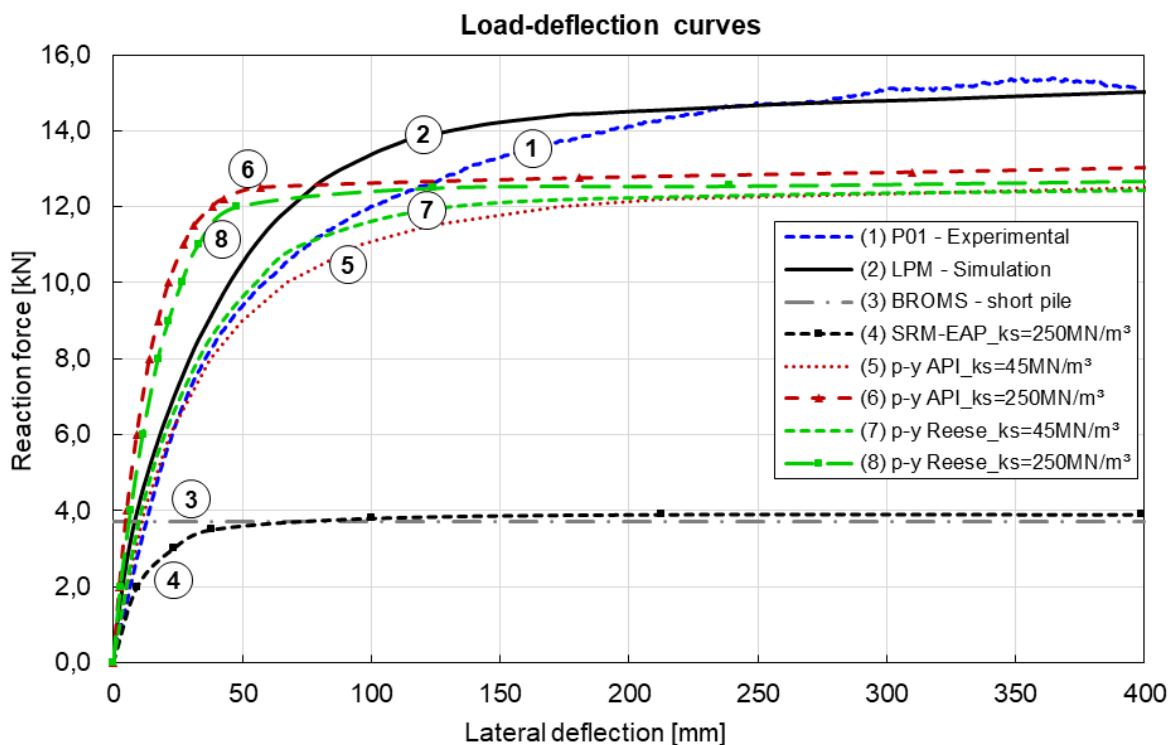


Fig. 6-14: Comparison of the load-deflection curves obtained by different methods for the IPE120 post under quasi-static loading

The ultimate capacity method after BROMS for short piles requires no further soil parameters than φ_p , c' and γ . The method underestimates the post resistance in cohesionless soils ($F_{\max}=3.7$ kN). Using The ultimate capacity method, the deflection of the soil and post cannot be calculated (see Fig. 6-14 curve 3).

For the approach recommended by the EAP [36], the subgrade reaction modulus was estimated from the oedometer test results as $k_s = E_s / D$, with the stiffness modulus E_s and the pile width D . The stiffness modulus was evaluated for a stress range of 10 to 22.5 kPa and the mean value was interpreted to $E_s = 16$ MN/m³ (see Fig. 6-15). Since the oedometer test results for the dense and loose specimens show a minor difference in this stress range, E_s was evaluated for the dense specimen. The initial subgrade reaction modulus for the post embedment assuming a constant value over depth was estimated by $k_s = 250$ MN/m³. The EAP recommendations adopts a linear elastic subgrade reaction method (SRM) with an ultimate soil pressure equal to the minimum of the plane or three-dimensional passive earth pressure [36]. The calculation was executed using GGU-LATPILE. Applying the interpreted value of $k_s = 250$ MN/m³ and the passive earth pressure as per DIN 4085 [21], the maximum reaction force reaches 3.9 kN (see Fig. 6-14 curve 4), which is in the range of the value estimated using BROMS method. The underestimation of the reaction force is attributed to the low three-dimensional passive earth pressure coefficient ($\mu = 8.16$) calculated for the shallow embedment depth.

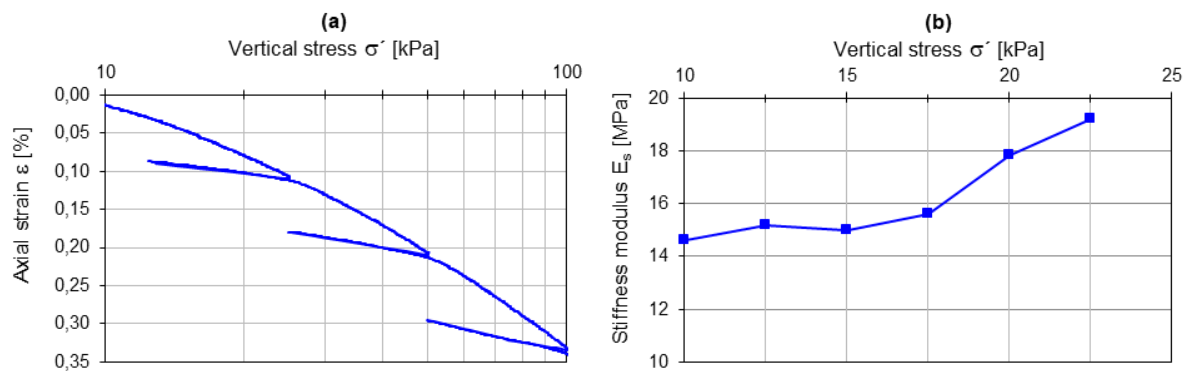


Fig. 6-15: Oedometer test results conducted on a very dense KSS032 specimen with a relative density $ID=0.98$ (a) Stress-strain diagram (b) Stiffness modulus evaluated for a stress range of 10 to 22.5 kPa

The non-linear p-y methods for sand after REESE 1974 [73] and as per API RP 2GEO [2] were utilised for the calculation of the post response. Since REESE recommends no specific value for the initial stiffness modulus, this value was selected based on the recommendations of the API for the non-cohesive soils equal to $k_{ini} = 45$ MN/m³ constant over depth. This value was applied in the calculations using both methods (see Fig. 6-14 curves 5 & 7). The calculated reaction forces and deflection values are closer to the experimental results compared to the aforementioned approaches BROMS and SRM-EAP. The calculations were further conducted using REESE and the API method with $k_s = 250$ MN/m³ (see Fig. 6-14 curves 6 & 8). The resulting load-deflection curves exhibit a much stiffer response and a slightly higher reaction force.

The comparison of the load-deflection curves calculated using the p-y method to the experimental data shows that the subgrade reaction modulus estimated by $k_s = E_s / D$ obviously overestimates the initial stiffness. For laterally loaded piles in general, the EAP

recommends a maximum value of $k_s = 100 \text{ MN/m}^3$. However, this value still overestimates the initial stiffness, when incorporated in the p-y method. The subgrade reaction modulus recommended by the API for shallow piles in sand $k_{ini} = 45 \text{ MN/m}^3$ shows a relatively better agreement with the experimental load-deflection data.

Table 6-4: Summary of the calculated post maximum reaction force, the corresponding deflection and the work done by the acting force using different approaches

Approach	k_s [MN/m ³]	F_{max} [kN]	$U@F_{max}$ [mm]	$W^{(3)}$ [kN.m]
Experimental	non-linear	15.4	364	5.1
LPM	non-linear	14.8	300	5.3
BROMS	-	3.7	-	-
SRM-EAP⁽¹⁾	250	3.9	100	1.5
p-y API⁽¹⁾	45	12.2	213	5.0
p-y API⁽²⁾	250	12.8	180	4.5
p-y Reese⁽¹⁾	45	12.3	243	4.8
p-y Reese⁽²⁾	250	12.6	238	4.6

(1) Subgrade reaction modulus: $k_s = E_s/D = 250 \text{ MN/m}^3$

(2) Initial stiffness as per API 2014: $k_{ini} = 45 \text{ MN/m}^3$

(3) Work done by the acting load evaluated up to a deflection of 400 mm for all methods

The performance of the LPM incorporating the p-y curves developed in this research show so far, the closest values to the experimental field test results.

Variation of the post section and soil relative density

in the next step, the application of the developed LPM approach is assessed for further guardrail post-sections and soil relative density. The model parameters are calibrated for the C125 post embedded in the silty gravel GU055. The experimental laboratory test data discussed under *4 Laboratory testing of soil materials* are used for this purpose. The soil relative density in-situ $I_D = 0.94$ is determined from the conducted field dry density tests (see *Appendix [A]: In-situ soil testing*).

The C125 post is modelled using the B31OS element type to consider warping under torsional actions. The post is simulated under lateral quasi-static loading and compared to the full-scale test M03. The test details are presented in *Appendix [C]: Quasi-static tests*. The LPM input parameters and the developed p-y curves are shown in Fig. 6-16.

The simulation results (Fig. 6-17) show a good agreement with the field test data. The load deflection curves up to unloading exhibit a coefficient of determination of $R^2 = 0.97$ and a performance metric of $W = 0.94$. The deviation of the curves trend during unloading can be attributed to the experimental testing constellation, which is simplified in the model by boundary conditions. The post rotation shows a minor deviation of 3.6° at the maximum post deflection. The post section shows plastic strains at a depth of 65 cm below ground level. This observation could not be verified by experimental observations, since the post could not be extracted after testing without further deformations.

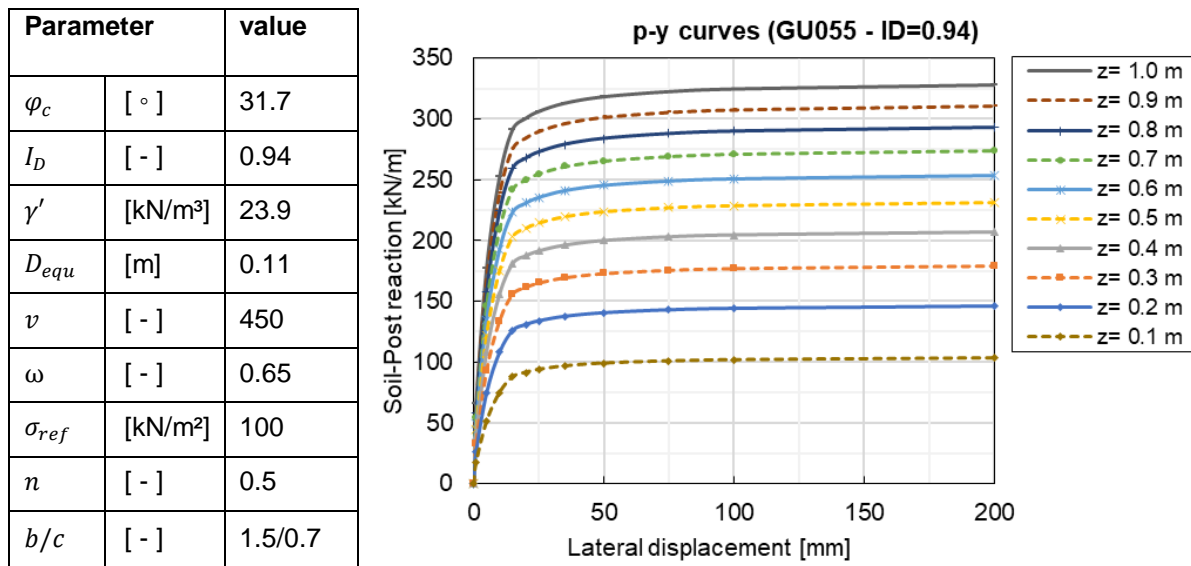


Fig. 6-16: LPM input parameters and p-y curves for the C125 post embedded in GU055

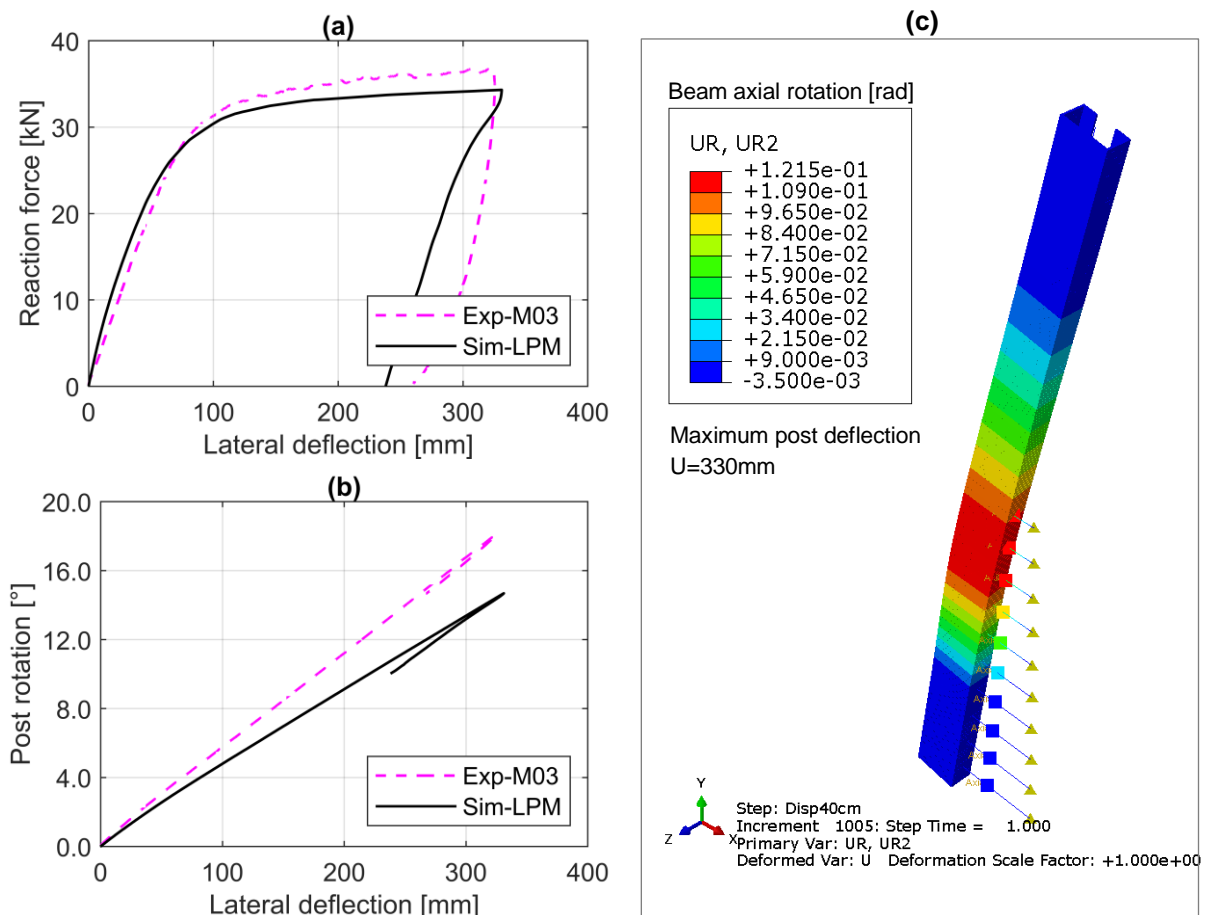


Fig. 6-17: Simulation results of the quasi-static loading on C125 post embedded in GU055 (a) load-deflection curves (b) post rotation (c) axial post rotation

The LPM has proven to adequately simulate the soil response in a different soil with higher relative density. The adopted modelling technique for the post was able to simulate the torsional effects in the asymmetrical C125 post, as observed in the field test.

LPM performance under impact loading

The LPM simulation results of the IPE120 post under dynamic impact loading are presented in Fig. 6-18 to Fig. 6-20. First, the reference test simulation with 3.2 kJ ($v_{\text{impactor}}=5.8$ m/s) is compared to the field test. The impact force shows strong vibrations at the first 3 ms, afterwards the maximum impact force reached is 13% higher than the measured value (see Fig. 6-18a). The maximum force is reached ca. 10 ms earlier in the simulation. This is attributed to the absence of the tyre piece in the simulation, which delays the occurrence of the maximum force. Since the contact conditions of the impactor and the post are different compared to the field test, the characteristic of the impact force-time history deviates significantly from the experimental data.

The reaction force-time history shows better agreement (see Fig. 6-18b). The reaction force could be simulated with a deviation of maximum 2.1 kN (9.5%), and the curve characteristic follows the experimental curve. The lateral post deflection, as well as the velocity-time history, coincide with the measured values up to the maximum deflection, afterwards the deviation increases (see Fig. 6-18c & d). The irreversible post deflection is underestimated in the simulation by ca. 25 mm (Fig. 6-18e). The simulated section strains lie in the same range of the strain gauge measurements (Fig. 6-18f). The values show its largest deviations at the section close to the rotation point.

The simulated bending moment, shear force, soil resistance and lateral deflection profiles were derived at the time point of maximum impact force and the time point of maximum deflection (see Fig. 6-19). The maximum bending moment is reached at a depth between 0.20 and 0.30 m below GL, respectively. The post rotation point is located at 0.45 m below GL at the maximum force and wanders to 0.7 m below GL at the maximum deflection.

Comparing the time required for the simulation task 3.2 kJ on the same processor, the LPM requires only 2.5% of the time consumed by the FE continuum model (Total CPU time: 735 seconds for LPM versus 28898 seconds for FE continuum). This comparison does not take into consideration the variation of the time step during the analysis, which may affect the total computation time. The significant computational efficiency of the LPM allows for the simulation of several posts within a VRS in a crash test simulation with much less cost and time.

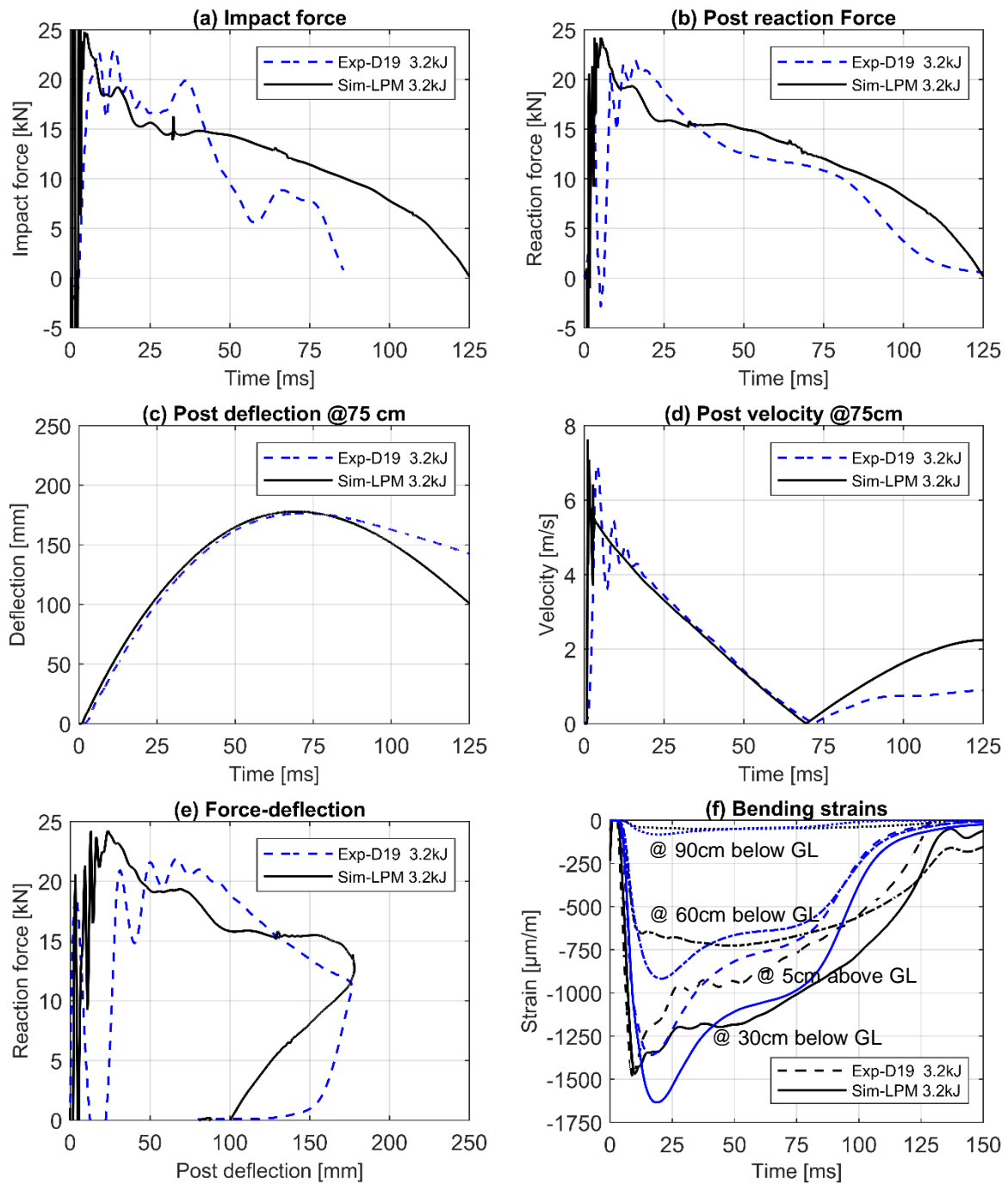


Fig. 6-18: Comparison of the simulation results using LPM to the experimental data for the impact test under 3.2 kJ

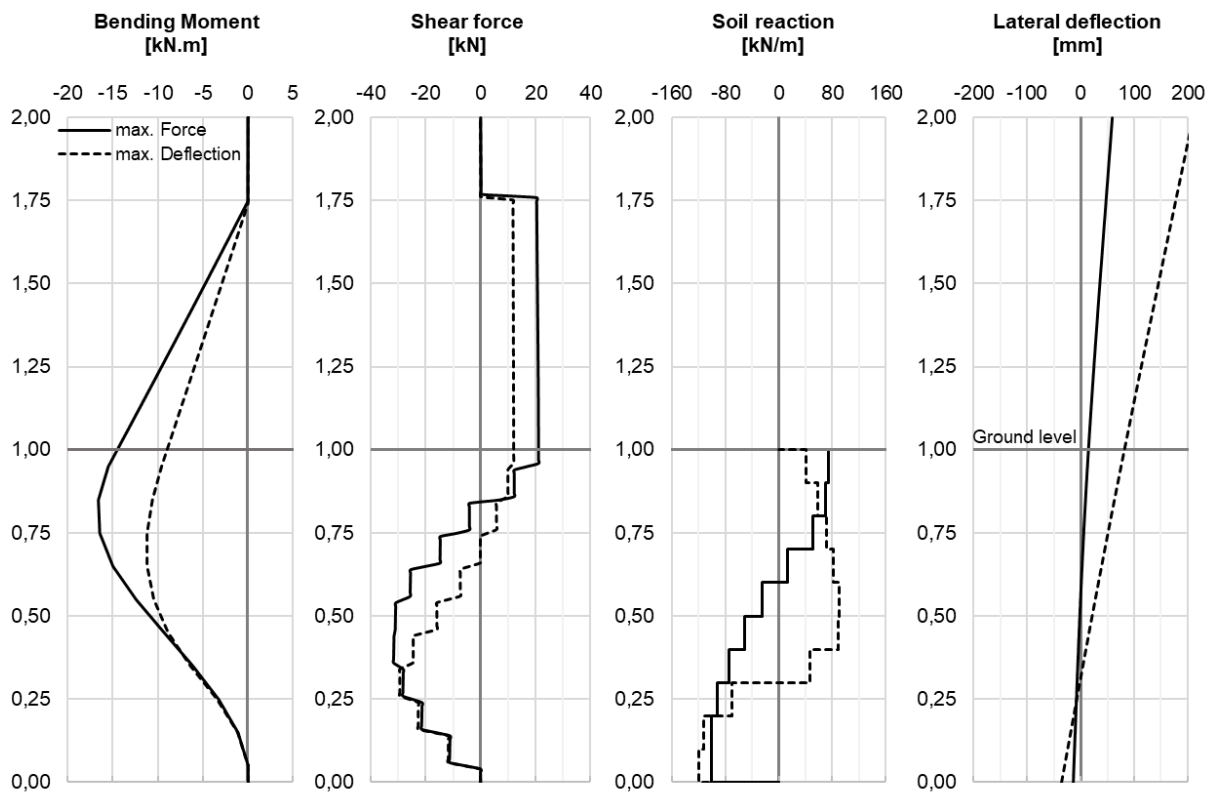


Fig. 6-19: LPM simulation results under impact loading with 3.2 kJ; post straining actions and deflection profile at maximum lateral deflection ($u_{\max}=174\text{mm}$) and at maximum reaction force ($F_{\max}=23.8\text{kN}$)

To check the capability of the model to simulate the post response at higher impact intensities, the model was run with an impactor velocity of 7.7 and 9.2 m/s to generate 5.7 and 8.2 kJ. These values correspond to the field test impact intensities. The results show the increase of the impact force, reaction force and post deflection (see Fig. 6-20 a, b and c). The load-deflection curves show relatively lower deflections after recoil (Fig. 6-20e). However, the irreversible post deflections after unloading increase with the impact energy, which coincides with the field test observations.

The post velocity-time history shows an approximately constant deceleration up to the recoil point, which is characteristic for the tests conducted in soils exhibiting the same relative density (Fig. 6-20d). The difference between the total absorbed energy at the maximum deflection and the applied impactor kinetic energy is the fraction dissipated in the dashpots, i.e. damping (Fig. 6-20f).

The connector forces were evaluated at each depth and dissociated into the spring force, representing the defined non-linear soil behaviour, and the dashpot force, representing the damping behaviour (see Fig. 6-21). Comparing, for example, the forces at the elevations showing the maximum soil pressure at 0.45 and 0.95 m below GL, the dashpot force did not exceed 23% to 16%, respectively.

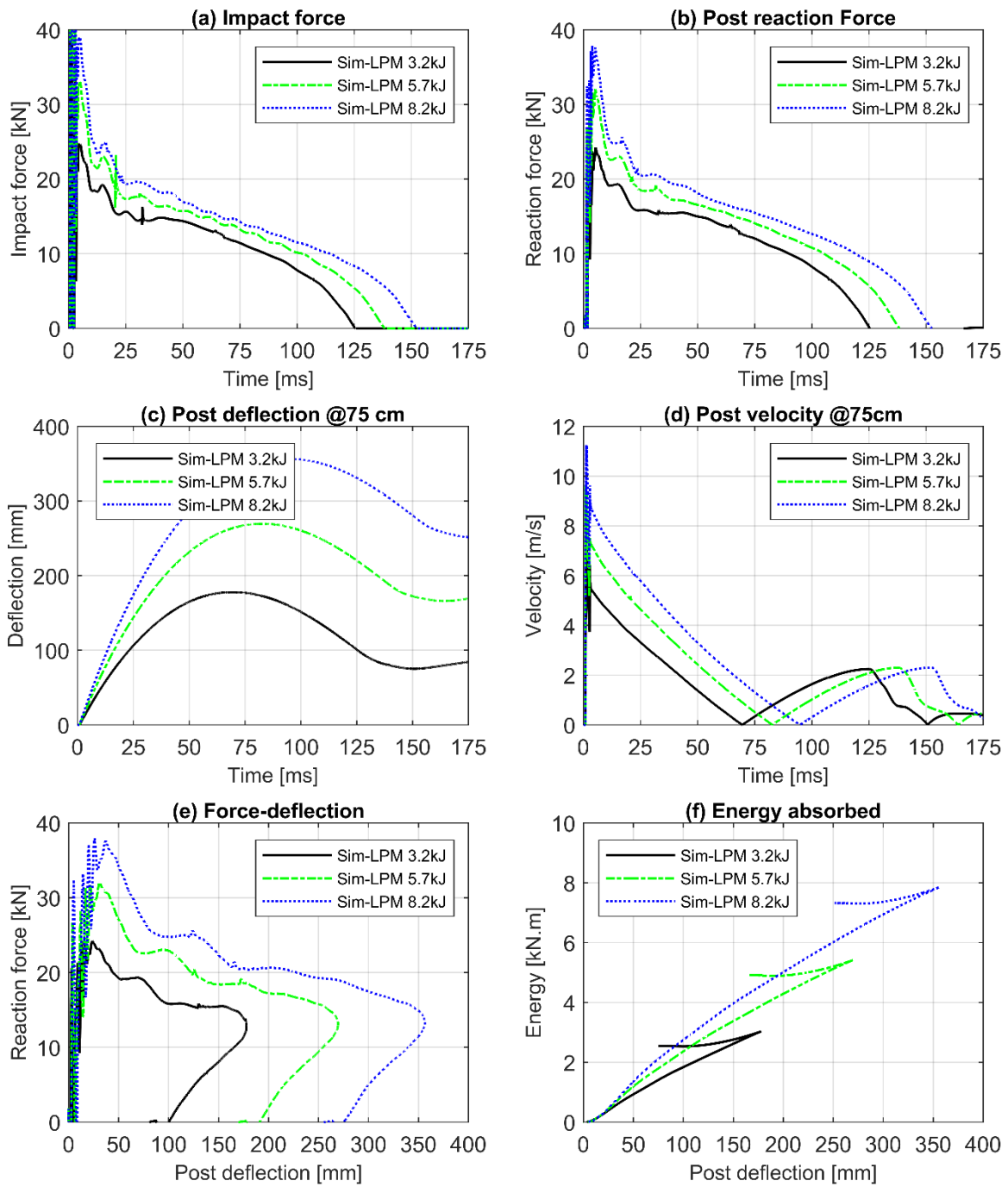


Fig. 6-20: LPM simulation results under variation of the impact energy 3.2, 5.7 and 8.2 kJ

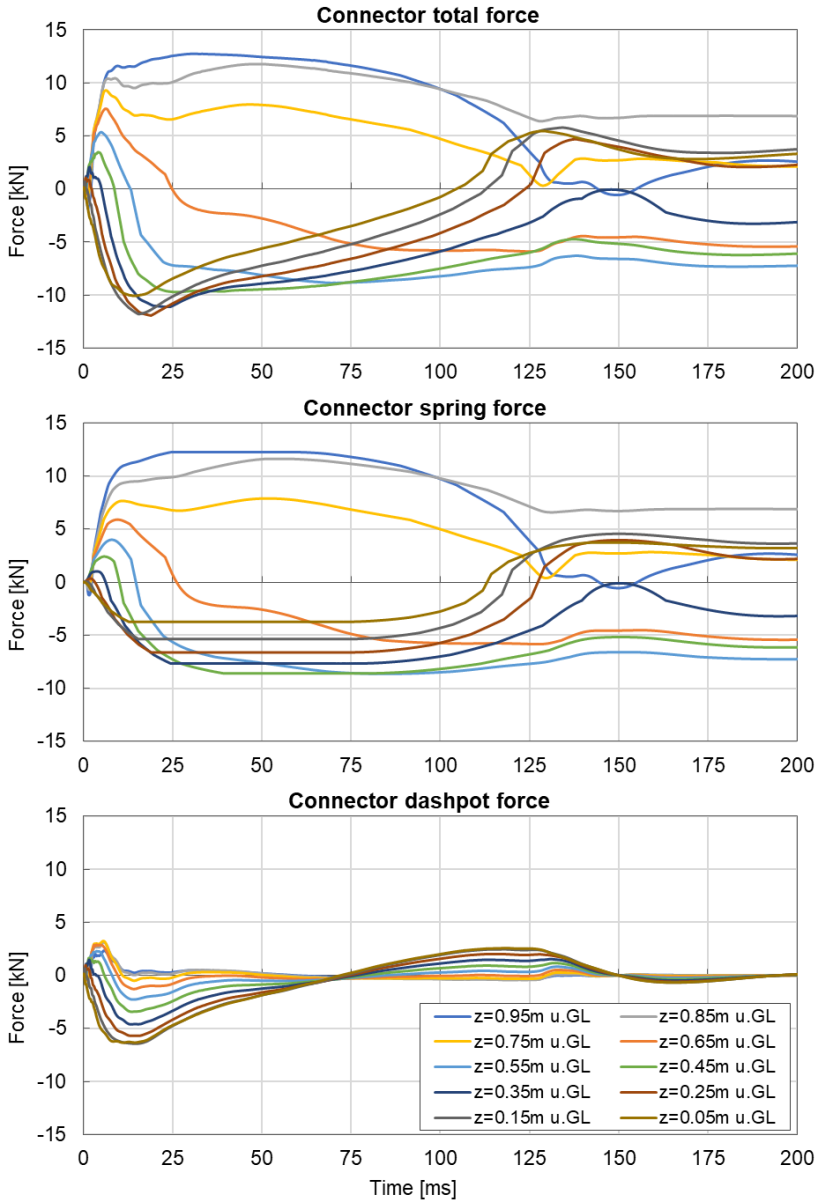


Fig. 6-21: Connectors force-time history presenting the total force as a sum of the spring force and dashpot force under impact loading

6.3 Discussion and conclusions

This chapter investigated the soil-structure interaction of the guardrail posts using the lumped-parameter modelling technique. Experimental load-transfer curves were developed using the field test strain gauge measurements. A simplified lumped-parameter model was developed and implemented in the FE-Code ABAQUS. The model is conceived to determine the dynamic post response from the post and soil properties, even without conducting a static push/pull test on the post. The model incorporates the non-linear soil strength and stiffness, as well as the soil state conditions. The required model parameters can be determined from simple laboratory tests. The model assumptions regarding the derived parameters were chosen carefully from well-established literature and standards.

The approach followed for the derivation of the p-y curves experimentally from the installed instrumentation measurements was successful. The derived post straining actions and deflections could be reproduced with a high agreement with the field test data. The most

important results of this approach are the estimated soil pressure distribution along the post embedment and the underground deflections, which cannot be measured directly by the instrumentation.

The proposed LPM is capable of predicting the single post response, represented in reaction force and lateral deflection as well as post velocity, with a high agreement with the experimental field test data. The post response can be reproduced using the same parameter set under quasi-static and impact loading with different intensities.

The model can be extended to function in the transversal direction to allow for three-dimensional analysis. The model can then be implemented for the simulation of the real crash test in a simplified way with much less computational effort. The procedure proposed for the determination of the damping coefficient can be further improved to dispense the required fitting factor. The lumped mass was assumed to be constant over the impact duration. This assumption may lead to overestimation of the impact force, since the mobilised wedge at the beginning of impact is relatively small, while the acceleration value is at its maximum. Therefore, a time-dependent lumped mass can be recommended based on the experimental and numerical observations.

The numerical simulation results obtained using the LPM and the FE continuum method are compared statistically to infer the efficiency of the models to simulate the guardrail post behaviour. To facilitate the comparative assessment of the simulation models, the response parameters are presented using TAYLOR diagrams. This mathematical presentation of data can be used to quantify the correspondence between the simulated and the experimental behaviour in terms of the following statistical measures [87]:

- Pearson correlation coefficient (PCC): which gauges the similarity in pattern between data sets. The coefficient is calculated as the covariance of two variable populations divided by the product of their standard deviations. Not to be confused with the coefficient of determination R^2 . The Pearson coefficient is presented in the diagram on the azimuthal angle. A Pearson coefficient value close to 1 indicates high agreement of the simulation model with the reference data, i.e. experimental observations.

$$PCC_{Model} = \frac{1}{N} \frac{\sum_{i=1}^N (f_{SIM,i} - \overline{f_{SIM}}) \cdot (f_{EXP,i} - \overline{f_{EXP}})}{(SD_{SIM} - SD_{EXP})} \quad \text{Equ. 6-33}$$

where; PCC_{Model} is the correlation coefficient for the simulation model, N is the number of discrete data points of the sample, $f_{SIM,i}$ is the simulated variable value at a given point, $f_{EXP,i}$ is the measured experimental value, and $\overline{f_{SIM}}$ and $\overline{f_{EXP}}$ are the mean values of each sample, respectively. SD_{SIM} and SD_{EXP} are the standard deviations of the simulated and the experimental data samples.

- Root-mean-square error (RMS): which measures the difference between the simulated data samples and the observed samples. The root-mean-square error of simulated data is proportional to the concentric distance from the experimental data point plotted on the x-axis in the diagram. Models close to the circle's centre can simulate the observations with low error.

$$RMS_{Model} = \sqrt{\frac{1}{N} \sum_{i=1}^N (f_{SIM,i} - f_{EXP,i})^2} \quad \text{Equ. 6-34}$$

where; RMS_{Model} is the root-mean-square error for the simulation model.

- Standard deviation (SD): which measures the amount of dispersion of a data sample from a mean value. In the TAYLOR diagram, the experimental data is set as the comparison sample data, therefore the standard deviation of the experimental data is divided by itself and therefore normalised ($SD_{EXP} = 1.0$).

$$SD_{Model} = \sqrt{\frac{1}{N} \sum_{i=1}^N (f_{SIM,i} - \overline{f_{SIM}})^2} \quad \text{Equ. 6-35}$$

where; SD_{Model} is the standard deviation for the simulation model.

Several TAYLOR diagrams were constructed to compare the performance of the lumped-parameter model (LPM), FE continuum model with hypoplastic soil model (HP), FE continuum model with elastoplastic soil model (MC) to the experimental field tests (EXP). The diagrams for the reference test conditions (KSS032, ID=0.8, IPE120, strong axis) are presented in Fig. 6-22 to Fig. 6-25.

For the quasi-static test, the load-deflection data series were extracted from each model as well as from the field test. The statistical coefficients were then calculated for the reaction force with respect to the same deflection scale for all data. The results show that all simulation models exhibit a high correlation $PCC \approx 0.98$ and low error $RMS \approx 0.2$, i.e. the simulated values agree well to the observations (see Fig. 6-22). The LPM show the lowest SD value, which indicates the best load-deflection curve characteristic agreement.

For the dynamic impact test, the data series had to be prepared in the form of time histories. The post reaction force, lateral deflection at the loading point and the energy absorbed up to 100 mm lateral deflection were extracted from the reference models under 3.2 kJ. Compared to the quasi-static test, the models show a slightly higher error $RMS = 0.4 - 0.55$ and a lower correlation of $PCC = 0.88 - 0.93$ (see Fig. 6-23). The hypoplastic model shows a very high correlation of $PCC \approx 0.99$, while the LPM shows the lowest value $PCC \approx 0.9$ (see Fig. 6-24). This is attributed to the underestimation of the irreversible deflections using the LPM.

The energy absorbed by the post up to 100 mm lateral deflection $E_{abs\ 100}$ shows for all models the best pattern correlation $PCC > 0.9$ and very low errors $RMS < 0.15$. Which indicates that the simulation models perform very well in terms of energy dissipation, which is crucial for the simulation of a crash test.

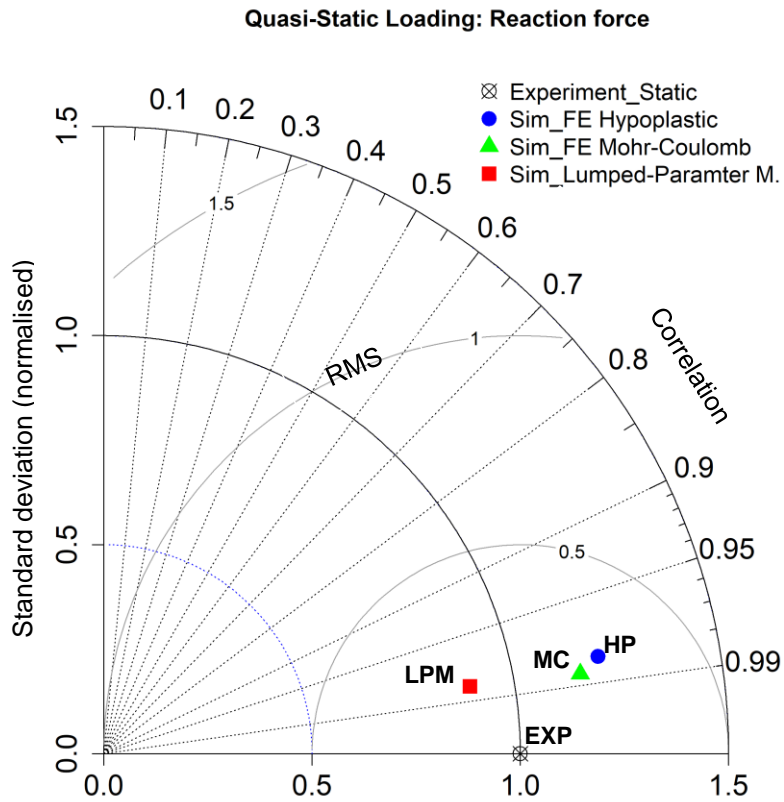


Fig. 6-22: TAYLOR diagram displaying a statistical comparison of the simulated quasi-static reaction force using different models

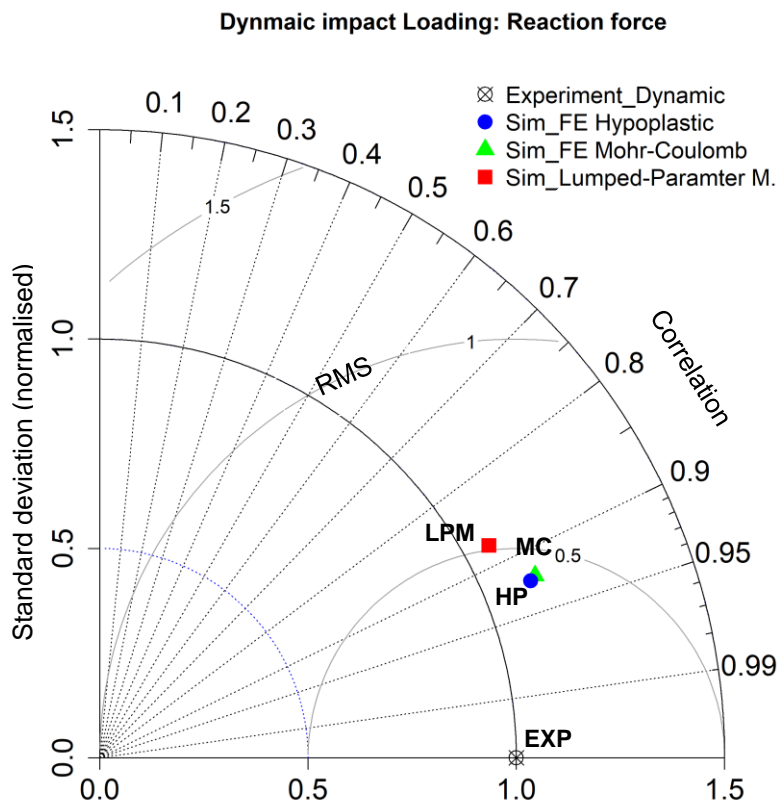


Fig. 6-23: TAYLOR diagram displaying a statistical comparison of the simulated post reaction force under impact loading using different models

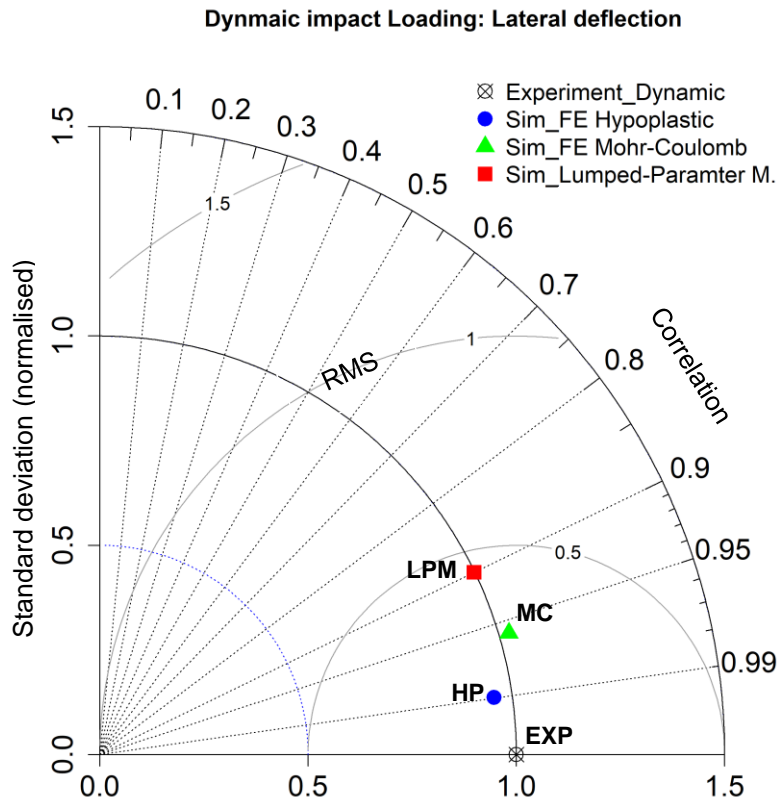


Fig. 6-24: TAYLOR diagram displaying a statistical comparison of the simulated post lateral deflection under impact loading using different models

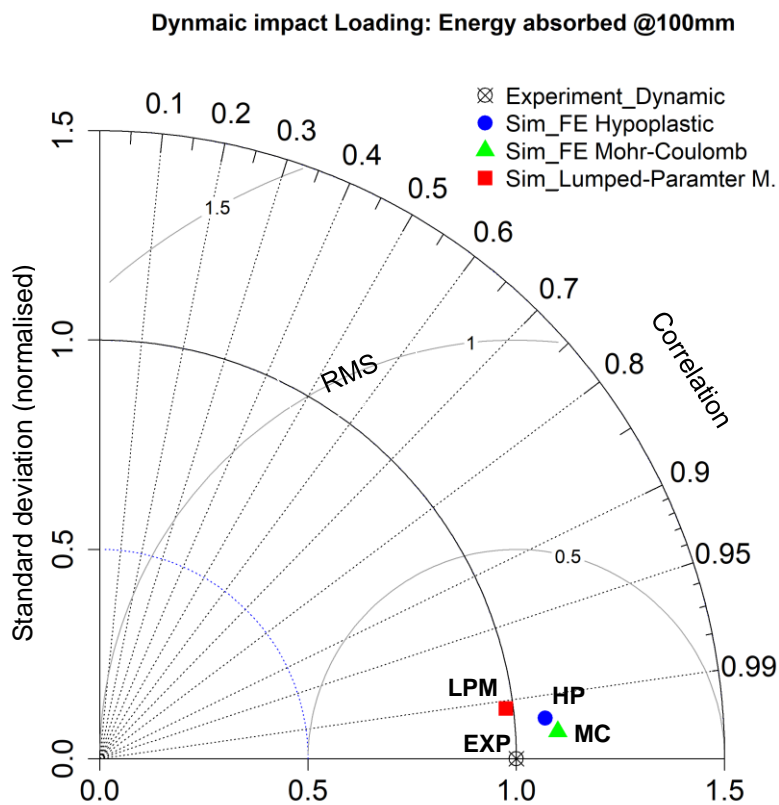


Fig. 6-25: TAYLOR diagram displaying a statistical comparison of the simulated absorbed energy at 100 mm lateral post deflection under impact loading using different models

Based on the results of the analysis conducted in this chapter, the following points can be concluded [83] [84]:

- The conventional pile analysis methods are very sensitive to the chosen soil parameters, especially the initial stiffness. The ultimate capacity methods underestimate the static post response significantly. The subgrade reaction method with the recommended modulus as per EAP for structural piles also underestimates the static post response.
- The soil shear strength parameters have to be determined for the low-stress levels in the shallow embedment layer.
- The p-y method can be used with modified soil parameters to predict the post behaviour realistically under quasi-static and impact loading.
- The analysis methods available for dynamic loading apply factors, which are calibrated either using finite element models or field test data. This feature limits the application of these methods to the test conditions of the data used for calibration (e.g. post section, soil type, relative density and loading range). Applying these models to simulate cases beyond the calibration data conditions can be misleading.
- The modelling techniques presented in this work avoid the reliability of post loading tests for parameters calibration. The model parameters rely mainly on the soil characteristics determined by laboratory tests and well-established approaches from standards and literature.
- Modelling the guardrail post response under impact loading requires considering the non-linearity of the soil material, irreversible deformations, inertial effects of the post and soil mass and radiation damping.
- The introduced LPM offers the same advantages as the FEA with hypoplastic soil model, with a much higher computational efficiency and a simpler parameters calibration routine. The LPM can be implemented in any FE code, in which non-linear elasticity, plasticity, damping and mass points can be defined.
- The computational efficiency of the applied model is crucial when modelling the full VRS system with several posts. As long as the post deflections are more relevant than the continuum deflections in the simulation, the LPM is regarded as more efficient.
- The proposed LPM is validated mainly against field tests conducted in road shoulder materials with horizontal surface. The effect of surface grading or slopes is not considered.
- The application of the developed LPM is limited to standard road shoulder materials. Soils comprising a higher fine content cannot be analysed using this approach without further modifications.

7 Summary and conclusions

Vehicle restraint systems (VRS) are vital elements of road safety hardware. The main function of a VRS is to redirect errant vehicles and prevent them from running into the opposite direction, as well as preventing crashing into structures along the road. The safety of the vehicle occupants and road users in a crash event depends immensely on the performance of the involved VRS. The response of steel VRS is a result of the interaction between the guardrail posts and embedment soil. Regarding the single post, the properties of soil material and the steel post are decisive for the mode of failure, deflections and energy dissipation capacity. So far, there is no validated standard technique for modelling the guardrail posts' behaviour in crash simulations. The modelling techniques applied for the simulation of the soil-post interaction are diverse and, in most cases, inadequate. This is either due to the oversimplification of the complex soil behaviour under such loading conditions or the absence of soil testing to calibrate sophisticated constitutive models. Furthermore, the soil-post interaction simulation is an interdisciplinary problem involving geotechnical and road safety engineering and computer science. In contrast to foundation piles, the guardrail post exhibits a much smaller diameter, a shallower embedment and is subjected to different loading conditions. Therefore, the conventional analysis methods for laterally loaded piles fail to predict the post response adequately. The guardrail posts can be described as sacrificial elements, which are allowed much larger deformations for the purpose of energy absorption. Subsequently, the guardrail posts' serviceability must be assessed by different performance criteria.

In this contribution, the soil-structure interaction of guardrail posts has been investigated experimentally and numerically under different loading conditions. With this aim, a series of full-scale quasi-static and impact loading tests were conducted on single posts exhibiting different section properties and embedded in various road shoulder materials. The selected soils are standard road shoulder materials fulfilling the highway construction specifications. The tested posts represent standard elements of a certified VRS. The primary purpose of the testing program was to investigate the influence of the soil material and grain properties as well as the post section characteristics and loading axis on the post response. Further, the test results form a unique experimental database for the validation of numerical simulation models. The tested posts were extensively instrumented using strain gauges, accelerometers and force transducers to allow for an interpretation of the soil-post interaction based on experimental measurements.

The novel experimental method applied for static and dynamic testing enabled consistent reproducibility and reliable evaluation of the test results. A set of soil properties and post characteristics were defined as the reference conditions. First, the posts were loaded laterally with a very low loading rate, i.e. quasi-static, to assure the exclusion of any inertial effects or undrained behaviour. In the next step, the posts were tested under lateral impact loads, keeping the same soil and post conditions. The test was conducted at least three times under different impact intensities. The selected impact energy levels are in the range of those experienced by VRS posts in a crash event. In all field tests, the lateral load is applied at the same height measured from the ground level. The static and dynamic reference test results build together the datum for the variations examined in the field tests.

The conducted laboratory soil testing program provides a comprehensive insight into the soil mechanical properties, mineralogical composition and grain characteristics. The testing

program was conceived with the purpose of calibrating the constitutive soil models, which were utilised later for the numerical investigation. Nevertheless, since the soil loading during a crash event is principally monotonic, the testing program was conceived to capture the soil materials' monotonic shear and compressive behaviour. Due to the relatively large grain size of the road shoulder materials, the soil specimens had to be tested in specially customised equipment not typically applied for conventional geotechnical tests.

The results of the experimental field and laboratory investigations show that, under quasi-static conditions, increasing the grain mineral strength and reducing the sand content of the road shoulder material causes an increase in the lateral bearing capacity of the post. Nevertheless, under impact loading, the influence of these parameters on the post response is negligible. Under both loading conditions, symmetrical posts show a maximum resistance ratio in the strong to weak axis equal to approximately two. The horizontal stiffness ratio under quasi-static loading equals the quotient of the elastic section modulus in the strong axis and the plastic section modulus in the weak axis. Asymmetric sections, like the C-posts, tend to twist around the longitudinal axis under lateral loading, which leads to reduction of the post resistance. The results of the full-scale field tests show that the soil relative density and the post embedment length are decisive for the mobilised post resistance and the failure mode.

To systematically investigate further parameters influencing the post response, the quasi-static and impact loading tests were numerically simulated using the FE method. First, the developed FE model was validated under quasi-static loading using the experimental full-scale reference test data. Then, the FE model was validated under impact loading with different intensities. The soil behaviour was modelled using a hypoplastic constitutive model, whereas the material parameters were determined based on the conducted laboratory soil testing. The same soil material parameter set was applied for both loading conditions and initial soil densities. The utilised modelling technique has proven to be efficient for the guardrail post simulations. The post is modelled using beam elements enclosed in a circular transition body consisting of continuum elements. This approach helps avoid stress concentrations and excessive mesh distortions in the post corners. The interface definition between the transition body and the soil continuum allows for large post deflections, which have to be considered in the guardrail post problem. To account for the soil stress state properly in the shallow layer, the compaction pressure must be considered in determining the earth pressure at-rest. The installation method of the post is considered by reducing the clearance required to mobilise the post contact pressure and by applying unloading-reloading parameters for the transition body.

In contrast to the FEA based on hypoplasticity, the analysis using an elastic-ideal plastic soil model demanded iterative calibration of the model parameters to the loading test data. Therefore, different parameter sets are required to simulate different initial soil densities and loading conditions. These results evidence that for a realistic prediction of the soil-post interaction, considering the principle features of the soil's mechanical behaviour under monotonic shearing, e.g. stress- and density-dependency of the material stiffness, strength and volumetric behaviour is mandatory. Obviously, simple elastic-ideal plastic models do not fulfil this requirement and are not suitable for numerical predictions of the post response.

The conducted parametric study examined the influence of the post and soil properties on the post response, which could not be investigated systematically in the field tests. The comprehensively validated FE models using the hypoplastic soil model were used for the parametric study. The FEA show, as also observed in the field tests, that the soil relative

density and the post embedment length are decisive for the failure mode and the reaction force of the post. Increasing the relative density above $I_D > 0.85$, i.e. very dense soil, leads to the development of a rotation constrain of the post below the ground surface and the formation of a plastic hinge during loading. The location of the plastic hinge depends on the loading type and the soil density. For impact loading, the plastic hinge is formed closer to the ground surface compared to the quasi-static loading. The posts embedded in soils exhibiting a medium to dense relative density show a rigid body rotation with no signs of section yielding. For the tested posts, increasing the embedment length beyond 1.0 m in dense soils leads to a combination of post rotation and section yielding. Post embedment lengths larger than 1.0 m in very dense soils show the formation of a plastic hinge. Posts with an embedment less than 0.9 m tend to rotate as an elastic body. The deceleration of the colliding body is governed by the soil relative density and the post embedment length. Longer posts in denser soils can stop the colliding body in a shorter time duration. The height of the loading point, i.e. collision point, has a significant effect on the post performance. For a given lateral deflection, the post can absorb more energy if the loading point is located closer to the ground level.

The post performance was evaluated in the investigated variations based on the parameters energy absorbed by the post at 100 mm deflection ($E_{abs\ 100}$) and the maximum acceleration generated on the colliding body ($A_{imp\ max}$). The soil relative density range $I_D = 0.8$ to 0.9 can be considered optimum for the post response, since the absorbed energy is relatively high and the impactor acceleration is low in this range. Posts with embedment lengths larger than 1.0 m exhibit a marginal effect on the absorbed energy. The acceleration is nearly unaffected by the embedment length in the investigated range. Increasing the section modulus for the section is very efficient in increasing the absorbed energy. However, the impactor acceleration increases as well. Lowering the height of the loading point results in increasing the absorbed energy, as well as the impactor acceleration. This effect is more significant when increasing the impact energy level.

The soil-post interaction was further investigated using a newly developed Lumped-Parameter model (LPM) based on the non-linear Winkler foundation model. The LPM incorporates non-linear load-transfer curves (also p-y curves) that can be derived through a novel approach proposed by the author. The proposed p-y curves were validated using experimental data derived from strain gauge measurements. The LPM is extended with mass points, damping and plasticity elements to simulate the inertial effects, energy dissipation and irreversible deflections, respectively. The model is conceived to estimate the static and impact response from the post and soil properties without the need for field tests. The model considers the non-linear soil strength and stiffness, as well as the soil state conditions. The required model parameters can be determined from conventional laboratory soil testing. The proposed LPM is capable of predicting the single post response with a good agreement with the experimental test data. The post response could be reproduced satisfactorily under quasi-static and impact loading with different intensities using the same model and parameter set. The proposed LPM requires on average less than 5% of the computational effort consumed by the FE continuum model. This advantage is crucial for crash test simulations, since the required time significantly increases when simulating the full VRS with several posts.

Based on the conducted experimental and numerical investigations, the soil-post interaction could be analysed under different loading conditions. The post response depends significantly on the loading rate. Under impact loading, the inertial effects of the post and soil masses are mobilised, adding to the maximum post resistance. For a given lateral deflection, the work done by the acting load is higher under impact loading compared to the quasi-static case. However, the maximum post resistance is capped by the ultimate soil resistance in both cases. Increasing the impact intensity beyond this limit yields no additional energy absorption by the system. The impact energy is dissipated in the soil-post system mainly through the deformation of the surrounding soil and yielding of the post section. A minor fraction of energy is dissipated through radiation damping. Since the standard road shoulder materials are mainly non-cohesive soils, the viscous component of the material damping can be neglected.

8 Recommendations and perspectives

Ultimately, the performance of a VRS cannot be evaluated only based on the response of a single post. However, the soil-post interaction of the single post is decisive for the overall performance of the VRS. In light of the findings of this research work, the following aspects are recommended for more precise testing of VRS and more realistic and efficient crash test simulations:

- The guardrail posts are sacrificial elements that undergo large deflections for the purpose of energy absorption under impact loads. Therefore, the conventional analysis methods for laterally loaded structural piles cannot be applied for the prediction of the post response without modifications.
- The experimental assessment of the soil-post response by conducting solely quasi-static tests is insufficient. Additional dynamic impact tests with variable intensities are required to evaluate the soil-post interaction and performance parameters. The load application point has to be set at the same elevation from the ground level for both loading conditions.
- In full-scale impact tests, the measurement of the reaction force by directly measuring the impact force at the contact point is susceptible to strong vibrations and inertial effects in the instrumentation, which may result in misleading measurements. Calculating the reaction force from strain gauge measurements along the post is more precise.
- The numerical modelling of the guardrail post, whether as a single post or as a part of a VRS in a crash test simulation, must consider the initial soil stress-state and the large deformations of post and soil.
- For numerical simulations using the FEM, the selected constitutive soil model must be capable of adequately simulating the stress- and density-dependent non-linear behaviour of the soil under monotonic shearing and compression. Only advanced elastoplastic and hypoplastic constitutive models fulfil this requirement.
- The selected constitutive model for the steel post must consider the strain-rate dependency of the material yield strength.
- The laboratory testing of soil material, as well as the determination of parameters, must consider the low stress range of the shallow guardrail post embedment.

- In a crash test simulation, the posts can be modelled satisfactorily using different techniques, e.g. FEM or the proposed Lumped-parameter model. The advantage of the LPM is its high computational efficiency and the simple model parameter determination approach. However, the lumped-parameter model application is limited to the standard road shoulder materials, and cannot be transferred to fine-grained soils without modifications.

The research conducted in this thesis on the soil-post interaction has a potential for future work. The influence of further parameters on the post response can be investigated, e.g. the effect of slopes in the post vicinity and the effect of surface gradients of the road shoulder. The investigation of soil materials beyond the standard road shoulder material opens the door for applying sustainable materials, e.g. recycled materials generated from construction debris, in the road shoulder construction. Lighter post sections with different geometries can be investigated for optimization purposes. The proposed LPM can be extended in two loading directions to function in three-dimensional numerical analysis, and ultimately to be implemented in crash test simulations. The parameters determination for the LPM still has room for improvement. The applicability and efficiency of further modelling techniques for the numerical simulation of the guardrail post behaviour can be investigated. The utilisation of emerging technologies like artificial intelligence can open the door for further improvement of crash test simulations, and consequently for the optimization of the VRS certification process.

Finally, to achieve a life-saving and economical system simultaneously, the designer has to optimise the performance of the vehicle restraint system, based on the outcomes of either full-scale testing or numerical simulations. In this contribution, the experimental investigation concepts, simulation techniques, findings and recommendations presented in this research work can be endorsed in the design of steel vehicle restraint systems for safer and cost-efficient highways.

References

1. ABAQUS (2016) Analysis User's Manual, Version 6.17, Dassault Systèmes Simulia Corp., Waltham, MA, USA.
2. API RP 2GEO (2014): Geotechnical and foundation design considerations, American Petroleum Institute (API), Washington D.C.
3. Atahan AO, Büyük M, Örnek M et al. (2019) Determination of optimum post embedment depth for C120 steel posts using field and full-scale crash test. *International Journal of Crashworthiness* 24:533–542. <https://doi.org/10.1080/13588265.2018.1479499>
4. Bielenberg RW, Faller RK, Lechtenberg KA et al. (2015) Design of an Improved Post for Use in a Non-Proprietary High-Tension Cable Median Barrier, Nebraska Department of Transportation Research Reports, Midwest Roadside Safety Facility, University of Nebraska, USA.
5. Bligh, R.P., Seckinger, N.R., Abu-Odeh, A.Y., Roschke, P.N., Menges, W.L. and Haug (2004) Dynamic Response of Guardrail Systems Encased in Pavement MOW Strips: FHWA/TX-04/0-4162-2, FHWA - Texas Transportation Institute, Texas.
6. Blum H (1932) Wirtschaftliche Dalbenformen und deren Berechnung. *Die Bautechnik* 10:50–58.
7. Bolton MD (1986) The strength and dilatancy of sands. *Géotechnique* 36:65–78. <https://doi.org/10.1680/geot.1986.36.1.65>
8. Briaud J-L (1997) SALLOP: Simple Approach for Lateral Loads on Piles. *J Geotech Geoenviron Eng* 123:958–964. [https://doi.org/10.1061/\(ASCE\)1090-0241\(1997\)123:10\(958\)](https://doi.org/10.1061/(ASCE)1090-0241(1997)123:10(958))
9. Broms BB (1964) Lateral resistance of piles in cohesionless soils. *Journal of the Soil Mechanics and Foundations Division, ASCE* 90:123–156.
10. Canadian geotechnical Society (2017) Canadian foundation engineering manual, 4th edn. 9780920505281, Richmond, BC, Canada.
11. Coon B. A., Reid J. D. , and Rohde J. R. (1999) Dynamic impact testing of guardrail posts embedded in soil, Midwest Roadside Safety Facility, University of Nebraska, USA.
12. Costa FV (1964) The Berthing Ship: The Effect of Impact on the Design of Fenders and Berthing Structures
13. Cowper G. & Symonds P. (1957) Strain-hardening and strain-rate effects in the impact loading of cantilever beams. Division of Applied Mathematics, Brown University, Providence, R.I.
14. Cudmani R, Henzinger C, Birle E et al. (2021) Requirements for building materials for durable, unbound road shoulders with low permeability. *Berichte der Bundesanstalt für Straßenwesen, Straßenbau Heft 158*. <https://doi.org/0194>
15. Dewey James F., Jeyapalan Jey K., Hirsch T.J. et al. (1983) A Study of the Soil Structure Interaction Behavior of Highway Guardrail Posts, Texas Transportation Institute, A&M University, USA.
16. DIN 18124:2019-02, Baugrund, Untersuchung von Bodenproben: Bestimmung der Korndichte - Weithalspyknometer, Deutsche Gesellschaft für Geotechnik e.V., Beuth Verlag GmbH, Berlin.
17. DIN 18125-2:2020-11, Baugrund, Untersuchung von Bodenproben_- Bestimmung der Dichte des Bodens: Teil_2: Feldversuche, Deutsches Institut für Normung e. V., Beuth Verlag, Berlin.
18. DIN 18126:2022-10, Baugrund, Untersuchung von Bodenproben: Bestimmung der Dichte nicht bindiger Böden bei lockerster und dichtester Lagerung, Deutsche Gesellschaft für Geotechnik e.V., Beuth Verlag, Berlin.

19. DIN 18127:2012-09, Baugrund, Untersuchung von Bodenproben - Proctorversuch, Deutsches Institut für Normung e. V., Beuth Verlag, Berlin.
20. DIN 18134:2012-04, Baugrund - Versuche und Versuchsgeräte: Plattendruckversuch, Deutsche Gesellschaft für Geotechnik e.V., Beuth Verlag, Berlin.
21. DIN 4085:2017-08, Baugrund - Berechnung des Erddrucks, Deutsches Institut für Normung e.V., Beuth Verlag, Berlin.
22. DIN EN 1317-1:2011-01, Rückhaltesysteme an Straßen: Teil_1: Terminologie und allgemeine Kriterien für Prüfverfahren, Deutsches Institut für Normung e.V., Beuth Verlag, Berlin.
23. DIN EN 1317-2:2011-01, Rückhaltesysteme an Straßen: Teil_2: Leistungsklassen, Abnahmekriterien für Anprallprüfungen und Prüfverfahren für Schutzeinrichtungen und Fahrzeugbrüstungen, Deutsches Institut für Normung e.V., Beuth Verlag, Berlin.
24. DIN EN 1317-5:2012-06, Rückhaltesysteme an Straßen: Teil_5: Anforderungen an die Produkte, Konformitätsverfahren und -bewertung für Fahrzeugrückhaltesysteme, Deutsches Institut für Normung e.V., Beuth Verlag, Berlin.
25. DIN EN 13286-47:2022-01, Unbound and hydraulically bound mixtures: Part 47: Test method for the determination of California bearing ratio, immediate bearing index and linear swelling, Deutsches Institut für Normung e. V., Beuth Verlag, Berlin.
26. DIN EN 16303:2020-10, Rückhaltesysteme an Straßen: Validierungs- und Nachweisverfahren für die Nutzung von Computersimulationen bei Anprallprüfungen an Fahrzeug-Rückhaltesysteme, Deutsches Institut für Normung e.V., Beuth Verlag, Berlin.
27. DIN EN ISO 14688-1:2020-11, Geotechnische Erkundung und Untersuchung: Teil_1: Benennung, Beschreibung und Klassifizierung von Boden, Deutsches Institut für Normung e.V., Beuth Verlag, Berlin.
28. DIN EN ISO 14688-2:2020-11, Geotechnische Erkundung und Untersuchung - Benennung, Beschreibung und Klassifizierung von Boden: Teil_2: Grundlagen für Bodenklassifizierungen, Deutsches Institut für Normung e.V., Beuth Verlag, Berlin.
29. DIN EN ISO 17892-5:2017-08, Geotechnische Erkundung und Untersuchung - Laborversuche an Bodenproben: Teil_5: Ödometerversuch mit stufenweiser Belastung, Deutsches Institut für Normung e.V., Beuth Verlag, Berlin.
30. DIN EN ISO 17892-9:2018-07, Geotechnische Erkundung und Untersuchung - Laborversuche an Bodenproben: Teil_9: Konsolidierte triaxiale Kompressionsversuche an wassergesättigten Böden, Deutsches Institut für Normung e.V., Beuth Verlag, Berlin.
31. DIN EN ISO 22476-2:2012-03, Geotechnische Erkundung und Untersuchung - Felduntersuchungen: Teil_2: Rammsondierungen, Deutsche Gesellschaft für Geotechnik e.V., Beuth Verlag, Berlin.
32. Einbauanleitung Super-Rail Eco (2020) - Version 02, Studiengesellschaft für Stahlschutzplanken e.V., Siegen, DE.
33. Elnaggar MH, Bentley KJ (2000) Dynamic analysis for laterally loaded piles and dynamic p - y curves. Canadian Geotechnical Journal 37:1166–1183. <https://doi.org/10.1139/t00-058>
34. Empfehlungen des Arbeitsausschusses "Ufereinfassungen" Häfen und Wasserstraßen EAU (2020). Deutsche Gesellschaft für Geotechnik e.V., 12. Auflage. 978-3-433-03317-3, Ernst Wilhelm & Sohn, Berlin.
35. Empfehlungen des Arbeitskreises "Baugrundndynamik" (2017). Deutsche Gesellschaft für Geotechnik e.V., 2. Auflage. 978-3-433-03210-7, Ernst Wilhelm & Sohn, Berlin.
36. Empfehlungen des Arbeitskreises "Pfähle" (2012). Deutsche Gesellschaft für Geotechnik e.V., 2. Auflage. 978-3-433-03005-9, Ernst & Sohn a Wiley brand, Berlin.

37. Goldsmith W (2015) *Impact: The theory and physical behaviour of colliding solids*, originally publ. in 1960, Dover Publications, Mineola, NY.
38. Habibagahi K, Langer JA (1984) Horizontal Subgrade Modulus of Granular Soils. Laterally Loaded Deep Foundations: Analysis and Performance:14-21. <https://doi.org/10.1520/STP36810S>
39. Hansen JB (1961) A General Formula for Bearing Capacity, Bulletin No. 11. Danish Geotechnical Institute, Copenhagen.
40. Harris W, Norman White G (2008) *X-ray Diffraction Techniques for Soil Mineral Identification*, American Society of Agronomy and Soil Science Society of America, Madison, WI, USA.
41. Herle I, Gudehus G (1999) Determination of parameters of a hypoplastic constitutive model from properties of grain assemblies. *Mechanics of Cohesive-frictional Materials* 4:461–486. [https://doi.org/10.1002/\(SICI\)1099-1484\(199909\)4:5<461:AID-CFM71>3.0.CO;2-P](https://doi.org/10.1002/(SICI)1099-1484(199909)4:5<461:AID-CFM71>3.0.CO;2-P)
42. Keil S (2017) *Dehnungsmessstreifen*, 2. Auflage, Springer Vieweg, Wiesbaden, Heidelberg.
43. Kondner RL (1963) Hyperbolic Stress-Strain Response: Cohesive Soils. *J Soil Mech and Found Div* 89:115–143. <https://doi.org/10.1061/JSFEAQ.0000479>
44. Koukoulidou A, Birle E, Heyer D (2017) *Baustoffe für standfeste Bankette*. Berichte der Bundesanstalt für Straßenwesen, Straßenbau Heft 107
45. Kramer SL (1996) *Geotechnical earthquake engineering*. Prentice-Hall international series in civil engineering and engineering mechanics, Prentice Hall, Upper Saddle River, NJ.
46. Krumbein WC, Sloss LL (1963) *Stratigraphy and sedimentation*, 2. ed., Freeman, San Francisco, California.
47. Lade P (2016) *Triaxial testing of soils*, Wiley Blackwell, Chichester West Sussex United Kingdom.
48. Lang H-J, Huder J, Amann P et al. (2011) *Bodenmechanik und Grundbau*, Springer Berlin Heidelberg, Berlin, Heidelberg.
49. LS-DYNA (2018) *Keyword user's manual: vol. II: Material models*, Livermore Software Technology Corp., United States.
50. Makris N, Gazetas G (1992) Dynamic pile-soil-pile interaction. Part II: Lateral and seismic response. *Earthquake Engng Struct Dyn* 21:145–162. <https://doi.org/10.1002/eqe.4290210204>
51. *Manual for assessing safety hardware: MASH (2016)*, Second edition. 978-1-56051-665-1, American Association of State Highway and Transportation Officials; AASHTO, Washington, DC.
52. Mašín D (2019) *Modelling of Soil Behaviour with Hypoplasticity*, Springer International Publishing, Cham, Switzerland.
53. Michie Jarvis D. (1970) *Response of Guardrail Posts During Impact*, Southwest Research Institute, San Antonio, Texas, USA.
54. Mirdamadi A (2014) *Deterministic and Probabilistic Simple Model for Single Pile Behavior under Lateral Truck Impact*, PhD Dissertation, Texas A&M University, USA.
55. Miura K, Maeda K, Toki S (1997) Method of Measurement for the Angle of Repose of Sands. *Soils and Foundations* 37:89–96. https://doi.org/10.3208/sandf.37.2_89
56. Mojdeh AP, Jean-Louis B (2020) TAMU-POST: An analysis tool for vehicle impact on in-line pile group. *Cogent Engineering* 7:1735694. <https://doi.org/10.1080/23311916.2020.1735694>

57. Montgomery DC (2013) Design and analysis of experiments, 8. ed., Wiley, Hoboken, NJ.
58. Mylonakis G.E. Crispin J.J. (2022) Analysis of pile foundations subject to static and dynamic loading, CRC Press, S.I.
59. Nasdala L (2015) FEM-Formelsammlung Statik und Dynamik, Springer Fachmedien Wiesbaden, Wiesbaden.
60. Niemunis A, Herle I (1997) Hypoplastic model for cohesionless soils with elastic strain range. *Mechanics of Cohesive-frictional Materials* 2:279–299. [https://doi.org/10.1002/\(SICI\)1099-1484\(199710\)2:4](https://doi.org/10.1002/(SICI)1099-1484(199710)2:4)
61. Nogami T, Otani J, Konagai K et al. (1992) Nonlinear Soil-Pile Interaction Model for Dynamic Lateral Motion. *J Geotech Engrg* 118:89–106. [https://doi.org/10.1061/\(ASCE\)0733-9410\(1992\)118:1\(89\)](https://doi.org/10.1061/(ASCE)0733-9410(1992)118:1(89))
62. Novak M (1974) Dynamic Stiffness and Damping of Piles. *Can Geotech J* 11:574–598. <https://doi.org/10.1139/t74-059>
63. Novak M, Aboul-Ella F, Nogami T (1978) Dynamic Soil Reactions for Plane Strain Case. *J Engrg Mech Div* 104:953–959. <https://doi.org/10.1061/JMCEA3.0002392>
64. Ogden RW (1973) Large Deformation Isotropic Elasticity—On the Correlation of Theory and Experiment for Incompressible Rubberlike Solids. *Rubber Chemistry and Technology* 46:398–416. <https://doi.org/10.5254/1.3542910>
65. Phromjan J, Suvanjumrat C (2018) Material Properties of Natural Rubber Solid Tires for Finite Element Analysis. *KEM* 775:560–564. <https://doi.org/10.4028/www.scientific.net/KEM.775.560>
66. Plaxico CA, Patzner GS, Ray MH (1998) Finite-Element Modeling of Guardrail Timber Posts and the Post-Soil Interaction. *Transportation Research Record* 1647:139–146. <https://doi.org/10.3141/1647-17>
67. Poulos HG, Davis EH (1980) Pile foundation analysis and design. Series in geotechnical engineering, Wiley, New York.
68. Prinz H, Strauß R (2018) Ingenieurgeologie, Springer, Berlin, Heidelberg.
69. RAA: Richtlinien für die Anlage von Autobahnen (2008). Forschungsgesellschaft für Straßen- und Verkehrswesen, Ausgabe 2008. FGSV R1 - Regelwerke. 9783939715511, FGSV Verlag, Köln.
70. Ray MH (1996) Repeatability of Full-Scale Crash Tests and Criteria for Validating Simulation Results. *Transportation Research Record* 1528:155–160. <https://doi.org/10.1177/0361198196152800117>
71. Ray MH, Patzner GS (1997) Finite-Element Model of Modified Eccentric Loader Terminal (MELT). *Transportation Research Record* 1599:11–21. <https://doi.org/10.3141/1599-02>
72. Reese LC, Cox WR, Koop FD (1974) Analysis of laterally loaded piles in sand. *Proceedings of the VI Annual Offshore Technology Conference, Houston, Texas, USA* OTC 2080:473–485.
73. Reese LC, van Impe WF (2011) Single piles and pile groups under lateral loading, 2nd ed., CRC Press/Balkema, Boca Raton, Florida.
74. Regimand A, Gilbert AB (1999) Apparatus and Method for Field Calibration of Nuclear Surface Density Gauges. In: Durham GN, Marr WA, Durham GN et al. (eds) *Field instrumentation for soil and rock*. ASTM American Society for Testing and Materials, West Conshohocken, Pa., 135-135-13.
75. Reid JD, Hascall JA, Sicking DL et al. (2009) Inertial Effects during Impact Testing. *Transportation Research Record* 2120:39–46. <https://doi.org/10.3141/2120-05>
76. REwS: Richtlinie für die Entwässerung von Straßen (2021). Forschungsgesellschaft für Straßen- und Verkehrswesen e.V, Ausgabe 2021, FGSV Verlag, Köln.

77. Richtlinien für die Standardisierung des Oberbaus von Verkehrsflächen (2012): RStO 12, Ausgabe 2012. FGSV R1 - Regelwerke. 9783864460210, FGSV Verlag GmbH, Köln.
78. Rudolph C, Mardfeldt B, Dührkop J (2011) Vergleichsberechnungen zur Dalbenbemessung nach Blum und mit der p-y-Methode. *geotechnik* 34:237–251. <https://doi.org/10.1002/gete.201100006>
79. Sassi A, Ghrib F (2014) Development of finite element model for the analysis of a guardrail post subjected to dynamic lateral loading. *International Journal of Crashworthiness* 19:457–468. <https://doi.org/10.1080/13588265.2014.910972>
80. Sassi A, Ghrib F (2016) Crashworthiness of guardrail posts embedded in cohesionless soils: a parametric study. *International Journal of Crashworthiness* 21:460–476. <https://doi.org/10.1080/13588265.2016.1167390>
81. Sefi F, Lav MA (2022) Evaluation of a new grain breakage factor based on the single grain crushing strength. *Transportation Geotechnics* 33:100733. <https://doi.org/10.1016/j.trgeo.2022.100733>
82. Sinnreich J, Ayithi A (2014) Derivation of p-y Curves from Lateral Pile Load Test Instrument Data. *Geotech Test J* 37:20130127. <https://doi.org/10.1520/GTJ20130127>
83. Soliman M, Cudmani R (2023) Numerical Modelling and Investigation of the Impact Behaviour of Single Guardrail Posts. *Geotechnics* 3:1135–1161. <https://doi.org/10.3390/geotechnics3040062>
84. Soliman M, Rebstock D, Cudmani R (2023) Experimental investigation of the response of guardrail posts embedded in road shoulder material under quasi-static and dynamic impact loading. *Transportation Geotechnics* 42:101104. <https://doi.org/10.1016/j.trgeo.2023.101104>
85. Suits LD, Sheahan TC, Yang K et al. (2007) Methods for Deriving p-y Curves from Instrumented Lateral Load Tests. *Geotechnical Testing Journal* 30:100317. <https://doi.org/10.1520/GTJ100317>
86. Tak Kim B, Kim N-K, Jin Lee W et al. (2004) Experimental Load–Transfer Curves of Laterally Loaded Piles in Nak-Dong River Sand. *Journal of Geotechnical and Geoenvironmental Engineering* 130:416–425. [https://doi.org/10.1061/\(ASCE\)1090-0241\(2004\)130:4\(416\)](https://doi.org/10.1061/(ASCE)1090-0241(2004)130:4(416))
87. Taylor KE (2001) Summarizing multiple aspects of model performance in a single diagram. *J Geophys Res* 106:7183–7192. <https://doi.org/10.1029/2000JD900719>
88. Teng T-L, Liang C-C, Tran T-T (2015) Effect of various W-beam guardrail post spacings and rail heights on safety performance. *Advances in Mechanical Engineering*. <https://doi.org/10.1177/1687814015615544>
89. Terzaghi K (1955) Evaluation of coefficients of subgrade modulus. *Geotechnique* V: 297–326.
90. TL SoB-StB: Technische Lieferbedingungen für Baustoffgemische und Böden zur Herstellung von Schichten ohne Bindemittel im Straßenbau (2007). Forschungsgesellschaft für Straßen- und Verkehrswesen e.V. FGSV R1 - Regelwerke. 9783939715399, FGSV Verlag, Köln.
91. Wichtmann T (2018) Kalibrierung der Parameter eines hypoplastischen Stoffmodells für granulare Böden: Vorlesungsskript, Bauhaus-Universität Weimar, DE.
92. Wichtmann T, Triantafyllidis T (2009) On the correlation of “static” and “dynamic” stiffness moduli of non-cohesive soils. *Bautechnik* 86:28–39. <https://doi.org/10.1002/bate.200910039>
93. Woo KS, Lee DW, Ahn JS (2018) Impact Behavior of a Laterally Loaded Guardrail Post near Slopes by Hybrid SPH Model. *Advances in Civil Engineering* 2018:1–12. <https://doi.org/10.1155/2018/9479452>

94. Wright Amy E., Ray MH (1996) Characterizing Guardrail Steel for LS-DYNA3D Simulations. *Transportation Research Record* 1528:138–145. <https://doi.org/10.1177/0361198196152800115>
95. Wu W, Thomson R (2007) A study of the interaction between a guardrail post and soil during quasi-static and dynamic loading. *International Journal of Impact Engineering* 34:883–898. <https://doi.org/10.1016/j.ijimpeng.2006.04.004>
96. ZTV E-StB: Zusätzliche technische Vertragsbedingungen und Richtlinien für Erdarbeiten im Straßenbau (2017). Forschungsgesellschaft für Straßen- und Verkehrswesen e.V. FGSV R1 - Regelwerke. 978-3-86446-188-0, FGSV Verlag, Köln.
97. ZTV FRS: Zusätzliche technische Vertragsbedingungen und Richtlinien für Fahrzeug-Rückhaltesysteme (2017). Forschungsgesellschaft für Straßen- und Verkehrswesen e.V. FGSV R1 - Regelwerke. 978-3-86446-207-8, FGSV Verlag, Köln.
98. ZTV SoB-StB: Zusätzliche Technische Vertragsbedingungen und Richtlinien für den Bau von Schichten ohne Bindemittel im Straßenbau (2020). Forschungsgesellschaft für Straßen- und Verkehrswesen e.V. FGSV R1 - Regelwerke. 978-3-86446-242-9, FGSV Verlag, Köln.

Appendix [A]: In-situ soil testing

A.1 Dynamic probing logs

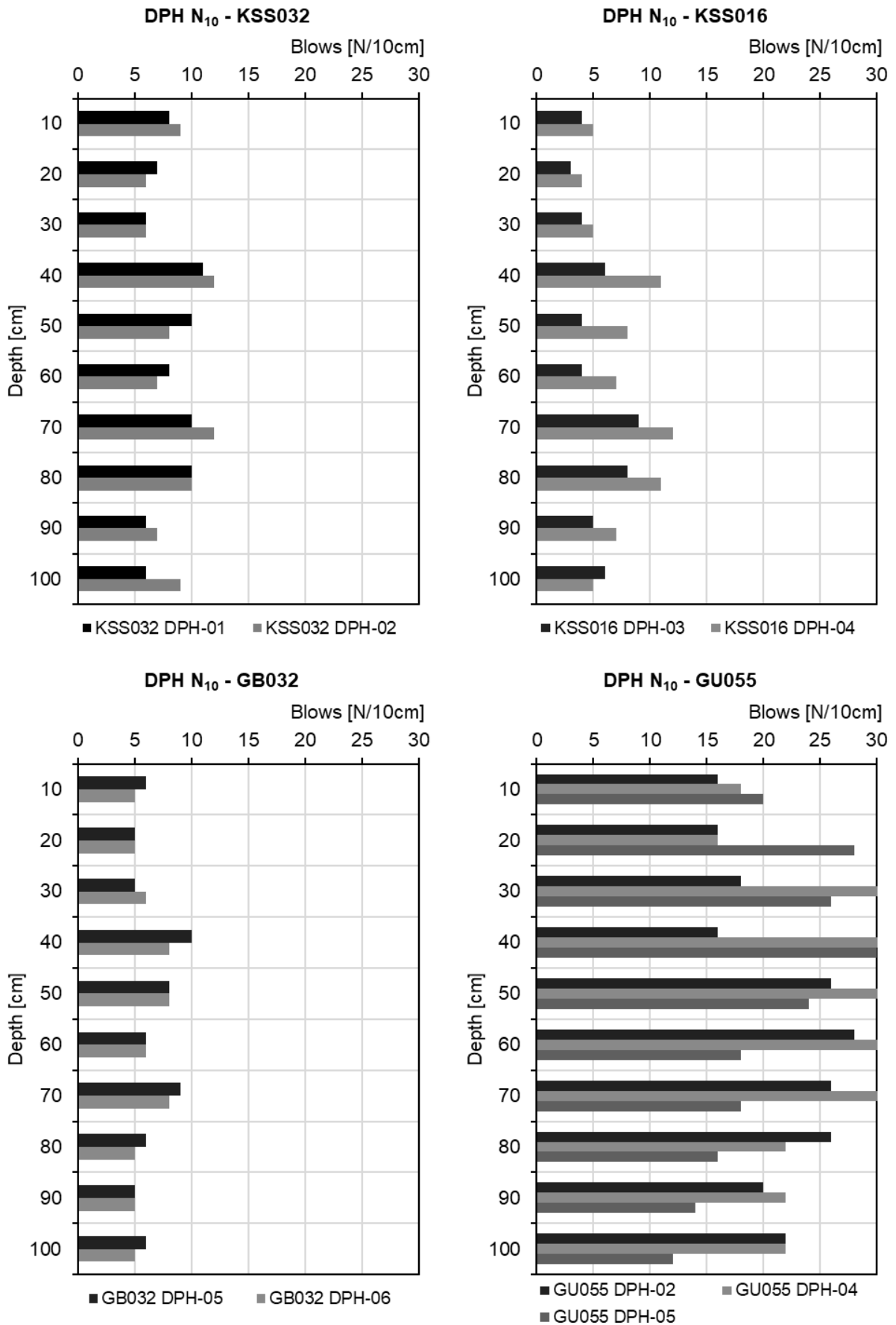


Fig. A1: Heavy dynamic probing logs (DPH) of the investigated road shoulder materials

A.2 Dynamic plate load test

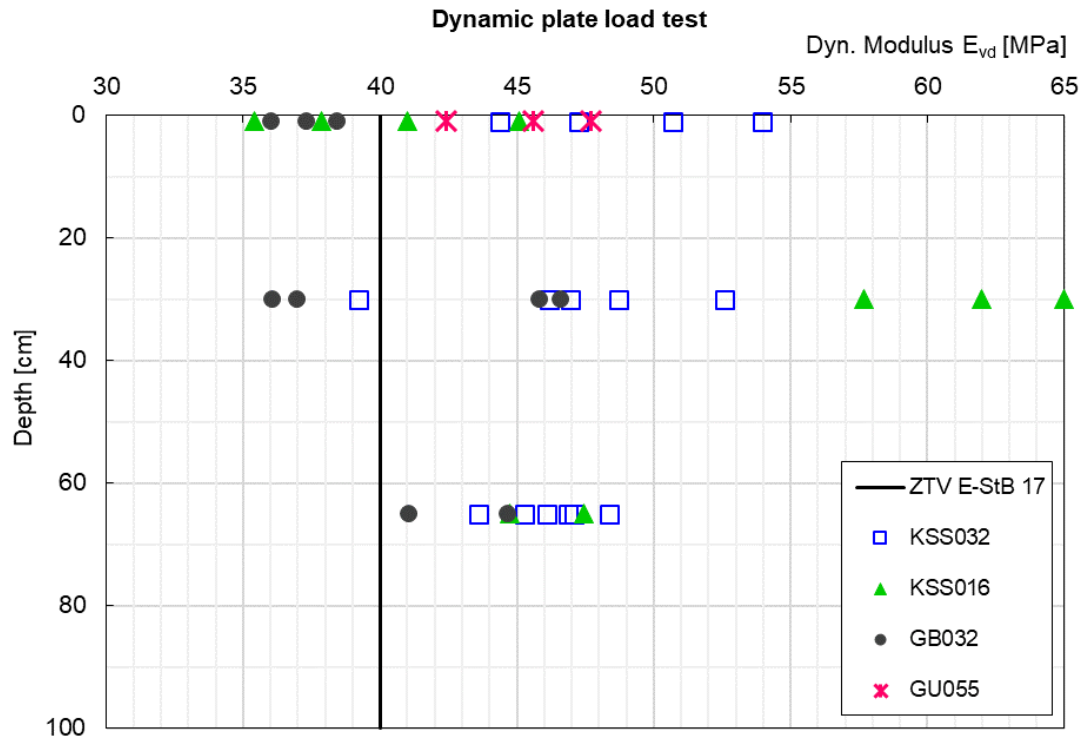


Fig. A2: Dynamic deformation modulus E_{vd} determined using the dynamic plate load test at the top of each layer during earthworks

A.3 Field dry density

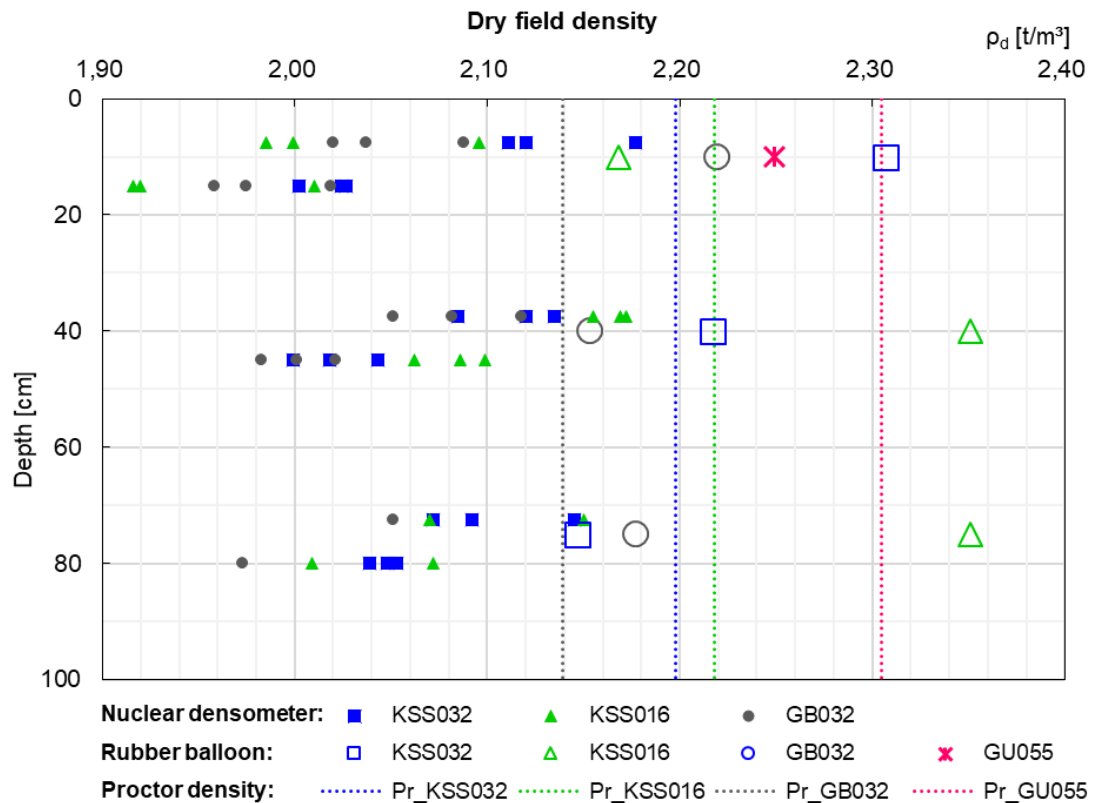
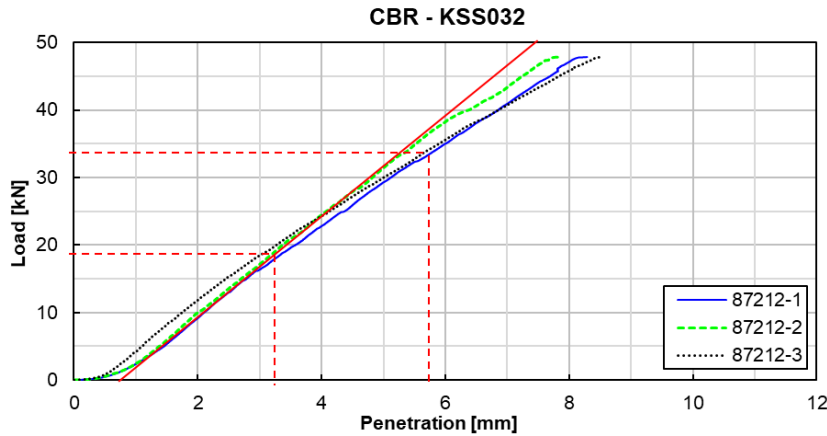


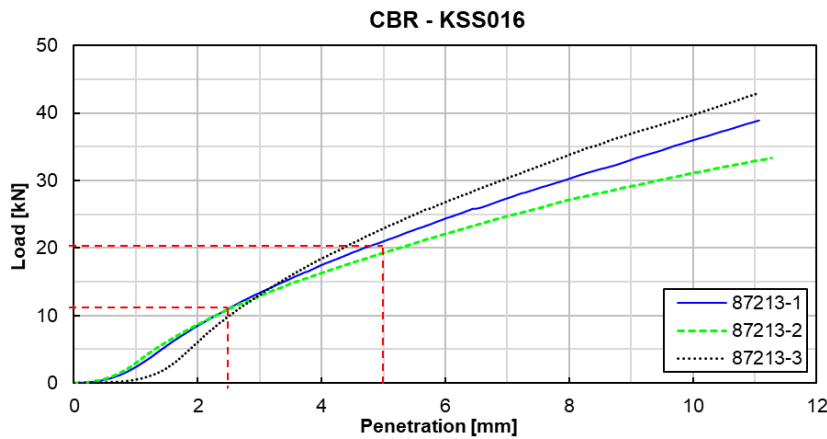
Fig. A3: Results of the determination of the field dry density using various methods

Appendix [B]: Laboratory test protocols

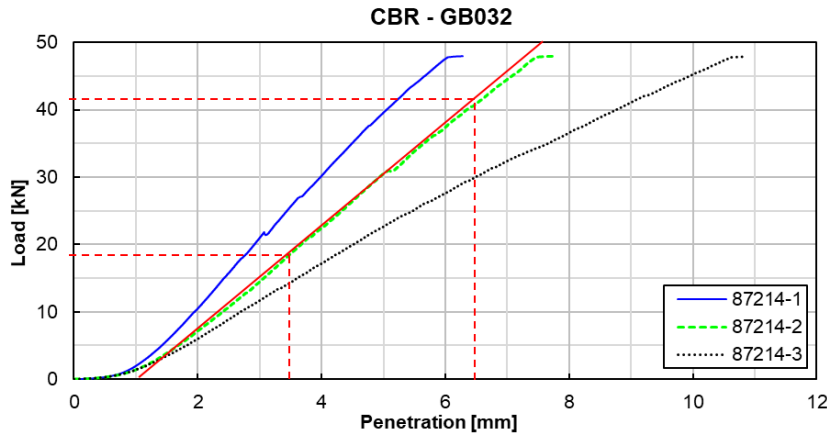
B.1 California bearing ratio tests



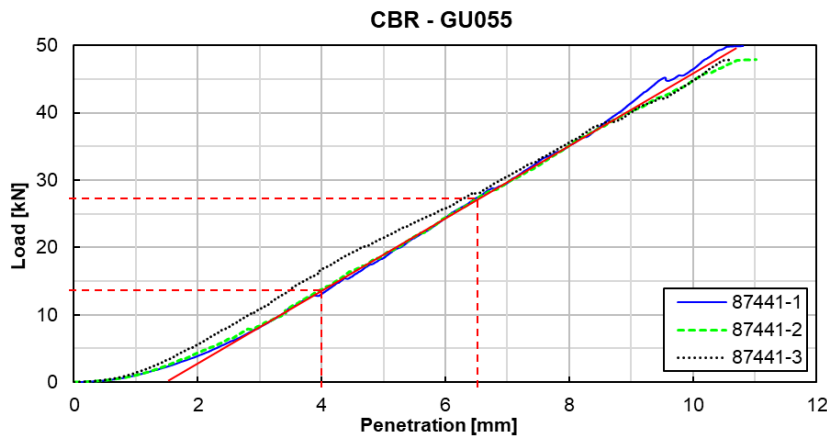
w [mm]	F [mm]
3.2	18.5
5.7	33.0
CBR [%]	140%
	165%



w [mm]	F [mm]
2.5	11.0
5.0	20.0
CBR [%]	83%
	100%



w [mm]	F [mm]
3.5	18.6
6.0	37.3
CBR [%]	141%
	187%



w [mm]	F [mm]
4.0	13.5
6.5	27.5
CBR [%]	102%
	138%

Fig. B1: Load-penetration curves and CBR-values of the investigated road shoulder materials

B.2 Large-Oedometer test results

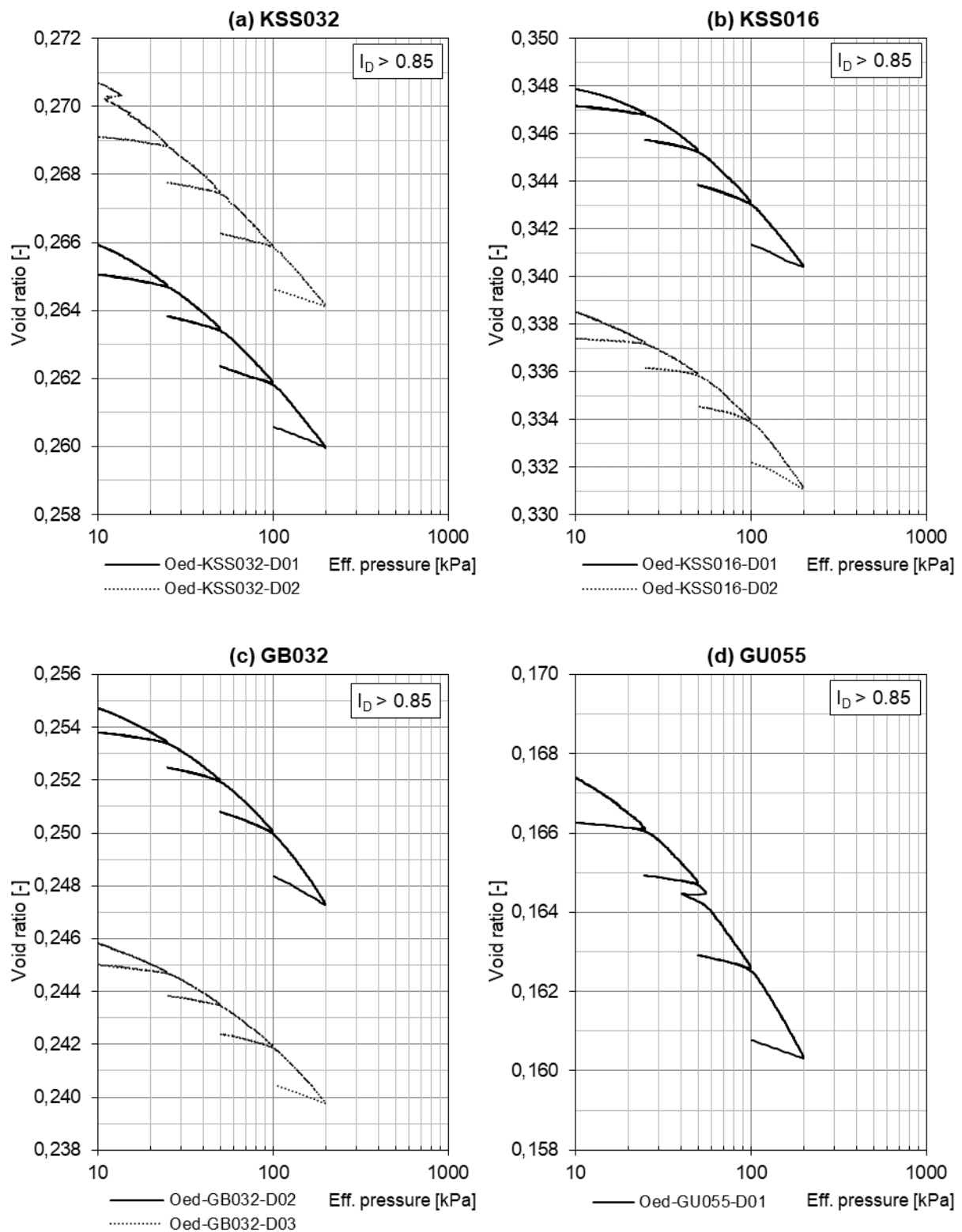


Fig. B2: Results of the oedometer tests conducted on very dense road shoulder material specimens ($e - \log \sigma'$ curves)

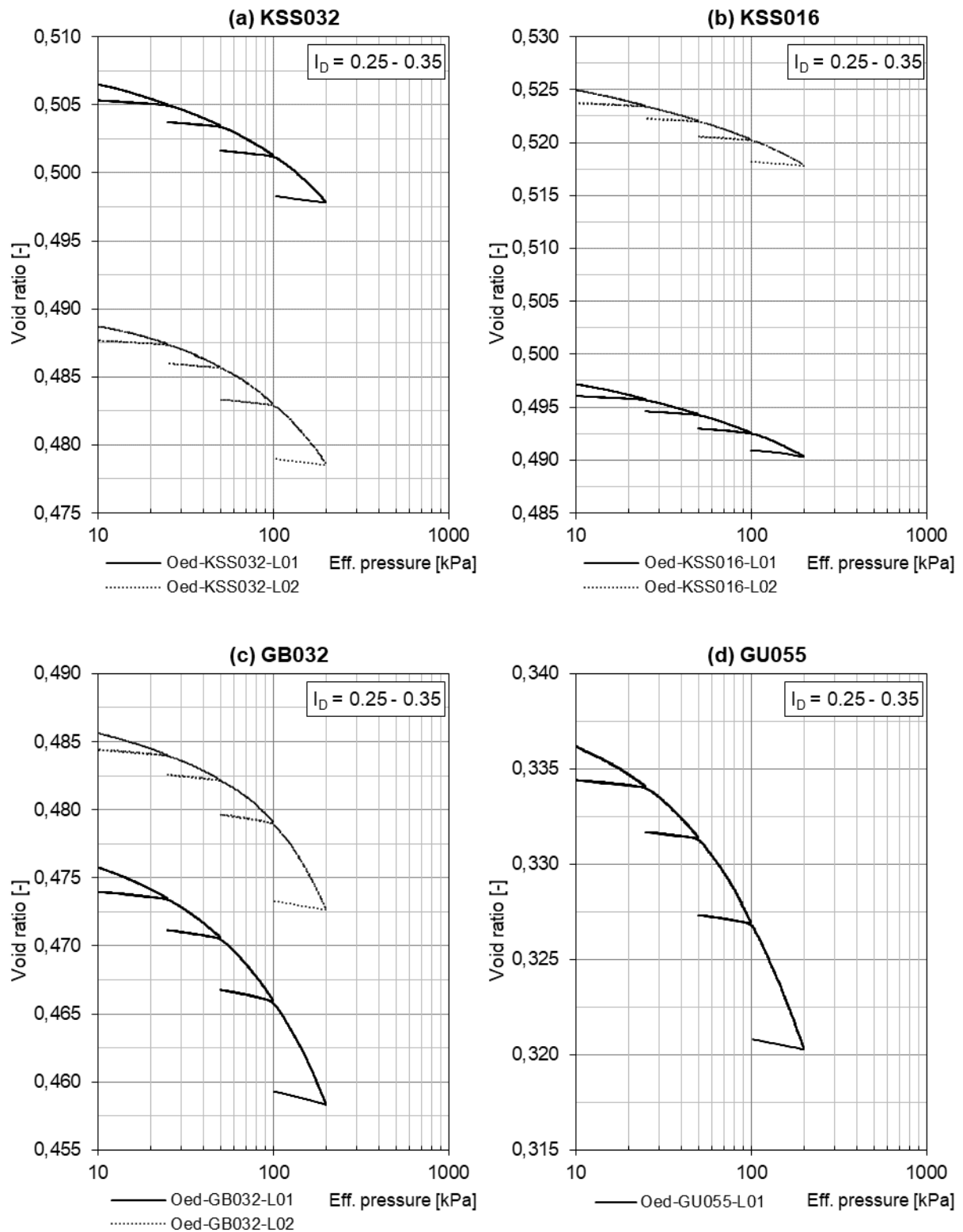
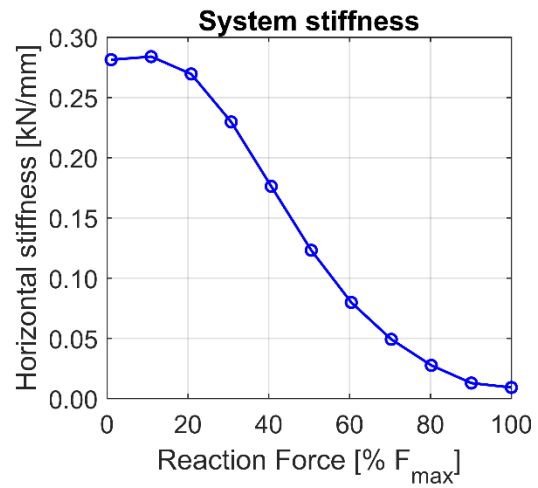
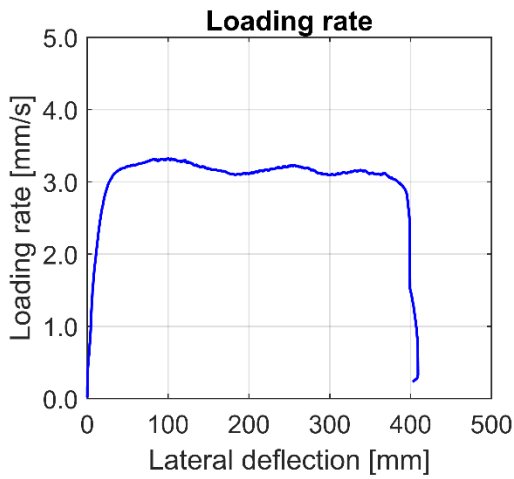
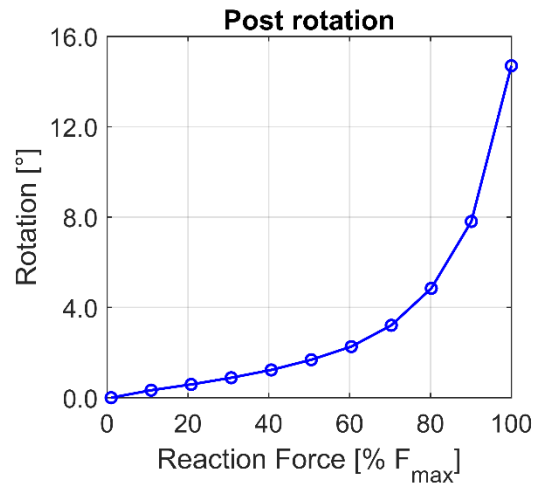
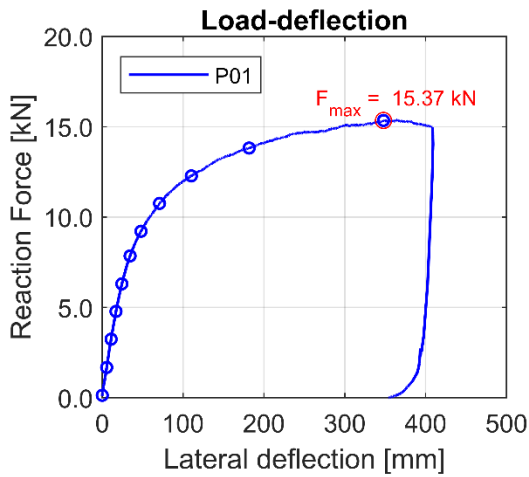


Fig. B3: Results of the oedometer tests conducted on loose road shoulder material specimens (e – log σ' curves)

Appendix [C]: Quasi-static tests

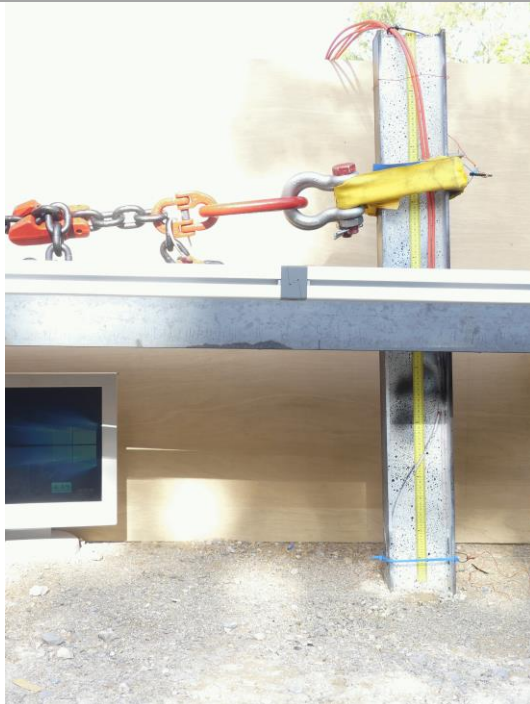
Reference Test No. P01

IPE120, KSS032, strong axis, t=100 cm



Sequential photographs

F=10% F_{max} = 1.54 kN, u=5 mm

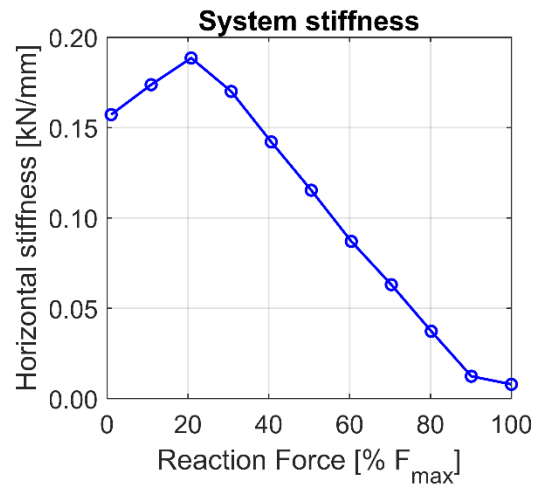
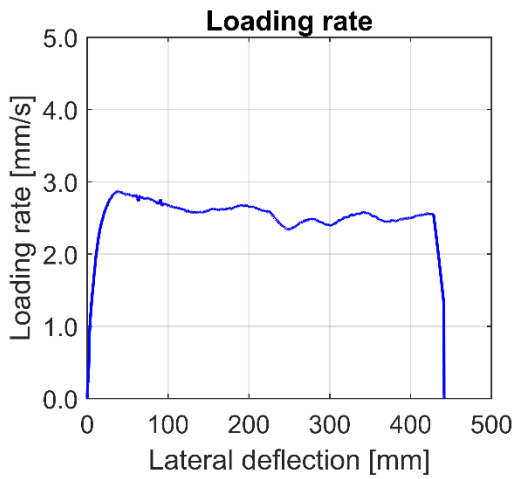
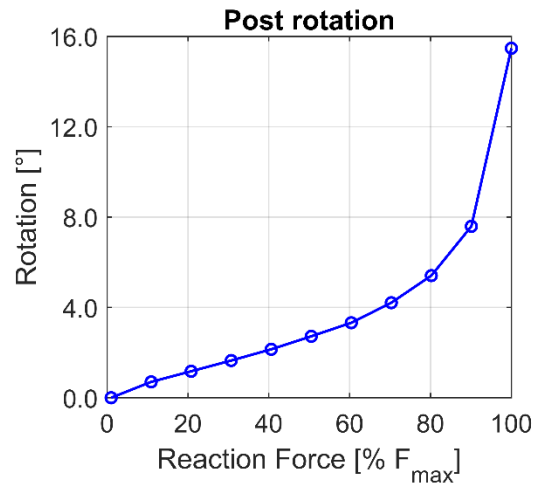
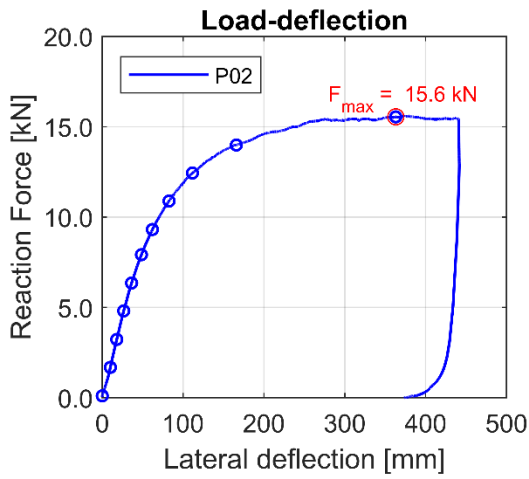


F=100% F_{max} = 15.37 kN, u=340 mm



Reference Test No. P02

IPE120, KSS032, strong axis, t=100 cm



Sequential photographs

F=10% F_{max} = 1.56 kN, u=9 mm

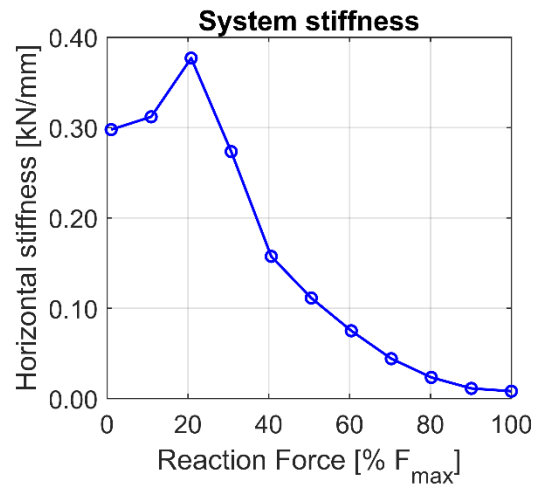
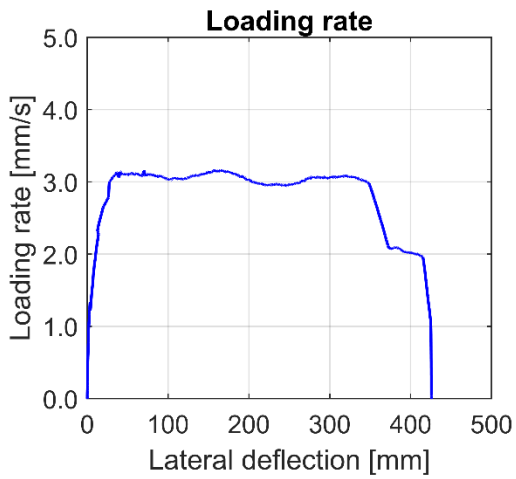
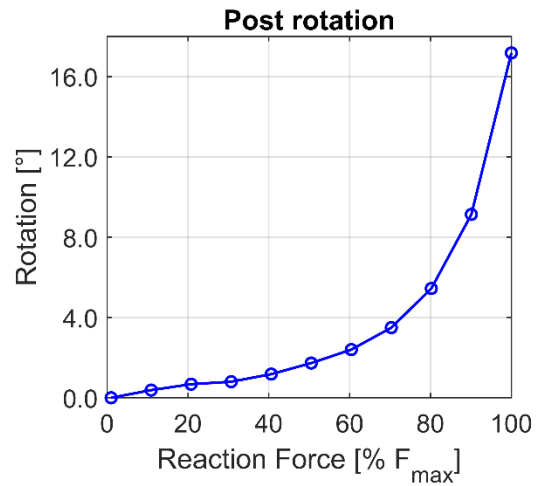
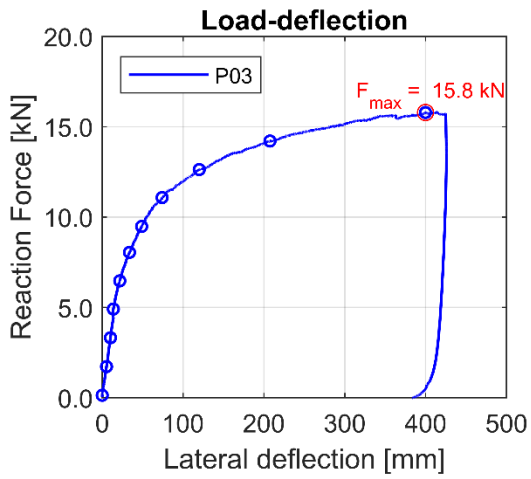


F=100% F_{max} = 15.60 kN, u=349 mm



Reference Test No. P03

IPE120, KSS032, strong axis, t=100 cm

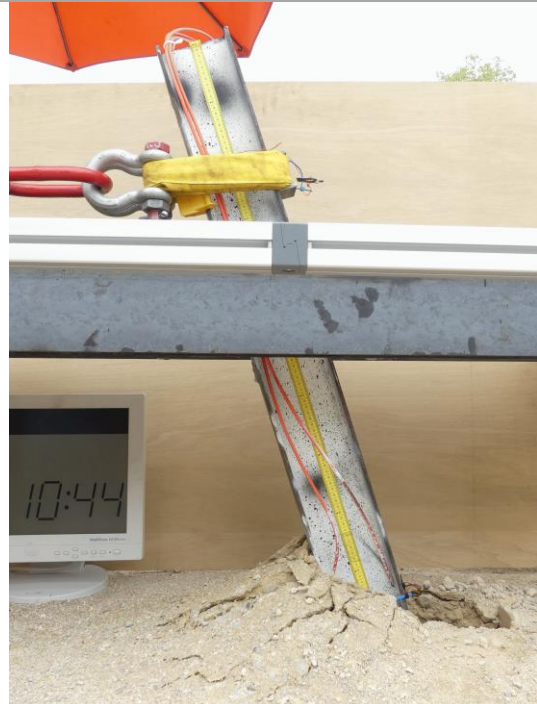


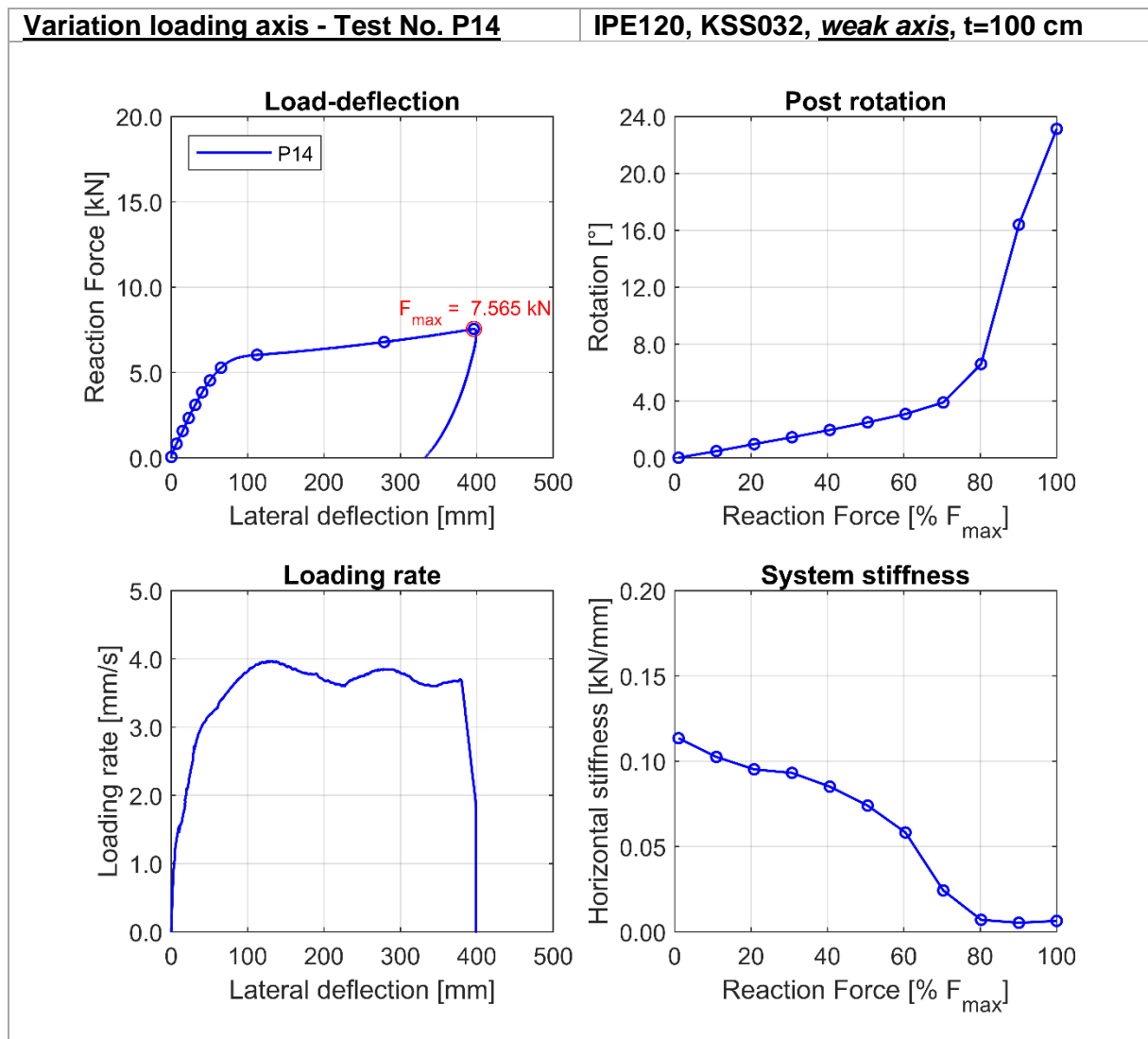
Sequential photographs

F=10% F_{max} = 1.58 kN, u=5 mm



F=100% F_{max} = 15.80 kN, u=393 mm





Sequential photographs

F=10% $F_{max} = 0.76 \text{ kN}$, u=5 mm

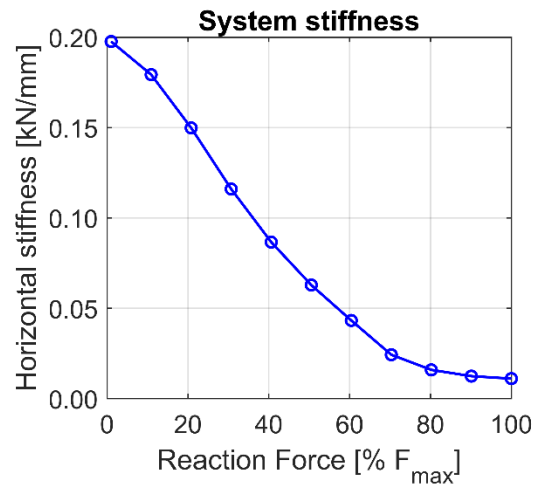
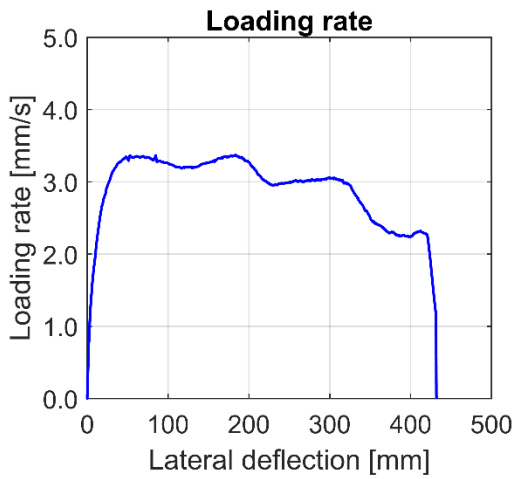
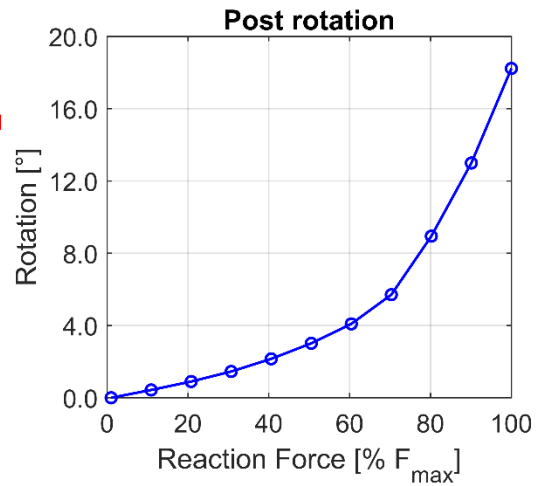
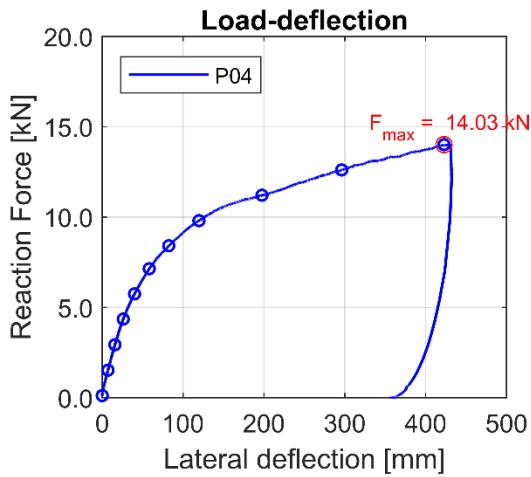


F=100% $F_{max} = 7.57 \text{ kN}$, u=385 mm



Variation post section - Test No. P04

C125, KSS032, strong axis, t=100 cm



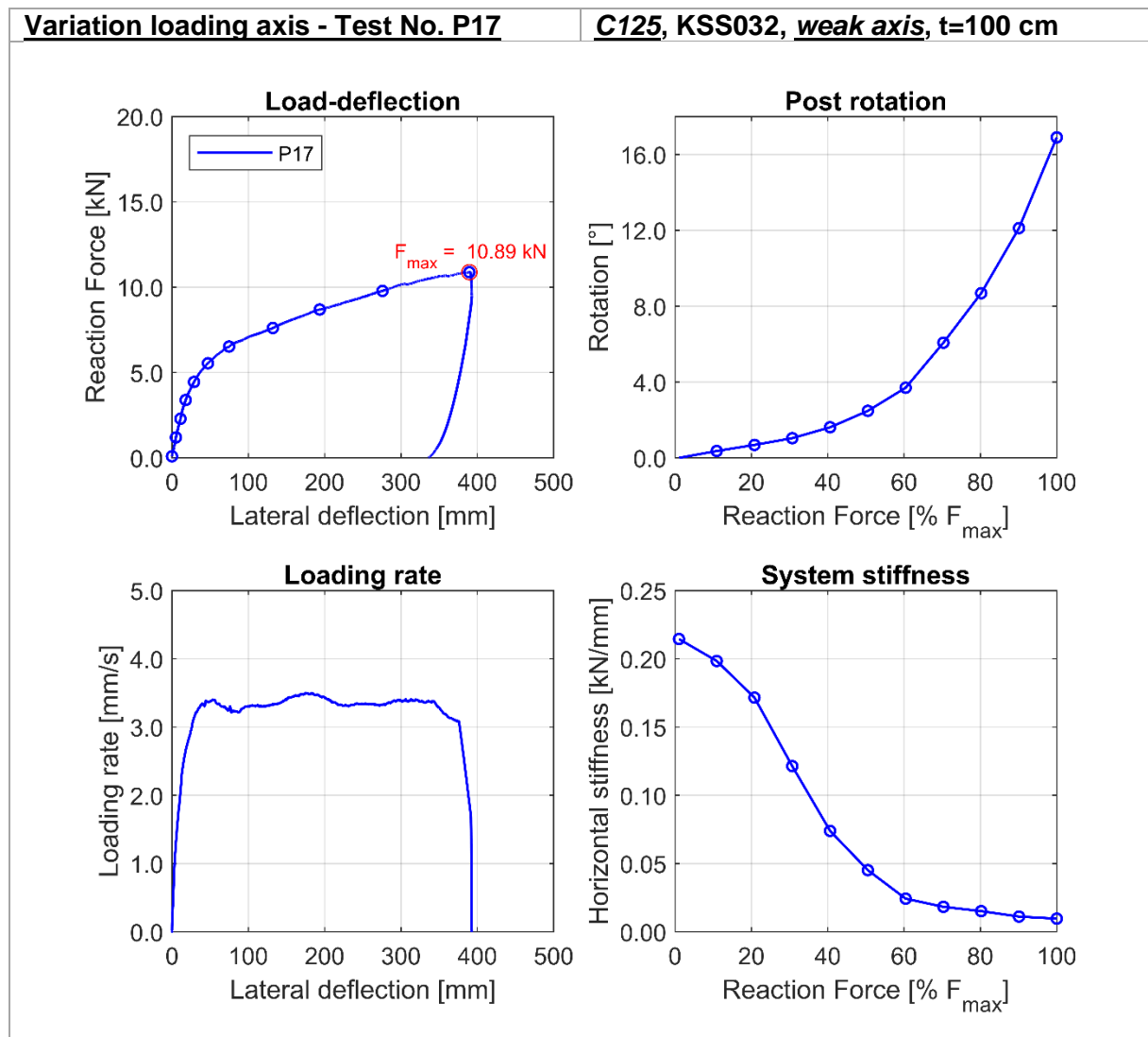
Sequential photographs

F=10% F_{max} = 1.40 kN, u=5.9 mm



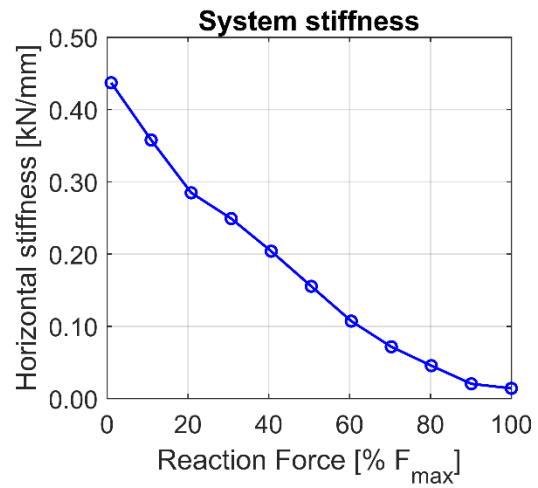
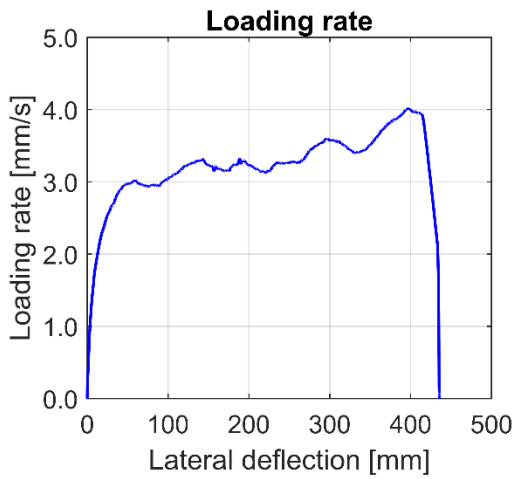
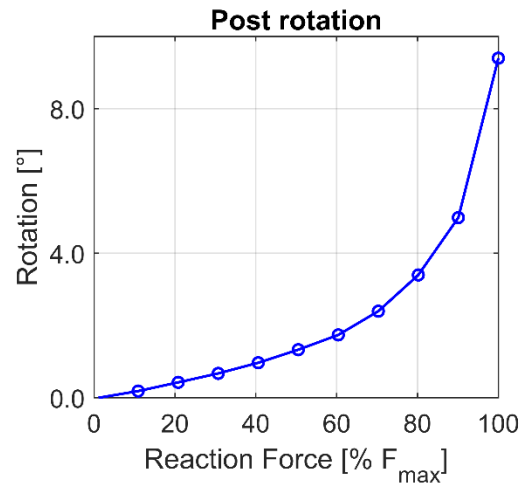
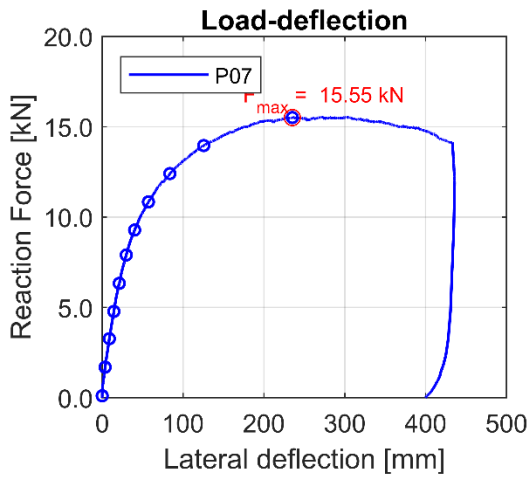
F=100% F_{max} = 14.03 kN, u=416.4 mm





Variation post section - Test No. P07

HEB120, KSS032, strong axis, t=100 cm



Sequential photographs

F=10% F_{max} = 1.56 kN, u=3.0 mm

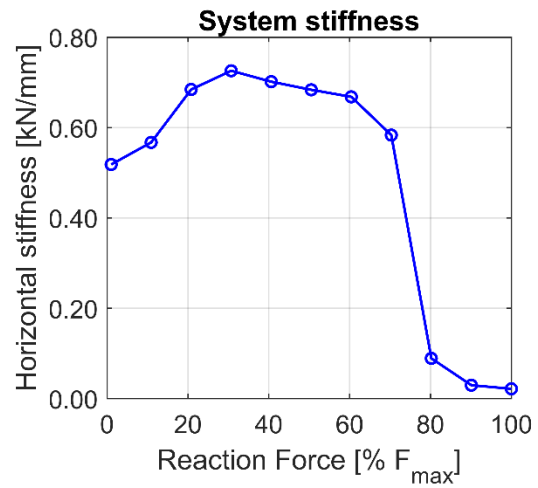
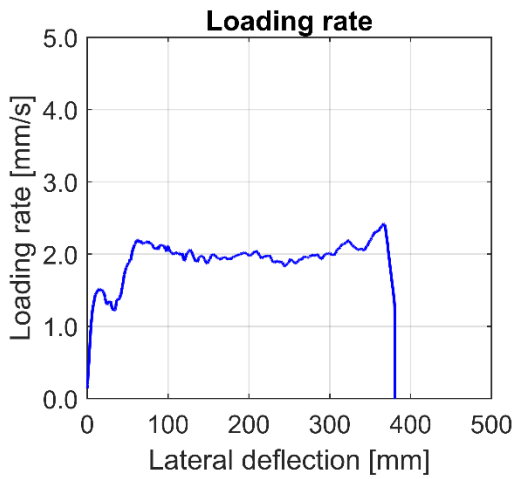
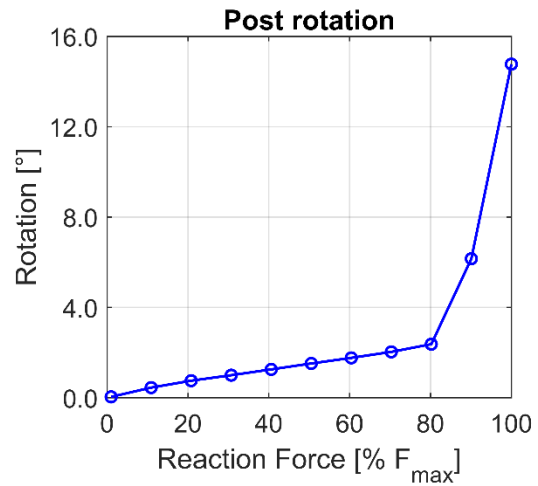
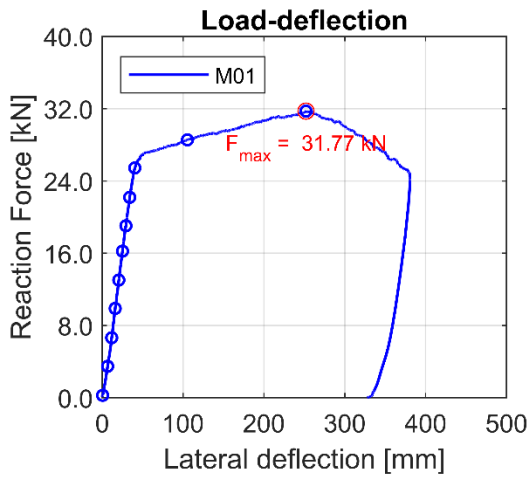


F=100% F_{max} = 15.56 kN, u=221.2 mm



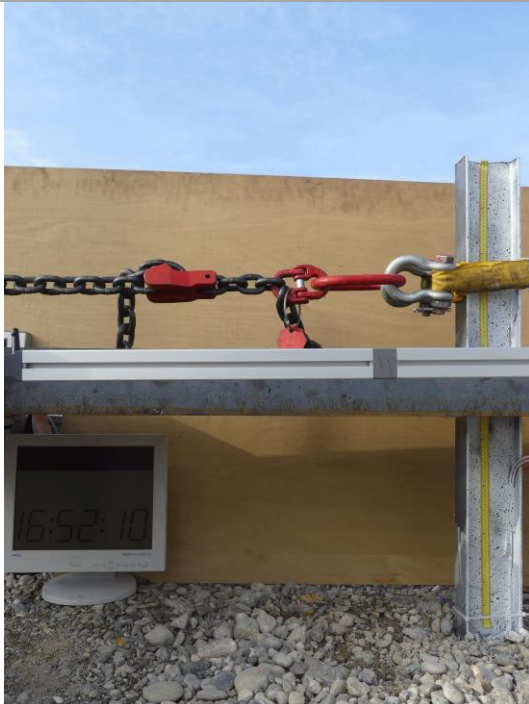
Variation soil material - Test No. M01

IPE120, GU055, strong axis, t=100 cm



Sequential photographs

F=10% F_{max} = 3.18 kN, u=6.0 mm

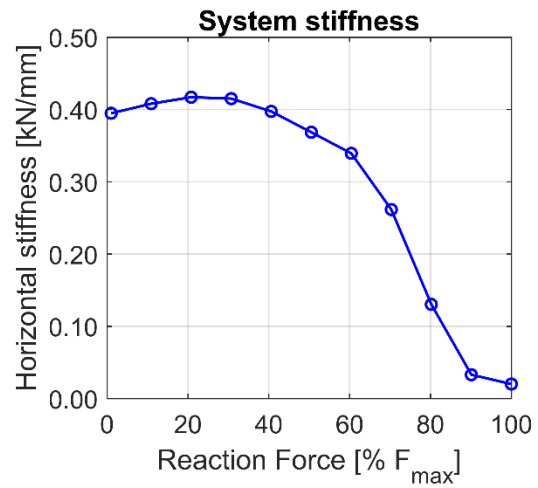
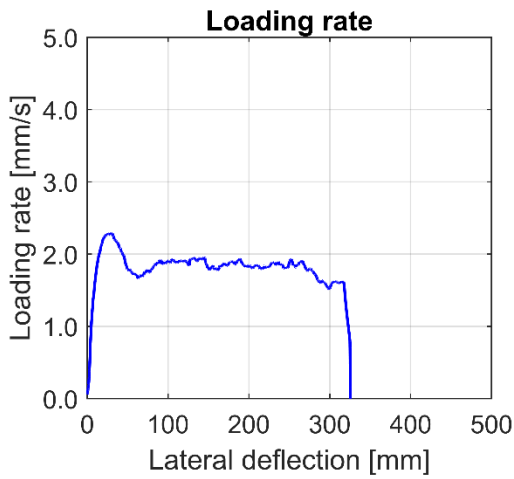
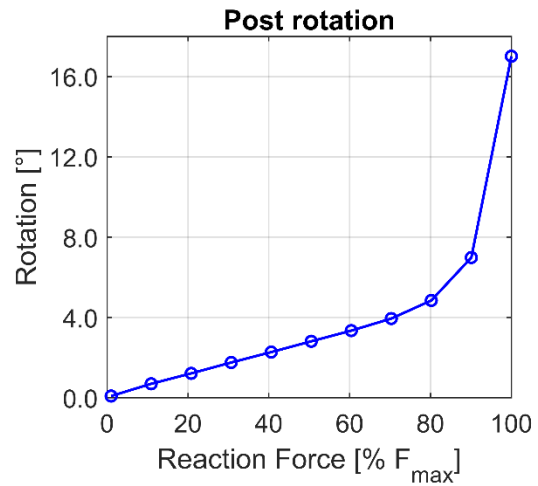
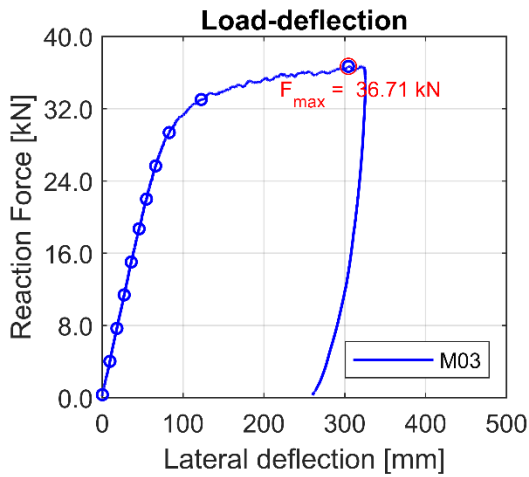


F=100% F_{max} = 31.77 kN, u=251.7 mm



Variation soil material - Test No. M03

C125, GU055, strong axis, t=100 cm



Sequential photographs

F=10% F_{max} = 3.67 kN, u=8.6 mm

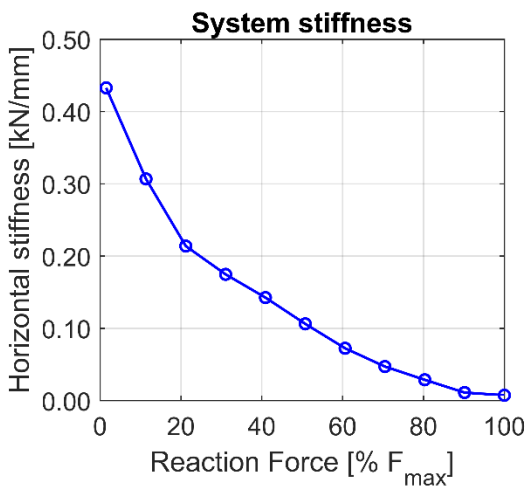
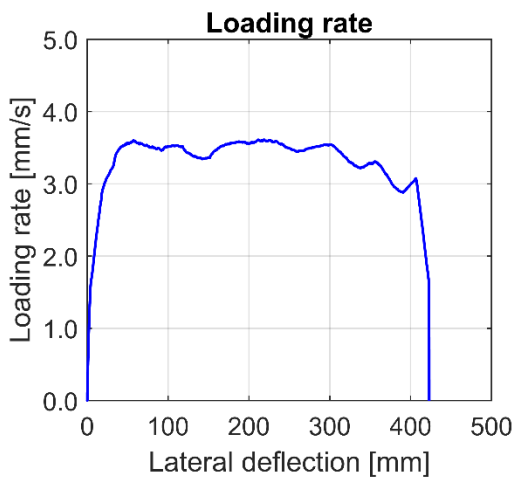
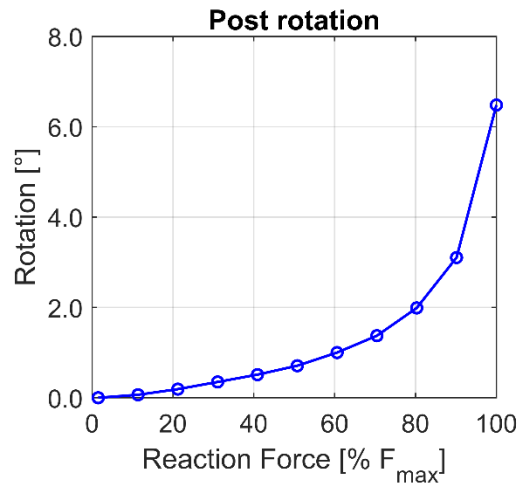
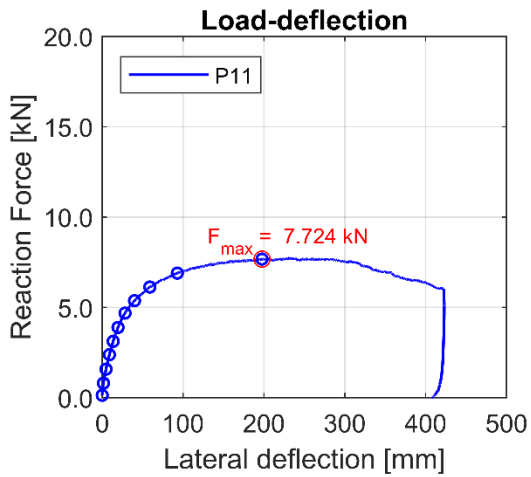


F=100% F_{max} = 36.71 kN, u=303.8 mm



Variation embed. length - Test No. P11

IPE120, KSS032, strong axis, $t=80\text{ cm}$



Sequential photographs

$F=10\% F_{max} = 0.77\text{ kN}$, $u=1.0\text{ mm}$

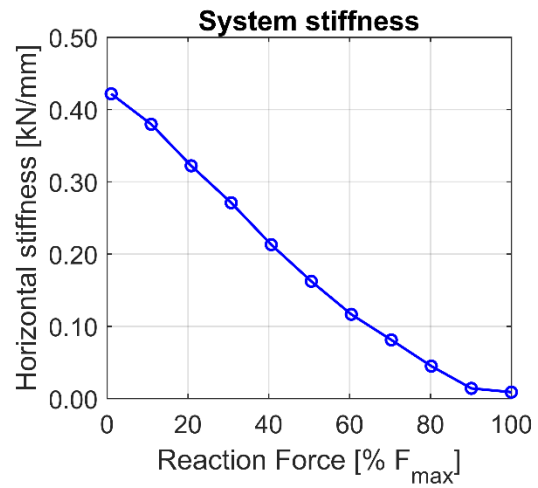
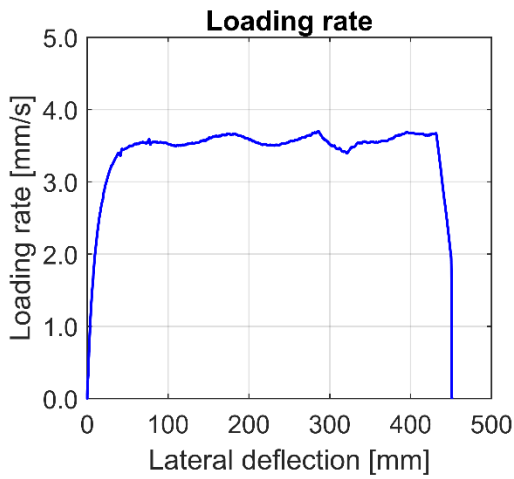
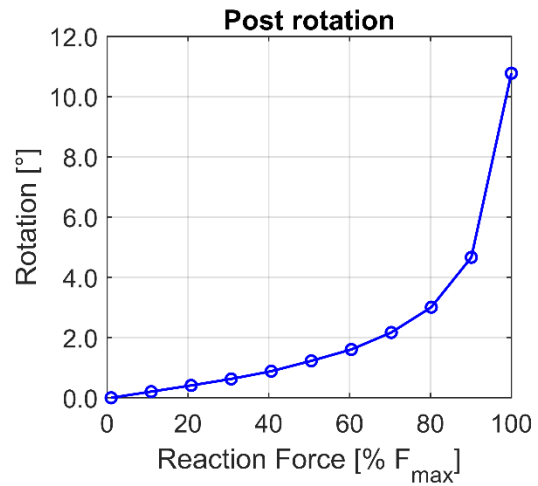
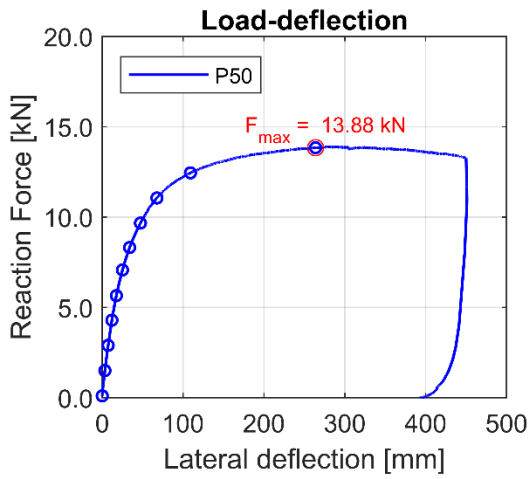


$F=100\% F_{max} = 7.72\text{ kN}$, $u=186.0\text{ mm}$



Variation soil material - Test No. P50

IPE120, *KSS016*, strong axis, t=100 cm



Sequential photographs

F=10% $F_{max} = 1.39 \text{ kN}$, u=2.8 mm



F=100% $F_{max} = 13.88 \text{ kN}$, u=250.7 mm



